cigre Turkey

EISSN 2791-6049

# TEPES

## TURKISH JOURNAL OF ELECTRICAL POWER AND ENERGY SYSTEMS

VOLUME 2 • ISSUE 2 • OCTOBER 2022

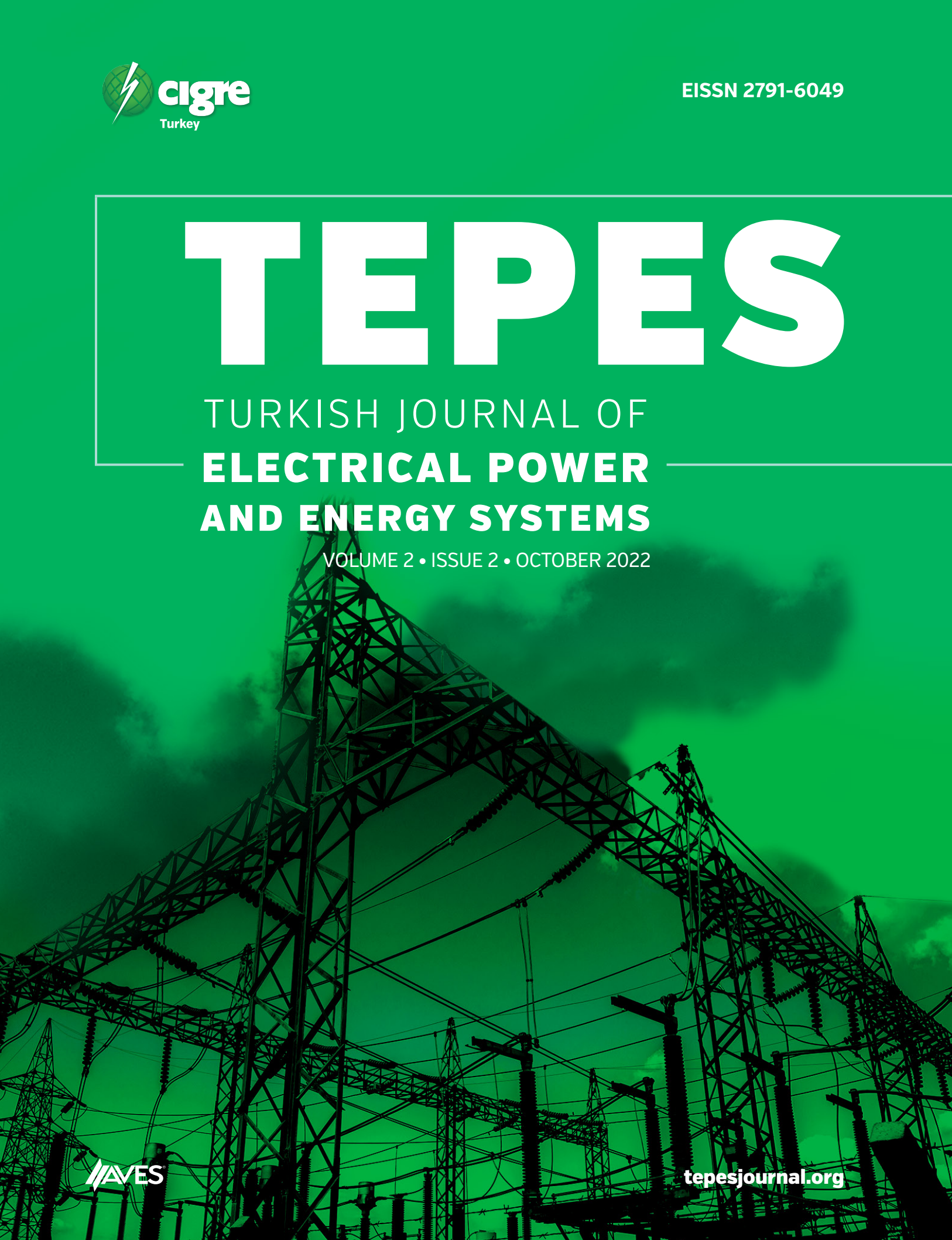

AVES

tepesjournal.org

cigre Turkey

TEPES
TURKISH JOURNAL OF
ELECTRICAL POWER
AND ENERGY SYSTEMS



AVES

**Founder**
İbrahim KARA

**General Manager**
Ali ŞAHİN

**Publishing Directors**
İrem SOYSAL
Gökhan ÇİMEN

**Publication Coordinators**
Arzu ARI
Deniz KAYA
Bahar ALBAYRAK
Gamze BİLGEN
Irmak BERBEROĞLU
Alara ERGİN
Hira Gizem FİDAN
Vuslat TAŞ
İrem ÖZMEN

**Web Coordinators**
Sinem Fehime KOZ
Doğan ORUÇ

**Finance Coordinator**
Elif YILDIZ ÇELİK

**Contact**
**Address** : Büyükdere Cad. No: 105/9 Şişli, İstanbul, Turkey
**Phone** : +90 212 217 17 00
**E-mail** : info@avesyayincilik.com

cigre Turkey

TEPES
TURKISH JOURNAL OF
ELECTRICAL POWER
AND ENERGY SYSTEMS

cigre Turkey

TEPES
TURKISH JOURNAL OF
ELECTRICAL POWER
AND ENERGY SYSTEMS

# AIMS AND SCOPE

Turkish Journal of Electrical Power and Energy Systems (TEPES) is an international, scientific, open access periodical published in accordance with independent, unbiased, and double-blinded peer-review principles. The journal is the official online-only publication with the support of Association of Turkish Electricity Industry (TESAB) and led by CIGRE Turkish National Committee. and it is published biannually in April and October. The publication language of the journal is English.

TEPES aims to contribute to the literature by publishing manuscripts at the highest scientific level on all fields of electrical power and energy systems. The journal publishes original research and review articles that are prepared in accordance with ethical guidelines.

The scope of the journals includes but not limited to:

1. Power Generation, Transmission and Distribution
- Conventional and renewable power generation
- Transmission systems
- Distribution Systems, automation and control
- Energy efficiency
- Electromagnetic analysis and compatibility in power systems
- HVDC and flexible AC transmission system (FACTS)
- Renewable energy technologies and system
- Transmission and distribution equipment
- Insulated cables
- Overhead lines
- Substations
- Electrical Power System Protection
- Smart-Grid
- Plasma physics and the pulsed power technology
- Information systems and telecommunication
- Electric vehicles and charging networks
- Measurement
- Power System control
- Demand Response

2. Power System Management
- Power system development and economics
- Power system operation, planning and control
- Power system environmental performance
- Power system technical performance
- Electricity markets and regulation
- Load modeling, estimation and forecast

3. High-Voltage Techniques
- Measurement systems
- Electrical materials
- Emerging test techniques
- Insulation condition and coordination in power systems
- Over-voltage, lightning protection and grounding
- Ultra-High Voltage (UHV) technologies
- Electrical installations

4. Electrical Machines
- Power electronics
- Electrical Machines and Drives
- Power transformers and reactors
- Design of Electrical Machines for Sustainable Energy Applications

TEPES is currently indexed in Gale.

The target audience of the journal includes academicians, specialists, researchers and professionals who are working and interested in the field of electrical power and energy systems.

The editorial and publication processes of the journal are shaped in accordance with the guidelines of the Institute of Electrical and Electronics Engineers (IEEE), the World Commission on the Ethics of Scientific Knowledge and Technology (COMEST), Council of Science Editors (CSE), Committee on Publication Ethics (COPE), European Association of Science Editors (EASE), and National Information Standards Organization (NISO). The journal is in conformity with the Principles of Transparency and Best Practice in Scholarly Publishing (doaj.org/bestpractice).

Processing and publication are free of charge with the journal. No fees are requested from the authors at any point throughout the evaluation and publication process. All manuscripts must be submitted via the online submission system, which is available at www.tepesjournal.org. The journal guidelines, technical information, and the required forms are available on the journal's web page.

All expenses of the journal are covered by the CIGRE Turkish National Committee. Potential advertisers should contact the Editorial Office. Advertisement images are published only upon the Editor-in-Chief's approval.

Statements or opinions expressed in the manuscripts published in the journal reflect the views of the author(s) and not the opinions of the CIGRE Turkish National Committee, editors, editorial board, and/or publisher; the editors, editorial board, and publisher disclaim any responsibility or liability for such materials.



You can find the current version of the Instructions to Authors at https://tepesjournal.org/.

Editor in Chief: Belgin EMRE TÜRKAY
Address: Department of Electrical Engineering, İstanbul Technical University (ITU) Faculty of Electrical and Electronics Engineering, İstanbul, Turkey
E-mail: info@tepesjournal.org

Publisher: AVES
Address: Büyükdere Cad., 105/9 34394 Mecidiyeköy, Şişli, İstanbul, Turkey
Phone: +90 212 217 17 00
Fax: +90 212 217 22 92
E-mail: info@avesyayincilik.com

cigre Turkey

TEPES
TURKISH JOURNAL OF
ELECTRICAL POWER
AND ENERGY SYSTEMS

# CONTENTS

## RESEARCH ARTICLES



## REVIEWS

cigre Turkey

TEPES
TURKISH JOURNAL OF ELECTRICAL POWER AND ENERGY SYSTEMS

TEPES, Vol. 2, Issue. 2, 103-114, 2022 **DOI:** 10.5152/tepes.2022.21006

RESEARCH ARTICLE

# Presentation of the New Method for Simultaneous Estimation of the Parameters and the Charge Situation of Used Batteries in Hybrid Vehicles

**Monireh Ahmadi**

Department of Electrical Engineering, Malekan Branch, Islamic Azad University, Malekan, Iran

**Cite this article as:** M. Ahmadi. Presentation of the new method for simultaneous estimation of the parameters and the charge situation of used batteries in hybrid vehicles. *Turk J Electr Power Energy Syst,* 2022; 2(2), 103-114.

## ABSTRACT

Estimating the state of charge (SOC) of a battery in the lithium-ion batteries used in hybrid vehicles is of high significance to ensure safe operation and to prevent overmuch charging and discharging. Despite the great importance of the parameter SOC, this parameter cannot be directly measured from the battery terminals. Thus, there is the need to estimate it. So far, various methods for estimating the SOC of lithium-ion batteries have been introduced. In this paper, by using the estimator of recursive least squares, firstly, the battery parameters are estimated and calculated and also the modified particle filter has been used for estimating the SOC of the battery. The standard particle filter has the problem of particle degeneracy phenomenon that decreases the estimation accuracy. Thus, in modified filter based PSO , the difference evolutionary algorithm (DEA) and Markov chain Monte Carlo (MCMC) applied to the standard PF that causes the estimation of SOC more accurate and consistent. To obtain an accurate and reliable method for estimating SOC, the desired battery must be modeled that in this paper, the first order resistor capacitor (RC) model has been used to have the high accuracy and low calculation complexity. This model is able to model the dynamic behavior of battery and for this reason it is suitable for hybrid vehicles application. To evaluate the performance of the proposed method, this method is compared with other methods that results represent the effective performance of the proposed method compared to other methods.

**Index Terms—**Hybrid vehicle, state of charge, particle filter, recursive least squares, lithium-ion battery

## I. INTRODUCTION

Todays, reducing of the fossil fuels has increased the need for discovering the renewable raw materials to design the stable systems and consistent with environment. The generation resources of renewable energies such as wind energy, sun energy, and hydropower energy and etc. are not steady and these energies must be saved somehow. The best storage system is battery. Due to the many advantages such as high power, high energy density, high voltage, less pollution, no effect of memory, longer lifetime and less self-discharge rate, the lithium-ion batteries have been vastly used compared to the other batteries Solenoid and toroid coils are the most common usage in HTS-SMES devices. Solenoids can be simply built and provide high stored energy per unit of the conductor. In comparison to toroid coils, due to their simpler construction solenoids are often preferred, but suffer from remarkable stray field [1]. Many researches have investigated the solenoid and toroid HTS-SMES coil design problem from different aspect such as coil volume, magnet volume, uniformity of the magnetic field inside the magnet and stray field. In [2] design of SMES solenoid considered the coil volume and magnet volume optimization by using Non-dominant sorting genetic algorithm (NSGA-II) is adopted for the two objective optimization. In [3] the objectives include the minimization of the solenoid volume and the uniformity of the magnetic field inside the magnet based on Pareto competition based evolutionary strategy. In order to reduce the leakage magnetic field and the vertical magnetic field the toroid magnet structure presented in [4]. In [5] proposed a cost estimation method of an HTS-SMES, which synthetically considers the design, operation, maintenance. In [6] the relationship between the maximum magnetic flux density within coil and superconducting wire usage of the SMES coil composed of solenoid or toroid coil wound by MgB2,Bi2223, REBCO wire was investigated.

They considered objective function optimization design of the HTS-SMES coil separately and not a comprehensive method.

For cover the problem in mentioned above, in this paper proposed three objective optimization model for HTS-SMES step-shaped cross sectional solenoid coil as, first objective function is mechanical stress of the HTS-SMES step-shaped coil, second objective function

**Corresponding author:** Monireh Ahmadi, e-mail: elec.ahmadi@gmail.com

**Received:** February 16, 2022
**Accepted:** March 8, 2022
**Publication Date:** May 12, 2022

is uniformity of the magnetic coil and third objective function is step-shaped solenoid coil volume and related constraints is that expressed as next by using a multi objective evolutionary algorithm based on decomposition (MOEA/D). [7]. For better operation of the lithium-ion battery and to ensure the safety and longer lifetime of which, there is a significant and fundamental need to the battery management system (BMS). The battery management system must have capability to supply the SOC accurate estimation, the state of battery integrity, and useful lifetime remaining in cell [8]. Estimating the state of charge of battery is one of the most essential of BMS tasks. Still, the accurate estimation of SOC is difficult. This is because the SOC is the internal state of battery cell and it cannot be directly measured. Thus, SOC must be estimated.

So far, the various methods have been proposed for estimating the battery's state of charge that generally they are divided into two groups: namely free model and model-based. The free models include the Ampere-hour (Ah) or coulomb counting [9], open circuit voltage (OCV) [10]. The ampere-hour counting technique is the most common method for calculating of SOC that can obtain the SOC by using of current integral over time. In this method, if the initial SOC is given, the estimation accuracy will be high. But, if it is estimated wrongly, the whole calculations of SOC afterwards will be wrong. So, this method has problems such as the measurement noise and wrong initial SOC. In open circuit voltage method, SOC is obtained in terms of OCV, but this method is inappropriate for on-line applications, since in this method, the battery must reach to steady state for a long time before measuring the OCV. This method can be combined with ampere-hour counting. Such combination allows the SOC to be calculated after a peaceful period using the OCV-SOC relation. This SOC is used as a recalibration point for the ampere-hour counting method [11-13].

In order to improve the estimation accuracy of state-of-charge of battery, the model-based estimation methods have been developed [14-17]. In model-based methods, firstly the battery is modeled and then an estimator is used to estimate the state of charge. The Extended Kalman Filter (EKF) is one of the most famous estimators for estimating the state of charge [18-22]. However, in this method, the Jacobin matrix calculation makes filter instability and incorrect estimation for many non-linear battery models. To improve this problem, methods of estimating battery state of charge based on the unscented Kaman filter (UKF) are presented [22-25]. This method by combining the Kalman filter and unscented transformation overcomes the weaknesses of low accuracy and weak stability of the Kalman filter-based method. However, the estimation method of the battery's SOC based on the unscented Kalman filter in inaccurate initial conditions, non-Gaussian noises, non-Gaussian distributions, and Cholesky's problem in decomposing of non-positive matrices leads to its divergence.

According to the mentioned problems, in recent years, attention has been paid to estimating the battery's SOC using the particle filter. The particle filter is an implementation based on the Monte Carlo method that is widely applied in estimating non-linear and non-Gaussian systems [14-15]. In a particle filter, the posterior probability density function is estimated with a collection of weighted particles.

The filter based PSO uses a weighted set of samples to approximate the posterior distribution function. The filter is appropriate for estimating the states of non-linear complicated systems that the noise distribution is non-Gaussian. So, the filter based PSO of estimating SOC of battery is suitable.

In this paper, a modified particle filter with the recursive least squares (RLS) algorithm is used for estimating the battery's SOC. The standard particle filter has the problem of particles degeneracy that reduces the accuracy of prediction. In modified particle filter, the difference evolutionary (DE) algorithm and Markov chain Monte Carlo (MCMC) method are applied to the standard PF that increases the accuracy of SOC estimation and consistency. This is because DE algorithm and MCMC method maintain the diversity among the particles and cause the particles to approximate the samples asymptotically from the posterior probability density function of the real states.

The structure of the rest of the paper is as follows. In section II, modeling of the lithium-ion battery using the first-order RC equivalent circuit is presented. In section III, simultaneous estimation of parameters and SOC of the battery with the proposed method is presented. The results include the identification of battery parameters and the estimation of SOC which are presented in section IV. Section V includes the conclusions.

**Main Points**

- In this paper, by using the estimator of recursive least squares (RLS), firstly, the battery parameters are estimated and calculated, and also the modified particle filter has been used for estimating the state of charge (SOC) of a battery.
- In modified particle filter, the difference evolutionary (DE) algorithm and Markov chain Monte Carlo (MCMC) method are applied to the standard PF that causes the estimation of SOC to be more accurate and consistent.
- In this paper, the first-order RC model is used for high accuracy and low computational complexity.
- One of the most important stages in designing a particle filter is to select the proposed distribution. Implementing the particle filter with this proposed distribution function is simple and has low computations. However, the measurements are not involved in sampling and as a result, the estimation's accuracy is decreased. For solving this problem and increasing the sampling accuracy, the DE algorithm has been entered into the sampling step of the particle filter.
- In other words, the proposed method prevents poverty of samples and consequently, there is no need for a great number of particles. The advantage of the new algorithm is that the proposed method for obtaining the same estimation accuracy as the particle filter needs fewer particles.

## II. MODELING

Modeling of a battery is a significant and challenging issue in the BMS. So far, various models have been reported for the battery modeling which are generally categorized into four groups [16]: ideal model, behavioral model, electrochemical model, and electrical equivalent circuit model. The equivalent circuit models include n-order RC grid

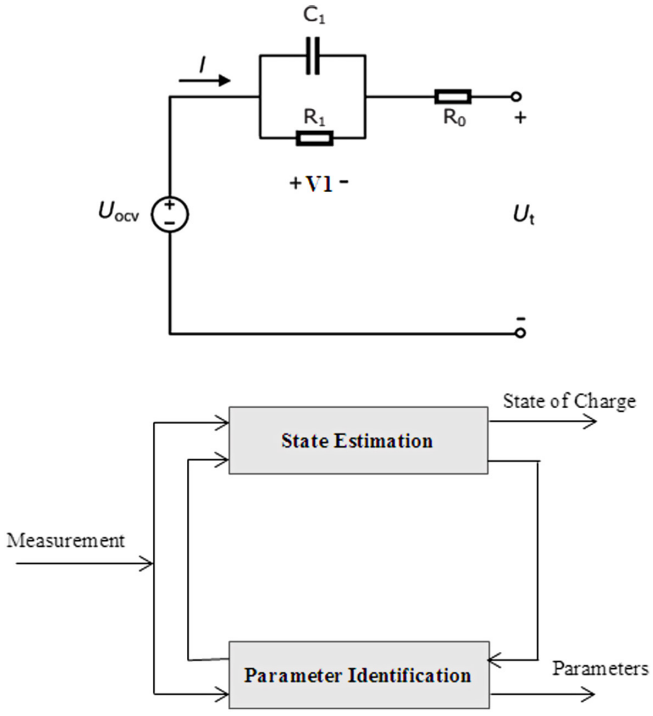


**Fig. 1.** Battery first-order model and the block diagram of the proposed method.

that is applied to describe the features of battery dynamics. In this paper, the first-order RC model is used for high accuracy and low computational complexity that is shown in Fig. 1.

This model includes a combination of voltage supply $U_{ocv}$, ohm resistance $R_0$, polarization resistance $R_1$, and capacitor $C_1$ that like other models, try to model the behavior of the battery. The state-space equations are as follow:

$$\dot{SOC} = -\frac{1}{Q_n} I \tag{1}$$

$$\dot{V_1} = -\frac{1}{R_{1C_1}} V_1 + \frac{1}{C_1}$$

$$U_t = U_{ocv}(SOC) - V_1 - R_0 I \tag{2}$$

Where $V_1$ is capacitor voltage, $Q_n$ is the permissible capacity of the battery cell, $U_t$ is the terminal voltage of the cell, $I$ is cell current with a positive value in discharge and a negative value in charge, and $U_{ocv}$ is OCV of the cell and a function of SOC.

## III. SIMULTANEOUS ESTIMATION OF PARAMETERS AND STATE-OF-CHARGE OF THE BATTERY

The block diagram of the proposed method for simultaneous estimation of battery parameters and its SOC estimation is shown in Fig. 1. In the proposed method, RLS is used for estimating the parameters and the modified particle filter is used for estimating the SOC that are scribed in the following subsections.

### A. Identification of Battery Parameters With RLS

In this paper, the RLS method is used to estimate battery parameters. The reason for use of this method is its low computational volume and high convergence rate. For using the RLS method in estimating the battery parameters, first, the voltage equation of battery terminals in the Laplace transform scope is written as follow:

$$U_t(s) = U_{ocv}(s) - \frac{R_1}{1 + R_1 C_1 s} I(s) - R_0 I(s) \tag{3}$$

By rewriting the equation as follow:

$$U_{ocv}(s) - U_t(s) = \left( \frac{R_1}{1 + R_1 C_1 s} + {}_{R_0} \right) I(s) \tag{4}$$

The transfer function *G(s)* is defined as follow:

$$G(s) = \frac{U_t(s) - U_{ocv}(s)}{I(s)} = \frac{R_0 + R_1 + R_1 C_1 R_0 s}{1 + R_1 C_1 s} \tag{5}$$

By using the two-line transform $= \frac{2}{T} \frac{1 - Z^{-1}}{1 + Z^{-1}}$, the equation 5 gets discrete as follow:

$$G(z^{-1}) = \frac{U_t(z^{-1}) - U_{ocv}(z^{-1})}{I(z^{-1})} = -\frac{\frac{R_0 T + R_1 T + 2R_0 R_1 C_1}{T + 2R_1 C_1} + \frac{R_0 T + R_1 T - 2R_0 R_1 C_1}{T + 2R_1 C_1} Z^{-1}}{1 + \frac{T - 2R_1 C_1}{T + 2R_1 C_1} Z^{-1}} \tag{6}$$

By defining the following parameters:

$$a_1 = \frac{T - 2R_1 C_1}{T + 2R_1 C_1}$$

$$a_2 = \frac{R_0 T + R_1 T + 2R_0 R_1 C_1}{T + 2R_1 C_1}$$

$$a_1 = \frac{R_0 T + R_1 T - 2R_0 R_1 C_1}{T + 2R_1 C_1}$$

The transform function is rewritten as follow:

$$\frac{U_t(z^{-1}) - U_{ocv}(z^{-1})}{I(z^{-1})} = \frac{a_2 + a_3 z^{-1}}{1 + + a_1 z^{-1}}$$

As a result, $U_t(k)$ is stated as follow:

$$U_t(k) = U_{ocv}(k) - a_1 U_{ocv}(k-1) + a_1 U_t(k-1) + 2I(k) + a_3 I(k-1) \tag{7}$$

Which by defining *M(k)*:

$$M(k) = U_{ocv}(k) - a_1 U_{ocv}(k-1) \tag{8}$$

We have

$$U_t(k) = M(k) + a_1 U_t(k-1) + a_2 I(k) + a_3 I(k-1) \quad (9)$$

Now, the vectors $\emptyset(k)$ and $\theta(k)$ are defined as follow:

$$\varnothing(k) = \begin{bmatrix} 1 & U_t(k-1) & I(k) & I(k-1) \end{bmatrix}$$

$$\theta(k) = \begin{bmatrix} M(k) a_1 a_2 a_3 \end{bmatrix}$$

As a result:

$$U_t(k) = \varnothing(k)\theta(k)$$

To estimate $\theta(k)$, RLS is used as follow:

$$U_t(k) = \varnothing(k)\theta(k) + e(k)$$

$$K(k) = \frac{P(k-1)\varnothing(k)^T}{\varnothing(k)P(k-1)\varnothing(k)^T + \lambda}$$

$$\hat{\theta}(k) = \hat{\theta}(k-1) + K(k)[y(k) - \phi(k)\hat{\theta}(k-1)$$

$$P(k) = \frac{(1 - K(k)\phi(k))P(k-1)}{\lambda}$$

**B. Estimation of Battery State of Charge Using the Modified Particle Filter**

In general state, the discrete form of battery equations is written as follows:

$$x_k = f(x_{k-1}, u_k) + w_k$$

$$P(\omega_K) \sim N(0, Q_K)$$

$$y_k = h(x_k, u_k) + v_k$$

$$P(v_K) \sim N(0, R_K) \quad (10)$$

$$f(x_{k-1}, u_k) = \begin{bmatrix} \frac{-T}{e^{R_{1,K}C_{1,K}}} & 0 \\ 0 & 1 \end{bmatrix} x_{k-1} + \begin{bmatrix} R_{p,k}.(1 - \frac{-T}{e^{R_{1,K}C_{1,K}}}) \\ \frac{-T}{C.3600} \end{bmatrix} I_k$$

$$h(x_k, U_k) = U_{OC,k} - V_{1,k} - R_{0,k} I_k$$

Where $x_k$ is the state vector, $u_k$ is the input vector of the system, $y_k$ is the measurement vector, $w_k$ is the process noise vector, $v_k$ is the measurement noise vector, $Q_K$ is the process noise covariance, and $R_K$ is measurement noise covariance. Also, *f(0)* and *h(0)* are non-linear functions. $I_k$ is the system input vector.

According to the equations of the battery model, it is observed that this system is non-linear. The Bayesian filter is the most general method for estimating the non-linear system. From the point of view of the Bayesian method, the state vector $X_k$ must be estimated based on the measurements $y_{0:k} = \{y_i, i = 0,1,\ldots,k\}$. In the rule of least mean squared error, the optimum estimation of conditional expectations $E(x_k | y_{0:k})$ is calculated as follows:

$$E(x_k | y_{0:k}) = \int x_{kp}(x_k | y_{0:k}) dx_k \quad (11)$$

When a new measurement is reached, the posterior probability density function $p(x|y)$ should be updated that complicated these computations. Thus, the Bayesian recursive filter includes two steps, namely prediction and updating. For the posterior probability density function of the state in time *k*, the step of updating and predicting is as follows:

$$p(x_k | y_{0:k-1}) = \int p(x_k | x_{k-1}) p(x_k | y_{0:k-1}) dx_{k-1} \quad (12)$$

$$p(x_k | y_{0:k}) = \frac{p(y_k | x_k) p(x_k | y_{0:k-1})}{\int p(y_k | x_k) p(x_k | y_{0:k-1}) dx_k}$$

It is observed that the Bayesian method does not present a closed and analytical solution. As a result, it is not appropriate for implementation. The most important non-parametric method for implementing the Bayesian filter is the particle filter [1]. The particle filter states the posterior probability density function $p(x_{0:k} | y_{1:k})$ as a set of the following weighted particles:

$$S_k = \{(x_k^i, w_k^i | i = 1,\ldots,N\} \quad (13)$$

Where *N* indicates the number of particles and $w_k^i$ is the weight related to $x_k^i$. In this case, $p(x_{0:k} | y_{1:k})$ is approximated by total weighted as follows:

$$p(x_{0:k} | y_{1:k}) \approx \sum_{i=1}^{N} w_k^i \delta(x_{0:k} - x_{0:k}^i) \quad (14)$$

Where $\delta(0)$ is the Dirac delta function. According to the extraction of samples from the real posterior probability density function $p(x_k | y_{1:k})$ is impossible or complicated, the important sampling method is used. In the importance sampling method, instead of sampling of the target function, a proposed distribution function $q(x_k | y_{1:k})$ is sampled [19]. The weight of the created particles from the proposed distribution function is as follow:

$$w_k^i \propto \frac{p\left(x_{0:k}^i | y_{1:k}\right)}{q\left(x_{0:k}^i | y_{1:k}\right)} \tag{15}$$

Suppose the proposed distribution function $q\left(x_k | y_{1:k}\right)$ is stated as follow:

$$q\left(x_{0:k}^i | y_{1:k}\right) = q\left(x_{0:k-1} | y_{1:k-1}\right) q\left(x_k | x_{0:k-1}, y_{1:k}\right) \tag{16}$$

The posterior probability density function is written as following recursive form:

$$\begin{aligned} p\left(x_{0:k} | y_{1:k}\right) &= \frac{p\left(y_{1:k} | x_{0:k}, y_{1:k-1}\right) p\left(x_{0:k} | y_{1:k-1}\right)}{p\left(z_{1:k} | y_{1:k-1}\right)} \\ &= \frac{p\left(y_{1:k} | x_{0:k}, y_{1:k-1}\right) p\left(x_k | x_{0:k-1}, y_{1:k-1}\right) p\left(x_{0:k-1} | y_{1:k-1}\right)}{p\left(z_{1:k} | y_{1:k-1}\right)} \\ &= \frac{p\left(y_{1:k} | x_k\right) p\left(x_k | x_{k-1}\right) p\left(x_{0:k-1} | y_{1:k-1}\right)}{p\left(z_{1:k} | y_{1:k-1}\right)} \\ &\propto p\left(y_{1:k} | x_k\right) p\left(x_k | x_{k-1}\right) p\left(x_{0:k-1} | y_{1:k-1}\right) \end{aligned} \tag{17}$$

The recursive weight of the particles is as follow:

$$\begin{aligned} w_k^i \propto \frac{p\left(x_{0:k}^i | y_{1:k}\right)}{q\left(x_{0:k}^i | y_{1:k}\right)} &= \frac{p\left(y_{1:k} | x_k^i\right) p\left(x_k^i | x_{k-1}^i\right) p\left(x_{0:k}^i | y_{1:k-1}\right)}{q\left(x_{0:k-1}^i | y_{1:k-1}\right) q\left(x_k^i | x_{0:k-1}^i, y_{1:k}\right)} \\ &= w_{k-1}^i \frac{p\left(y_{1:k} | x_k^i\right) p\left(x_k^i | x_{k-1}^i\right)}{q\left(x_k^i | x_{k-1}^i, y_{1:k}\right)} \end{aligned} \tag{18}$$

In summary, estimating the battery's SOC based on particle filter has the following steps:

1. Initialization
   Initialization of particles $\left\{x_k^i\right\}_{i=1}^N = p\left(x_0\right)$ and the determining their weights $\left\{w_0^i\right\}_{i=1}^N = \frac{1}{N}$.
2. Sampling and calculations of their weights
   The sampling is the generation of particles from the proposed distribution $p\left(x_k^i | x_{k-1}^i, u_k\right)$

$$w_k^i = w_{k-1}^i \frac{p\left(y_k | x_k^i\right) p\left(x_k^i | x_{k-1}^i, u_k\right)}{q\left(x_k^i | x_{k-1}^i, y_{1:k}\right)}$$

3. Normalization of weights

$$w_k^i = \frac{w_k^i}{\sum_{i=1}^N w_k^i}$$

**C. Improvement of Sampling**

One of the most important stages in designing a particle filter is to select the proposed distribution. In the researches related to particle filter, it is represented that the optimum proposed distribution function for particle filter is as follow:

$$q\left(x_k^i | x_{0:k-1}^i, y_{1:k}\right) = p\left(x_k^i | x_{k-1}^i, u_k, y_k\right) \tag{19}$$

However, in practice, it is difficult to obtain an analytical form for the proposed distribution function and generally to obtain the samples from it. The simplest form of the proposed distribution function applied in particle filter is as follows:

$$q\left(x_k^i | x_{0:k-1}^i, y_{1:k}\right) = p\left(x_k^i | x_{k-1}^i, u_k\right) \tag{20}$$

By placing it in the relation related to weights, the weight of each particle is calculated as follows:

$$w_k^i = w_{k-1}^i p\left(y_k | x_k^i\right) \tag{21}$$

Implementing the particle filter with this proposed distribution function is simple and has low computations. However, the measurements are not involved in sampling and as a result, the estimations' accuracy is decreased. For solving this problem and increasing the sampling accuracy, the DE algorithm has been entered into the sampling step of the particle filter. In fact, after sampling using the DE algorithm, the particles are displaced such that to be in locations that the likelihood function $p\left(y_k | x_k\right)$ is maximized.

For this aim, the particles $\left\{x_k^i, i = 1, \ldots, N\right\}$ are the target vectors of the current population and their corresponding weights $\left\{w_k^i, i = 1, \ldots, N\right\}$ are the target functions of target vectors DE. The DE algorithm combines the particles by an iterative process of bounce, cutting, and iteration, so that the particles are placed in the area with high likelihood function. Suppose $C_k^t = \left\{x_{k,1}^t, \ldots, x_{k,N}^t\right\}$ indicates the present population of DE that includes *N* target vector with dimensions D, DE algorithm uses a vector $x_{k,i}^t$ for providing each candidate of response *i* in iteration *t* and given time step *k*. For each target vector $x_{k,i}^t$, the DE algorithm creates a test vector *u* by perturbing it by adding one or more weighted differential vector as follows:

$$v_k = x_{k,i}^t - \beta\left(x_{k,i_2}^t - x_{k,i_3}^t\right) \tag{22}$$

where $x_{k,i}^t$ is the target vector for perturbing at iteration *k*. $x_{k,i_2}^t$ and $x_{k,i_3}^t$ are two members of the population that are selected randomly so that $i_2$ and $i_3$ are not equal to each other. The parameter $\beta$ is a scale factor that controls the variance differential amplitude $\left(x_{k,i_2}^t - x_{k,i_3}^t\right)$.

For increasing the diversity of new population vectors, a cutting mechanism is introduced as follows:

$$x_{k,j}^{t'} = \begin{cases} v_{k,ij} & j \in J \\ x_{k,ij}^t & otherwise \end{cases}$$

$$x_{k,i}^{'} = \left\{ x_{k,ij}^{'} \right\} u_{k,i} = \left\{ u_{k,ij} \right\}$$

$$x_{k,i} = \left\{ x_{k,ij} \right\}, j = 1, \ldots, D$$

Where $x_{k,ij}$ refers to j[th] element of vector $x_{k,i}$ and $J$ is a set of cutting points. For binomial cutting, the cutting points are randomly selected from the set of possible points {1,2,...,D} that $D$ is the problem dimensions. To decide whether $x_k'$ should be a member of the population $C_{k+1}$, a new vector is compared to $x_k$. If the vector $x_k'$ gets a better value for the criterion function, $x_k$ will be replaced with $x_k'$ in the new population. Otherwise, the prior value $x_k$ is maintained for the new population. The criterion function of the vector $x_k'$ is calculated as follows:

$$f\left( x_k^{'} \right) = p\left( y_k | x_k^{'} \right) \tag{23}$$

When a new population is generated, the process of cutting, bouncing, and selecting is repeated until it gets a minimum or reaches the predetermined minimum. In our intended issue, DE does not need a great number of iterations. This is because, in our application, the search space is a small area around the state in the time step $k-1$. When the best fitting value reaches a certain threshold, the iterations are stopped.

**D. Improving of Diversity Among Particles**

Another problem with particle filters is the degeneracy issue. This problem has a serious influence on the accuracy of particle filter estimations. When this problem occurs, only a few numbers of particles weigh large, while most particles weigh low. So, many calculations are spent on updating the particles that work rarely. Resampling decreases degeneracy by removing the particles with trivial weight and reproducing the particles with high weight. But it also decreases the diversity among particles and generates a problem called sample poverty. This phenomenon intensifies especially when the process has few noises and causes particles to fall to a point. As a result, the particles set cannot approximate accurately the posterior probability density function and the estimations' accuracy will be reduced. To overcome this problem, it is significant to determine the time and how to resample. To determine the time of resampling, the effective particles number criterion $N_{eff}$ is used.

$$N_{eff} = \frac{1}{\sum_{i=1}^{N} (w_k^i)^2}$$

Resampling is done when $N_{eff}$ is less than the predetermined value $N_{eff}$. To increase the number of the particles and guarantee the diversity among particles, a sampling method is presented to reduce the degeneracy. To maintain the diversity among particles, it is essential to generate diversity among particles after resampling, in such a way that it does not affect the approximation validity. For this aim, the MCMC method is applied to increase the diversity among particles after resampling without having an influence on the approximation validity.

To describe MCMC, suppose the particles are distributed corresponding to posterior $p\left( \tilde{x}_{0:k} | y_{1:k} \right)$, then by using a kernel of Markov-chain transfer $k\left( x_{0:k} | \tilde{x}_{0:k} \right)$ with invariable distribution $p\left( x_{0:k} | y_{1:k} \right)$, we have:

$$\int k\left( x_{0:k} | \tilde{x}_{0:k} \right) p\left( \tilde{x}_{0:k} | y_{0:k} \right) = p\left( x_{0:k} | y_{0:k} \right) \tag{24}$$

We still have a set of the distributed particles according to the posteriori $p\left( \tilde{x}_{0:k} | y_{1:k} \right)$. However, the new particles may move toward a high likelihood area and the total variance of present distribution with respect to invariable distribution can only be decreased. The MH method is one of the common MCMC methods [17-18]. The MH algorithm uses a conditional distribution as a proposed distribution function for creating the Marcov-Chain with invariable distribution [20]. The standard MH algorithm is supposed as follows that sampling $u \sim U_{[0,}1_{]}$, where $U_{[0,}1_{]}$ is the uniform distribution in the interval [0,1]:

1. Sampling of proposed distribution function $x_k^{*i} \sim p\left( x_k | x_{k-1}^i \right)$
2. If $u \le min\left\{ 1, \frac{p\left( y_k | x_k^{*i} \right)}{p\left( y_k | x_k^i \right)} \right\}$, $x_{0:k}^i = \left( \tilde{x}_{0:k-1}^i, x_k^{*i} \right)$

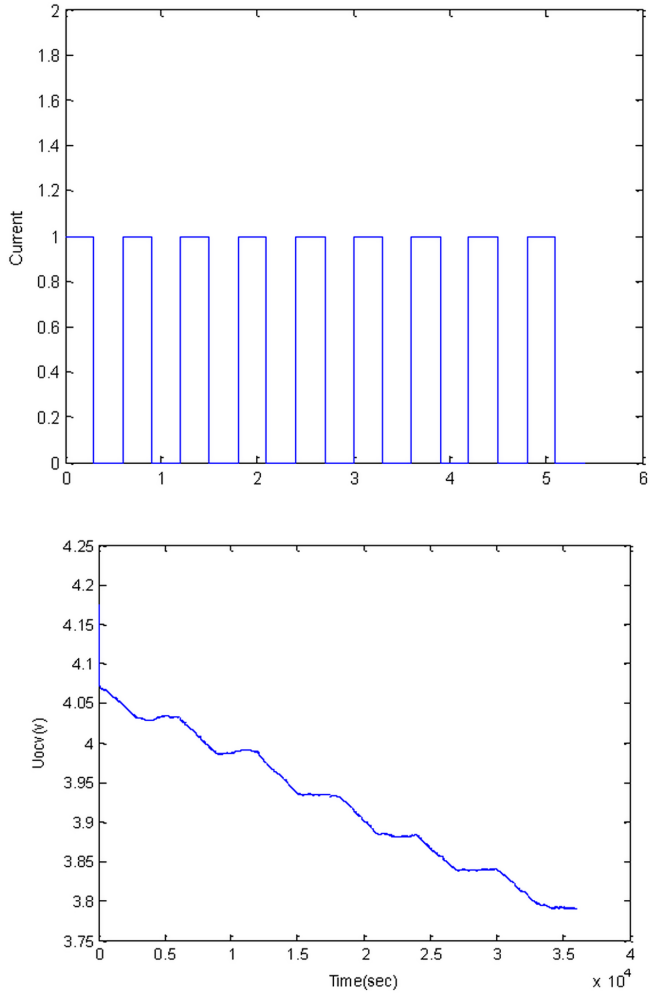


**Fig. 2.** Input current, voltage $U_{OCV}$.

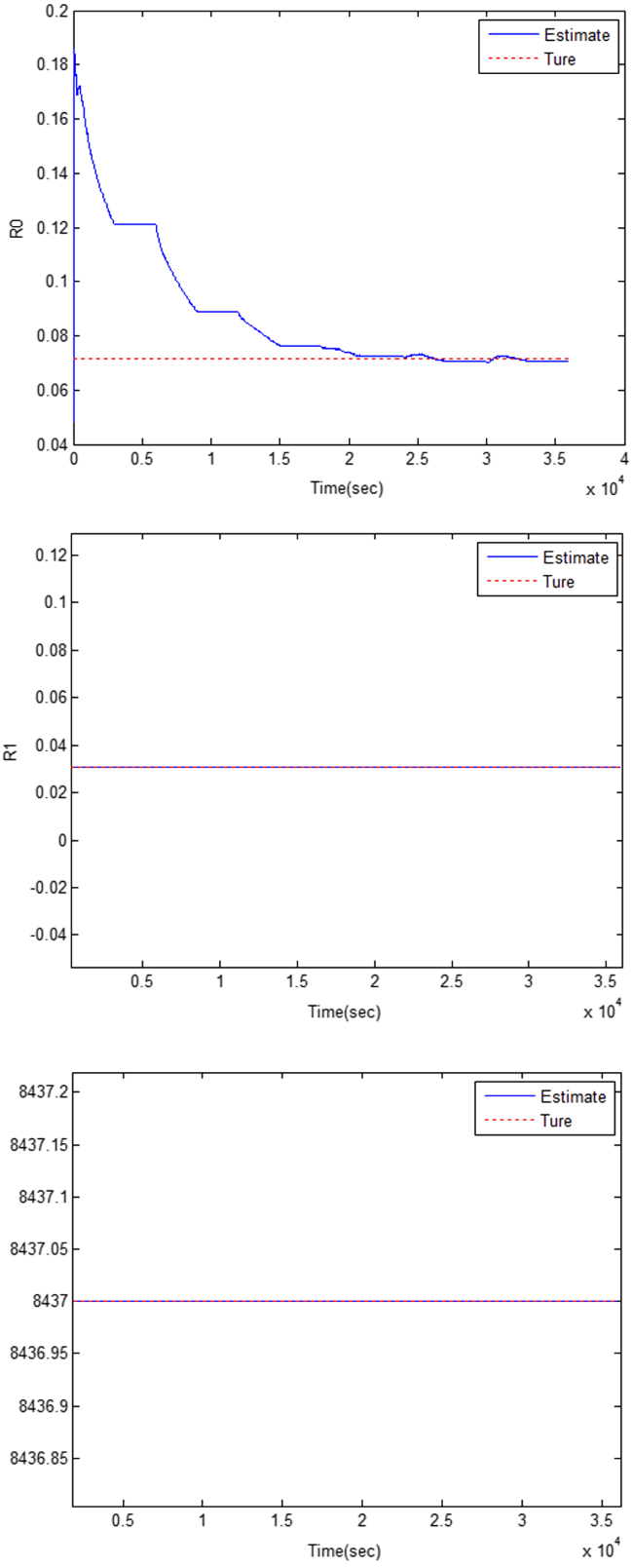


**Fig. 3.** Ohmic resistance $R_0$, capacitor $C_1$, and ohmic resistance $R_1$.

Otherwise,

$$x_{0:k}^{i} = \left(\tilde{x}_{0:k}^{i}\right)$$

3. End of condition

## IV. RESULTS

### A. Identification of Parameters

The estimation of the battery parameters on-line is very important. There are various methods to identify the battery parameters. These methods identify the parameters of the battery model versus the out-line SOCs without considering the impact of battery operation conditions on the battery parameters. As seen in the equivalent circuit model, the parameters of the battery model that include $R_0$, $R_1$, and $C_1$ should be determined and identified. The input current is arbitrarily selected. The operation of the proposed method does not depend on the input current and in all states, its

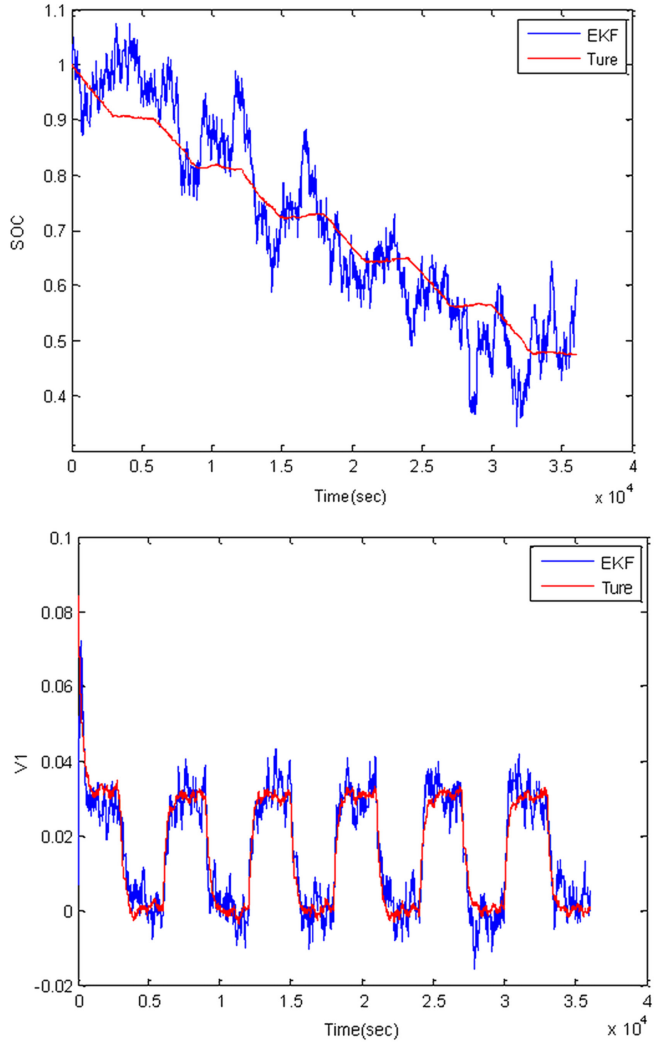


**Fig. 4.** Results of estimation by EKF method.

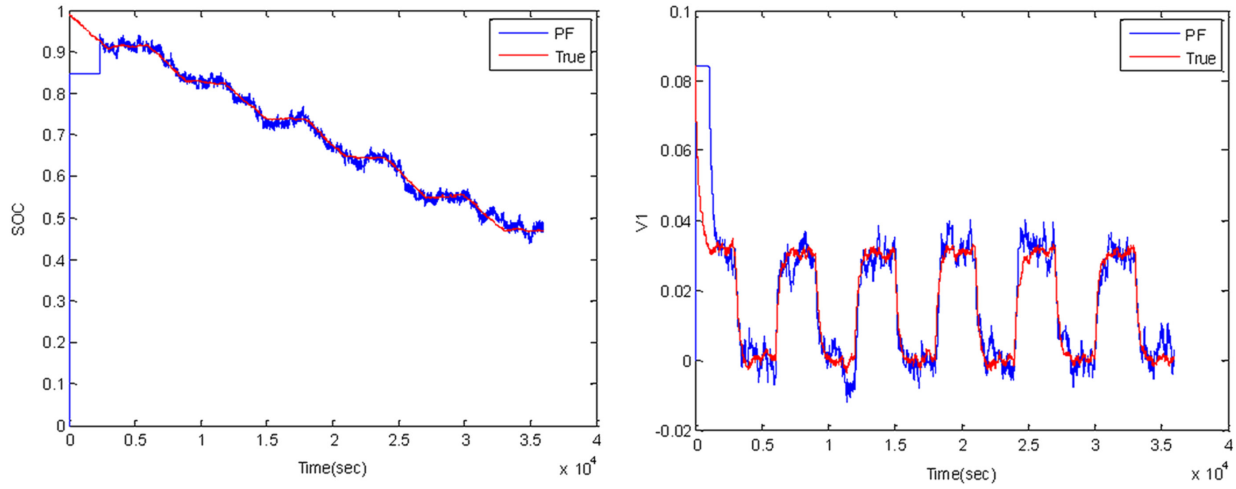


**Fig. 5.** Results of estimation by PF method.

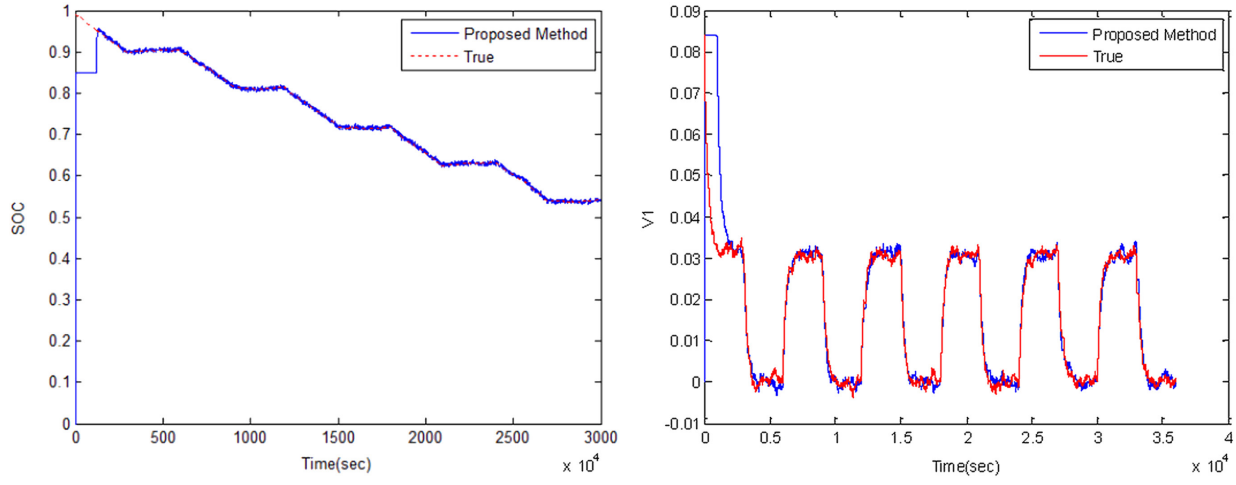


**Fig. 6.** Results of estimation by the proposed method.

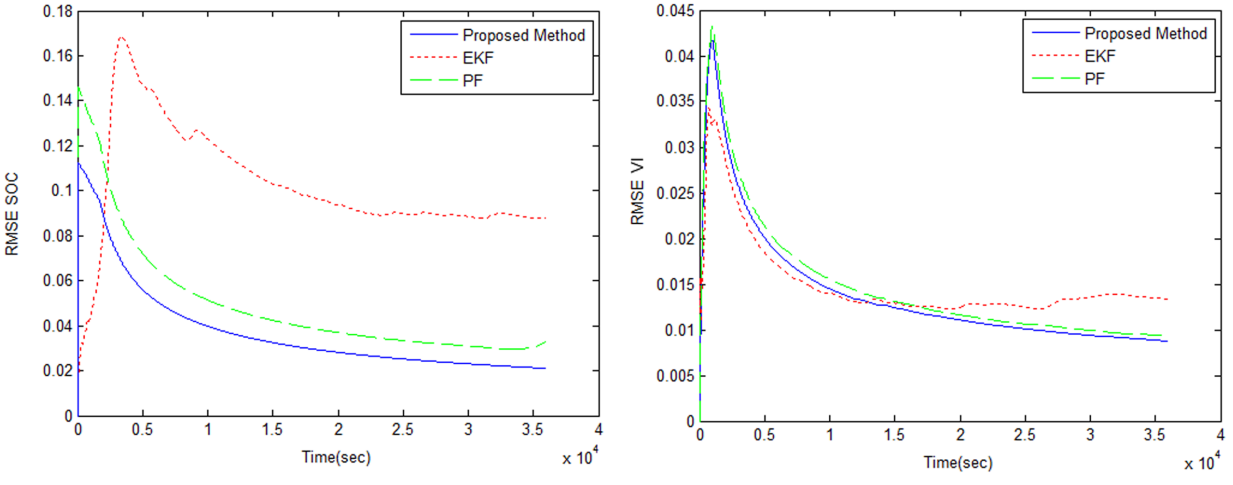


**Fig. 7.** RMSE is related to SOC and RMSE of voltage $V_1$.

**TABLE I.**
PERFORMANCE OF FILTERS WITH DIFFERENT NUMBER OF PARTICLES

| Number Particle | Methods | RMSE | Processing Time |
|---|---|---|---|
| 100 | Proposed Method | 0.02 | 31 |
| | PF | 0.05 | 14 |
| 50 | Proposed Method | 0.021 | 16 |
| | PF | 0.1 | 9 |
| 10 | Proposed Method | 0.023 | 8 |
| | PF | 0.2 | 6 |

performance is superior compared to the other methods. In this paper, the current *I* is used in the pulsed form that is a famous profile for identifying and estimating the battery's SOC which is used in various articles. The input current and voltage $U_{OCV}$ are as Fig. 2 respectively.

The Fig. 3 shows the results of the estimation of the parameters using RLS. As can be seen, the estimated parameters of the proposed method have been well converged to their real values.

**B. Performance Evaluation**

In this section, the performance of the proposed method is evaluated by estimating the battery's SOC based on the estimators EKF and PF. Figs. 4, 5, and 6 show the results obtained in the various methods. The results include the real value of SOC and polarization voltage $V_1$ and their estimated values using the EKF and PF represent that the proposed method is more accurate compared to the other methods.

For better and more accurate estimation, root mean square error (RMSE) related to SOC has been investigated by using various estimators. The results are represented in Fig. 7. These figures show the comparison of RMSE with EKF, PF, and the proposed method.

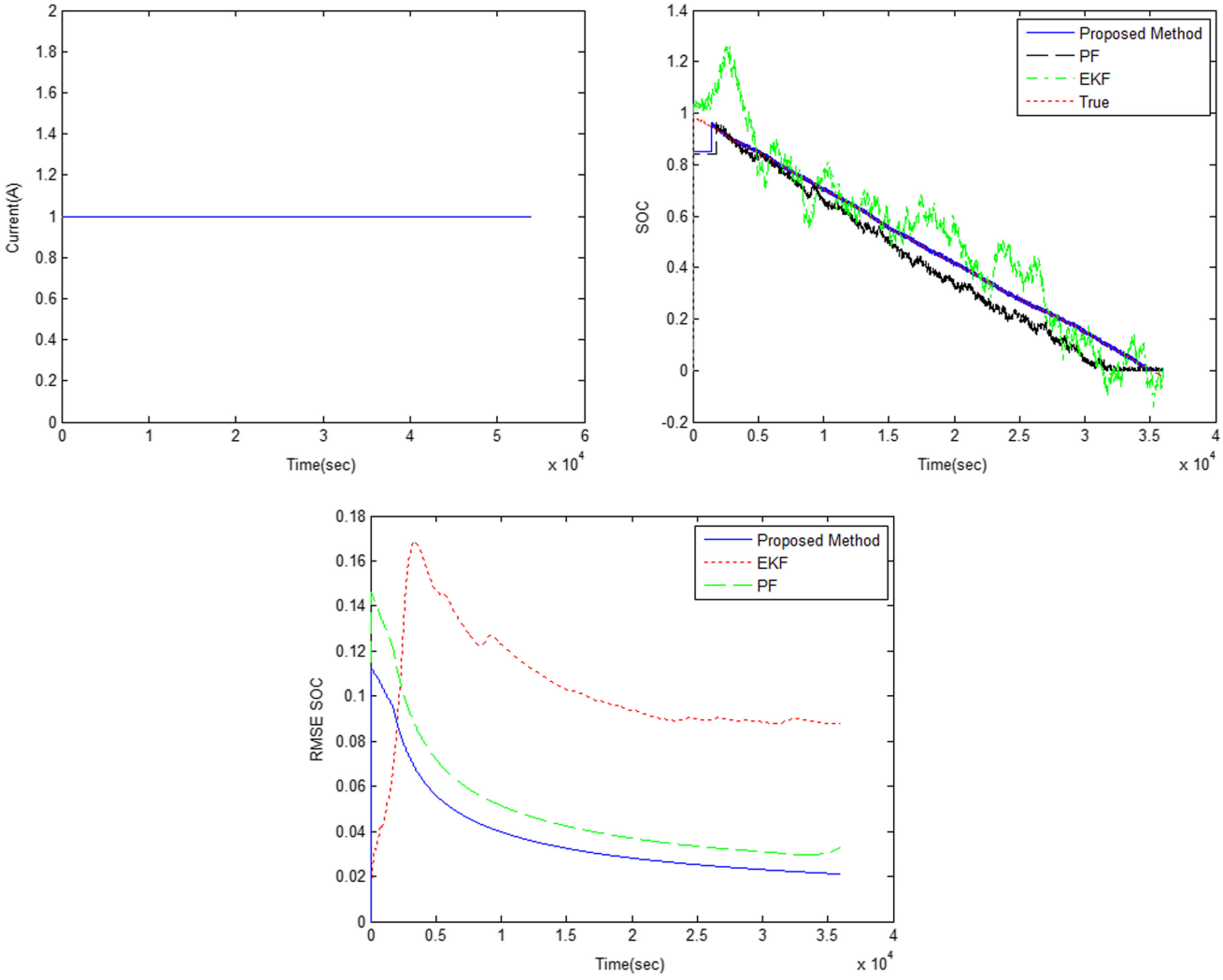


**Fig. 8.** Input current profile, comparison of SOC estimation with constant current, and RMSE related to SOC with a constant current.

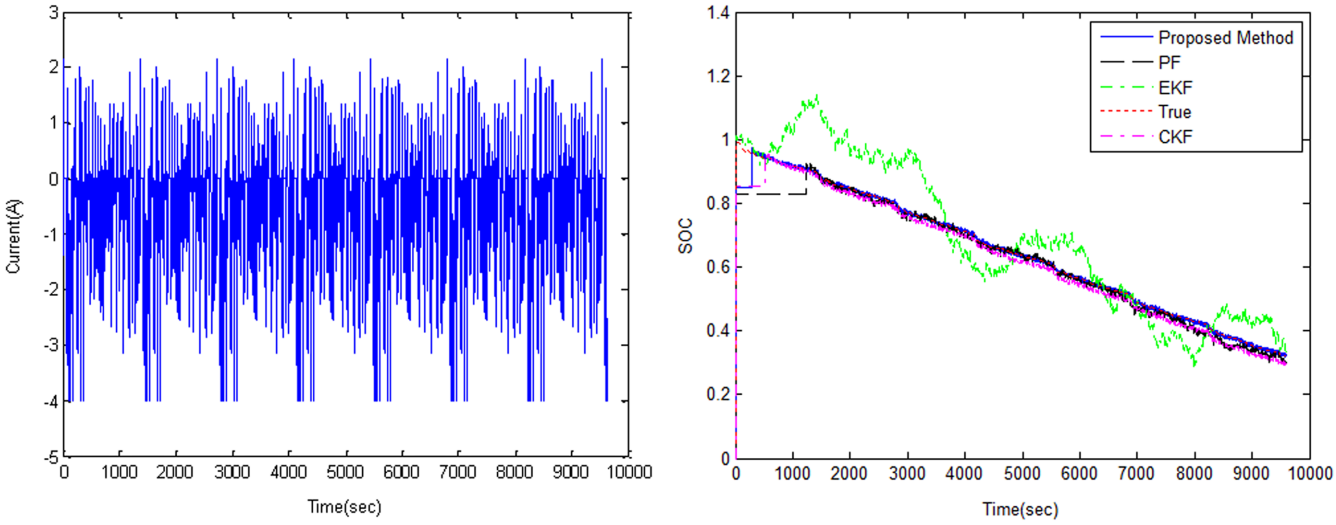


**Fig. 9.** Input current profile FUDS and the comparison of SOC estimation in the FUDS test.

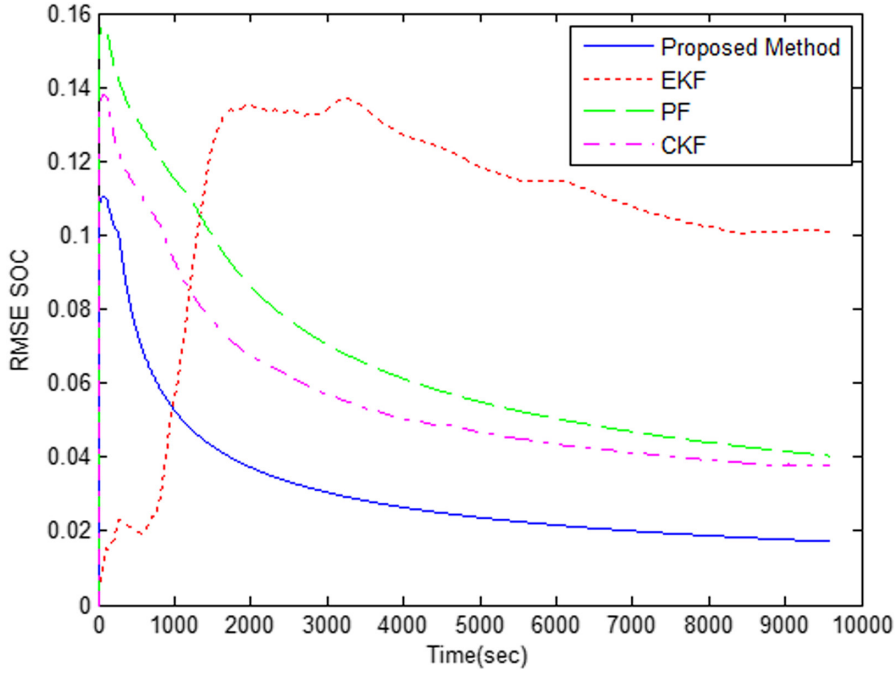


**Fig. 10.** RMSE related to SOC in FUDS test.

Fig. 7 shows RMSE for the battery's SOC and shows RMSE for the polarization voltage $V_1$.

The performance of filters with a different number of particles is represented in Table I. It is seen that the dependence of PF performance on the number of particles is more than the proposed method. This is because, in the proposed method, the proposed distribution function has been improved. Moreover, the proposed method maintains the diversity among particles and causes the resampled particles to approximate samples asymptotically from the posterior probability density function of the true state. In other words, the proposed method prevents poverty of samples and consequently, there is no need for a great number of particles. The advantage of the new algorithm is that the proposed method for obtaining the same estimation accuracy as the particle filter needs fewer particles.

### C. Further Evaluation of Proposed Method Operation

To more evaluate the operation of the proposed method, firstly, its operation is investigated when the consuming current of the

**TABLE II.**
RMSE COMPARISON

| RMSE | | | |
|---|---|---|---|
| **Proposed Method** | **PF** | **EKF** | **CKF** |
| 0.017 | 0.04 | 0.12 | 0.038 |

RMSE: root mean square error, PF: particle filter, EKF: extended Kalman filter, CKF: cubature Kalman filter.

battery is direct current. The input current in this case is represented in Fig. 8. Fig. 8 indicates the results obtained from the various methods. The results include the real value of SOC and their estimated values using the EKF and PF. It can be seen that in this case, the proposed method also is more accurate compared to the other methods.

To further evaluate the proposed method in SOC estimation from the point of view of accuracy and strength, its performance in a complicated current profile called the Federal Urban Driving Program (FUDS) is investigated [19]. This experiment is more complex than previous experiments in terms of the rate of current charge and discharge. The profile related to current in the FUDS test has been shown in Fig. 9. In this test, the performance of the proposed method has been compared to PF, EKF, and Cubature filter [20-22]. Fig. 9 represents the comparison of results using various methods. The results include the real value of SOC and their estimated values. The results show that the proposed method is more accurate compared to the other methods. Fig. 9 shows that the proposed method has followed the real value well.

Fig. 10 shows the RMSE error criterion of the battery's SOC in this test. The results show that RMSE related to the proposed method has more convergence than other methods. In Table II, RMSE obtained from the various methods has been compared.

## V. CONCLUSION

In this paper, a modified particle filter with the RLS algorithm is applied for improving the accuracy of estimating the lithium-ion battery's SOC in electric vehicles. In this method, according to the advantages and disadvantages of the equivalent circuit models, the first-order RC thevenin's circuit was used for modeling the non-linear behaviors of the lithium-ion battery. In the proposed method, the DE algorithm and MCMC method were used to improve the PF performance in estimating the battery's SOC causing the estimation to be more accurate and consistent than the other methods. The results represent the effective operation of the proposed method compared to the other methods.

**Peer review:** Externally peer-reviewed.

**Declaration of Interests:** The author have no conflict of interest to declare.

**Funding:** The author declared that this study has received no financial support.

## REFERENCES

1. Y. Zhang, R. Xiong, H. He, and W. Shen, "Lithium-ion battery pack state of charge and state of energy estimation algorithms using a hardware-in-the-loop validation," *IEEE Trans. Power Electron.*, vol.32, no. 6, pp.4421–4431, 2017. [CrossRef]
2. H. Ahmadi-Nezamabad, M. Zand, A. Alizadeh, M. Vosoogh, and S. Nojavan, Hamed Ahmadi-Nezamabad, et al. "Multi-objective optimization based robust scheduling of electric vehicles aggregator," *Sustain. Cities Soc.*, vol. 47, p. 101494, 2019. [CrossRef]
3. M. Zand, M. A. Nasab, P. Sanjeevikumar, P. K. Maroti, and J. B. Holm-Nielsen, "Energy management strategy for solid-state transformer-based solar charging station for electric vehicles in smart grids," *IET Renew. Power Gener.*, vol. 14, no. 18, 3843–3852, 2020. [CrossRef]
4. H. Dong, W. Huang, and Y. Zhao, "Low complexity state-of-charge estimation for lithium-ion battery pack considering cell inconsistency," *J. Power Sources*, vol. 515, p. 230599, 2021. [CrossRef]
5. J. Xie, J. Ma, K. Bai, and K., "Enhanced coulomb counting method for state-of-charge estimation of lithium-ion batteries based on peukert's law and coulombic efficiency," *J. Power Electron.*, vol. 18, no. 3, pp. 910–922, 2018.
6. S. C. Huang, K. H. Tseng, J. W. Liang, C. L. Chang, and M. G. Pecht, " An online SOC and SOH estimation model for lithium-ion batteries," *Energies*, vol. 10, no. 4, pp. 512–529, 2017. [CrossRef] .
7. X. Dang, L. Yan, K. Xu, X.Wu, H. Jiang, and H.Sun, "Open-circuit voltage-based state of charge estimation of lithium- ion battery using dual neural network fusion battery model," *Electrochim. Acta*, vol.188, pp.356–366, 2016. [CrossRef]
8. X. Lin, Y. Tang, J. Ren, and Y. Wei, "State of charge estimation with the adaptive unscented Kalman filter based on an accurate equivalent circuit model," *J. Energy Storage*, vol. 41, p. 102840, 2021. [CrossRef]
9. M. Ghasemi, E. Akbari, M. Zand, M. Hadipour, S. Ghavidel, and L. Li, "An efficient modified HPSO-TVAC-based dynamic economic dispatch of generating units," *Electr. Power Compon. Syst.*, vol. 47, no. 19–20, 1826–1840, 2019. [CrossRef]
10. Azimi Nasab et al, "An efficient robust optimization model for the unit commitment considering of renewables uncertainty and Pumped-Storage Hydropower," *Comput. Electr. Eng.*, 2022.
11. M. Azimi Nasab, M. Zand, S. Padmanaban, and B. Khan, "Simultaneous long-term planning of flexible electric vehicle photovoltaic charging stations in terms of load response and technical and economic indicators," *World Electr. Veh. J.*, vol. 12, no. 4, 2021. [CrossRef]
12. M. Zand et al., "Big data for SMART sensor and intelligent electronic devices–building application," *Smart Buildings Digitalization*. Boca Raton: CRC Press, pp. 11–28. [CrossRef], 2022.
13. P. Nian, Z. Shuzhi, and Z. Xiongwen, "Co-estimation for capacity and state of charge for lithium-ion batteries using improved adaptive extended Kalman filter," *J. Energy Storage*, vol. 40, p. 102559, 2021. [CrossRef]
14. Y. Guo, Z. Zhao, and L. Huang, "SoC Estimation of Lithium Battery Based on AEKF Algorithm. " *Energy Procedia*, vol.105, pp. 4146–4152, 2017. [CrossRef]
15. M. Lagraoui, A.Nejmi, H. Rayhane, and A. Taouni, "Estimation of lithium-ion battery state-of-charge using an extended kalman filter," *Bulletin EEI*, vol. 10, no. 4, pp.1759–1768, 2021. [CrossRef]
16. Z. He, M. Gao, C. Wang, L. Wang, and Y. Liu, "Adaptive state of charge estimation for Li-ion batteries based on an unscented kalman filter with an enhanced battery model," *Energies*, vol. 6, no. 8, pp.4134–4151, 2013. [CrossRef]
17. Q. Q.YU, R.Xiong, C.Lin, W. X.Shen, and J. I.Deng, "Lithium-ion battery parameters and state-of-charge joint estimation based on H infinity and unscented Kalman filters," *IEEE Trans. Veh. Technol.*, vol.66, no.10, pp. 8693 –8701, 2017. [CrossRef]

18. C. I. Ossai, N. Raghavan, and C. I. Ossai, "'Stochastic model for Lithium ion battery lifecycle prediction and parametric uncertainties'," IEEE, in 2018 Annual Reliability and Maintainability Symposium (RAMS), vol. 2018, pp. 1–6, 2018.
19. A. Perez *et al.*, "Characterization of the degradation process of lithium-ion batteries when discharged at different current rates," *Proc. Inst. Mech. Eng. I*, vol. 232, no. 8, pp. 1075–1089, 2018. [CrossRef]
20. J. C. Álvarez Antón, P. J. García Nieto, F. J. de Cos Juez, F. Sánchez Lasheras, C. Blanco Viejo, and N. Roqueñí Gutiérrez, "Battery state-of-charge estimator using the MARS technique," *IEEE Trans. Power Electron.*, vol.28, no. 8, pp.3798–3805, 2013. [CrossRef]
21. D. Kong, S. Wang, and P. Ping, "A novel parameter adaptive method for state of charge estimation of aged lithium batteries," *J. Energy Storage*, vol. 44, p. 103389, 2021. [CrossRef]
22. X. Shu, G. Li, J. Shen, W. Yan, Z. Chen, and Y. Liu, "An adaptive fusion estimation algorithm for state of charge of lithium-ion batteries considering wide operating temperature and degradation," *J. Power Sources*, vol. 462, p. 228132, 2020. [CrossRef]
23. P. Magron, R. Badeau, and B. David, "Phase-dependent anisotropic Gaussian model for audio source separation," In IEEE International Conference on Acoustics, Speech and Signal Processing (ICASSP). IEEE Publications, Vol. 2017, no. Mar 5, 2017, pp. 531–535.
24. W. He, N. Williard, C. C. Chen, and M. Pecht, "Robust and adaptive estimation of state of charge for lithium-ion batteries," *Int. J. Power Electron.*, vol. 62, pp. 783–791, 2014.
25. J. Peng,J. Luo, H. Hea, and B. Lu, "An improved state of charge estimation method based on cubature Kalman filter for lithium-ion batteries," *Appl. Energy*, vol.253, 2019. [CrossRef]
26. H.Yang, X.Sun, Y.An, X.Zhang, T.Wei, and Y. Ma, "Online parameters identification and state of charge estimation for lithium-ion capacitor based on improved Cubature Kalman filter," *J. Energy Storage*, vol.24, 2019. [CrossRef]
27. J. Linghu, L. Kang, M. Liu, X. Luo, Y. Feng, and C. Lu, "Estimation for state-of-charge of lithium-ion battery based on an adaptive high-degree cubature Kalman filter," *Energy*, vol.189, 2019. [CrossRef]

cigre Turkey

TEPES
TURKISH JOURNAL OF ELECTRICAL POWER AND ENERGY SYSTEMS

TEPES, Vol. 2, Issue. 2, 115-123, 2022 **DOI:** 10.5152/tepes.2022.22015

RESEARCH ARTICLE

# Enhancement of Transmission System Security with Archimedes Optimization Algorithm

**Erdi Doğan[1], Nuran Yörükeren[2]**

[1]North-West Anatolian Dispacthing Center of Turkish Electricity Transmission Co.
[2]Department of Electrical Engineering, Kocaeli University, Kocaeli, Turkey

**Cite this article as:** E. Doğan, N. Yörükeren. Enhancement of transmission system security with archimedes optimization algorithm, *Turk J Electr Power Energy Syst*, 2022; 2(2), 115-123.

## ABSTRACT

The reliability of the transmission system is crucial in terms of both economic and social welfare. On one hand, the transmission lines getting overloaded because of a single outage situation may give rise to even a blackout. On the other hand, the excessive short-circuit current might cause distortion of valuable system devices. Therefore, the static security of the transmission system should be provided so as to protect consumers and system components. The bus splitting optimization (BSO) is a tool that maintains system security by distributing transmission feeders to the suitable busbars. The BSO is a non-convex, combinatorial, and binary problem due to AC power flow equations, short-circuit calculations, and the nature of the representation of the feeder position. Hence, the novel Archimedes optimization algorithm (AOA) is utilized in order to solve the BSO problem instead of the deterministic approaches in this study. Analyses we implemented show that the AOA algorithm has the efficacy and robustness to solve the BSO problem in the Istanbul Anatolian Region of the Turkish Electricity Transmission System and to enhance the power system security.

**Index Terms—**Meta-heuristics, N-1 security, optimization in transmission network, restriction of short-circuit current.

## I. INTRODUCTION

Bus splitting optimization (BSO), also known as network topology reconfiguration, bus layout optimization, or transmission line switching, has been recognized as an effective improvement in power system operations for maximizing network infrastructure resources and lowering operational costs [1]. Furthermore, the BSO is implemented in order to both restrict short-circuit current (SCC) [2] level and to maintain static security of the power system in contingency [3,4]. Therefore, the BSO method is a significant and cost-effective way to enhance the system condition in terms of economic and technical aspects.

A higher SCC value results from enhanced network connections as well as an increase in the number of generators [5]. Excessive SCC has already been a concern in several regions such as in the China Power System [5] and the Turkish Electricity Transmission System (TETS) [6]. If the over SCC that the circuit breaker cannot interrupt is not prevented, the system equipment can get exposed to significant damages and large interruptions that reduce social welfare can take place. The impedance of the transmission system can be varied by regulating the network topology in a way that the operation costs are alleviated and the N-1 security is strengthened [7]. Furthermore, although designing an efficient transmission reconfiguration is a convenient approach in order to decline the SCC, the power system reliability might weaken in the N-1 situation due to the alteration of the topological framework. However, the power system reliability decreases in contingency due to alteration of the topological framework. Hence, the appropriate bus layout should be created not only to restrict the SCC but also to provide power system static security in the N-1 contingency.

The BSO problem that focuses to reduce operational costs is described as a mixed-integer non-linear programming problem, with each feeder representing one binary variable. Bus splitting optimization is an Non-Polynomial-hard (NP)-hard problem, and its low computational efficiency prevents it from being used in real-world power system operations [5]. Many techniques such as the Benders decomposition method [8], second-order cone programming incorporating

**Corresponding author:** Erdi Doğan, erdi.dogan.teias@gmail.com

**Received:** February 23, 2022
**Accepted:** March 23, 2022
**Publication Date:** May 18, 2022

heuristic [9], and DC equations in optimal power flow [7,8,10] are used to deal with the complexity of this problem. On other hand, the BSO problem regarding an improvement of the system security relieving the loading levels and SCC instead of reducing operational costs is considered as an integer non-linear programming problem [3,4,6]. Another option with regard to the BSO problem is to intentionally island in cascading failures so as to hinder large-scale blackouts in the power system [11-14].

Over the last two decades, meta-heuristic optimization approaches have grown in popularity [15]. The reason for the common use of the meta-heuristic techniques in a variety of engineering areas is their simple, derivative-free, and flexible implementation properties. However, the no free lunch theorem showed that on one set of problems, a meta-heuristic may produce excellent results, while on another set of problems, the same approach may produce terrible results [16]. In order to tackle diverse problem sets, various spectacular meta-heuristic strategies such as genetic algorithm [17], particle swarm optimization [18], gravitational search algorithm [19], and ant colony optimization [20] were proposed. Therefore, it is necessary to determine which algorithm can effectively solve the BSO problem in the real-world large-scale power system. This is the main motivation of this research, which utilizes a novel meta-heuristic optimization algorithm for solving the BSO problem.

There are two main voltage levels, one is 154 kV and the other is 400 kV in TETS and bulk power generation in market is connected to a 400 kV voltage level but the over SCC occurs at a 154 kV voltage level. As a result, the focus of this work is on the BSO problem, which was adopted to increase power system security because the optimal power flow at 154 kV voltage level is not required in TETS. The Archimedes optimization algorithm (AOA) [21], a novel physic-based meta-heuristic, is used to tackle the BSO problem in TETS. The Python programming language is used in order to create related software and all information about power flow equations and SCC in TETS is retrieved from the PSS/E version 35.2 program. Mealpy software [22], a collection of the state-of-the-art meta-heuristics algorithms in Python, is utilized to solve the BSO problem with AOA. In order to deal with the binary structure of the BSO problem, some alterations have been implemented to the optimizer module of the Mealpy software.

**Main Points**

- Formulation of bus splitting optimization problem incorporating short-circuit current and N-1 security in Turkish Electricity Transmission System.
- Introducing how to enhance the static security of the power system without extra cost by solving a problem with non-convex, non-linear, multi-objective, and binary nature through a meta-heuristic optimization algorithm.
- Implementing Archimedes optimization algorithm, a novel math-based algorithm, in order to deal with a real-world large-scale challenging problem.
- Suggesting the two-byte transformation technique from the decimal search space into the binary one so as to achieve a better solution in binary problem from meta-heuristics designed for the continuous problem.

The rest of the paper is organized as follows: section II reveals the structure and mathematical formulation of the BSO problem, the basic principle of the AOA, and how to integrate the AOA into the BSO problem. Section III presents numerical results and discussion on the TETS to demonstrate the efficiency of the suggested strategy. Ultimately, in section IV, conclusions are drawn.

## II. METHODS

### A. Bus Splitting Optimization Problem Formulation

Bus splitting optimization is related to the network topology reconfiguration (NTR); however, they are not equal concepts since BSO just creates bus islanding by changing the feeder positions of the substations, whereas NTR implements both bus islanding and transmission switching actions. As transmission switching action in the large-scale real-world power system might lead to security violations in a single outage situation, it is not considered in the optimization problem of this study. The objective function of the BSO problem is to minimize overloading of transmission lines and voltage violation of all busbars in both base case and N-1 situations which can be formulated as follows:

$$min.\sum_{l:1}^{N}\frac{S_l}{S_l^{limit}}x\frac{100}{n_l}+\sum_{c:1}^{N_c}\sum_{l:1}^{N}\frac{S_{c,l}}{S_l^{Max}}x\frac{100}{n_l}+\sum_{c:1}^{N_c}\sum_{i:1}^{B}\left(V_{vio}{}^{c}\right)^2*n_R, l\neq c \quad (1)$$

$$if\ V_{vio}{}^{c}>V_{vio}{}^{limit}\rightarrow V_{vio}{}^{c}=\frac{V_i^c-1}{V_i^{max}-V_i^{min}} \quad (2)$$

$$if\ S_l<S_l^{limit}\rightarrow n_l=n\ and\ if\ S_l\geq S_l^{limit}\rightarrow n_l=1 \quad (3)$$

$$if\ S_{c,l}<S_l^{Max}\rightarrow n_l=n\ and\ if\ S_{c,l}\geq S_l^{Max}\rightarrow n_l=1 \quad (4)$$

where $n_l$ symbolizes a constant coefficient for line $l$, $S_l$ and $S_{c,l}$ represent apparent power flow of line $l$ in base case and contingency case, and $S_l^{limit}$ and $S_l^{Max}$ stand for the thermal limit of line $l$ and maximum allowable power flow before overcurrent protection trips at line $l$, respectively. $B$, $V_{vio}{}^{c}$, $n_R$, $V_i^c$, $V_i^{max}$, $V_i^{min}$, and $V_{vio}{}^{limit}$ represent the number of busbar, the voltage violation for busbar $i$ in contingency $c$, the constant weight for bus voltage violation, voltage at the bus $i$ in contingency $c$, the maximum and minimum voltage for bus $i$, and the voltage violation limit of busbar, respectively:

$$st.\sum_{i:1}^{B}\left(\frac{sc_i}{c_{SC}}\right)^n, if\ sc_i>sc_{limit} \quad (5)$$

$$if\ N_b\geq 4\rightarrow z_b\epsilon K, \forall b \quad (6)$$

$$r=2\leq\sum_{i:1}^{N_b}bc_i\leq N_b-2, \forall b \quad (7)$$

$$if\ r=True\rightarrow z_b=0\ else\ z_b=1, \forall b \quad (8)$$

where $sc_i$, $sc^{limit}$, $c_{sc}$, $z_{sub}$, $K$, $N_b$, $b_{ci}$, and $r$ represent SCC of bus i, SCC limit at related voltage level, a constant coefficient, zero impedance line in a substation, substation list having zero impedance line, the number of lines in substation $b$, binary code of line $i$ at substation $b$, and the necessary condition to disconnect a zero impedance line, respectively.

The SCC is considered as a constraint in the BSO problem in this study. However, various numerical analyses implemented show that if the SCC level of busbars in the power system studied is around the SCC limit, the algorithm does not manage to overcome the SCC constraint, resulting in divergence. Therefore, any violation in the SCC constraint incorporates into the objective function as a punishment. This technique is known as aggregating method and it is used as follows:

$$min.f + \mu_I * f_{sc} \tag{9}$$

$$f_{sc} : \sum_{i:1}^{B} \frac{sc_i}{2m + m * sgn\left(sc^{limit} - sc_i\right)} \tag{10}$$

where $f$, $m$, $\mu_I$, and $sgn$ represent original objective function shown in eq-1, constant coefficients, and signum function, respectively.

The topological framework created in the transmission system should cover the needs of the power flow equations. If the binary codification designed by the meta-heuristic algorithm brings about a busbar that its only feeder is a transformer, the base case power flow equations do not converge. Therefore, any divergence of power flow equations in created bus layout should be included in the problem as either a constraint or an objective and it can be attached to the objective function by using the aggregate method as follows:

$$min.f + \mu_I * f_{sc} + M \tag{11}$$

where $M$ is a big number to be used in order to punish related topology due to divergence in power flow equations.

**B. Archimedes Optimization Algorithm**

The AOA, a physic-based meta-heuristic algorithm, is based on the principle that when an object is immersed in a fluid, the fluid enforces an upward buoyant force on the object equivalent to the weight of the fluid displaced by the object [21]. We focus on the mathematical formulation of the AOA but further information about the inspiration of the algorithm can be viewed from the original paper.

$$O_i = lb_i + rand * \left(ub_i - lb_i\right), \forall i \tag{12}$$

$$den_i, vol_i = rand, \forall i \tag{13}$$

$$acc_i = lb_i + rand * \left(ub_i - lb_i\right), \forall i \tag{14}$$

Where $O_i$, $lb$, $ub$, $den$, $vol$, $acc$, and $rand$ represent object i of the population, lower and upper bounds of the search space, density, volume, acceleration, and randomly generated number between 0 and 1. These equations are used to create initial positions ($x_{best}$) of entire population and $x_{best}$, $den_{best}$, $vol_{best}$, and $acc_{best}$ are determined by evaluating the performance of each position.

$$den_i^{t+1} = den_i^t + rand * \left(den_{best} - den_i^t\right), \forall i \tag{15}$$

$$vol_i^{t+1} = vol_i^t + rand * \left(vol_{best} - vol_i^t\right), \forall i \tag{16}$$

$$TF = exp\left(\frac{t - t_{max}}{t_{max}}\right) \tag{17}$$

$$d^{t+1} = exp\left(\frac{t_{max} - t}{t_{max}}\right) - \left(\frac{t}{t_{max}}\right) \tag{18}$$

$$if\ TF \le 0.5 \rightarrow acc_i^{t+1} = \frac{den_k + vol_k * acc_k}{den_i^{t+1} * vol_i^{t+1}} \tag{19}$$

$$if\ TF > 0.5 \rightarrow acc_i^{t+1} = \frac{den_{best} + vol_{best} * acc_{best}}{den_i^{t+1} * vol_i^{t+1}} \tag{20}$$

$$acc_{i-norm}^{t+1} = 0.9 * \frac{acc_i^{t+1} - \min\left(acc\right)}{\max\left(acc\right) - \min\left(acc\right)} + 0.1 \tag{21}$$

$$if\ TF \le 0.5 \rightarrow x_i^{t+1} = x_i^t + C_1 * rand * acc_{i-norm}^{t+1} * d * \left(x_{rand} - x_i^t\right) \tag{22}$$

$$if\ TF > 0.5 \rightarrow x_i^{t+1} = x_{best}^t + F * C_2 * rand * acc_{i-norm}^{t+1} * d * \left(C_3 * TF * x_{best} - x_i^t\right) \tag{23}$$

$$F = \begin{cases} +1\ if\ 2 * rand - C_4 \le 0.5 \\ -1\ if\ 2 * rand - C_4 > 0.5 \end{cases} \tag{24}$$

where $den_{best}$, $vol_{best}$, and $rand$ are density and volume of the best object found so far and uniformly distributed random number, respectively, $TF$, $d$, $t$, and $t_{max}$ represent transfer operator, density factor, current, and maximum number of iteration, $den_k$, $vol_k$, and $acc_k$ symbolize density, volume, and acceleration of kth object randomly chosen from the population, respectively, $acc_{i-norm}^{t+1}$ is the normalization of $acc_i^{t+1}$, $x_i^{t+1}$ is the next position of the object i, $C_1$, $C_2$, $C_3$, and $C_4$ are constant coefficients, $F$ is utilized like a flag changing the direction of motion. Further explanation about these variables can be examined from [22].

The balance between exploration and exploitation phases is ensured through transfer operator $TF$ and density factor $d$. Transfer operator imitates the idea that if two objects are immersed in the fluid, a collision between objects occurs but the objects reach an equilibrium state after a period of time. In this direction, the exploration phase is operated by using the concept that if the transfer operator is lower than 0.5, the collision between two agents of the population happens through equations 19 and 22. However, if the objects arrive at an equilibrium state, the exploitation phase is served via using equations 20 and 23.

### C. Integration of the Archimedes Optimization Algorithm into the Bus Splitting Optimization Problem

The AOA algorithm is designed to solve problems having continuous search space although the structure of the BSO problem is binary. Hence, we should deal with the transition process from continuous to binary search space. There have been used various transfer functions (TF) and position updating rules (PUR) in order to handle this problem [23,24]. However, additional stochastic operations are attached to the original meta-heuristic algorithm in case TF and PUR are utilized. Therefore, we focus on decimal to binary transition without using an additional operator in this study.

#### 1) Position Structure of the BSO Problem

The binary codes representing the busbar location of the feeder are used to accomplish proper distribution. Fig. 1 shows that if line-1 has zero binary code, this means that it will be connected to the bus-1. Therefore, the position of all feeders in each substation can be symbolized with the binary codification.

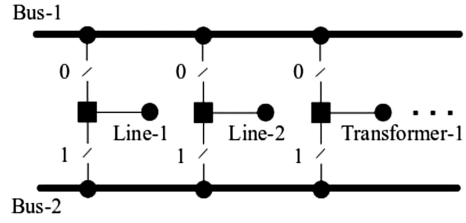


**Fig. 1.** Binary representation of the position of the feeders.

#### 2) Transition from Decimal to Binary (Two-Byte Transformation)

The direct transformation can be implemented, nonetheless as mentioned in [25], the length of the binary codification should be rigorously chosen. It is worth stating the phenomenon that if decimal codification is changed from 3 to 4, the binary codification will alter from "011" to "100." This is a great example to see that small changes in decimal codification can result in a significant alteration in binary codification. Therefore, the maximum length of the binary code related to decimal has been chosen as two in this study and the structure of the transformation can be seen in Fig. 2.

As seen in Fig. 2, one decimal variable is related to six binary codes in which two of them represent the integer part while the rest symbolize the fractional part. Since the length of the binary code corresponding to one integer number is chosen as two, the upper bound of the integer should be three ("11"). Nevertheless, because the fractional part of the decimal code can be greater than three, the modulo operation is implemented for the fractional part.

#### 3) Algorithm

A meta-heuristic technique is only interested in input and output, and the internal structure of the problem is considered as a black

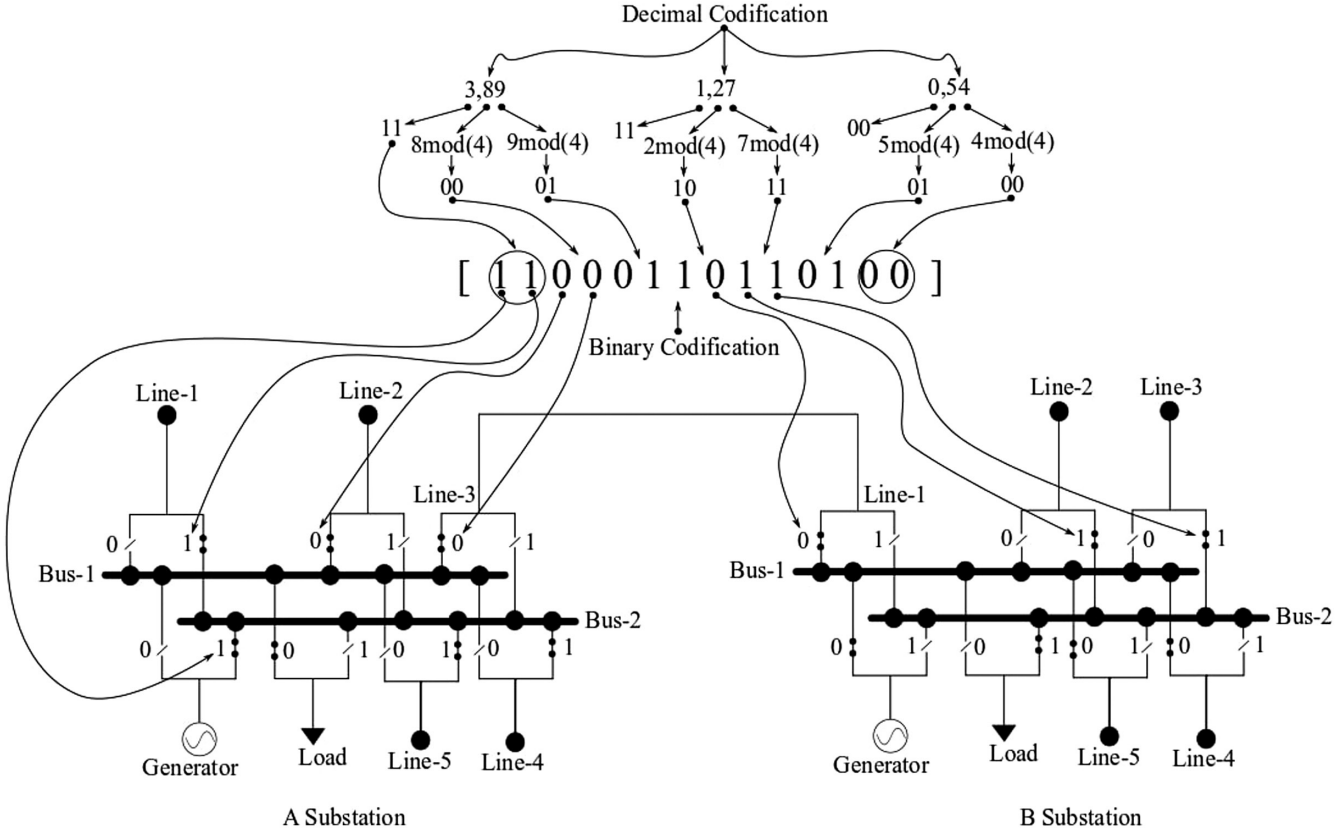


**Fig. 2.** Transition from decimal to binary codification regarding the representation of the bus layout.

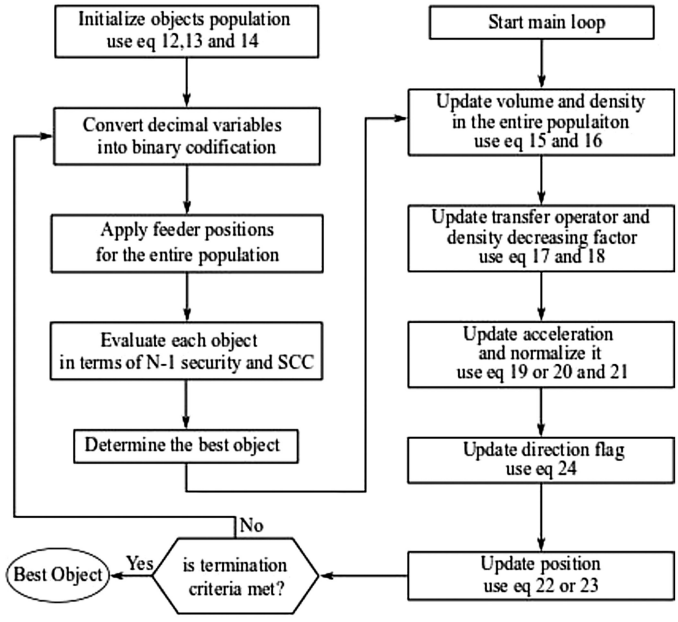


**Fig. 3.** Algorithm used to solve the BSO problem with the AOA. BSO, bus splitting optimization; AOA, Archimedes optimization algorithm.

**TABLE I**
SHORT-CIRCUIT CURRENTS OF BUSES IN ISTANBUL ANATOLIAN REGION FOR THE BASE CASE (ALL ZERO IMPEDANCE LINES ARE IN SERVICE) AND AFTER BUS SPLITTING OPTIMIZATION

| | | Base Case | | After Bus Splitting Optimization | |
|---|---|---|---|---|---|
| **No** | **Bus Name** | **Three-Phase Fault** | **Line-Ground Fault** | **Three-Phase Fault** | **Line-Ground Fault** |
| 1 | 210121 | **35983.9** | **32259.8** | 30279.8 | 27820.5 |
| 2 | 210122 | **33029.3** | 28882.9 | 28594.0 | 25684.1 |
| 3 | 211221 | **42774.5** | **39715.6** | 28900.8 | 25200.1 |
| 4 | 211321 | 29045.9 | 23935.9 | 24548.5 | 20085.2 |
| 5 | 211421 | 27196.9 | 21426.3 | 23258.4 | 18391.0 |
| 6 | 211521 | **35417.3** | **37813.5** | 23743.5 | 24302.1 |
| 7 | 211522 | **35417.3** | **37813.5** | 26318.6 | 27992.4 |
| 8 | 211621 | **35723.6** | **33319.2** | 21269.1 | 19722.5 |
| 9 | 211622 | **35723.6** | **33319.2** | 20676.6 | 19301.2 |
| 10 | 211821 | **35112.4** | 28549.7 | 26483.8 | 21588.8 |
| 11 | 211822 | **35112.4** | 28549.7 | 16371.6 | 11225.5 |
| 12 | 214321 | **33965.4** | **33267.0** | 24714.3 | 24918.4 |
| 13 | 214322 | **33965.4** | **33267.0** | 14096.0 | 10422.8 |
| 14 | 214821 | **33650.0** | 30762.0 | 21543.4 | 19767.4 |
| 15 | 214822 | **33650.0** | 30762.0 | 7026.6 | 4120.0 |
| 16 | 216721 | **30488.5** | 25602.0 | 6849.7 | 3986.0 |
| 17 | 216722 | 30488.5 | 25602.0 | 15797.4 | 12236.6 |
| 18 | 217221 | 24871.6 | 22444.0 | 21238.0 | 19828.1 |

box. In this paper, AOA provides binary codes representing the position of the feeders as an input by using the transformation from decimal to binary and alterations of positions in substations according to this binary codification are implemented. The overall algorithm related to the search process is presented in Fig. 3.

First, an initial population is created with randomly generated objects. Then, the main loop is started after evaluating initial positions and determining the best fitness. The normalized accelerations for the entire population are calculated by utilizing obtained volumes, densities, transfer operator, and density decreasing factor. In the final step used for the main loop of the AOA, positions are updated in continuous search space after determining the position direction flag and these obtained decimal positions are converted into the binary codification. These new positions are evaluated in terms of SCC and N-1 security and the performance of the solution is transferred to the AOA as an output. A number of modifications in binary codification are performed by the AOA at each step and this process goes on over iterations in order to obtain a better solution.

## III. RESULTS AND DISCUSSION

Archimedes optimization algorithm that mimics the idea that the weight of the displaced fluid is proportionate to the buoyant force produced upward on an object immersed in a fluid is used to solve the BSO problem of the Istanbul Anatolian Side of the TETS. For the sake of protecting information security, any impedance value or substation name related to the TETS is not presented. The algorithm is coded using Python programming language and PSS/E version 35.2 program on an Intel® Core™ i7-8850U CPU at 2.60GHz with 16GB of RAM.

The Istanbul Anatolian Region contains 28 substations and 51 lines with a voltage of 154 kV. In 14 of these substations, there is a coupling circuit breaker between busbars. On one hand, many autotransformer connections between 400 kV and 154 kV voltage levels have been built in this region resulting in the generation of high-level SCCs. It is worth mentioning that the SCC limit of the circuit breakers in this region remains at 31.5 kA for the 154 kV voltage level. On the other hand, the intensive consumption of this region requires that special attention should be devoted to N-1 security [6].

$C_1$, $C_2$, $C_3$, and $C_4$ coefficients used in the equations 22-24 are set as 2, 6, 2, and 0.5, respectively. The population size and the number of iterations of the AOA have been applied as 100 and 500. Obtaining a quality solution to the BSO problem in the real-world power system took 119 hours. If all zero impedance lines are in service in the related region, the N-1 security score of the power system will be 3.13, while the SCC score will reach $1.142415 \times 10^6$. Table I also shows that almost every busbar is exposed to the over SCC before the implementation of the suitable bus splitting. After the best solution obtained from the AOA is executed to the power system, both the system static security in the single outage is preserved by acquiring the 3.11 score and the SCC score is reduced to 131.9, which do not lead to any complication in the related region of the real-world power system.

The convergence curve showing the solution quality of the algorithm over iterations is demonstrated in Fig. 4. As can be seen in this curve, the best fitness is obtained around 200th iterations (exactly 176th) which means that a quality solution that can be implemented in the power system is achieved in around 60 hours. The maximum function evaluation number was implemented to be able to avoid local optimal points. The amount of the function evaluation can

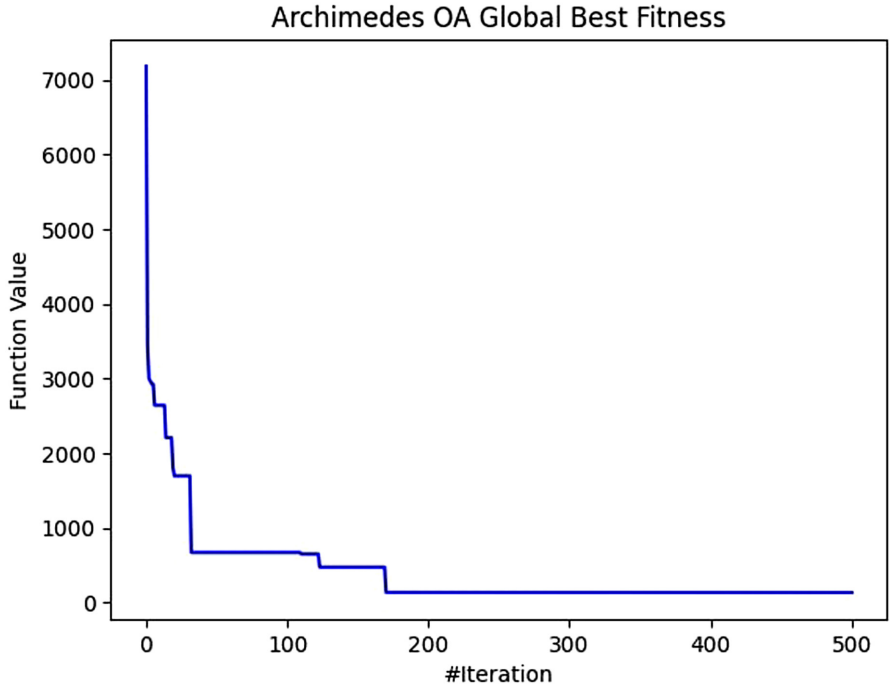


**Fig. 4.** Convergence curve of the AOA in the BSO problem. BSO, bus splitting optimization; AOA, Archimedes optimization algorithm.


**Fig. 5.** Trajectory of some individuals of the population at first and second dimension.

be reduced in order to decrease the solution time of the problem. However, it is worth mentioning that the lower function evaluation might lead to the algorithm not converging to the global minimum.

There are 11 substations to be split and 96 feeders to be distributed in the Istanbul Anatolian Region of the TETS and so there are 96 decision variables in the binary search space of the problem. However, the number of continuous variables to be used in AOA is 16 because of implementing the transition from the decimal to the binary. The trajectory for the first element of the 6th, 18$^{th}$, and 23rd individuals, each of whom has 16 dimensions, is presented in Fig. 5 and the qualified bus splitting strategy, produced for the

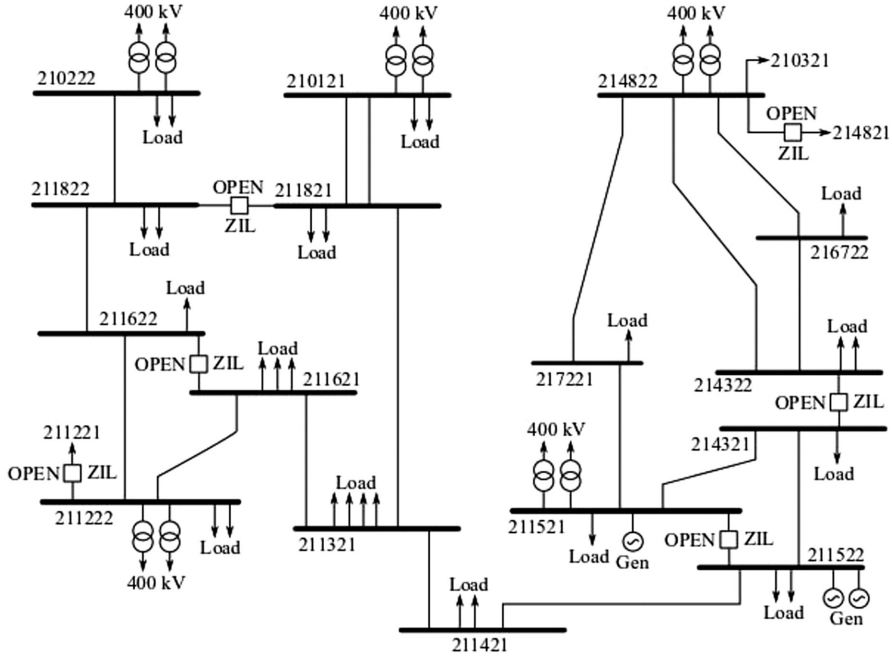


**Fig. 6.** Feeder distributions at substations in the Istanbul Anatolian Region of TETS obtained from AOA. AOA, Archimedes optimization algorithm; TETS, Turkish Electricity Transmission System.

Istanbul Anatolian Side of TETS acquired from AOA, is shown in Fig. 6. The trajectory of the first agents shows that individuals investigate different regions of the search space.

The zero impedance lines between "211821-211822," "211621-211622," "211221-211222," "211521-211522," "214321-214322," and "214821-214822" are disconnected in order to reduce the over SCC as depicted in Fig. 6. This topological framework not only restricts the SCC but maintains the system security in the N-1 situation. Therefore, the results demonstrate the efficacy of the AOA technique in presenting valuable solutions that can help the system operators in their decision process.

## IV. CONCLUSION

The BSO problem is one of the most substantial problems that transmission system operators might encounter with everyday operations in the power system due to a large number of possibilities. Although the bus splitting technique is beneficial in terms of curtailing the SCCs, the static security of the transmission system should be sustained after splitting. To deal with this crucial problem in the real-world large-scale power system, the novel AOA is used in this study. The approach for the transformation from decimal to binary is introduced in order to cope with the BSO problem. The numerical study on the TETS substantiates the effectiveness of the AOA with the proposed decimal-binary transition architecture in order to enhance the power system security in terms of SCC reduction and avoidance of overloading.

As mentioned in the numerical results section, 50 000 function evaluation was implemented to be able to deal with the BSO problem, and therefore, the solution time of the optimization process reached long hours. Network reduction might be applied or DC power flow equations instead of AC can be utilized to decrease the solution time of the problem. Another option is machine learning techniques that can be performed so as to handle this problem in future works. However, it is worth keeping in mind that any negligence in power flows or SCC may bring about an inappropriate topology since the related region studied in TETS is operated already in its extremity.

**Peer-review:** Externally peer-reviewed.

**Declaration of Interests:** The author has no conflicts of interest to declare.

**Funding:** The authors declared that this study has received no financial support.

## REFERENCES

1. P. Dehghanian, and M. Kezunovic, "Probabilistic impact of transmission line switching on power system operating states," IEEE Publications/PES Transmission and Distribution Conference and Exposition (T&D), Dallas, TX, USA, 3–5 May 2016, pp. 1–5.
2. S. Namchoat, and N. Hoonchareon, "Optimal bus splitting for short-circuit current limitation in metropolitan area," 10th International Conference on Electrical Engineering/Electronics, Computer, Telecommunications and Information Technology, ECTI-CON 2013, Krabi, Thailand, 15–17 May 2013, pp. 1–5.
3. E. Doğan, and N. Yörükeren, "Binary pathfinder algorithm for bus splitting optimisation problem," *IET Gener. Transm. Distrib.*, vol. 14, no. 26, pp. 6613–6623, 2020. [CrossRef]
4. E. Doğan, and N. Yörükeren, "Optimal bus layout in transmission system by using meta-heuristic approaches," *Electr. Power Compon. Syst.*, vol. 48, no. 12–13, pp. 1390–1400, 2020. [CrossRef]
5. Z. Yang, H. Zhong, Q. Xia, and C. Kang, "Optimal transmission switching with short-circuit current limitation constraints," *IEEE Trans. Power Syst.*, vol. 31, no. 2, pp. 1278–1288, 2016. [CrossRef]
6. E. Doğan, and N. Yörükeren, "Optimal bus layout in electricity transmission system by using binary particle swarm optimization: Turkey case study," *SEERC Colloq.*, vol. 2021, 2021, Austria-online.
7. M. Heidarifar, and H. Ghasemi, "A network topology optimization model based on substation and node-breaker modeling," *IEEE Trans. Power Syst.*, vol. 31, no. 1, pp. 247–255, 2016. [CrossRef]
8. M. Heidarifar, M. Doostizadeh, and H. Ghasemi, "Optimal transmission reconfiguration through line switching and bus splitting," IEEE PES Gen. Meeting | Conference & Exposition, National Harbor, MD, USA, 27–31 July 2014, 2014, pp. 1–5.
9. M. Heidarifar, P. Andrianesis, P. Ruiz, M. C. Caramanis, and I. C. Paschalidis, "An optimal transmission line switching and bus splitting heuristic incorporating AC and N-1 contingency constraints" *Int. J. Electr. Power Energy Syst.*, vol. 133, p. 107278, 2021. [CrossRef]
10. Y. Zhou, A. S. Zamzam, A. Bernstein, and H. Zhu, "Substation-level grid topology optimization using bus splitting," Am. Control. Conference (ACC), New Orleans, LA, USA, 25–28 May 2021, pp. 2868–2874.
11. T. Ding, K. Sun, Q. Yang, A. W. Khan, and Z. Bie, "Mixed integer second order cone relaxation with dynamic simulation for proper power system islanding operations," *IEEE J. Emerg. Sel. Top. Circuits Syst.*, vol. 7, no. 2, pp. 295–306, 2017. [CrossRef]
12. N. Z. Saharuddin, I. Z. Abidin, H. Mokhlis, A. R. Abdullah, and K. Naidu, "A power system network splitting strategy based on contingency analysis," *Energies*, vol. 11, no. 2, 2018. [CrossRef]
13. P. Fernández-Porras, M. Panteli, and J. Quirós-Tortós, "Intentional controlled islanding: When to island for power system blackout prevention," *IET Gener. Transm. Distrib.*, vol. 12, no. 14, pp. 3542–3549, 2018. [CrossRef]
14. P. Demetriou, A. Kyriacou, E. Kyriakides, and C. Panayiotou, "System splitting strategy considering power system restoration," *IEEE Manchester PowerTech*, vol. 2017, pp. 1–6, 2017.
15. S. Mirjalili, S. M. Mirjalili, and A. Lewis, "Grey wolf optimizer," *Adv. Eng. Softw.*, vol. 69, pp. 46–61, 2014. [CrossRef]
16. D. H. Wolpert, and W. G. Macready, "No free lunch theorems for optimization," *IEEE Trans. Evol. Comput.*, vol. 1, no. 1, pp. 67–82, 1997. [CrossRef]
17. J. H. Holland, "Genetic algorithms," *Sci. Am.*, *Scientific American*, vol. 267, no. 1, pp. 66–72, 1992. [CrossRef]
18. R. Eberhart, and J. Kennedy, "A new optimizer using particle swarm theory," Sixth International Symposium on Micro Machine and Human Science, Nagoya, Japan, 4–6 October 1999, pp. 39–43.
19. E. Rashedi, H. Nezamabadi-pour, and S. Saryazdi, "GSA: A Gravitational Search Algorithm" *Inf. Sci.*, vol. 179, no. 13, pp. 2232–2248, 2009. [CrossRef]
20. M. Dorigo, M. Birattari, and T. Stutzle, "Ant colony Optimatization," *IEEE Comp. Intell. Mag.*, vol. 1, no. 4, pp. 28–39, 2006.
21. F. A. Hashim, K. Hussain, E. H. Houssein, M. S. Mabrouk, and W. Al-Atabany, "Archimedes optimization algorithm: A new metaheuristic

algorithm for solving optimization problems," *Appl. Intell.*, vol. 51, no. 3, pp. 1531–1551, 2021. [CrossRef]

22. N. van Thieu, and D. Molina, "Meta-heuristic algorithms using Python (MEALPY-software)," *Zenodo*, 2021. [CrossRef]
23. E. Rashedi, H. Nezamabadi-Pour, and S. Saryazdi, "BGSA: binary gravitational search algorithm," *Nat. Comput.*, vol. 9, no. 3, pp. 727–745, 2010. [CrossRef]
24. S. Mirjalili, and A. Lewis, "S-shaped versus V-shaped transfer functions for binary Particle Swarm Optimization," *Swarm Evol. Comput.*, vol. 9, pp. 1–14, 2013. [CrossRef]
25. R. A. Romero, A. Monticelli, and R. Romero, "Transmision system expansion planning by an extended genetic algorithm," *IEE Proc. Gener. Transm. Distrib.*, vol. 145, no. 3, pp. 329 – 335, 1998. [CrossRef]

cigre Turkey

TEPES
TURKISH JOURNAL OF ELECTRICAL POWER AND ENERGY SYSTEMS

TEPES, Vol. 2, Issue. 2, 124-133, 2022 **DOI:** 10.5152/tepes.2022.21046

RESEARCH ARTICLE

# Impact Study of Distributed Generations in Voltage Sag Mitigation Using an Improved Three-Phase Unbalanced Load Flow for Active Distribution Network

**Ujjal Sur**

Department of Electrical engineering, Future Institute of Engineering and Management, Sonarpur Station Road, Kolkata, West Bengal, India

**Cite this article as:** U. Sur. Impact study of distributed generations in voltage sag mitigation using an improved three-phase unbalanced load flow for active distribution network. *Turk J Electr Power Energy Syst,* 2022; 2(2), 124-133.

## ABSTRACT

In this paper, a new three-phase unbalanced distribution load flow (DLF) technique is proposed to study the impact of distributed generations (DGs) installed in the distribution networks in mitigating the voltage sag. Distributed generations are modeled as variable reactive power and constant power factor source with both wind- and solar-powered DG in the case study. The proposed DLF technique is based on the application of set theory. Effect of DGs in mitigating voltage sag is mathematically explained with the help of phasor diagram. The proposed technique is tested over standard IEEE 13 and IEEE 123 bus distribution networks with programming in MATLAB platform. To justify the claims, different cases have been studied like load increment and increasing maximum power limit of DGs. Also, a comparison is drawn between proposed DLF technique and traditional backward–forward sweep method where the efficacy of proposed technique is proved over the traditional method.

**Index Terms—**Distributed generations (DGs), distribution load flow (DLF), distributed generations (DGs), voltage sag, radial distribution network.

## I. INTRODUCTION

Distribution load flow (DLF) is a key mathematical method for analyzing the steady-state response of a power distribution system. Distribution automation needs fast and efficient power flow solution both at its planning and in operating condition. Distribution feeders are characterized by their inherently unbalanced loading for asymmetrical spacing of conductors and single-phase loads. Conventional load flow programs cannot be applicable for distribution systems due to these factors. Nowadays, small captive power plants as well as renewable power generations are widely used called distributed generators (DGs), which give low carbon footprint. Therefore, power industry is having positive environmental impacts as they mostly run by renewable energy sources. With the installation of DGs, DLF results of a system also alter which affects the flat voltage profile of bus voltages and line losses. Moreover, a DG-based distribution network can cater the growing load over the buses with time. The number of research articles on optimal DG allocation can be obtained in [1].

Backward–forward sweep (BFS) method is mostly used for the DLF studies like in [2] where Shirmohammadi et al. have performed a compensating power flow method for the weakly meshed radial distribution and transmission systems by using the concept of multiport compensation, where radial part is solved in two steps. In the beginning, branch currents are calculated with which the node voltages are updated in second step. In [3], a modified BFS technique has been used where the loop analysis is used to formulate the DLF problem. Another kind of BFS method is proposed in [4] to analyze weakly meshed radial distribution system which involves some unique equations formulation to solve DLF problem. A novel DLF technique utilizing Newton–Raphson method with node voltages as state variables is proposed in [5]. In DG modeling, reviewing different works in [6-9] reveals that most of the modeling has been done on the PV and PQ node basis like in [10] where the synchronous and induction types DGs are approximately modeled as PQ nodes in load flow studies. Teng in [11] proposed some modeling schemes of DGs for DLF in different manner considering the reactive power output, power factor, and voltage as the parameters for modeling. In papers [12-14], authors have studied the effect of DGs over voltage sag mitigation by optimal DG placement in the network.

**Corresponding author:** Ujjal Sur, ujjalsur@gmail.com

**Received:** March 13, 2022
**Accepted:** May 5, 2022
**Publication Date:** May 12, 2022

The theme of this work to develop an improved DLF technique suitable for handling the DG models incorporated within the network for analyzing its effect in voltage sag mitigation. To study the effect of DG integration over voltage sag, the DG power generation limit has to be varied with the load increment. Also, calculation of DG penetration level with maximum DG power generation will help in analyzing the effect of DG modeling over voltage dip conditions. A comparative study of traditional BFS method with proposed DLF technique is studied here.

This paper started with an introduction organized in different sections as components modeling under which modeling of DGs has been proposed with different other associated components followed by proposed DLF method. After this, a section is dedicated in mathematical explanation of how the DGs mitigate the effect of voltage sag in the system. In the result section, the proposed method is verified over different radial distribution systems and the results are presented using a comparative study. Finally, the discussions are made over the proposed method and conclusion is drawn with a hint of further progress in this regard.

## II. COMPONENTS MODELING

Based on the energy sources, DGs can be classified into stable or constant energy sources like gas turbines, fuel cells and unstable or variable energy sources like solar and wind. Also, based on different power converter devices connected, the classification of DGs will be different. Here in this paper, DGs have been classified based on their output power characteristics like constant power factor model and variable reactive power model. Some other references have classified the DGs as PV- and PQ-based model.

### A. Variable Reactive Power Model

Induction generators (IGs) used for wind energy conversion falls under this category where the real power is kept constant as it can be derived from wind turbine power curve for each corresponding wind speed. The IG model presented here is based on reference [15]. Using Boucherot's theorem for conservation of complex power, the expression for the reactive power consumed by the machine is given as:

$$Q_{ig}^{w} = V^2 \frac{X_c - X_m}{X_c X_m} + X \frac{V^2 + 2RP_{ig}}{2(R^2 + X^2)} - X \frac{\sqrt{(V^2 + 2RP_{ig})^2 - 4P_{ig}^2(R^2 + X^2)}}{2(R^2 + X^2)} \quad (1)$$

**Main Points**

- This paper proposes a set theory-based novel load flow approach.
- This enables one-time construction of impedance matrix to solve load flow problem and eradicates the problems associated with backward–forward sweep load flow method.
- Different distributed generations and loads are being modeled for load flow study.
- Voltage sag reduction study has been done with the association of distributed generations.
- Proposed method has been tested over benchmark IEEE 13 bus and IEEE 123 bus active distribution networks.

where $Q_{ig}^{w}$ is the reactive power consumed, $V$ is the voltage, $P_{ig}$ is the real power, $X$ is the sum of the stator and rotor leakage reactance, $X_c$ is the capacitor bank equivalent reactance, and $R$ is the sum of the stator and rotor resistances.

Now from the steady state point of view, the reactive power can be represented as a function of real power as:

$$Q_{ig}^{w} = -Q_0 - Q_1 P_{ig} - Q_2 P_{ig}^2 \quad (2)$$

where $Q_0, Q_1$, and $Q_2$ are experimentally obtained constant parameters.

An approximation of (1) to (2) can be made by means of the McLaurin polynomial taking into account the first two derivatives of (1) and neglecting the resistance $R$, the expression for the reactive power is:

$$Q_{ig}^{w} \approx V^2 \frac{X_c - X_m}{X_c X_m} + \frac{X}{V^2} P_{ig}^2 \quad (3)$$

The reactive power compensation by installed capacitor banks may not be done fully sometimes as due to huge reactive power demand.

### B. Constant Power Factor Model

Most of the commonly used DGs are modeled as constant power factor like solar energy and gas turbines where the energy is harvested through power electronic converters and synchronous generators, respectively. As both the real power and power factors are specified for this type of DGs, the reactive power for the DG is calculated as:

$$Q_{dg}^{s} = P_{dg} \tan(\cos^{-1}(pf_{dg}))$$

$$\text{or}, Q_{dg}^{s} = \frac{P_{dg}\sqrt{1 - pf_{dg}^2}}{pf_{dg}} \quad (4)$$

where $Q_{dg}^{s}$ is the reactive power supplied by the DG, $P_{dg}$ is the active power supplied, and $pf_{dg}$ is the power factor of the DG unit installed.

Different other components associated with the distribution system network have to be modeled mathematically which include distribution transformer, voltage regulator, and capacitor bank. Modeling of distribution transformers of any connection and phase group can be performed as described by Baran and Staton in [16] and it has been followed here in modeling distribution transformers. A voltage regulator is used to control the voltage up to 5%–10%. In this paper, a voltage regulator is modeled as series impedance and a transformer having a tap is placed on the secondary side. That is, in other words, the voltage regulator may be treated as a distribution transformer modeled previously with series impedance connected with it. Capacitor banks are installed at the distribution end to supply the reactive power to the system. A capacitor bank being a voltage-dependent component is modeled in respect of internal impedance and the charge stored by capacitor in terms of internal capacitor current as follows:

$$Z_i = \frac{|V_i|^2}{S_i^*} \text{ and } I_i = \frac{V_i}{Z_i} \quad (5)$$

Here, all these above terms will be calculated as phase to neutral for star connected capacitor bank and as phase to phase for delta connected capacitor bank.

## III. PROPOSED DLF METHOD

Proposed method starts with phase impedance matrix (PIM) formation by three-phase line modeling. This PIM does not require any lower–upper factorization of matrix. Classical set theoretic approach has been envisaged here in the PIM formulation. Set theory has been applied to branch path set and branch impedance set. Thus, no other node and branch identification property is required in this DLF solution. In the beginning, a three-phase line is modeled here because the distribution system taken to analyze is an unbalanced one and when has to be analyzed using the PIM matrix, it requires a three-phase line model to solve the DLF problem.

The following method of three-phase line modeling can be easily applicable for unbalanced distribution system. Assuming a generalized impedance model of a three-phase line with the self and mutual impedances, Carson's equations for three-phase four-wire grounded system can be constructed as:

$$\left[z_{i,i+1}^{abcn}\right]=\begin{bmatrix} z_{i,i+1}^{aa} & z_{i,i+1}^{ab} & z_{i,i+1}^{ac} & z_{i,i+1}^{an} \\ z_{i,i+1}^{ba} & z_{i,i+1}^{bb} & z_{i,i+1}^{bc} & z_{i,i+1}^{bn} \\ z_{i,i+1}^{ca} & z_{i,i+1}^{cb} & z_{i,i+1}^{cc} & z_{i,i+1}^{cn} \\ z_{i,i+1}^{na} & z_{i,i+1}^{nb} & z_{i,i+1}^{nc} & z_{i,i+1}^{nn} \end{bmatrix} \tag{6}$$

Now applying Kron's reduction technique [17] with an assumption that the line is having a multi grounded neutral point, the above impedance matrix can be reduced to a 3 × 3 matrix as in (7). Using this reduced three-phase impedance matrix, the branch path set will be designed which is required for the formation of PIM matrix.

$$\left[z_{i,i+1}^{abc}\right]=\begin{bmatrix} z_{i,i+1}^{aa\_n} & z_{i,i+1}^{ab\_n} & z_{i,i+1}^{ac\_n} \\ z_{i,i+1}^{ba\_n} & z_{i,i+1}^{bb\_n} & z_{i,i+1}^{bc\_n} \\ z_{i,i+1}^{ca\_n} & z_{i,i+1}^{cb\_n} & z_{i,i+1}^{cc\_n} \end{bmatrix} \tag{7}$$

Phase impedance matrix is the only matrix required for DLF solution. A three-phase unbalanced system is taken for derivation purpose as shown in Fig. 1. Phase-wise branch impedance (PBI) has been constructed at first as:

$$\left.\begin{aligned} \phi_2 &= \left\{\left[z_{1,2}^{abc}\right]\right\} \\ \phi_3 &= \left\{\left[z_{1,2}^{abc}\right],\left[z_{2,3}^{ab}\right]\right\} \\ \phi_4 &= \left\{\left[z_{1,2}^{abc}\right],\left[z_{2,4}^{bc}\right]\right\} \\ \phi_5 &= \left\{\left[z_{1,2}^{abc}\right],\left[z_{2,4}^{bc}\right],\left[z_{4,5}^{c}\right]\right\} \end{aligned}\right\} \tag{8}$$

$I_{Bi}$ can be formulated as:

$$v_{15}=I_{B1}\left[z_{1,2}^{abc}\right]+I_{B3}\left[z_{2,4}^{bc}\right]+I_{B4}\left[z_{4,5}^{c}\right] \tag{9}$$

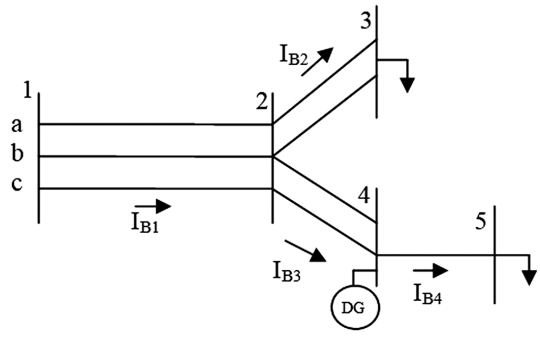


**Fig. 1.** Single line diagram of a three-phase unbalanced system with DG. DG, distributed generation.

The branch current's parameters in terms of injected load current to the branch is expressed as:

$$I_{B1}=\sum_{k=2}^{5}\left(\frac{S_k}{V_k}\right)^{*},\ I_{B2}=\sum_{k=4}^{5}\left(\frac{S_k}{V_k}\right)^{*},\ I_{B4}=\left(\frac{S_5}{V_5}\right)^{*}$$

Applying the conversions in branch current in (9), we get,

$$v_{15}=\sum_{k=2}^{5}\left(\frac{S_k}{V_k}\right)^{*}\left[z_{1,2}^{abc}\right]+\sum_{k=4}^{5}\left(\frac{S_k}{V_k}\right)^{*}\left[z_{2,4}^{bc}\right]+\left(\frac{S_5}{V_5}\right)^{*}\left[z_{4,5}^{c}\right] \tag{10}$$

So on rearranging (10), the new equation will be:

$$\begin{aligned} v_{15}=&\left(\frac{S_2}{V_2}\right)^{*}\left[z_{1,2}^{abc}\right]+\left(\frac{S_4}{V_4}\right)^{*}\left(\left[z_{1,2}^{abc}\right]+\left[z_{2,4}^{bc}\right]\right) \\ &+\left(\frac{S_5}{V_5}\right)^{*}\left(\left[z_{1,2}^{abc}\right]+\left[z_{2,4}^{bc}\right]+\left[z_{4,5}^{c}\right]\right) \end{aligned} \tag{11}$$

Next, by the application of PBI set which has been formed earlier, equation (11) can be modified with the help of classical set theory as:

$$v_{15}=\left(\frac{S_2}{V_2}\right)^{*}\Sigma\left(\phi_2\cap\phi_5\right)+\left(\frac{S_4}{V_4}\right)^{*}\Sigma\left(\phi_4\cap\phi_5\right)+\left(\frac{S_5}{V_5}\right)^{*}\Sigma\left(\phi_5\cap\phi_5\right) \tag{12}$$

Where,

$$\Sigma\left(\phi_2\cap\phi_5\right)=\left[z_{1,2}^{abc}\right]$$

$$\Sigma\left(\phi_4\cap\phi_5\right)=\left(\left[z_{1,2}^{abc}\right]+\left[z_{2,4}^{bc}\right]\right)$$

$$\Sigma\left(\phi_5\cap\phi_5\right)=\left(\left[z_{1,2}^{abc}\right]+\left[z_{2,4}^{bc}\right]+\left[z_{4,5}^{c}\right]\right)$$

Equation (12) can be rewritten as:

$$v_{15}=\sum_{k=2}^{5}\left(\frac{S_k}{V_k}\right)^{*}\Sigma\left(\phi_k\cap\phi_5\right)$$

Now the generalized version of derived formulation including the slack bus component as $\Sigma\left(\phi_1\cap\phi_5\right)=0$, where $\varphi_1$ is a null set. We get,

$$v_{15}=\left(\frac{S_1}{V_1}\right)^{*}\Sigma\left(\phi_1\cap\phi_5\right)+\sum_{k=2}^{5}\left(\frac{S_k}{V_k}\right)^{*}\Sigma\left(\phi_k\cap\phi_5\right)$$

$$\text{or, } v_{1i}=\sum_{k=1}^{i}\left(\frac{S_k}{V_k}\right)^{*}\Sigma\left(\phi_k\cap\phi_i\right) \tag{13}$$

Therefore, the *i*th bus voltage can be evaluated as the sum of voltage drop starting from slack bus,

$$V_i=V_1-v_{1i}$$

$$\text{or, } V_i=V_1-\sum_{k=1}^{i}\left(\frac{S_k}{V_k}\right)^{*}\Sigma\left(\phi_k\cap\phi_i\right)$$

$$\text{or, } V_i=V_1-\sum_{k=1}^{i}\left(\frac{1}{V_k}\right)^{*}S_k\Sigma\left(\phi_k\cap\phi_i\right) \tag{14}$$

$$\begin{bmatrix}V_1\\V_2\\V_3\\V_4\\V_5\end{bmatrix}=\begin{bmatrix}V_1\\V_1\\V_1\\V_1\\V_1\end{bmatrix}-\begin{bmatrix}0 & 0 & 0 & 0 & 0\\ 0 & S_2^{*}\sum\left(\phi_2\cap\phi_2\right) & S_2^{*}\sum\left(\phi_3\cap\phi_2\right) & S_2^{*}\sum\left(\phi_4\cap\phi_2\right) & S_2^{*}\sum\left(\phi_5\cap\phi_2\right)\\ 0 & \vdots & \vdots & \vdots & \vdots\\ 0 & \vdots & \vdots & \vdots & \vdots\\ 0 & S_5^{*}\sum\left(\phi_2\cap\phi_5\right) & S_5^{*}\sum\left(\phi_3\cap\phi_5\right) & S_5^{*}\sum\left(\phi_4\cap\phi_5\right) & S_5^{*}\sum\left(\phi_5\cap\phi_5\right)\end{bmatrix}\begin{bmatrix}\frac{1}{V_1}\\ \vdots\\ \vdots\\ \vdots\\ \frac{1}{V_5}\end{bmatrix}^{*} \tag{15}$$

Therefore, equation (14) can be written in matrix format as (15). $\phi_1$ being a null set, every element of first row and column is zero. The matrix equation (15) is generalized in a reduced form as:

$$\left[V\right]=\left[V_1\right]-\left[PIM\right]\left[\frac{1}{V}\right]^{*} \tag{16}$$

So the desired PIM matrix has been formulated where no singularity of matrix clause will be required to solve for DLF solution. Flow chart of the proposed DLF algorithm has been shown in Fig. 2.

## IV. VOLTAGE SAG MITIGATION BY DG

To study the impact of the DGs in mitigating the effect of voltage sag, the mathematical method using phasor diagram is proposed here considering the DG connection as in Fig. 1. Fig. 3 shows the phasor diagram of the sending and receiving end bus connected with DG. The incoming bus 4 is considered as source end where DG is connected and bus 5 is considered as receiving end. $V_S$ is the source end voltage, $V_R$ is the receiving end voltage, and $V_{DG}$ is the voltage supplied by the DG. Under the normal condition, the DG voltage is calculated as:

$$V_{DG}=\sqrt{V_R^2+V_S^2-2V_RV_S\cos\delta}$$

As for a lossless system, the source-end and receiving-end voltage magnitude are to be kept the same ($V_R = V_S$), therefore,

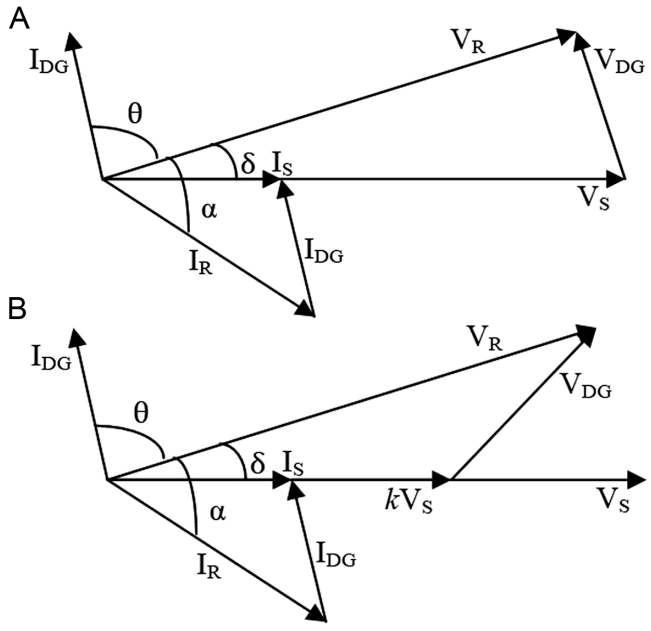


**Fig. 2.** Phasor diagram of the DG connected distribution system (a) under normal condition and (b) during voltage sag. DG, distributed generation.

$$\begin{aligned}V_{DG}&=\sqrt{V_S^2+V_S^2-2V_SV_S\cos\delta}\\&=V_S\sqrt{2\left(1-\cos\delta\right)}\end{aligned} \tag{17}$$

Let us assume that the maximum injected voltage ($V_{DG}$) for DG be a fraction of the desired receiving-end voltage, then $V_{DG\max}=k_vV_R$ ($k_v$ is ratio of the maximum injected voltage to DG to the desired receiving end voltage). So the injected voltage to DG can be determined by using (17) as:

$$V_{DG\max}=V_S\sqrt{2\left(1-\cos\delta\right)}=k_vV_R \tag{18}$$

Since the relationship $V_R=V_S$ is maintained, the maximum phase angle is obtained as:

$$\delta_{\max}=\cos^{-1}\left(1-0.5k_v^2\right) \tag{19}$$

As source voltage ($V_s$) is reduced to $kV_s$ ($0\le k\le 1$) due to $k_{Sag}$ p.u. sag at source end (where, $k_{Sag}=1-k$). The sag can possibly be reduced applying DG injected voltage ($V_{DG\max}=k_vV_R$), used in reactive power compensation, can be determined as:

$$V_R^2+\left(kV_S\right)^2-2V_R\left(kV_S\right)\cos\delta=V_{DG\max}^2$$

Putting $V_{DG\max}=k_vV_R$ and $V_S=V_R$ in the above equation, we get:

$$k^2-2k\cos\delta+1-k_v^2=0$$

$$\text{or, } k=\cos\delta\pm\sqrt{\cos^2\delta+k_v^2-1} \tag{20}$$

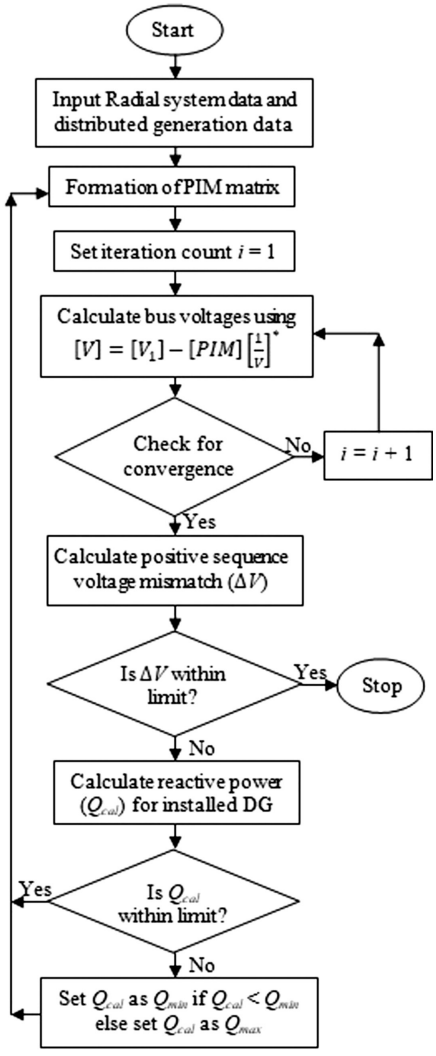


**Fig. 3.** Flow chart of proposed load flow method with DG. DG, distributed generation.

Therefore, the value of $k_{Sag}$ can be obtained as:

$$k_{Sag} = 1 - k = 1 - \left(\cos\delta \pm \sqrt{\cos^2\delta + k_v^2 - 1}\right) \quad (21)$$

From (19) and (21), a explicit solution for maximum value is calculated as:

$$k_{Sag\_\max} = k_v^2 \quad (22)$$

With higher value of $k_v$, higher amount of voltage sag can be reduced but the VA rating of the DG increases. So a standard choice of $k_v$ is required for the desirable amount of voltage sag mitigation.

## V. RESULTS

The experimental study is performed to demonstrate the proposed algorithm by programming it using MATLAB R2015b software and executed in a computer with Intel core i3, 2.4 GHz processor, and 2GB RAM over IEEE 13 bus and 123 bus standard radial distribution networks [18] test cases. The allowable high and low value of node voltage limits for IEEE 13 bus system are set as 1.05 and 0.9 p.u., respectively. For the IEEE 123 bus system, these are taken as ±6% of the substation voltage. This basically helps to demonstrate how voltage sag can be mitigated with the percentage change of the distributed generation and the loading of the system with the DG model. The DGs connected to the IEEE 13 bus system are at nodes 634 and 652 whereas two DGs are connected with IEEE 123 bus system at nodes 56 and 83.

The percentage of DG penetration level is determined as:

$$\%\ DG\ penetration = \frac{P_{dg}}{\left(P_{dg} + P_{sub}\right)} * 100 \quad (23)$$

Where $P_{dg}$ is the total active power supplied by DGs and $P_{sub}$ is the voltage at the distribution substation.

Anticipating the future load growth, DG penetration is increased with increase in the real and reactive power of loads in all the phases of nodes with load. With the change in loading and power generation limit of DG, the maximum and minimum reactive power limit changes for different cases. Both wind and solar power models are used here in each test case. The wind turbine generator used here is a pitch-regulated fixed speed IG with internal circuit details tabulated in appendix and the wind power curve is given in [19]. The capacitor bank used for power factor correction is a single-step capacitor bank. Solar-powered DG is modeled as a three-phase, 220 kW photovoltaic system with a constant power factor of 0.8 lagging. Fig. 4 shows the voltage profile for both the test cases with and without DGs, where the DGs are operated at their base rating. Four different aspects are taken for a more elaborate and in-depth study on the impact of DGs in voltage sag mitigation.

### A. Effect of Change in Power Generation Limit of DGs

To study the effect of the change in maximum DG power generation limit, the load flow is run by setting the limit of DG power generation as 50, 100, and 150 kW for IEEE 13 and IEEE 123 bus system. A performance comparison is obtained with maximum DG power generation limit using following cases over the two test system:

*Case A*: Varying solar-powered DG limit keeping wind-powered DG constant.

*Case B*: Varying wind-powered DG limit keeping solar-powered DG constant.

*Case C*: Varying both solar- and wind-powered DGs limit simultaneously.

The results in Fig. 5 show that the DG penetration level is high for IEEE 123 bus system whereas the rate of change of the DG penetration level is more in the case of the IEEE 13 bus system.

Also, it is found that the rate of DG penetration level is higher by at least 6% when both the solar- and wind-powered DGs generation

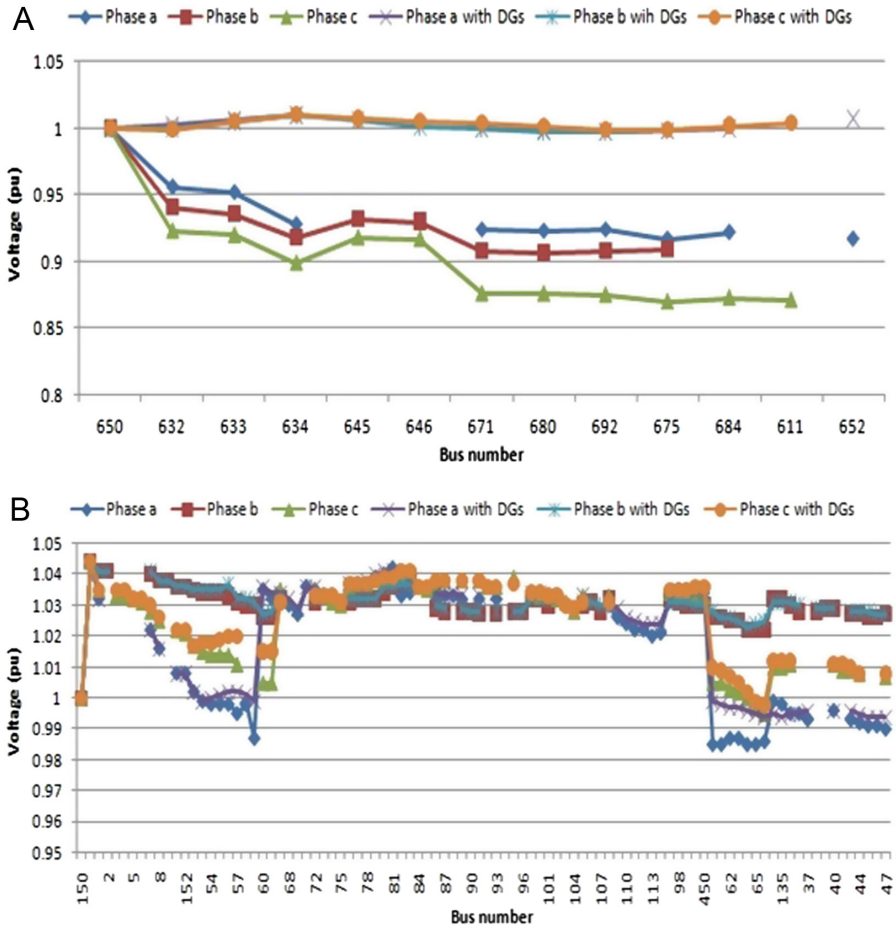


**Fig. 4.** Voltage profile with and without DGs for (a) IEEE 13 bus system and (b) IEEE 123 bus system. DG, distributed generation.

are varying simultaneously. As with increase in DG power generation limit, the DG penetration level is also getting higher but it also violates the voltage and thermal limits at the nodes. Fig. 6 and 7 show the effect of change in maximum DG power generation limit over the voltage profile of IEEE 13 and IEEE 123 bus system where the DG power generation limit is varied according to case C, that is, both the solar- and wind-powered DGs are varied simultaneously. On analyzing Fig. 6 and 7, it is understood that though the voltage sag is mitigated using DG integration, with optimal placement of DGs, the voltage profile will be smooth and loss will be minimized.

**B. Effect of Load Increment**

The performances of the solutions obtained with different planning cases are assessed with load growth test to test their capabilities in sustaining future load and also to test the ability of DGs in mitigating the voltage drop due to load growth. For IEEE 13 bus system, nodes 634, 646, 611, 675, and 652 are subjected to equal percentage load growth rate, whereas for IEEE 123 bus system, nodes 4, 16, 22, 28, 35, 47, 49, 53, 65, 76, 79, 88, 94, 102, 105, and 112 are subjected to equal percentage load growth rate. This uneven mixed selection of nodes for load increment is done to make the system more real and to check the reliability of the proposed method. The performance study on the basis of per unit voltage deviation with the load increment in each selected node is shown in Fig. 8. In case of IEEE 13 bus system, the highest per unit voltage deviation occurs on a load increment of 30% of 0.13 at node 634, whereas for IEEE 123 bus system, it occurs at buses 736 and 732 of 0.142 p.u. deviation in node voltage at an increment of 30%. It is found that on a heavy load increment also the per unit voltage deviation is much less, thus mitigating the effect of sudden voltage drop.

**C. Effect on Voltage Sag Limit**

The main causes of the voltage dip are overloads, faults, short circuits, transformer switching, starting of large motors, and many others. Here, this is based on overloaded condition or gradual increment of load and its effect on voltage sag which is to be mitigated by DG power supply. As mathematically deduced earlier to limit the voltage sag, DGs' maximum power generation limit should be increased to limit the voltage sag. Therefore, both the load and maximum DG power generation has been varied and the voltage sag variation is plotted against these two parameters. Fig. 9 shows the effect of overloading in the system which results in voltage dip at nodes. To

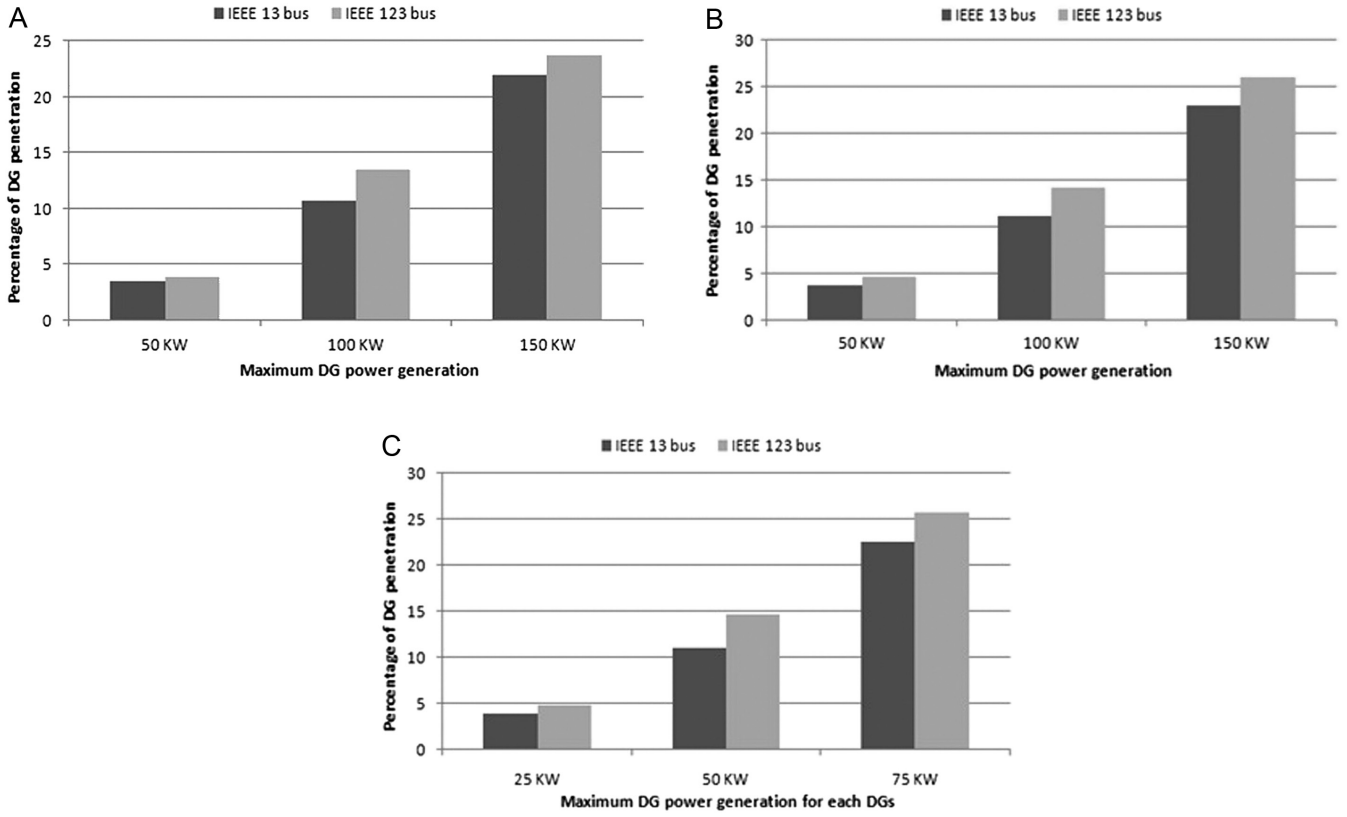


**Fig. 5.** Percentage of DG penetration due to change in maximum power generation limit of DGs for (a) case A, (b) case B, and (c) case C. DG, distributed generation.

mitigate the effect of voltage dip at different nodes, the maximum power generation limits of installed DGs are increased slowly corresponding to the load increment. From Fig. 9, it has been found that with increase in load, the per unit voltage sag limit also gets increased and so to mitigate its effect over the nodes, the power generation limit of the DGs has been also increased. For both the test cases, the nature of the graph is almost linear with nearly equal slope. Hence, the mathematical deduction about the voltage sag limit which is directly proportional to the power rating of DG is proven with experimental results.

### D. Performance Comparison with BFS Method

The results obtained with the proposed three-phase unbalanced DLF method is compared with those obtained with standard DLF technique, BFS method [4]. The comparative study of total power loss, execution time, and the number of iterations is given in Table I and Table II for IEEE 13 and IEEE 123 bus system, respectively. The result shows that the proposed method is much better than the BFS method in respect of execution time and the number of iterations. Also, the test systems with and without DGs show a remarkable change in total power loss where the system with DGs is having a sharp decrease in the power loss of nearly about 65% in every case, whereas on comparing the BFS method and the proposed method on the basis of total power loss, both the methods show nearly the same result with a negligible change of approximately 2% in the power loss data. So on comparing with BFS method, it is evident that the proposed method is much faster than the BFS method in respect of execution time as the proposed DLF method takes almost half of the time required by the BFS method for both the cases with and without DGs.

## VI. CONCLUSION

In this paper, a new DLF technique has been proposed for a radial distribution network where the DGs connected to the network are evaluated on the basis of their impact on voltage sag mitigation. To have voltage sag or dip at the nodes, the load increment at selected nodes has been done to test the effect of DGs. Simulation result shows that the DGs, are capable of mitigating the voltage sag though with increase in voltage sag limit the kVA rating of DGs should be increased. In other words, DG penetration level becomes higher with the rise in load at each node. Also, the proposed load flow technique is much better in comparison with standard BFS method used for DLF. Using the proposed DLF technique, the analysis of distribution networks coupled with DGs is faster than the BFS method irrespective of execution time and the number of iterations. Distributed generation modeling used in this paper is more flexible than other models like PV and PQ models as proposed in different research paper.

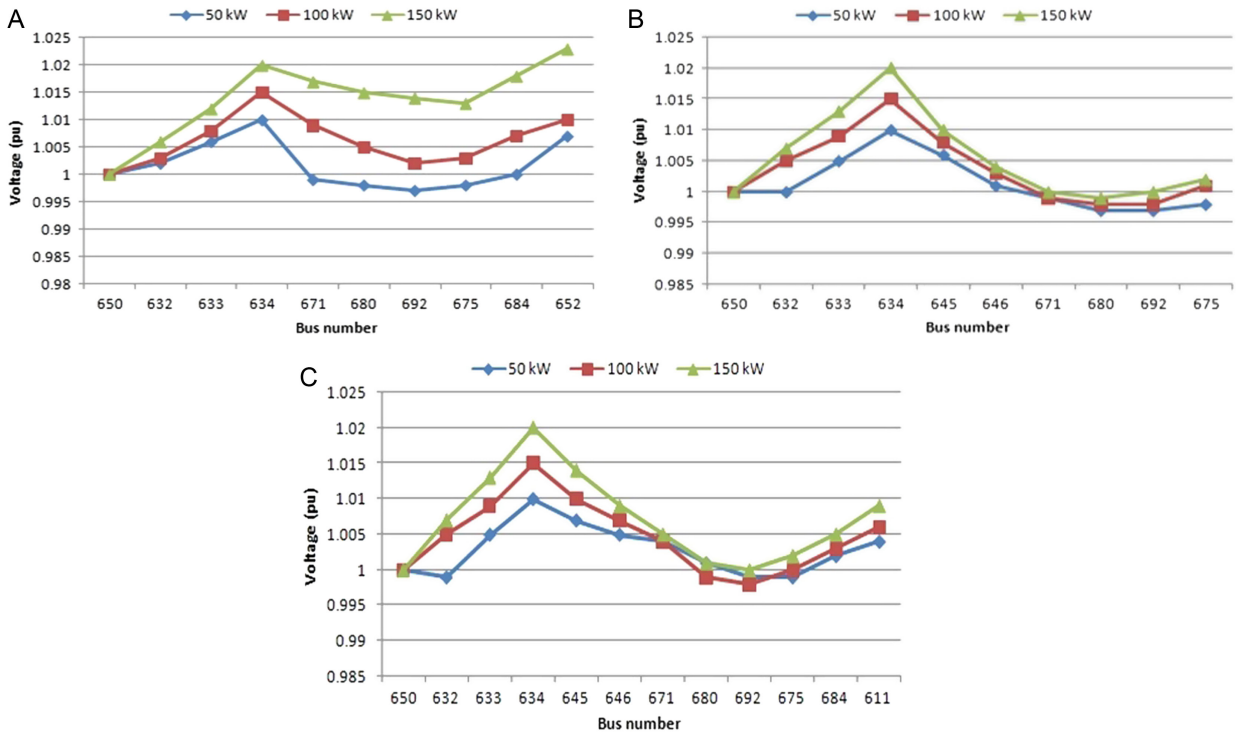


**Fig. 6.** Effect of change in DG power generation limit on voltage profile of IEEE 13 bus system in (a) phase a, (b) phase b, and (c) phase c. DG, distributed generation.

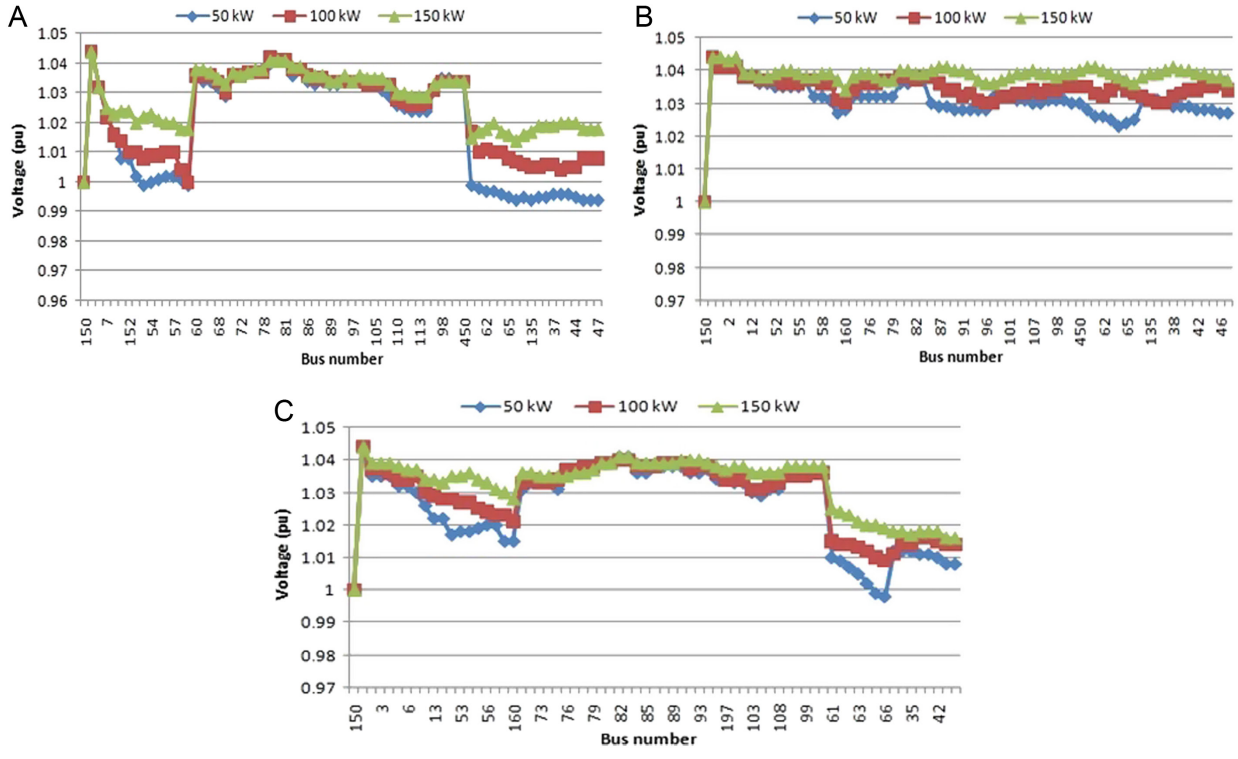


**Fig. 7.** Effect of change in DG power generation limit on voltage profile of IEEE 123 bus system in (a) phase a, (b) phase b, and (c) phase c. DG, distributed generation.

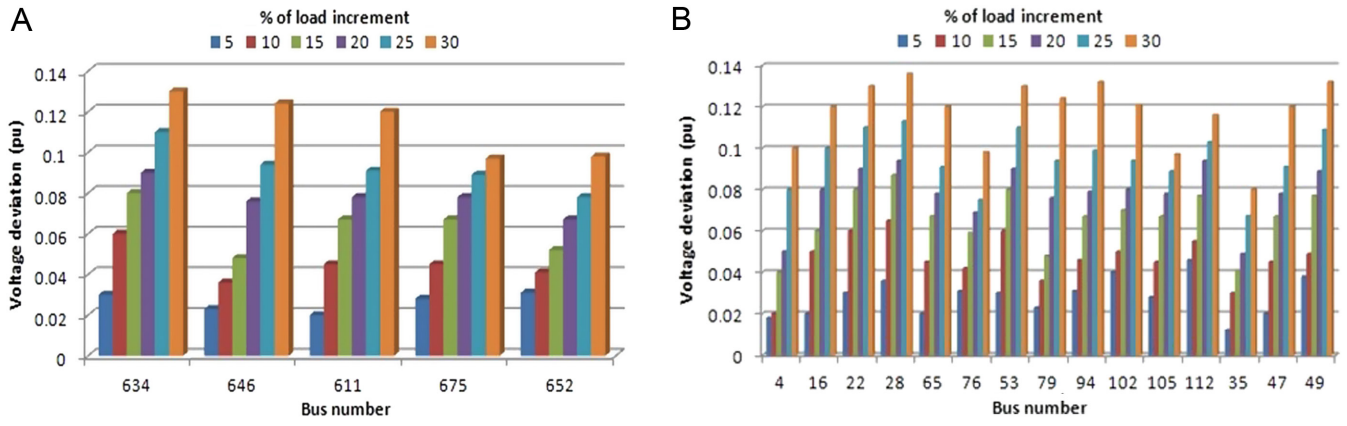


**Fig. 8.** Impact of load increment for (a) IEEE 13 bus system and (b) IEEE 123 bus system.

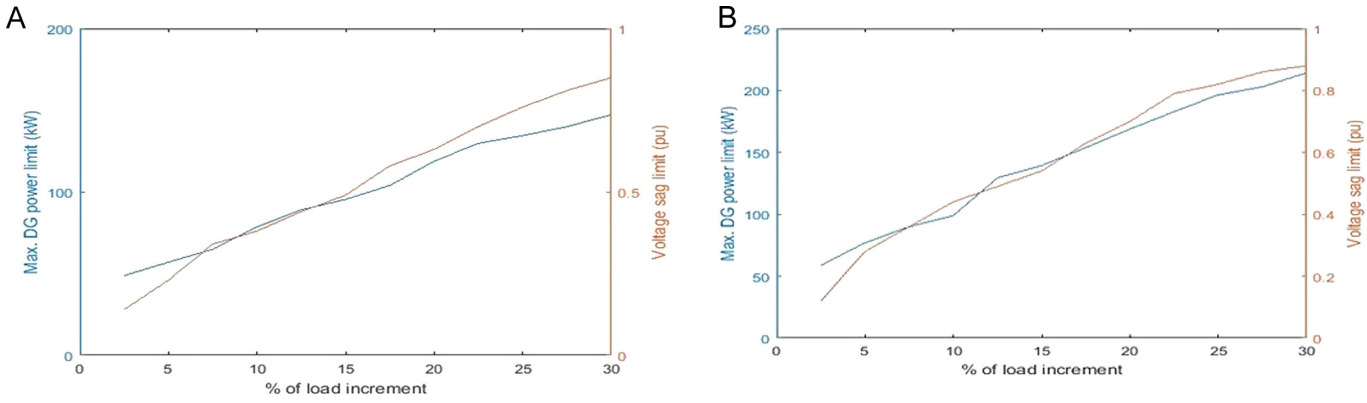


**Fig. 9.** Effect on voltage sag limit for (a) IEEE 13 bus system and (b) IEEE 123 bus system.

**TABLE I.**
COMPARISON OF THE SOLUTION OBTAINED WITH DIFFERENT METHOD FOR IEEE 13 BUS SYSTEM

| | Total Power Loss (kW) | | Number of Iterations | | Execution Time (s) | |
|---|---|---|---|---|---|---|
| **Distribution Load Flow Method** | **Without DG** | **With DG** | **Without DG** | **With DG** | **Without DG** | **With DG** |
| BFS method [4] | 90.68 | 30.32 | 6 | 6 | 0.103 | 0.115 |
| Proposed method | 88.54 | 28.93 | 4 | 3 | 0.051 | 0.58 |

**TABLE II.**
COMPARISON OF THE SOLUTION OBTAINED WITH DIFFERENT METHOD FOR IEEE 123 BUS SYSTEM

| | Total Power Loss (kW) | | Number of Iterations | | Execution Time (s) | |
|---|---|---|---|---|---|---|
| **Distribution Load Flow Method** | **Without DG** | **With DG** | **Without DG** | **With DG** | **Without DG** | **With DG** |
| BFS method [4] | 207.43 | 76.81 | 10 | 11 | 0.194 | 0.205 |
| Proposed method | 202.84 | 74.73 | 8 | 8 | 0.098 | 0.103 |

**Peer-review:** Externally peer-reviewed.

**Declaration of Interests:** The authors have no conflict of interest to declare.

**Funding:** The authors declared that this study has received no financial support.

## REFERENCES

1. A. Keane *et al.*, "State-of-the-art techniques and challenges ahead for distributed generation planning and optimization," *IEEE Trans. Power Syst.*, vol. 28, no. 2, pp. 1493–1502, May 2013. [CrossRef]
2. D. Shirmohammadi, H. W. Hong, A. Semlyen, and G. X. Luo, "A compensation- based power flow method for weakly meshed distribution and transmission networks," *IEEE Trans. Power Syst.*, vol. 3, no. 2, pp. 753–762, May 1988. [CrossRef]
3. W. C. Wu, and B. M. Zhang, "A three-phase power flow algorithm for distribution system power flow based on loop-analysis method," *Int. J. Electr. Power Energy Syst.*, vol. 30, no. 1, pp. 8–15, January 2008. [CrossRef]
4. A. N. Augugliaro, L. U. Dusonchet, S. A. Favuzza, M. G. Ippolito, and E. R. Sanseverino, "A backward sweep method for power flow solution in distribution networks," *Int. J. Electr. Power Energy Syst.*, vol. 32, no. 4, pp. 271–280, May 2010. [CrossRef]
5. Jen-Hao Teng, and Chuo-Yean Chang, "A novel and fast three-phase load flow for unbalanced radial distribution systems," *IEEE Trans. Power Syst.*, vol. 17, no. 4, pp. 1238–1244, November 2002. [CrossRef]
6. S. Khushalani, J. M. Solanki, and N. N. Schulz, "Development of three-phase unbalanced power flow using PV and PQ models for distributed generation and study of the impact of DG models," *IEEE Trans. Power Syst.*, vol. 22, no. 3, pp. 1019–1025, August 2007. [CrossRef]
7. Y. Zhu, and K. Tomasovic, "Adaptive power flow method for distribution systems with dispersed generation," *IEEE Trans. Power Del.*, vol. 17, no. 3, pp. 822–827, July 2002. [CrossRef]
8. C. S. Cheng, and D. Shirmohammadi, "A three-phase power flow method for real-time distribution system analysis," *IEEE Trans. Power Syst.*, vol. 10, no. 2, pp. 671–679, May 1995. [CrossRef]
9. S. M. Moghaddas-Tafreshi, and E. Mashhour, "Distributed generation modeling for power flow studies and a three-phase unbalanced power flow solution for radial distribution systems considering distributed generation," *Electr. Power Syst. Res.*, vol. 79, no. 4, pp. 680–686, April 2009. [CrossRef]
10. T. -H. Chen, M. -S. Chen, T. Inoue, P. Kotas, and E. A. Chebli, "Three-phase cogenerator and transformer models for distribution system analysis," *IEEE Trans. Power Del.*, vol. 6, no. 4, pp. 1671–1681, October 1991. [CrossRef]
11. J. -H. Teng, "Modelling distributed generations in three-phase distribution load flow," *IET Gener. Transm. Distrib.*, vol. 2, no. 3, pp. 330–340, May 2008. [CrossRef]
12. S. Biswas, S. K. Goswami, and A. Chatterjee, "Optimal distributed generation placement in shunt capacitor compensated distributed systems considering voltage sag and harmonics distortions," *IET Gener. Transm. Distrib.*, vol. 8, no. 5, pp. 783–797, May 2014. [CrossRef]
13. S. Biswas, S. K. Goswami, and A. Chatterjee, "Optimum distributed generation placement with voltage sag effect minimization," *Energy Convers. Manag.*, vol. 53, no. 1, pp. 163–174, January 2012. [CrossRef]
14. S. Ganguly, and D. Samajpati, "Distributed generation allocation on radial distribution networks under uncertainties of load and generation using genetic algorithm," *IEEE Trans. Sustain. Energy*, vol. 6, no. 3, pp. 688–697, July 2015. [CrossRef]
15. A. E. Feijoo, and J. Cidras, "Modeling of wind farms in load flow analysis," *IEEE Trans. Power Syst.*, vol. 15, no. 1, pp. 110–115, February 2000. [CrossRef]
16. M. E. Baran, and E. A. Staton, "Distribution transformer models for branch current based feeder analysis," *IEEE Trans. Power Syst.*, vol. 12, no. 2, pp. 698–703, May 1997. [CrossRef]
17. G. Kron, "Tensorial analysis of integrated transmission systems, Part I, the six basic reference frames," *Trans: AIEE*, vol. 70, no. 2, pp. 1239–1248, July 1951. [CrossRef]
18. IEEE, "PES distribution test feeders". Available: http://ewh.ieee.org/soc/pes/dsacom/testfeeders/index.html.
19. Vestas Corp. Available: http://www.vestas.dk.

APPENDIX: The wind turbine model used here is of 3 phase, 4 pole, 60 Hz, 12.66 kV, and 1 MW rating. The induction generator circuit parameters are tabulated below:

| **Parameters** | **Value (p.u.)** |
|---|---|
| Stator resistance ($R_1$) | 0.005986 |
| Rotor resistance ($R_2$) | 0.01690 |
| Stator leakage reactance ($X_1$) | 0.08212 |
| Rotor leakage reactance ($X_2$) | 0.107225 |
| Magnetizing reactance ($X_m$) | 2.5561 |
| Reactance of capacitor bank ($X_c$) | 2.8956 |

cigre Turkey

TEPES
TURKISH JOURNAL OF ELECTRICAL POWER AND ENERGY SYSTEMS

TEPES, Vol. 2, Issue. 2, 134-146, 2022 **DOI:** 10.5152/tepes.2022.22012

RESEARCH ARTICLE

# Comparative Study of the Performances of Three Metaheuristic Algorithms in Sizing Hybrid-Source Power System

**Titus Oluwasuji Ajewole[1], Olatunde Oladepo[1], Kabiru Alani Hassan[2], Abdulsemiu Alabi Olawuyi[3], Opeyemi Onarinde[1]**

[1]Department of Electrical and Electronic Engineering, Osun State University, Osogbo, Nigeria
[2]Department of Electrical and Electronic Engineering, Federal Polytechnic, Ede, Nigeria
[3]Department of Electrical and Electronic Engineering, Osun State Polytechnic, Iree, Nigeria

**Cite this article as:** T.O. Ajewole, O. Oladepo, K.A. Hassan, A.A. Olawuyi, O. Onarinde, Comparative study of the performances of three metaheuristic algorithms in sizing hybrid-source power system. *Turk J Electr Power Energy Syst*, 2022; 2(2), 134-146.

## ABSTRACT

This paper presents compared performances of three metaheuristic algorithms in determining the cost of hybrid renewable energy system. Using genetic algorithm (GA), particle swarm optimization (PSO), and artificial bee colony (ABC), the best affordable sizes of solar photovoltaic array, battery bank, and a minimum-rated diesel generator that could be hybridized to meet the demand of a community in Southwest Nigeria were determined. Load profile, solar radiation, and temperature data were employed as required inputs, and the parameters of the algorithms were properly set to ensure the best result. Bonferroni–Holm method was deployed to ascertain the statistical significance among the algorithms. It was found that ABC produced the best configuration comprising 427 numbers of solar photovoltaic panels, 19 battery units, and 163.2 kW-rated diesel generator. With this, a total annualized cost of $167 284 and 0.2443 estimated cost of energy were obtained. These were the lowest when compared with PSO and GA. The *t*-test between PSO and ABC are both $5.83 \times 10^{-10} < 0.01666667$, between ABC and GA are $6.09 \times 10^{-6} < 0.01666667$ and $6.09 \times 10^{-6} < 0.025$, while between GA and PSO are $9.13 \times 10^{-1} > 0.01666667$ and $9.13 \times 10^{-1} > 0.05$. PSO/ABC and ABC/GA groups are clarified significant, while GA/PSO group is insignificant; post hoc test reveals that ABC produced the best result. Hence, a reliable and sustainable power supply at a reduced cost is guaranteed for the community.

**Index Terms—**Artificial bee colony, Bonferroni–Holm method, diesel generator, genetic algorithm, particle swarm optimization

## I. INTRODUCTION

In recent years, hybrid renewable energy system (HRES) has been a choice for the electrification of isolated areas where grid extension is difficult and costly or area where there is an epileptic power supply. Hybrid system is the combination of one or more renewable energy sources, such as solar photovoltaic (PV), wind energy, hydro system, and so on, to produce energy [1]. Furthermore, integrating energy storage systems like battery banks or conventional energy sources (such as diesel generators) makes HRESs more cost-effective and reliable [2]. HRES will not only minimize the reliance on the fossil fuels (such as gas, oil, or coal) that produce environmental pollutants but will also allow the use of more natural resources with energy storage system to guarantee stable and reliable energy, which is the major concern of energy users across the world [3, 4].

The development of sustainable power supply is facing two challenges of how to efficiently generate sufficient energy by using sustainable energy resources and generation at a reasonable cost for the users [5]. However, the use of estimated sizing method to determine the appropriate size and selection of HRES components has resulted in either undersized or oversized components. It should be noted that undersizing HRES may result in shortages of energy delivered and operational constraints, while oversizing causes higher initial setup costs and other issues. Part of the solution to these challenges is to employ software tools. In [1, 6], hybrid optimization of multiple energy resources (HOMER) was used in component sizing of HRESs. While [1] deployed HOMER to perform an economic evaluation on PV/distributed generation (DG) with flywheel as a storage system and by which it was shown that integration of HRES greatly reduced the level of diesel fuel consumption, authors in

**Corresponding author:** Kabiru Alani Hassan, kabirzan.hk@gmail.com

**Received:** February 12, 2022
**Accepted:** April 16, 2022
**Publication Date:** May 20, 2022

[6] presented a HOMER-based optimal configuration and sizing of HRES in supplying reliable energy to a university campus community. However, software tools face the challenges of mono function reduction, more processing time, and frequent stuck in local minima [7]. Therefore, artificial intelligence (AI) technique, such as metaheuristic algorithms, has emerged to develop cost-effective and sustainable HRES [8]. Metaheuristic algorithms solve the problems of HRES in many applications with minimum processing time and achieving optimality [9]. Thus, the use of AI optimization method has become important in order to lower initial costs and increase efficiencies [3], and many studies have been carried out using single or two different algorithms.

Using genetic algorithm (GA), authors in [10] calculated the best cost value from the best configuration of a hybrid energy system; the economic impact of optimal sizing on a rural village microgrid that produces sustainable electricity at a lower cost was analyzed in [11]. Using both GA and traditional system, various components of an HRES system have been analyzed [12], with the results showing that a combination of PV and diesel energy systems yielded the best result at reduced cost. In [13], particle swarm optimization (PSO) was deployed to determine the required components' optimal sizing of a renewable energy-based electric power systems for residential areas, while [14] presented sizing of HRES using PSO algorithms and concluded that the operational cost of fuel usage was greatly minimized using a combination of PV and battery storage. In a study carried out in two different locations, Rabat and Baghdad, the economic cost and size of HRES were determined using PSO techniques [15]. A study intended to achieve the overall minimum system cost of a solar energy system while considering pollution criteria of DG was conducted in [16] using PSO, while a modified heuristic approach based on PSO and GA was deployed in [17] for a study on hybrid system operation using four comparison scenarios, and the result shows that the PSO algorithm is better than the GA. In [18], performances of GA and PSO were evaluated in a study on metaheuristic-based analyses, with comparison of the two algorithms carried out based on iteration convergence time, memory usage time, and solution quality, and the result showed that PSO outperformed GA. In sizing renewable energy and battery storage systems for an HRES, [19] deployed GA, with the use of two cost-effective scenarios of combining PV, wind energy, and battery storage system to determine the cost of energy of the designs.

There are many studies on HRES in the literature, wherein a single algorithm was deployed. Also, in a number of research, two different algorithms have been employed for comparison. In this present study, a comprehensive comparison of the performances of three metaheuristic methods in achieving optimal configuration of HRES is presented. Significances of the algorithms, GA, PSO, and ABC, when applied to an HRES at Ayetoro community in Southwest Nigeria, are also presented.

**Main Points**

- The proposed hybrid power system is optimized using, comparatively, three metaheuristic algorithms.
- In testing for the statistical significance of the algorithms, Bonferroni–Holm test method is applied.
- Artificial bee colony gives the best result in terms of design, total annualized and estimated energy costs.

## II. METHODS

### A. Brief Description of the Study Area and the Data Collection Approach

Ayetoro community is a suburb of Ede in Osun State, Southwest Nigeria. It is on Lat. 7.727637˚S/Long 4.428045˚W coordinate. There are 122 houses in the community, with the inhabitants being farmers, civil servants, or shop owners (petty traders). Electrical loads in the community are majorly domestic and commercial. In profiling the loads, the housing population was grouped into eight sections based on the structures of the buildings and the electrical equipment found the houses. By random approach, eight homes were selected from each section of the community, and a well-structured questionnaire was administered to the stratified sample to obtain information on energy consumption patterns.

Data on the solar radiation and temperature of the location were collected from the National Aeronautics and Space Administration (NASA) surface meteorology and solar energy database online. The solar energy database of NASA has a long-term climatological estimate of meteorological quantities and surface solar energy data majorly needed for the study of environmental process [20].

### B. Modeling of the Hybrid System

Presented in Fig. 1 is the block diagram of the proposed HRES. Energy output from the battery source served as input to the inverter, where the DC voltage was converted to AC and fed the electrical load. Components of the system are modeled to determine the numbers of PV panels, battery units required, and the rating of the DG needed to be hybridized to effectively sustain the community load. The modeling was achieved in the MATLAB environment.

#### 1) Solar Panel Modelling

The output power of the panel ($P_{pt}$) depends on the output voltage ($V_{pt}$) and the current ($I_{pt}$) in the panel and is expressed as [21, 22]:

$$P_{pt} = V_{pt} \times I_{pt} \tag{1}$$

While the output voltage is [22]:

$$V_{pt} = V_{\max} + \left(\mu_{voc} \times \Delta T\right), \tag{2}$$

where $V_{max}$ is the maximum value of voltage, $\mu_{voc}$ represents the temperature coefficient for open-circuit voltage (V/˚C), and $\Delta T$ represents the time step. The corresponding output current ($I_{pt}$) is obtained as [22]:

$$I_{pt} = I_{sht}\left\{1 - A\left[\exp\left(\frac{V_{\max}}{B \times V}\right) - 1\right]\right\} + \Delta I \tag{3}$$

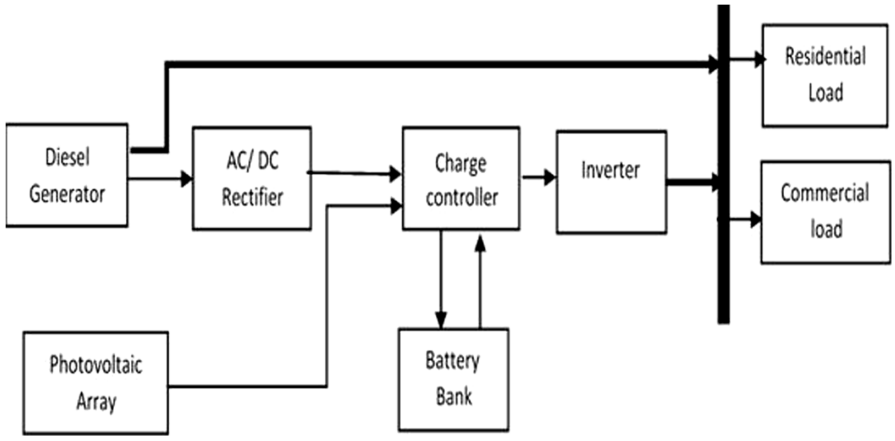


**Fig. 1.** Block diagram of photovoltaic/distributed generation system.

With the corresponding values of *A* and *B* expressed as [21, 22]:

$$A = \left[1 - \left(\frac{I_{mx}}{I_{sht}}\right)\right] \exp\left(\frac{-V_{mx}}{B \times V_{oc}}\right) \tag{4}$$

$$B = \left(\frac{V_{mx}}{V_{oc}}\right) - 1 \times \left[\ln\left(1 - \frac{I_{mx}}{I_{sht}}\right)\right]^{-1} \tag{5}$$

where $I_{mx}$ and $V_{mx}$ are the maximum current and voltage, respectively, while $I_{sht}$ is the short circuit current and $V_{oc}$ denotes the open-circuit voltage. The change in the value of the current and temperature over time is [21]:

$$\Delta I = I_{sht} \times \left(\frac{R_T}{R_{fo} - 1}\right) + \mu_{sht} \times \Delta K \tag{6}$$

$$\Delta K = K_c - K_{cr} \tag{7}$$

$R_T$ is the hourly irradiation value of the solar panel on a tilted surface, and $R_{fo}$ is the reference point of the radiation energy at 1000 W/m$^2$. $\mu_{sht}$ is the short-circuit temperature coefficient, while $K_c$ and $K_{cr}$ are solar panel specified temperature and reference working point (25˚C), respectively. The value of $K_c$ is further evaluated as [22]:

$$K_c = T_{am} + \left[\left(\frac{NOCT - 20}{800}\right) \times G_T\right] \tag{8}$$

where $T_{am}$ is the ambient temperature. Normal operating cell temperature (NOCT) ranges from 42˚C to 46˚C [22].

**2) Modeling of Battery Storage**

Nominal capacity of a battery storage system is the product of the initial capacity of the battery ($B_i$) and the ampere-hour (Ah). Therefore, it is important to initially specify the permissible depth of discharge (DOD, %) when determining optimal sizing as [19]:

$$SOC_{\min} = (1 - DOD).Bi \tag{9}$$

The stored energy requires accurate estimation of the state of charge (SOC) because the SOC of battery varies with time as [7]:

$$SOC(t + \Delta t) = SOC(t) + \left(P_{bat}(t) B_{Teff} \times \Delta t\right)\left(\frac{1}{V_{dc}}\right) \tag{10}$$

where $P_{bat}(t)$ is the energy of the battery, $V_{dc}$ is the DC voltage of the battery, and *t* is the step value in 1 hour. The battery charges when $P_{bat}(t)$ is greater than zero and drains when $P_{bat}(t)$ is less than zero. Furthermore, the round-trip efficiency of a battery, $B_{Teff}$, is defined as [7]

$$B_{Teff} = \left(B^{ch}_{Teff} + B^{d}_{Teff}\right)^{0.5} \tag{11}$$

where $B^{ch}_{Teff}$ and $B^{d}_{Teff}$ denote the charging and discharging round-trip efficiency, the charging and discharging efficiencies vary and are typically around 85% and 100%, respectively. The maximum charge or discharge power at any time is also vital in battery modeling. It is determined by the maximum charge current as [7]

$$I_m = \frac{P_{bat}(t) \times 1000}{N_b \times V_{dc}}. \tag{12}$$

where $N_b$ is the number of batteries connected together. The storage constraints are obtained in [7], where $SOC_{\min}$ and $SOC_{\max}$ are the minimum and maximum SOC of the battery.

$$SOC_{\min} \le SOC(t) \le SOC_{\max} \tag{13}$$

**3) Inverter System Modeling**

The inverter rating capacity is designed with an increase of 20% to compensate for losses and enable the system to meet the maximum load demand [22], with $P_{inv}$, $P_{loadmax}$, and $eff_{inv}$ given as [22, 23]:

$$P_{inv} = 120\% p_{load\max} \tag{14}$$

$$eff_{inv} = \frac{P_{out}(t)}{P_{in}} \tag{15}$$

where $P_{inv}$ is the nominal rating of the inverter, $P_{loadmax}$ is the maximum required load energy demanded, $eff_{inv}$ is the efficiency, and $P_{out}$ is the output power of the inverter.

**4) Diesel Generator Modeling**

The DG operational cost for the design was obtained as [22]:

$$C_{DF}(t) = P_F(t) \times \left[ AP_D(t) + BP_{DE}(t) \right] \tag{16}$$

where $A$ and $B$ are fuel curve coefficients, $P_F(t)$ is the fuel price, $P_D(t)$ and $P_{DE}(t)$ are the output power (W) and rated power (W) of the DG, respectively.

The operational strategy was formulated such that when the renewable resource was insufficient to satisfy the load demand, the battery bank provided the necessary power as given in Fig. 2 [24]. $\Delta P(t)$ denotes the change in power value, either excess or deficit, after the design utilizes the solar source. The following scenarios are considered regarding the value of $\Delta P(t)$ given in (6):

$$\Delta P(t) = P_{load}(t) - \left( P_{pt}(t) + P_{bat} \right) \tag{17}$$

**Scenario I:** If the energy supplied by the solar source is insufficient to meet up the load demand, then more energy is needed from the battery bank (i.e., $\Delta P_{(t)} > 0$), and SOC of the battery bank is then fully monitored. The DG system is utilized if SOC drops within the minimum preset value of 20%.

**Scenario II:** If the energy supplied by the PV source is in excess compared to the load demand (i.e., $\Delta P_{(t)} < 0$), then excess energy is diverted to the battery bank for the charging process. When maximum SOC is met, excess energy is dumped for future usage. The DG system is switched off.

**Scenario III:** If the energy supplied by the solar source meets the load demand (i.e., $\Delta P_{(t)} = 0$), then the battery bank is placed on standby for an emergency, and the DG system is switched off.

**C. Formulation of Objective Function**

As one of the important economic measures used for system cost analysis, the cost of energy (COE) is the total cost of the HRES multiplied by the amount of electrical energy generated annually within the system. COE is given as [25]:

$$COE\left(\$/\text{kWh}\right) = \text{TASC} \times \frac{C_{capRef}(j,z)}{\sum_{t=1}^{8760} P_g(t)} \tag{18}$$

where the total annualize system cost (TASC) is achieved by identifying the various decision parameters and their corresponding variables. Formulating the objective function is subject to constraints to make the sizing optimal. TASC is obtained as [22]:

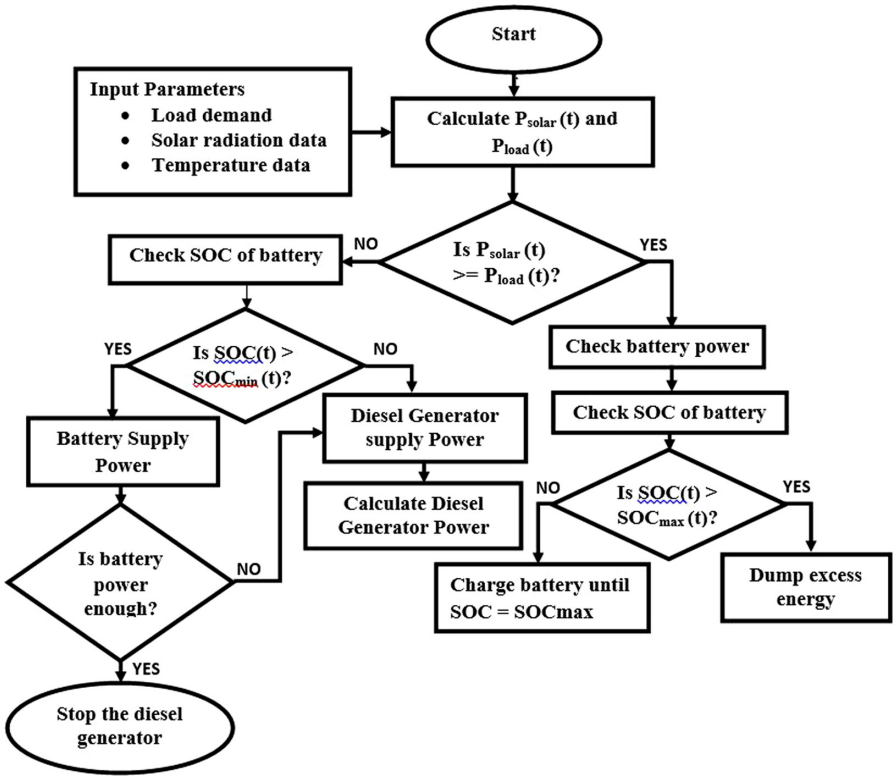


**Fig. 2.** Flowchart of system operation strategies.

$$\min TASC = \min\left(N_{PV}TC_{PV} + N_B TC_B + P_D TC_D + P_{inv}TC_{inv}\right) \quad (19)$$

where $TC_{PV}$ is the PV panel cost, $TC_B$ is the battery storage cost, $TC_D$ is the DG cost, and $TC_{inv}$ is the inverter cost. Also $N_{pv}$ and $N_B$ are the number of panels and batteries required while $P_D$ and $P_{inv}$ are the power ratings of the generator and inverter system needed to achieve minimum cost. The total costs of $TC_{PV}$, $TC_B$, and $TC_D$ can be further calculated using [22]:

$$TC_{PV} = C_{PVC} + C_{PVI} + C_{PVM} \quad (20)$$

$$TC_B = C_{BC} + C_{BI} + C_{BM} + C_{BO} \quad (21)$$

$$TC_D = C_{DC} + C_{DI} + C_{DM} + C_{DO} \quad (22)$$

where $C_{BC}$ is the battery capital cost, $C_{BI}$ is the battery installation cost, $C_{BM}$ is battery maintenance cost, and $C_{BO}$ is the battery operational cost. Table I presents the cost and life expectancies of the components. The capital recovery factor is a ratio to determine the present worth of the annuity using the real interest rate and the project's lifetime as given in [26]:

$$C_{capRef}\left(j,z\right) = \frac{j\left(1+j\right)^z}{\left(1+j\right)^z - 1} \quad (23)$$

where $j$ denotes the annualized interest rate and $z$ represents the useful lifetime in years. The interest rate is given as [26]:

$$j = \frac{\left(i_n - a_f\right)}{\left(1+a_f\right)} \quad (24)$$

where $i_n$ denotes the nominal interest rate and $a_f$ represents the inflation rate. The objective function was minimized by deploying the following sets of constraints:

$$1 \le N_{PV} \le N_{PV\max} \quad (25)$$

**TABLE I.**
ANALYSIS OF COMPONENT PARAMETERS [7]

| S/N | Item | Component | Parameter | Value |
|---|---|---|---|---|
| 1. | Solar panel | Capital cost | 250 | $ each |
| | | Replacement cost | 150 | $ |
| | | Maintenance and operation cost | 10 | $/year |
| | | Solar panel life | 20 | Years |
| 2. | Inverter | Capital cost | 1250 | $ each |
| | | Replacement cost | 750 | $ |
| | | Maintenance and operation cost | 50 | $/year |
| | | Inverter life | 20 | Years |
| | | Inverter efficiency | 90 | % |
| 3. | Battery bank | Capital cost | 750 | $ each |
| | | Replacement cost | 250 | $ |
| | | Maintenance and operation cost | 10 | $/year |
| | | Battery life | 7 | Years |
| | | Inverter efficiency | 90 | % |
| | | Minimum state of charge | 20 | % |
| | | Maximum state of charge | 100 | % |
| 4. | Diesel generator | Capital cost | 520 | $ each |
| | | Replacement cost | 350 | $ |
| | | Maintenance and operation cost | 80 | $/year |
| | | Diesel generator life | 25 | Years |
| | | Diesel generator efficiency | 80 | % |
| | | Fuel cost | 0.38 | $/L |

$$1 \le P_D \le P_{D\max} \tag{26}$$

where $N_{PV\max}$ and $P_{D\max}$ are the maximum numbers of solar panels and maximum power demand from DG.

**D. Brief Descriptions of the Algorithms**

**1) PSO Algorithm**

PSO was first described in 1995 by Kennedy and Eberhart, and has been successfully applied in many scientific domains [27]. The PSO technique influenced the combined intelligence of a group of animals, such as a flock of birds, animals travelling in herds, or schools of fish moving together. Each particle utilized the distance between the current position and the new position. A change in the velocity and position of each particle is performed using [28]:

$$V_{pw}(t+1) = \alpha\left[\left(\mathrm{V}_{\mathrm{pw}}(t) + C_a U_a\right)\left(p_{bestpw}(t) - X_{pw}(t)\right) + \left(C_b U_b\right)\left(g_{bestpw}(t) - X_{pw}(t)\right)\right] \tag{27}$$

$$X_{pw}(t+1) = X_{pw}(t) + X_{pw}(t+1) \tag{28}$$

where $\alpha$ is the factor of the inertial component that affects the algorithm, $V_{\mathrm{pw}}(t)$ is particle velocity in the algorithm. $C_{\mathrm{a}}$ and $C_{\mathrm{b}}$ represent parameters of the metacognitive components, $U_{\mathrm{a}}$ and $U_{\mathrm{b}}$ represent two random variables in the range of 0 and 1 employed to keep the population diverse, and $X_{\mathrm{pw}}(t)$ is the change of position toward the particle best positions. The PSO algorithm offers a certain appealing feature of good memory where the particles retain the knowledge of good solutions compared to the GA approach [29].

**2) Genetic Algorithm**

It is a search algorithm that is based on the natural selection process. It is based on one of the most significant survivals of the fittest values. The best person represents the optimal solution after a few generations until the population can no longer endure. GA simulates the evolutionary mechanism by which inherited traits are passed on from one generation to the next. A gene is the most fundamental unit of inheritance [11]. Chromosome exchange and reordering are known as crossover. The steps taken for the technique are as follows: It starts with the initialization of the algorithm's process and checks for the condition for process continuation, as shown in Fig. 3. The fitness function examines and evaluates the result generated to determine the best outcome to be retained for the process. Population diversity is achieved through mutation. It produces new results in the system; the procedure is repeated on several occasions until it converges, indicating the optimum solution [30].

**3) Artificial Bee Colony**

In 2005, Karaboga devised the ABC method [31] that mimics the well-organized social structure and division of labor in honeybee colonies. There are three major bee colony classifications: employed, onlooker, and scout bees. At first, employed bees will randomly select a set of food source locations. The amount of nectar they generate will be measured, and they returned with specialized dances to communicate with the other bees about that food source. Onlooker bees are another type of bee that waits on the dance floor to select which food sources to pursue after collecting information about

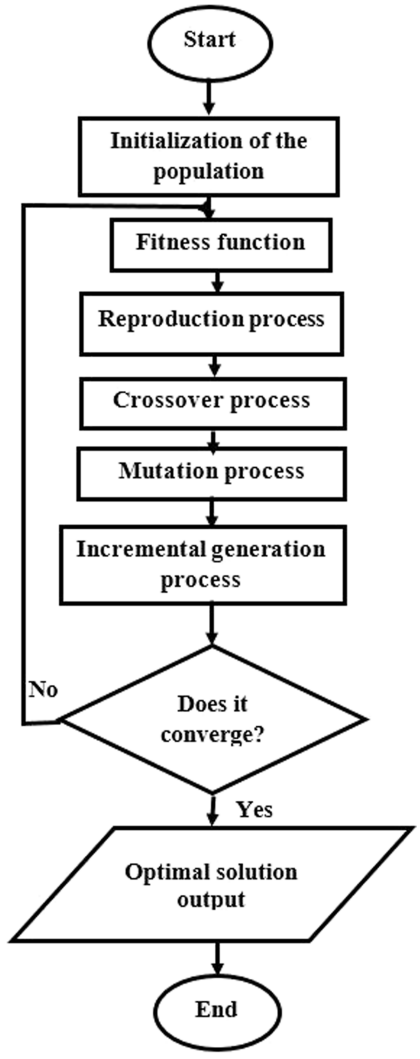


**Fig. 3.** Flow chart of genetic algorithm.

it from employed bees [32]. Scout bees go on a random quest for new food sources. The quality of the fitness is related to the solution achieved, which indicates the quantity of available food that corresponds to it in this method. The position of the available food reflects the possible point of solution to the problem. Compared to other algorithms, it has fewer control parameters and convergence speed increased due to its direct operation. The probability $P_{\mathrm{x}}$ of selecting a food source $x$ is determined as given in:

$$P_x = \frac{fit_x}{\sum_{q=1}^{N_f} fit_q} \tag{29}$$

where $fit_{\mathrm{x}}$ represents the fitness value of the amount of food source at $x$ position and $N_{\mathrm{f}}$ is the number of food sources.

**E. Statistical Analysis**

One of the most used statistical tools in research is the analysis of variance (ANOVA) approach [33], which focuses on analyzing the differences in group means by comparing between- and within-group

variance differences. The dependent and independent variables are utilized in the test. When comparing the means of three groups, the null hypothesis is identified if the population means of the three groups are all the same. However, the alternative hypothesis is identified when at least one of the population means of the three groups is different, rather than the population means of the three groups are all the same. The null hypothesis ($H_0$) and alternative hypothesis ($H_1$) are given as [34]:

$$H_0: \mu_1 = \mu_2 = \mu_3 \quad (30)$$

$$H_1: \mu_1 \neq \mu_2 \text{ or } \mu_1 \neq \mu_3 \text{ or } \mu_2 \neq \mu_3 \quad (31)$$

As a result, if the means of any two of the three groups differ, the null hypothesis can be rejected.

The Bonferroni-Holm technique is a statistical procedure used to compare two groups of a data set and solve the problem of multiple comparisons by modifying the rejection parameters for each assumption the most generally suggested method to examine the significant effects [35].

## III. RESULTS AND DISCUSSION

The load profile of the community, as obtained during raining season (June–November) and the dry season (December–May), is presented in Fig. 4. The profile shows there was low demand between 21:00 h and 2:00 h and between 7:00 h and 15:00 h, while the demand slightly rise from 4:00 h to 6:00 h when people are preparing for their various places of work. The peak load of the community exists between the period of 16:00 h and 20:00 h when most of the people arrive from work. It can also be noted that peak load is higher during the dry season than in the rainy season. The peak and the minimum demand during the rainy season are 148.28 kW and 45.03 kW, respectively, while 163.29 kW peak demand with corresponding 45.04 kW minimum demand was obtained during the dry season. Daily and yearly load demands are 2089.48 kWh and 680 850 kWh, respectively.

As shown in Fig. 5, the irradiation level in the community, which is 1561.99 kWh/m$^2$/day during the dry season, is high enough to produce reliable solar energy. Likewise, the locality has a good temperature gradient with the maximum recorded being 38.44˚C in the dry season and the minimum being 17.447˚C in the rainy season as presented in Fig. 6.

Fig. 7 shows the plot of numbers of solar panels, battery units, and the system cost of the 50 runs.

Table II shows the results obtained for the total number of solar panels, the battery unit, minimum DG required, and component cost analysis of the components. The results are 423, 38, and 163.2 kW for GA; 426, 27, and 163.2 kW for PSO; 430, 20, and 163.2 kW for ABC, respectively. The result indicates that ABC shows the lowest total annualized cost (TAC) of $167 284 compared to PSO and GA with TAC of $167,693 and $168 566, respectively. The COE of the optimal sizing for GA, PSO, and ABC are 0.2476, 0.2463, and 0.2457, respectively, indicating that ABC has the lowest COE. Table III presents the results of optimal sizing when based on PV solar system only and battery storage system only respectively. Fig. 8 presents the comparison of the cost analysis of three scenarios used for different component configurations.

ANOVA test for the three algorithms was conducted using data analysis available in Microsoft Excel. Table IV shows the algorithms' sum, average, and variance of the total cost of energy, while Table V

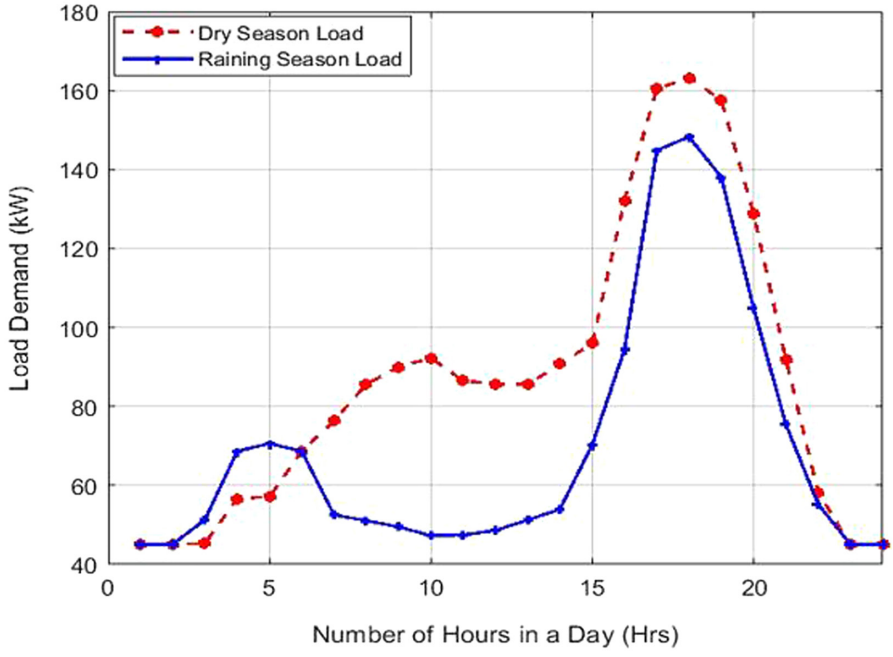


**Fig. 4.** Raining season and dry season load demand profile of the community.

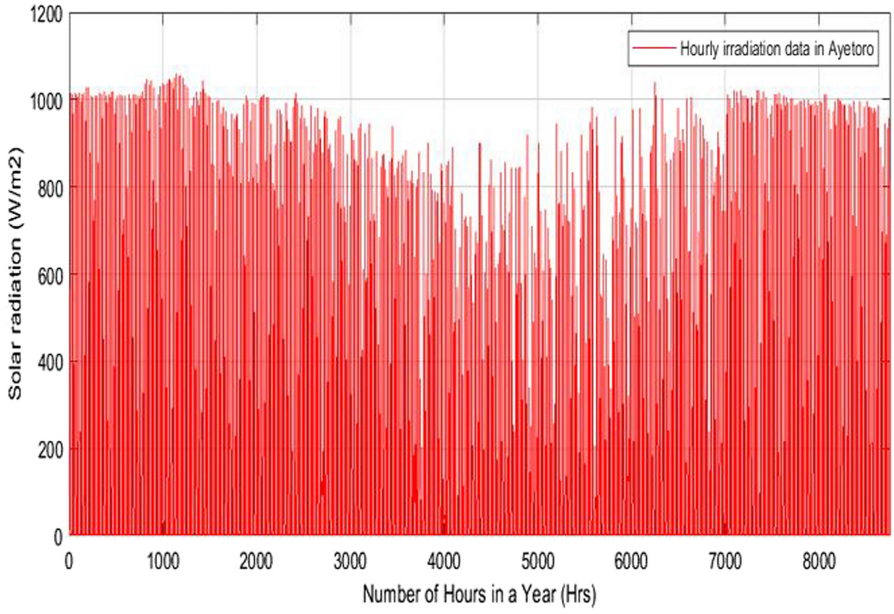


**Fig. 5.** Solar radiation plot of the community.

shows the sources of variance between groups and within groups with their sum of squares, degree of freedom, and the mean square. The *F*-statistic of one-way ANOVA has a *P* value of $1.822 \times 10^{-7}$ which is less than the alpha value of 0.05. The results show that statistical differences exist in the data group. The null hypothesis is therefore rejected, and the result is statistically significant. The results obtained from using the Bonferroni-Holm method of multiple comparison tests indicate that the *t*-test between PSO and ABC are both $5.83 \times 10^{-10} < 0.01666667$, between ABC and GA are $6.09 \times 10^{-6} < 0.01666667$ and $6.09 \times 10^{-6} < 0.025$ while between GA and PSO are $9.13 \times 10^{-1} > 0.01666667$ and $9.13 \times 10^{-1} > 0.05$ as shown in Table VI. This further clarifies that PSO/ABC group and ABC/GA are significant while GA/PSO group is insignificant. These post hoc tests reveal that two treatment pairs are statistically different and ABC produces the best result. The convergence plot of the three algorithms is presented in Fig. 9.

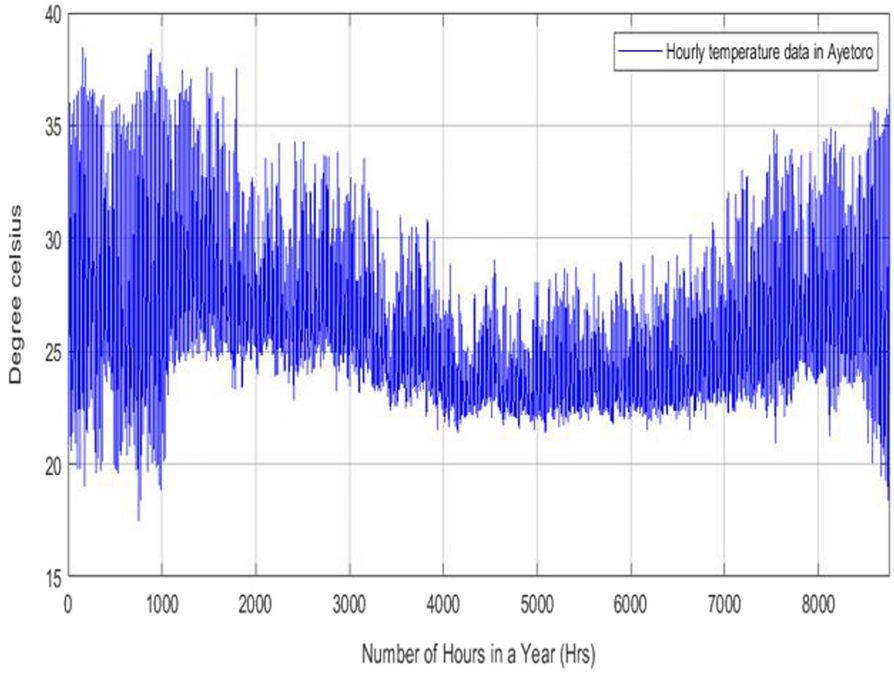


**Fig. 6.** Hourly temperature plot of Ayetoro community.

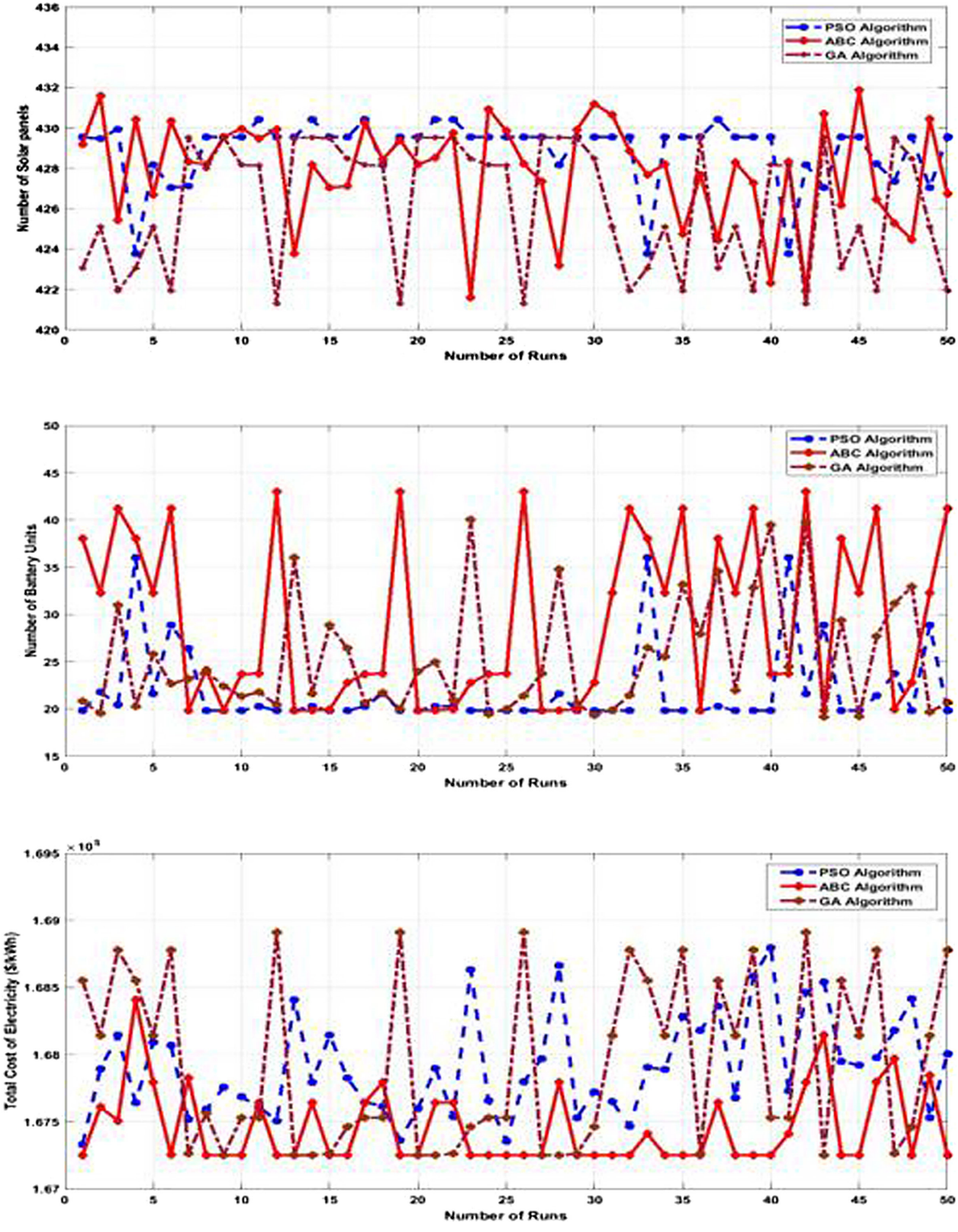


**Fig. 7.** Plot for the three algorithms showing the solar photovoltaic required, battery units, and total cost of electricity.

**TABLE II.**
COMPARATIVE RESULTS OF THE OPTIMAL SIZING AND COST ANALYSIS

| Parameter | GA | PSO | ABC |
|---|---|---|---|
| Number of solar panels required (kW) | 423 | 426 | 430 |
| Number of battery units | 38 | 27 | 20 |
| Total load of community (kW) | 680 850 | 680 850 | 680 850 |
| Total solar cost ($) | 143 260 | 144 368 | 145 450 |
| Diesel generator cost ($) | 735.69 | 735.69 | 735.69 |
| Total battery cost ($) | 7308.30 | 5327.31 | 3836.29 |
| Power inverter cost ($) | 17 262 | 17 262 | 17 262 |
| Total annualized cost ($/year) | 168 566 | 167 693 | 167 284 |
| Cost of energy ($) | 0.2476 | 0.2457 | 0.2443 |

ABC, artificial bee colony; GA, genetic algorithm; PSO, particle swarm optimization.

**TABLE III.**
OPTIMAL SIZING OF SOLAR PV PANEL-ONLY AND BATTERY-ONLY POWER SOURCE

| | PV Solar Panel-Only Power Source | | | Battery-Only Power Source | | |
|---|---|---|---|---|---|---|
| **Algorithms** | **GA** | **PSO** | **ABC** | **GA** | **PSO** | **ABC** |
| Number of solar panels | 175 | 175 | 175 | 0 | 0 | 0 |
| Number of battery units | 0 | 0 | 0 | 10 | 37 | 49 |
| DG energy generation (kW) | $4.537 \times 10^5$ | $4.537 \times 10^5$ | $4.537 \times 10^5$ | $6.749 \times 10^5$ | $6.594 \times 10^5$ | $6.516 \times 10^5$ |
| Total annualized cost ($/year) | $3.5469 \times 10^5$ | $3.5469 \times 10^5$ | $3.5463 \times 10^5$ | $3.9356 \times 10^5$ | $3.9055 \times 10^5$ | $3.8917 \times 10^5$ |
| Cost of energy ($) | 0.5210 | 0.5210 | 0.5209 | $1.4687 \times 10^4$ | $1.4687 \times 10^4$ | $1.4687 \times 10^4$ |

ABC, artificial bee colony; DG, distributed generation; GA, genetic algorithm PSO, particle swarm optimization; PV, photovoltaic.

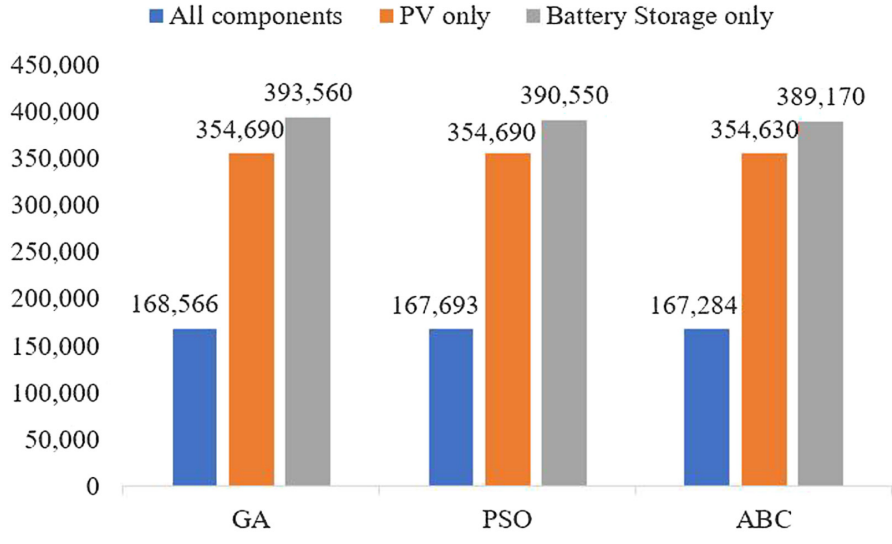


**Fig. 8.** Cost analysis of three different scenarios used in sizing.

**TABLE IV.**
ONE-WAY ANOVA RESULT FOR ALGORITHMS

| Groups | Count | Sum | Average | Variance |
|---|---|---|---|---|
| PSO | 50 | 8 395 454.816 | 167 909.0963 | 142 282.2543 |
| ABC | 50 | 8 372 446.689 | 167 448.9338 | 81 742.71787 |
| GA | 50 | 8 396 030 | 167 920.6 | 404 458.8163 |

ABC, artificial bee colony; GA, genetic algorithm PSO, particle swarm optimization.

**TABLE V.**
SHOWS THE VALUE OF *P* VALUES AND F CRITICAL VALUES WHERE ($\propto = 0.05$)

| Source of Variation | Sum of Squares | Degree of Freedom | Mean Square | F-Stat | *P*-Value | *F* Critical |
|---|---|---|---|---|---|---|
| Between groups | 7 239 182.17 | 2 | 3 619 591.085 | 17.27773008 | 1.822E-07 | 3.057620 |
| Within groups | 30 795 705.64 | 147 | 209 494.5962 | | | |
| Total | 38 034 887.81 | 149 | | | | |

**TABLE VI.**
BONFERRONI AND HOLM POST HOC TEST

| Algorithms | *P* Value (*t*-test) | Bonferroni | Rank | Holm | Significant |
|---|---|---|---|---|---|
| PSO vs. ABC | 5.83E-10 | 0.01666667 | 1 | 0.0166667 | Yes |
| ABC vs. GA | 6.09E-06 | 0.01666667 | 2 | 0.025 | Yes |
| PSO vs. GA | 9.13E-01 | 0.01666667 | 3 | 0.05 | No |

ABC, artificial bee colony; GA, genetic algorithm PSO, particle swarm optimization.

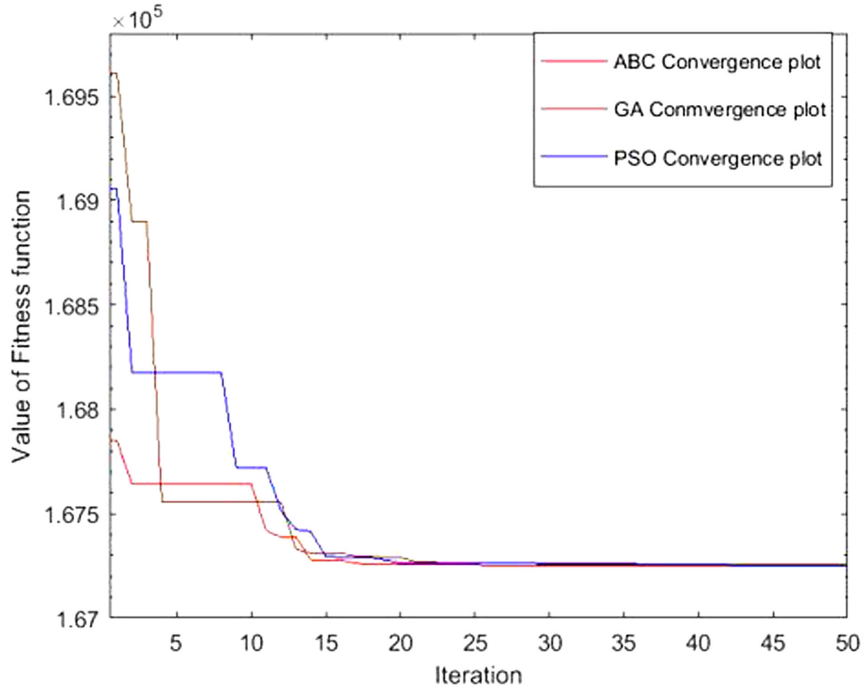


**Fig. 9.** Convergence plot of particle swarm optimization, artificial bee colony, and genetic algorithm.

## IV. CONCLUSION

A hybrid energy system that consists of PV panels and battery storage units has been designed to provide sustainable and reliable electrical energy to a community in Nigeria. This paper uses a mathematical model of the components to determine the optimal size and ensure that the design's constraints are not violated. Results obtained from the three metaheuristic algorithms (GA/PSO/ABC) show that ABC produces the best configurations with 427 numbers of solar PV panels, 19 battery units, and 163.2 kW diesel generator ratings with the lowest TAC of $167 284 as compared to PSO and GA with $167 693 and $168 566, respectively. The COE estimate is 0.2443 for ABC, 0.2476 for GA, and 0.2457 for PSO. The results obtained from Bonferroni-Holm multiple comparison tests indicate that the *t*-test between PSO and ABC are both $5.83 \times 10^{-10} < 0.01666667$, between ABC and GA are $6.09 \times 10^{-6} < 0.01666667$ and $6.09 \times 10^{-6} < 0.025$ while between GA and PSO are $9.13 \times 10^{-1} > 0.01666667$ and $9.13 \times 10^{-1} > 0.05$. This further clarifies that PSO/ABC and ABC/GA groups are significant while GA/PSO group is insignificant. These post hoc tests reveal that two treatment pairs are statistically different and ABC produces the best result. It is concluded that the hybrid system completely satisfied the load demand of the community.

**Peer-review:** Externally peer-reviewed.

**Declaration of Interests:** The authors have no conflict of interest to declare.

**Funding:** The authors declared that this study has received no financial support.

## REFERENCES

1. M. A. M. Ramli, A. Hiendro, and S. Twaha, "Economic analysis of PV/diesel hybrid system with flywheel energy storage," *Renew. Energy*, vol. 78, pp. 398–405, Jun. 2015. [CrossRef]
2. S. M. Zahraee, M. Khalaji Assadi, and R. Saidur, "Application of artificial intelligence methods for hybrid energy system optimization," *Renew. Sustain. Energy Rev.*, vol. 66, pp. 617–630, Dec. 2016. [CrossRef]
3. O. E. Olabode, T. O. Ajewole, I. K. Okakwu, A. S. Alayande, and D. O. Akinyele, "Hybrid power systems for off-grid locations: A comprehensive review of design technologies, applications and future trends," *Scientific African*, vol. 13, p. e00884, Jul. 2021. [CrossRef]
4. S. Kamaruzzaman *et al.*, "Optimization of a stand-alone wind/PV hybrid system to provide electricity for a house in Malaysia," *Proceedings of the 4th IASME/WSEAS International Conference on Energy & Environment*, 2019.
5. M. Pang, Y. Shi, W. Wang, and S. Pang, "Optimal sizing and control of hybrid energy storage system for wind power using hybrid Parallel PSO-GA algorithm," *Energy Explor. Exploit.*, vol. 37, no. 1, pp. 558–578, Jan. 2019. [CrossRef]
6. T. O. Ajewole, O. D. Momoh, O. D. Ayedun, and M. O. Omoigui, "Optimal component configuration and capacity sizing of a mini integrated power supply system," *Environ. Qual. Manag.*, 2019. [CrossRef]
7. S. Singh, M. Singh, and S. C. Kaushik, "Feasibility study of an islanded microgrid in rural area consisting of PV, wind, biomass and battery energy storage system," *Energy Conversion and Management*, vol. 128, pp. 178–190, 2016. [CrossRef]
8. W. Zhang, A. Maleki, M. A. Rosen, and J. Liu, "Optimization with a simulated annealing algorithm of a hybrid system for renewable energy including battery and hydrogen storage," *Energy*, vol. 163, pp. 191–207, 2018. [CrossRef]
9. H. Demolli, A. S. Dokuz, A. Ecemis, and M. Gokcek, "Location-based optimal sizing of hybrid renewable energy systems using deterministic and heuristic algorithms," *Int. J. Energy Res.*, vol. 45, no. 11, pp. 16155–16175, 2021. [CrossRef]
10. A. H. Shahirinia, S. M. M. Tafreshi, A. H. Gastaj, and A. R. Moghaddamjoo, "Optimal sizing of hybrid power system using genetic algorithm," *Proceedings of the 2005 International Conference on Future Power Systems*, IEEE, November 18, 2005, Amsterdam, Netherlands, ISBN:90-78205-02-4, pp. 1-6.
11. M. Suresh, and R. Meenakumari, "An improved genetic algorithm-based optimal sizing of solar photovoltaic/wind turbine generator/diesel generator/battery connected hybrid energy systems for standalone applications," *International Journal of Ambient Energy*, vol. 42, no. 10, pp. 1136–1143, 2021. [CrossRef]
12. R. Dufo-López, and J. L. Bernal-Agustín, "Design and control strategies of PV-Diesel systems using genetic algorithms," *Sol. Energy*, vol. 79, no. 1, pp. 33–46, 2005. [CrossRef]
13. O. Abuzeid, A. Daoud, and M. Barghash, "Optimal off-grid hybrid renewable energy system for residential applications using particle swarm optimization," *Jordan J. Mech. Ind. Eng.*, vol. 13, no. 2, pp. 117–124, 2019.
14. O. A. A. Cancelliere, *"Methodology for sizing hybrid power generation systems (solar-diesel), battery-backed in non-interconnected zones using PSO,"* Vol. 121, 2019.
15. M. Kharrich, O. Mohammed, and M. Akherraz, "Design of hybrid microgrid PV/Wind/Diesel/Battery system: Case study for Rabat and Baghdad," *EAI Endorsed Trans. Energy Web*, vol. 7, no. 26, p. e1–e9, 2020. [CrossRef]
16. S. Charfi, A. Atieh, and M. Chaabene, "Optimal sizing of a hybrid solar energy system using particle swarm optimization algorithm based on cost and pollution criteria," *Environ. Prog. Sustainable Energy*, vol. 38, no. 3, p. e13055, 2019. [CrossRef]
17. A. Maleki, M. Rosen, and F. Pourfayaz, "Optimal operation of a grid-connected hybrid renewable energy system for residential applications," *Sustainability*, vol. 9, no. 8, p. 1314, 2017. [CrossRef]
18. B. Tudu, S. Majumder, K. K. Mandal, and N. Chakraborty, "Comparative performance study of genetic algorithm and particle swarm optimization applied on off-grid renewable hybrid energy system," in *Evolutionary, and Memetic Computing, Lecture Notes in Computer Science*. Berlin, Heidelberg, pp. 151–158, 2011. [CrossRef]
19. S. Rajanna, and R. P. Saini, "Development of optimal integrated renewable energy model with battery storage for a remote Indian area," *Energy*, vol. 111, pp. 803–817, 2016. [CrossRef]
20. "NASA Power," *NASA Prediction of Worldwide Energy Resources*. (2021, May 8). Retrieved from Power Data Access Viewer: https://power.larc.nasa.gov/data-access-viewer/.
21. R. Belfkira, L. Zhang, and G. Barakat, "Optimal sizing study of hybrid wind/PV/diesel power generation unit," *Solar Energy*, vol. 85, no. 1, pp. 100–110, 2011. [CrossRef]
22. M. Z. Farahmand, M. E. Nazari, and S. Shamlou, "Optimal sizing of an autonomous hybrid PV-wind system considering battery and diesel generator," *2017 Iranian Conference on Electrical Engineering (ICEE)*, 2017. [CrossRef]
23. J. Lian, Y. Zhang, C. Ma, Y. Yang, and E. Chaima, "A review on recent sizing methodologies of hybrid renewable energy systems," *Energy Convers. Manag.*, vol. 199, p. 112027, 2019. [CrossRef]
24. K. Gia Ing, J. J. Jamian, H. Mokhlis, and H. A. Illias, "Optimum distribution network operation considering distributed generation mode of operations and safety margin," *IET Renew. Power Gener.*, vol. 10, no. 8, pp. 1049–1058, 2016. [CrossRef]
25. S. Upadhyay, and M. P. Sharma, "Development of hybrid energy system with cycle charging strategy using particle swarm optimization for a remote area in India," *Renew. Energy*, vol. 77, pp. 586–598, 2015. [CrossRef]

26. B. Shi, W. Wu, and L. Yan, "Size optimization of stand-alone PV/wind/diesel hybrid power generation systems," *J. Taiwan Inst. Chem. Eng.*, vol. 73, pp. 93–101, 2017. [CrossRef]
27. R. Poli, J. Kennedy, and T. Blackwell, "Particle swarm optimization," *Swarm Intell.*, vol. 1, no. 1, pp. 33–57, 2007. [CrossRef]
28. M. A. Mohamed, A. M. Eltamaly, and A. I. Alolah, "PSO-Based Smart Grid Application for Sizing and Optimization of Hybrid Renewable Energy Systems," *PLoS ONE*, vol. 11, no. 8, p. e0159702, 2016. [CrossRef]
29. W. F. Abd-El-Wahed, A. A. Mousa, and M. A. El-Shorbagy, "Integrating particle swarm optimization with genetic algorithms for solving nonlinear optimization problems," *J. Comp. Appl. Math.*, vol. 235, no. 5, pp. 1446–1453, 2011. [CrossRef]
30. M. S. Ismail, M. Moghavvemi, and T. M. I. Mahlia, "Genetic algorithm based optimization on modeling and design of hybrid renewable energy systems," *Energy Convers. Manag.*, vol. 85, pp. 120–130, 2014. [CrossRef]
31. M. Kefayat, A. Lashkar Ara, and S. A. Nabavi Niaki, "A hybrid of ant colony optimization and artificial bee colony algorithm for probabilistic optimal placement and sizing of distributed energy resources," *Energy Conversion and Management*, vol. 92, pp. 149–161, 2015. [CrossRef]
32. M. R., Javadi, K., Mazlumi, and A. Jalilvand, "Application of GA, PSO and ABC in optimal design of a stand-alone hybrid system for the northwest of Iran," ELECO 2011 - 7th International Conference on Electrical and Electronics Engineering, 2011.
33. "Analysis of variance (ANOVA)," *Stat. Solut.*, 2009. Available: https://www.statisticssolutions.com/anova-analysis-of-variance/ [Accessed: September 1, 2021].
34. T. K. Kim, "Understanding one-way ANOVA using conceptual figures," *Korean J. Anesthesiol.*, vol. 70, no. 1, p. 22–26, 2017. [CrossRef]
35. D. B. Rubin, "Evaluations of the optimal discovery procedure for multiple testing," *Int. J. Biostat.*, vol. 12, no. 1, pp. 21–29, 2016. [CrossRef]

cigre Turkey

TEPES
TURKISH JOURNAL OF ELECTRICAL POWER AND ENERGY SYSTEMS

TEPES, Vol. 2, Issue. 2, 147-157, 2022 **DOI:** 10.5152/tepes.2022.22008

RESEARCH ARTICLE

# Heuristic Algorithms on Economic Dispatch of Multi-Microgrids with Photovoltaics

**Esra Aydın, Mikail Pürlü, Belgin Emre Türkay**

Department of Electrical Engineering, İstanbul Technical University, İstanbul, Turkey

**Cite this article as:** E. Aydın, M. Pürlü & B. E. Türkay. Heuristic algorithms on economic dispatch of multi-microgrids with photovoltaics. *Turk J Electr Power Energy Syst,* 2022; 2(2), 147-157.

## ABSTRACT

In this study, an application for economic load dispatch of multi-microgrid systems has been solved by meta-heuristic methods such as particle swarm optimization and genetic algorithm. The solution to the economic dispatch problem should both provide the optimum cost schedule and satisfy the power system constraints. Multi-microgrid system in this study consists of four fuel-based power generation units and two microgrids with photovoltaic panels as renewable energy sources. Simulations were carried out in two case studies, with and without microgrids. While both proposed methods gave better results than the literature study, the best solution was presented by particle swarm optimization with $106583.7/day and $108395.3/day for the systems with and without microgrids, respectively. The simulation results show that both algorithms achieve optimum and reliable results. Multi-microgrids with renewable energy resources increase system reliability and power quality and decrease emissions, transmission losses, and operating costs.

**Index terms—**Economic load dispatch, genetic algorithm, multi-microgrids, particle swarm optimization, photovoltaics.

## I. INTRODUCTION

Depending on the increasing population and developing technology, energy consumption is increasing steadily. Since large-scale power plants generally use fossil fuels, increasing energy consumption over the years has led to a significant decrease in fossil fuel reserves. In addition, concerns based on the increase in carbon emissions have made the renewable energy demand more important. In this case, distributed generation (DG) technology has significant importance and it allows the grid to take full advantage of renewable energy sources (RESs) [1, 2]. Renewable energy sources also reduce emissions, improve power quality, and have high reliability and high efficiency in resource access [1-3].

Since traditional power plants are far from residential and industrial areas, huge power losses occur during energy transmission. Connecting the microgrids (MGs) to the distribution system or operating in an islanded mode eliminates this disadvantage. The aforementioned MGs include DGs which are small-scale power generation units such as photovoltaic panels (PVs) and wind turbines [4-6].

Increasing energy demand increases the orientation toward RESs and gives more importance to economic load dispatch (ELD). The ELD problem (ELDP) basically aims to minimize the costs and has to meet the constraints of the system. The first of these constraints is to meet the demand. The second is that the generation power should be within the generator capacity limits [7].

There are many optimization methods to solve the ELDP. In addition to the classical optimization techniques, meta-heuristic methods are also used to solve these problems. Particle swarm optimization (PSO) and genetic algorithm (GA) are the most preferred meta-heuristic methods. Heuristic methods gain importance due to their advantages such as convenience in solving complex problems and short solution time.

Generic algorithm [1] and PSO [3] were used to ensure ELD of distribution system with two MGs. Authors in [5] proposed the corresponding dynamic programming to ELD of MGs with a battery energy storage system. In [8], various types of ELDP were examined using PSO and classical evolutionary programming. Particle swarm optimization was proposed to ELD considering non-linear generator constraints [9]. Authors in [10] proposed that GA and PSO solve dynamic ELD with valve point effect. In [8], the decomposition and calculation model of the multi-MG (MMG) system was created and the ELDP

**Corresponding author:** Mikail Pürlü, purlu@itu.edu.tr

**Received:** January 31, 2022
**Accepted:** April 18, 2022
**Publication Date:** June 10, 2022

was solved with the differential evolution method considering the transmission losses. The authors in [9] formulated the ELDP for MG and solved it using four methods such as lambda iteration, PSO, direct search method, and lambda logic. Authors in [10] proposed an advanced analytical target cascading theory-based decentralized autonomous dispatching model for an active distribution system with MMGs.

This study examines the ELDP of the MMG system. Multi-microgrid system has four fuel-based generators and two MGs containing PV. The PSO and GA algorithms are developed in matrix laboratory (MATLAB) to solve ELDP for both systems with and without MGs with PV.

The rest of this study is arranged as follows. In section II, the mathematical expression of the ELDP is introduced. In section III, definitions, implementation steps, and parameter settings of the proposed algorithms are given. In section IV, the application and simulation results are presented. Finally, the conclusion part is provided in section V.

## II. PROBLEM FORMULATION

### A. Objective Function

Economic load dispatch operation minimizes the total operating cost of the system [6]. The total generation cost of generators and MGs can be expressed in (1) and (2), respectively.

$$F_G = \sum_{i=1}^{N} \left( a_i P_i^2 + b_i P_i + c_i \right) \tag{1}$$

$$F_{MG} = \sum_{j=1}^{n} \delta_j \left( P_{MGj} \right) \tag{2}$$

where $F_G$ is the total generation cost of generators [$/h]; $P_i$ is the real power output of *i*th generation unit [MW]; $a_i$, $b_i$, and $c_i$ are the fuel cost coefficients of the *i*th generation unit [$/(MW)$^2$h, $MW/h, $/h]; *N* is the number of generation units of the system; $F_{MG}$ is generation cost of MGs [$/h]; $\delta_j$ is selling or buying price of *j*th MG [$]; $P_{MGj}$ is the real power output of *j*th MG [MW]; n is the number of MGs.

If $P_{MGj}$ has positive value, the *j*th MG supplies real power to the grid and that means $\delta_j$ is the selling price of $MG_j$. If $P_{MGj}$ has negative value, the *j*th MG gets real power from the grid and that means $\delta_j$ is the buying price of MGj [1].

The total generation cost of the MMG system ($F_{MMG}$ [$/h]) is the sum of the costs of generators and MGs and it can be expressed as follows:

$$F_{MMG} = F_G + F_{MG} \tag{3}$$

### B. Problem Constraints

The power balance of the power system is a major constraint and it can be expressed as follows:

$$P_D = \sum_{i=1}^{N} P_{Gi} + \sum_{j=1}^{n} P_{MGj} \tag{4}$$

where $P_D$ is total load demand [*MW*].

Each generator and also MG have generation limits and their power output should be within these limits. The capacity constraints of generators and MGs can be expressed as follows:

$$P_{Gi}^{min} \le P_{Gi} \le P_{Gi}^{max} \tag{5}$$

$$P_{MGj}^{min} \le P_{MGj} \le P_{MGj}^{max} \tag{6}$$

where $P_{Gi}^{min}$ and $P_{Gi}^{max}$ are the lower and upper limits of the *i*th generation unit [*MW*] and $P_{MGj}^{min}$ and $P_{MGj}^{max}$ are the lower and upper limits of the *j*th MG [*MW*].

### C. Characteristics of MGs

Microgrids can be both consumer and producer. The power outputs of MGs are variable and unstable due to the uncertainties of RES. Therefore, the power output of MGs can be in both negative and positive values. A positive value means that it operates as an energy generation source, and a negative value means that it operates as a load.

Microgrids have controllable and uncontrollable power output, and both must be considered in ELDP. Equations (7) and (8) indicate the minimum and maximum power outputs of MGs.

$$P_{MGj}^{max} = \sum_{i=1}^{N} P_{Sj}^{max} + \sum_{i=1}^{n_{us}} P_{usj} - P_{dj} \tag{7}$$

$$P_{MGj}^{min} = \sum_{i=1}^{N} P_{Sj}^{min} + \sum_{i=1}^{n_{us}} P_{usj} - P_{dj} \tag{8}$$

**Main Points**

- Proposed heuristic methods, such as genetic algorithm (GA) and particle swarm optimization (PSO), have been used in the application of economic dispatch problem to both systems, with and without microgrids (MGs).
- Proposed heuristic methods obtained more economical results for MMGs systems, especially with PSO.
- Proposed heuristic methods provided an environmental contribution by reducing carbon emissions, as well as technical contributions such as reducing transmission losses and fuel costs by using renewable energy-based MGs.
- Proposed heuristic methods validated the robustness and effectiveness of proposed algorithms by the literature comparison.
- As future work, the dependency on fuel-based generators can be reduced and the reliability of the system can be increased by adding a storage system or different renewable energy sources.

where $P_{MGj}^{max}$ : maximum power output of MGs [MW]; $P_{Sj}^{max}$ : maximum power output of controllable DGs [MW]; $P_{usj}$ : forecast power output of uncontrollable DGs [MW]; $P_{dj}$ : the load of MGs [MW]; $P_{MGj}^{min}$ : minimum power output of MGs [MW]; $P_{Sj}^{min}$ : minimum power output of controllable DGs [MW].

## III. OVERVIEW OF THE PROPOSED METHODS

### A. Particle Swarm Optimization

The PSO algorithm inspired by the social behavior of bird and fish packs is a population-based heuristic optimization technique developed by Dr. Eberhart and Dr. Kennedy in 1995 [11]. It is developed for solving non-linear problems and is used to find solutions to multi-parameter and multivariate optimization problems [12]. Individuals in the bird or fish herd have a simple behavior of reaching the food by following the movements of the herd, and this movement can be mathematically defined as the discovery of optimal areas in a search space [13]. Based on this simple behavior, in the PSO algorithm, individuals in the swarm are identified as particles and are released at random positions in the search area. Particles tend to change positions, influenced by the successful movements of other members of the swarm. By reason of this interaction, PSO exhibits a symbiotic behavior feature. As a result of this social behavior, particles present a random movement toward previously found optimal results in the search space [14].

In PSO algorithm, a swarm of particles is assumed to move in a search space to minimize the problem's objective function [15]. Each particle is defined by its position and velocity vectors [3]. $x_i$ describes the current position of the particle and $v_i$ describes the current velocity of the particle. These two vectors for each iteration are defined in (9) and (10). In every iteration, position and velocity vectors are updated according to two parameters. One of these parameters is the best solution that a particle has received so far and it is called $p_{besti}$. The other one is the particle value that gives the best solution obtained by all particles so far in the entire population and it is called $g_{besti}$. Each particle's velocity and position vectors are updated according to (11) and (12). The vectoral path followed by each particle is illustrated in Fig. 1.

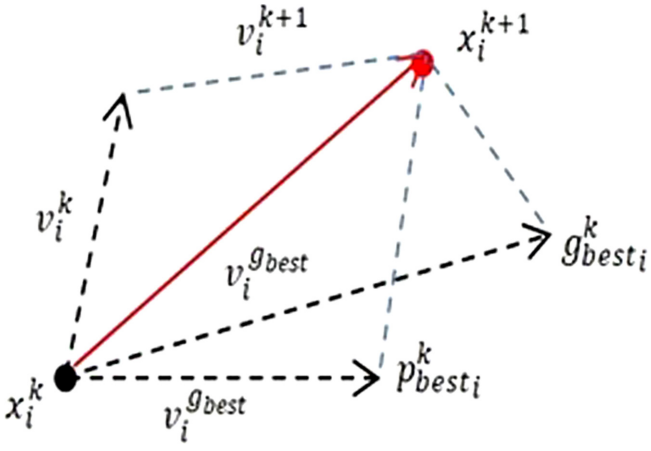


**Fig. 1.** The vectoral path of each particles [3].

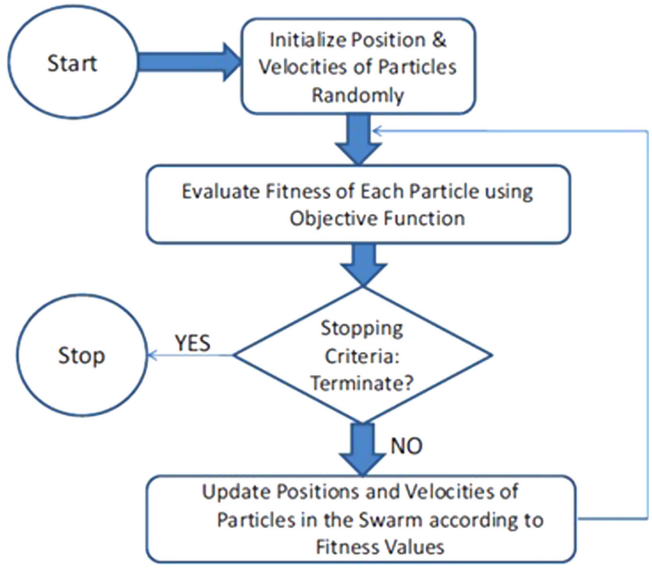


**Fig. 2.** Flowchart of PSO [16]. PSO, particle swarm optimization.

$$x_i^k = \left[x_{i1}, x_{i2}, \ldots, x_{iD}\right] \tag{9}$$

$$v_i^k = \left[v_{i1}, v_{i2}, \ldots, v_{iD}\right] \tag{10}$$

$$v_i^{k+1} = wv_i^k + c_1 r_1 \left(p_{best\,i}^k - x_i^k\right) + c_2 r_2 \left(g_{best\,i}^k - x_i^k\right) \tag{11}$$

$$x_i^{k+1} = x_i^k + v_i^{k+1} \tag{12}$$

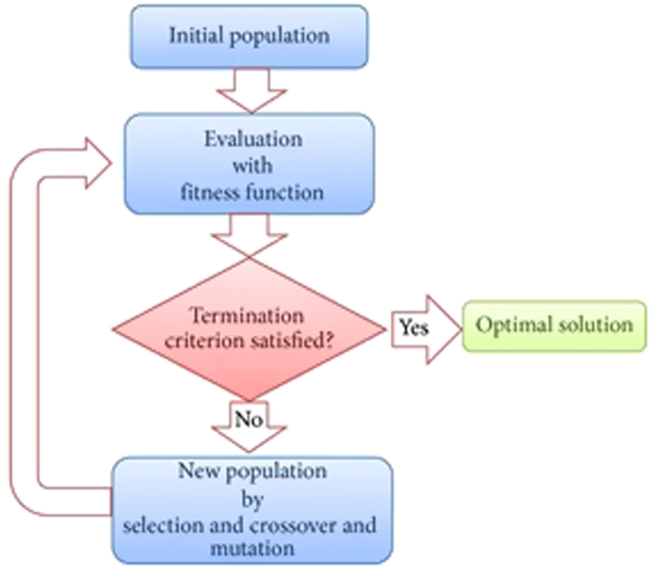


**Fig. 3.** Flowchart of GA [23]. GA, generic algorithm.

where $v_i^{k+1}$ : velocity of *i*th particle in (*k*+1)th iteration; $v_i^k$ : velocity of *i*th particle in *k*th iteration;*W*: inertia weight;$C_1$, $C_2$: acceleration constant;$r_1$, $r_1$: uniform random value; $p_{best\,i}^k$ : *i*th particle's best solution in *k*th iteration; $g_{best\,i}^k$ : best solution of all particles in *k*th iteration; $x_i^k$ : position of *i*th particle in *k*th iteration; $x_i^{k+1}$ : position of *i*th particle in (*k*+1)th iteration.

Acceleration constants are usually chosen as equal and 2 but [0, 4] is the general range for this quantity [12, 16]. The inertia weight can be defined as follows:

$$w(k) = w_{max} - \left( \frac{w_{max} - w_{min}}{K} \right) \times k \tag{13}$$

where $W_{max}$ is maximum inertia weight; $W_{min}$ is minimum inertia weight; *K* is the number of iterations; *K* is the current iteration number.

The standard flowchart of PSO is shown in Fig. 2 [16].

**B. Genetic Algorithm**

The GA is an iterative evolution-based algorithm that searches for the best solution in a complex multi-dimensional search space according to the survival of the fittest principle. Generic algorith which is inspired by Darwin's evolution theory was developed by John Holland in 1975 [17, 18]. In GA, the birth, reproduction, and extinction of individuals by natural selection are simulated [19].

Genetic algorithm creates a solution set consisting of independent solutions, each of which is a vector on a multidimensional space. In this way, the probability of reaching a solution by evaluating a single point increases [20, 21]. Besides, it has an advantage with the variety of solutions it provides and its application to multivariate problems [21].

The GA modifies the population iteratively. In each iteration, new individuals are created by randomly selecting individuals and a new generation emerges. This process continues until the maximum number of iterations is reached and the optimum result is obtained. Firstly, for the implementation of algorithm, a random population is created. Each individual in a population is called as a chromosome. Each chromosome in a population represents possible solution and has a fitness value [22]. This value was calculated for each individual with the fitness function. The chromosome with the best fitness value gives the most optimal result. Equation (1) indicates the fitness function.

$$F(x) = \frac{1}{1 + f(x)} \tag{14}$$

where $F(x)$ is fitness function and $f(x)$ is the cost function. $F(x)$ ranges from 0 to 1. As $F(x)$ gets closer to 1, the probability of an individual being transferred to the next generation increases [17, 18].

After the population is created, a new population is produced from this population by means of genetic operators. These genetic operators are selection, crossover, and mutation:

**Selection:** Roulette wheel technique is generally used for this process. Selection is made according to the fitness values of the individuals. The selected individuals are called parents.

**Crossover:** New individuals are created from the selected parents via the crossover operator. The crossover rate is considered when considering this process.

**Mutation:** After the crossover operation, new individuals are randomly mutated. The mutation rate is considered when considering this process.

The schematic flowchart of GA is given in Fig. 3 [23].

**C. Implementation of the Proposed Algorithms on ELDP**

Implementation steps of PSO on ELDP are given as follows [24]:

**Step 1:** PSO parameters (number of particles, iteration number, $W_{min}$, $W_{max}$, $C_1$, $C_2$) and system data ( $P_{Gi}^{min}$ , $P_{Gi}^{max}$ , $a_i$, $b_i$, $c_i$, $P_D$) are defined.

**TABLE I.**
PSO PARAMETERS

| PSO Parameter | Value |
|---|---|
| Number of particles | 50 |
| Maximum iteration | 50 |
| Acceleration constants: $C_1$=$C_2$ | 2 |
| Inertia weights: $W_{min}$ & $W_{max}$ | 0.1 and 0.9 |

PSO, particle swarm optimization.

**TABLE II.**
GA PARAMETERS

| Parameter | Value |
|---|---|
| Population size | 50 |
| Maximum iteration | 50 |
| Crossover rate | 0.8 |
| Mutation rate | 0.1 |

GA, generic algorithm.

**TABLE III.**
GENERATOR PARAMETERS

| Parameters | G1 | G2 | G3 | G5 |
|---|---|---|---|---|
| $a_i$ | 0.168 | 0.168 | 0.505 | 0.674 |
| $b_i$ | 21.05 | 16.8 | 12.63 | 27.39 |
| $c_i$ | 40 | 40 | 30 | 30 |
| $P_{Gi}^{min}$ | 20 | 10 | 10 | 10 |
| $P_{Gi}^{max}$ | 80 | 55 | 55 | 55 |

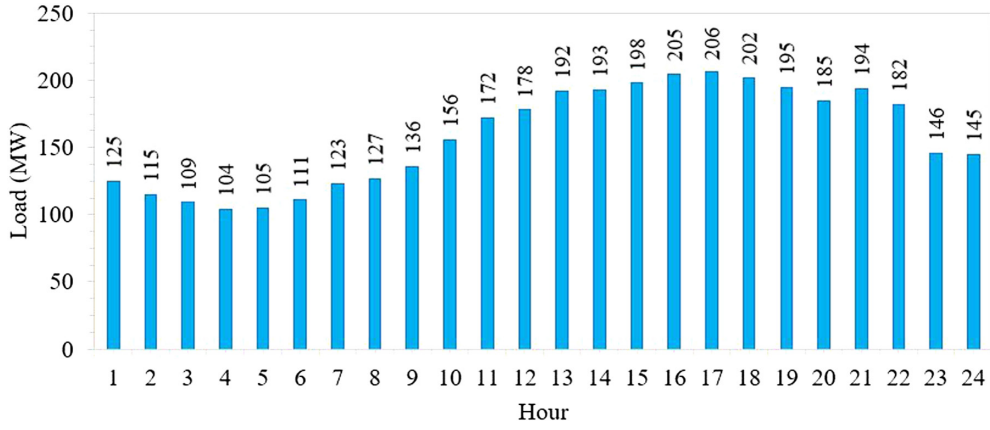


**Fig. 4.** Daily load.

**Step 2:** Particles of the swarm are generated randomly by using (15):

$$P_i = P_i^{min} + rand \times \left( P_i^{max} - P_i^{min} \right) \quad (15)$$

where $P_i$ is the power output [MW] and $P_i^{min}$ and $P_i^{max}$ are generation limits [MW]

**Step 3:** It is evaluated whether the generation power meets the demand and whether it is within the generation limits. When the number of particles that meet these constraints reaches the desired number, the next step is started.

**Step 4:** $p_{besti}$ and $g_{besti}$ are determined.

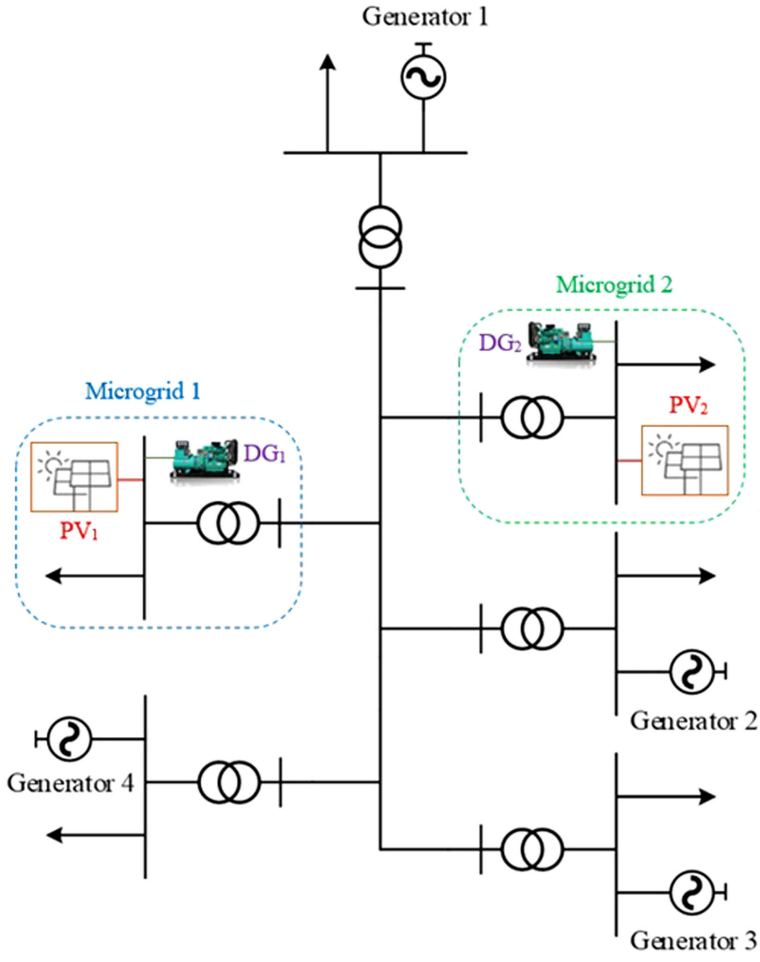


**Fig. 5.** Single-line diagram of the system.

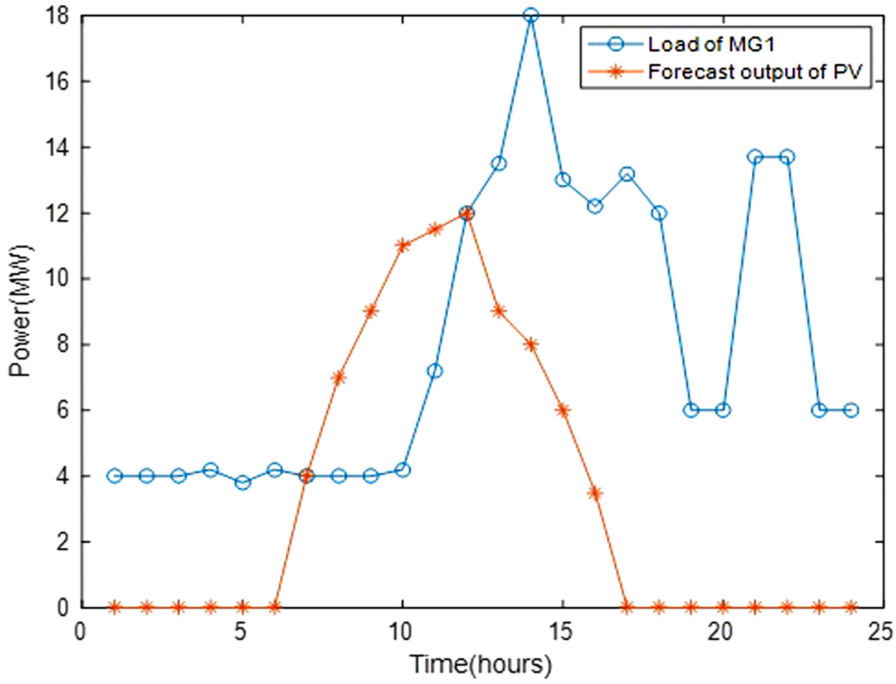


**Fig. 6.** Forecast PV power output and daily load of MG1 [1]. PV, photovoltaic; MG1, microgrid1.

**Step 5:** The iteration is started and the inertia weight is calculated according to (13). In each iteration, velocity and positions of particles are updated according to (11) and (12).

**Step 6:** $p_{besti}$ and $g_{besti}$ are updated.

**Step 7:** When the maximum number of iterations is reached, the algorithm is stopped and the optimum solution results are obtained.

Implementation steps of GA on ELDP are given as follows:

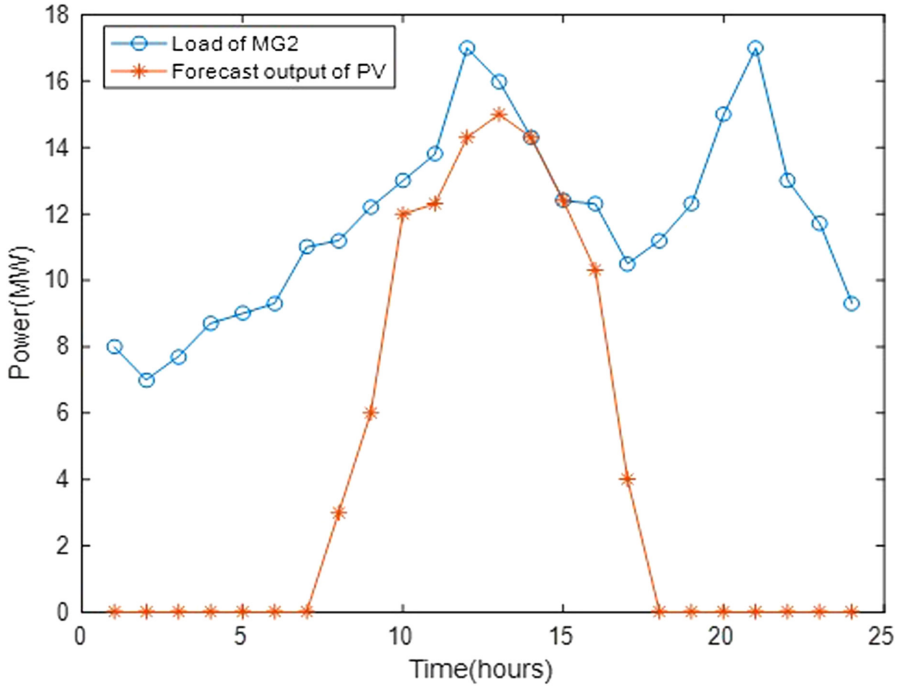


**Fig. 7.** Forecast PV power output and daily load of MG2 [1]. PV, photovoltaic; MG2, microgrid2.

**TABLE IV.**
POWER DISPATCH FOR THE SYSTEMS WITH MGS AND WITHOUT MG BY USING PSO

| | Power System Without MG | | | | Power System With MGs | | | | | |
|---|---|---|---|---|---|---|---|---|---|---|
| **Hour** | **G1 [MW]** | **G2 [MW]** | **G3 [MW]** | **G4 [MW]** | **G1 [MW]** | **G2 [MW]** | **G3 [MW]** | **G4 [MW]** | **MG1 [MW]** | **MG2 [MW]** |
| 1 | 31.30 | 43.95 | 18.75 | 30.99 | 29.73 | 42.38 | 18.23 | 27.06 | 5.3 | 2.3 |
| 2 | 29.23 | 41.88 | 18.06 | 25.82 | 29.23 | 41.88 | 18.06 | 25.82 | 1 | -1 |
| 3 | 27.99 | 40.63 | 17.65 | 22.72 | 28.63 | 41.28 | 17.86 | 24.33 | -1.8 | -1.3 |
| 4 | 26.95 | 39.60 | 17.30 | 20.14 | 27.94 | 40.59 | 17.63 | 22.62 | -1.4 | -3.4 |
| 5 | 27.16 | 39.81 | 17.37 | 20.66 | 28.21 | 40.86 | 17.72 | 23.29 | -0.6 | -4.5 |
| 6 | 28.40 | 41.05 | 17.78 | 23.76 | 28.92 | 41.57 | 17.96 | 25.05 | 2.5 | -5 |
| 7 | 30.89 | 43.54 | 18.61 | 29.96 | 29.66 | 42.31 | 18.21 | 26.91 | 5.9 | 0 |
| 8 | 31.72 | 44.36 | 18.89 | 32.02 | 27.28 | 39.93 | 17.41 | 20.97 | 15.5 | 5 |
| 9 | 33.58 | 46.23 | 19.51 | 36.67 | 28.69 | 41.34 | 17.88 | 24.48 | 16.3 | 7.3 |
| 10 | 37.73 | 50.37 | 20.89 | 47 | 31.38 | 44.03 | 18.78 | 31.20 | 14.5 | 16.1 |
| 11 | 41.16 | 53.81 | 22.03 | 55 | 34.29 | 46.93 | 19.74 | 38.43 | 15.6 | 17 |
| 12 | 44.76 | 55 | 23.23 | 55 | 35.96 | 48.61 | 20.30 | 42.61 | 14.8 | 15.7 |
| 13 | 55.27 | 55 | 26.72 | 55 | 40.34 | 52.99 | 21.76 | 53.51 | 6.9 | 16.5 |
| 14 | 56.02 | 55 | 26.97 | 55 | 41.29 | 53.93 | 22.07 | 55 | 0.7 | 20 |
| 15 | 59.77 | 55 | 28.22 | 55 | 47.69 | 55 | 24.20 | 55 | 3.8 | 12.3 |
| 16 | 65.02 | 55 | 29.97 | 55 | 50.77 | 55 | 25.22 | 55 | 2.3 | 16.7 |
| 17 | 65.77 | 55 | 30.22 | 55 | 62.62 | 55 | 29.17 | 55 | 0 | 4.2 |
| 18 | 62.77 | 55 | 29.22 | 55 | 55.19 | 55 | 26.70 | 55 | 2.4 | 7.7 |
| 19 | 57.52 | 55 | 27.47 | 55 | 51.07 | 55 | 25.32 | 55 | 2.7 | 5.9 |
| 20 | 50.01 | 55 | 24.98 | 55 | 42.81 | 55 | 22.58 | 55 | 4.2 | 5.4 |
| 21 | 56.77 | 55 | 27.22 | 55 | 59.47 | 55 | 28.12 | 55 | -1.8 | -1.8 |
| 22 | 47.76 | 55 | 24.23 | 55 | 47.84 | 55 | 24.25 | 55 | -1.8 | 1.7 |
| 23 | 35.65 | 48.30 | 20.20 | 41.84 | 36.32 | 48.97 | 20.42 | 43.49 | -1 | -2.2 |
| 24 | 35.45 | 48.09 | 20.13 | 41.32 | 32.59 | 45.24 | 19.18 | 34.19 | 6 | 7.8 |

PSO, particle swarm optimization; MG, microgrid.

**Step 1:** GA parameters (population size, crossover rate, mutation rate, iteration number) and system data ( $P_{Gi}^{min}$ , $P_{Gi}^{max}$ , $a_i$, $b_i$, $c_i$, $P_D$) are defined.

**Step 2:** Chromosomes are randomly generated by using (15).

**Step 3:** When the number of chromosomes satisfying the system constraints is reached, the fitness value for each chromosome is calculated using (14).

**Step 4:** The roulette wheel selection is applied and the parents are selected randomly.

**Step 5:** Crossover and mutation operations are applied.

**Step 6:** The fitness value is calculated for the chromosomes in the new generation and the next iteration is passed.

**Step 7:** When the stopping criteria (max. iteration number) is met, the algorithm is stopped and the optimum results are obtained.

**D. Parameter Settings**

Partilce swarm optimization and GA parameters used in this study to optimize ELD problem are given in Table 1 and Table 2, respectively.

**TABLE V.**
POWER DISPATCH FOR THE SYSTEMS WITH MGS AND WITHOUT MG BY USING GA

| | Power System Without MG | | | | Power System With MGs | | | | | |
|---|---|---|---|---|---|---|---|---|---|---|
| **Hour** | **G1 [MW]** | **G2 [MW]** | **G3 [MW]** | **G4 [MW]** | **G1 [MW]** | **G2 [MW]** | **G3 [MW]** | **G4 [MW]** | **MG1 [MW]** | **MG2 [MW]** |
| 1 | 31.35 | 43.77 | 18.77 | 31.12 | 29.78 | 42.20 | 18.24 | 27.19 | 5.3 | 2.3 |
| 2 | 29.28 | 41.70 | 18.08 | 25.94 | 29.28 | 41.70 | 18.08 | 25.94 | 1 | -1 |
| 3 | 28.03 | 40.47 | 17.66 | 22.84 | 28.68 | 41.11 | 17.88 | 24.45 | -1.8 | -1.3 |
| 4 | 26.99 | 39.43 | 17.32 | 20.26 | 27.99 | 40.43 | 17.65 | 22.74 | -1.4 | -3.4 |
| 5 | 27.20 | 39.64 | 17.39 | 20.77 | 28.26 | 40.69 | 17.74 | 23.41 | -0.6 | -4.5 |
| 6 | 28.45 | 40.88 | 17.80 | 23.88 | 28.97 | 41.39 | 17.97 | 25.17 | 2.5 | -5 |
| 7 | 30.94 | 43.35 | 18.63 | 30.08 | 29.71 | 42.14 | 18.22 | 27.03 | 5.9 | 0 |
| 8 | 31.77 | 44.18 | 18.91 | 32.15 | 27.33 | 39.76 | 17.43 | 21.09 | 15,5 | 5,9 |
| 9 | 33.64 | 46.04 | 19.53 | 36.81 | 28.74 | 41.17 | 17.90 | 24.60 | 16.3 | 7.3 |
| 10 | 37.78 | 50.16 | 20.91 | 47.15 | 31.44 | 43.85 | 18.79 | 31.32 | 14.5 | 16.1 |
| 11 | 41.29 | 53.65 | 22.07 | 55 | 34.34 | 46.74 | 19.76 | 38.56 | 15.6 | 17 |
| 12 | 44.78 | 55 | 23.23 | 55 | 36.02 | 48.41 | 20.32 | 42.75 | 14.8 | 15.7 |
| 13 | 55.27 | 55 | 26.72 | 55 | 40.40 | 52.76 | 21.78 | 53.66 | 6.9 | 16.5 |
| 14 | 56.02 | 55 | 26.97 | 55 | 41.41 | 53.77 | 22.11 | 55 | 0.7 | 20 |
| 15 | 59.78 | 55 | 28.22 | 55 | 47.70 | 55 | 24.21 | 55 | 3.8 | 12.3 |
| 16 | 65.03 | 55 | 29.97 | 55 | 50.77 | 55 | 25.23 | 55 | 2.3 | 16.7 |
| 17 | 65.78 | 55 | 30.22 | 55 | 62.63 | 55 | 29.17 | 55 | 0 | 4.2 |
| 18 | 62.78 | 55 | 29.22 | 55 | 55.20 | 55 | 26.70 | 55 | 2.4 | 7.7 |
| 19 | 57.53 | 55 | 27.47 | 55 | 51.07 | 55 | 25.33 | 55 | 2.7 | 5.9 |
| 20 | 50.03 | 55 | 24.98 | 55 | 42.82 | 55 | 22.58 | 55 | 4.2 | 5.4 |
| 21 | 56.78 | 55 | 27.22 | 55 | 59.48 | 55 | 28.12 | 55 | -1.8 | -1.8 |
| 22 | 47.77 | 55 | 24.23 | 55 | 47.85 | 55 | 24.26 | 55 | -1.8 | 1.7 |
| 23 | 35.71 | 48.10 | 20.22 | 41.97 | 36.37 | 48.76 | 20.44 | 43.63 | -1 | -2.2 |
| 24 | 35.50 | 47.89 | 20.15 | 41.45 | 32.64 | 45.05 | 19.19 | 34.32 | 6 | 7.8 |

MG, microgrid; GA, generic algorithm.

## IV. SIMULATION RESULTS AND DISCUSSION

The MMG system used in this study consists of two MGs including RESs and four fuel-based units of generator sets. Generator parameters and daily load profile of the system are given in Table 3 and Fig. 4, respectively [1]. The single-line diagram of the MMG system is given in Fig. 5.

As the MG1 and MG2 are solar-based DGs, their power output is not indefinite. Therefore, just like in local daily load, power outputs should be estimated according to historical and environmental factors. Since the MGs contain PVs, MG1 provides power to the system in periods 6.00–17.00 and MG2 in periods 7.00–18.00.

The controllable DG power output capacity of MG1 is 12 MW, while the output capacity of MG2 is 20 MW. The forecast PV power output and daily local load curve for MG1 and MG2 are given in Fig. 6 and Fig. 7, respectively.

Microgrids should primarily meet local load. If the generation power of the MG cannot meet their local load, the lack of power amount is supplied from the system. If the MG generates more power than its local load, excess power is supplied to the system. Microgrid1's selling price is $27/MW and MG2's selling price is $28/MW. Likewise, the buying price of both MGs is equal to $22/MW.

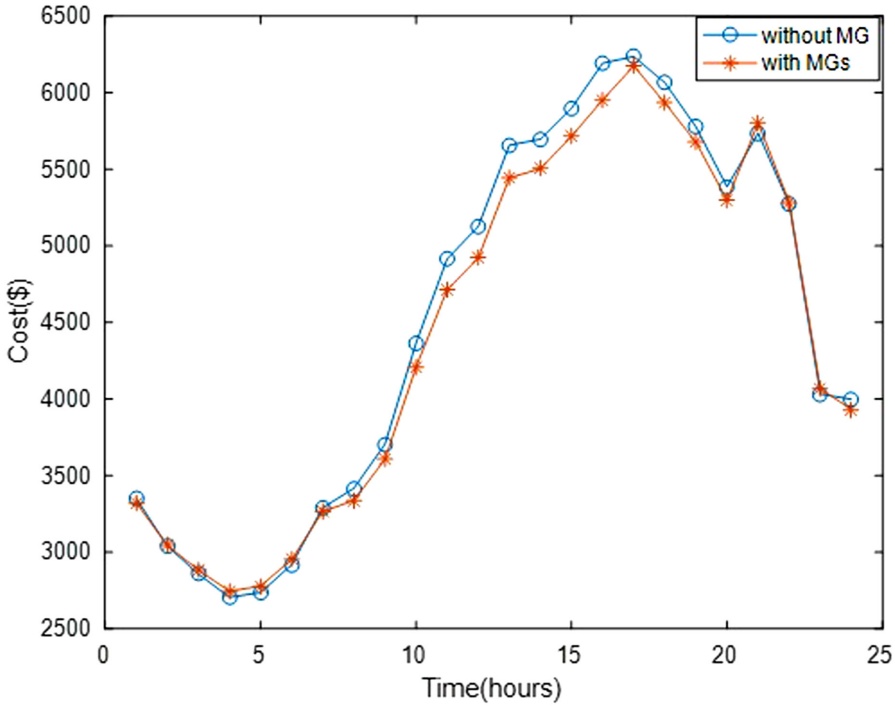


**Fig. 8.** Optimal costs in 24 hours by PSO. PSO, particle swarm optimization.

Tables 4 and 5 show the economic dispatch results of the system with and without MGs by PSO and GA, respectively. Hourly optimal costs of the system both with and without MGs are illustrated graphically in Fig. 8 for PSO and Fig. 9 for GA. The total costs have been obtained as $108395.3/day in the system without MG and as $106583.7/day in the system with MGs by PSO and $108456.6/day and $106642.9/day by GA. It is clearly seen that MMG-containing RES provides economic benefits.

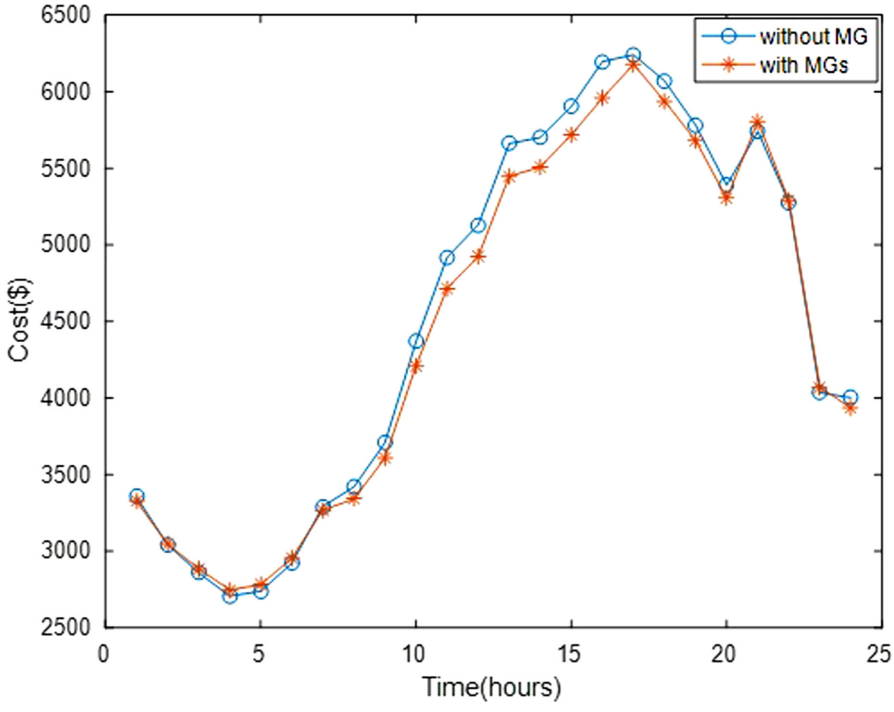


**Fig. 9.** Optimal costs in 24 hours by GA. GA, generic algorithm.

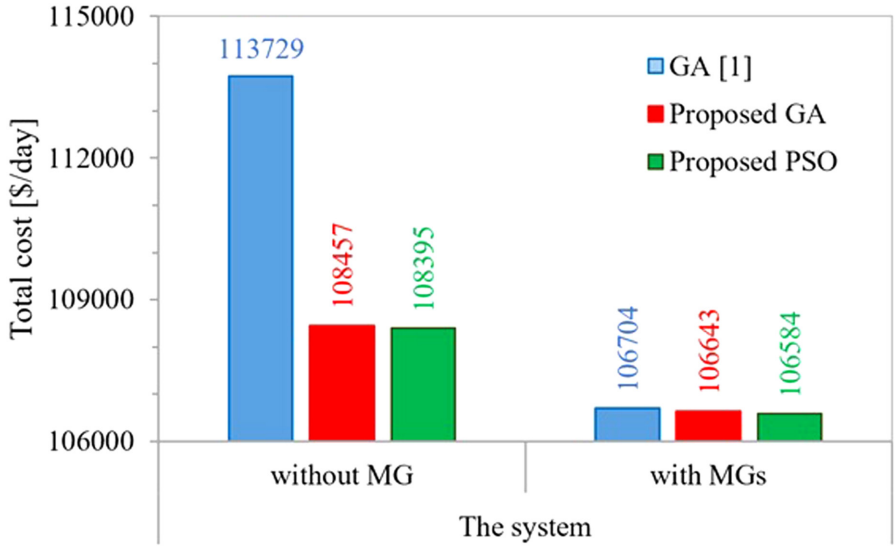


**Fig. 10.** Comparison of the proposed GA and PSO with the GA [1] in the literature. PSO, particle swarm optimization; GA, generic algorithm.

It is seen clearly from the comparison of Fig. 8 and Fig. 9 that the inclusion of MGs resulted in a reduction in cost. From 12:00 to 18:00 hours, when is the most efficient interval of PVs, the total cost difference between with MGs and without MGs is the greatest. Even if in the night time, the difference is great. The reason is that the MGs are insufficient to meet local loads during these hours, so power should be purchased from the system. It is normal for this difference to occur when the purchase cost is considered.

The comparison of the proposed algorithms in this study and GA in [1] is shown in Fig. 10.

## VI. CONCLUSIONS

The inclusion of MGs including RES in distribution systems is one of the most effective factors in the near future. Renewable energy-based MGs increase power quality and efficiency while reducing transmission line losses and carbon emissions.

In this study, the ELDP of an MMG system with two MGs including PV and four fuel-based generators is approached by using PSO and GA algorithms, and the total fuel cost is calculated as $106583.7/day and $106642.9/day, respectively. When MGs are neglected, the total cost is calculated as $108395.3/day for PSO method and $108456.6/day for GA. The inclusion of MGs including RES resulted in a cost reduction of approximately $1800/day. Optimal, reliable, and close results were obtained in both methods. Also, these results are better than the study in the literature. Since GA algorithm has more complex structure in practice, its calculation process is longer than that of PSO.

Multi-microgrid systems including PV provided a significant reduction in total operation cost. Besides the other advantages, MMG system with PV reduces the load dispatching on the fuel-based generators and provides a significant reduction in fuel costs and emissions.

**Peer-review:** Externally peer-reviewed.

**Declaration of Interests:** The authors have no conflict of interest to declare.

**Funding:** The authors declared that this study has received no financial support.

## REFERENCES

1. Z. Qiongyao, L. Shirong, Z. Ying, C. Xueting, and Z. Lingwei, "Economic dispatch of distribution network with multi-microgrid," in 2015 34th Chinese Control Conference (CCC), 2015, pp. 9060–9065.
2. G. Liao, "The optimal economic dispatch of smart microgrid including Distributed Generation," in International Symposium on Next-Generation Electronics, 2013, pp. 473–477.
3. U. Firdaus, and O. Penangsang, "Economic dispatch of multi microgrid systems with renewable energy sources using particle swarm optimization," in International Seminar on Intelligent Technology and Its Applications (ISITIA), 2016, pp. 595–600.
4. J. Zhu, *Optimization of Power System Operation*. Hoboken, NJ, USA: John Wiley & Sons, Inc, 2015.
5. L. Xiaoping, D. Ming, H. Jianghong, H. Pingping, and P. Yali, "Dynamic economic dispatch for microgrids including battery energy storage," in The 2nd International Symposium on Power Electronics for Distributed Generation Systems, 2010, pp. 914–917.
6. P. Li, X. Guan, J. Wu, and D. Wang, "An integrated energy exchange scheduling and pricing strategy for multi-microgrid system," in IEEE International Conference of IEEE Region 10 (TENCON 2013), 2013, pp. 1–5.
7. A. J. Wood, and B. F. Wollenberg, *Power Generation Operation and Control*. New York, USA: John and Sons, 1996.
8. X. Li, Y. Zeng, and Z. Lu, "Decomposition and coordination calculation of economic dispatch for active distribution network with multi-microgrids," *Int. J. Electr. Power Energy Syst.*, vol. 135, p. 107617, 2022. [CrossRef]
9. A. Maulik, and D. Das, "Optimal operation of microgrid using four different optimization techniques," *Sustain. Energy Technol. Assess.*, vol. 21, pp. 100–120, 2017. [CrossRef]

10. M. Xie, X. Ji, X. Hu, P. Cheng, Y. Du, and M. Liu, "Autonomous optimized economic dispatch of active distribution system with multi-microgrids," *Energy*, vol. 153, pp. 479–489, 2018. [CrossRef]
11. R. Eberhart, and J. Kennedy, "A new optimizer using particle swarm theory," in MHS, Proceedings of the Sixth International Symposium on Micro Machine and Human Science, 1995, pp. 39–43.
12. S. Tamer, and C. Karakuzu, "Parçacık sürüsü optimizasyon algoritması ve Benzetim Örnekleri," in ELECO 2006 Elektrik-Elektronik- Bilgisayar Sempozyumu, 2006, pp. 302–306.
13. J. Kennedy, and R. Eberhart, "Particle swarm optimization," in *Proceedings of ICNN'95 - International Conference on Neural Networks*, vol. 4, 1995, pp. 1942–1948.
14. Y. Zeybekoğlu, *Ünite Yüklenme Probleminin Parçacık Sürü Optimizasyon Yöntemi ile Çözümü* [M.Sc. dissertation]. Istanbul, Turkey: Istanbul Technical University, 2011.
15. Z. -L. Gaing, "Particle swarm optimization to solving the economic dispatch considering the generator constraints," *IEEE Trans. Power Syst.*, vol. 18, no. 3, pp. 1187–1195, 2003. [CrossRef]
16. K. Gopalakrishnan, "Neural network-swarm intelligence hybrid nonlinear optimization algorithm for pavement moduli back-calculation," *J. Transp. Eng.*, vol. 136, no. 6, pp. 528–536, 2010. [CrossRef]
17. M. Purlu, and B. E. Turkay, "Dynamic economic dispatch with valve point effect by using GA and PSO algorithm," in 6th International Conference on Control Engineering & Information Technology (CEIT), 2018, pp. 1–6.
18. D. E. Goldberg, *Genetic Algorithms in Search, Optimization & Machine Learning*. Reading, United States of America: Addison-Wesley, 1989.
19. T. Murata, and H. Ishibuchi, "Performance evaluation of genetic algorithms for flowshop scheduling problems," in Proceedings of the First IEEE Conference on Evolutionary Computation, IEEE World Congress on Computational Intelligence, 1994, pp. 812–817.
20. Ö. P. Arslan, *Güç Sistemlerinin Ekonomik ve Çevresel Ekonomik Yük Dağıtımında Yeni Optimizasyon Tekniklerinin Kullanımı* [M.Sc. dissertation]. Kırıkkale, Turkey: Kırıkkale University, 2015.
21. M. Pürlü, *Üretim Sistemlerinde Valf-Nokta Etkili Konveks Olmayan Dinamik Ekonomik Yük Dağıtımı* [M.Sc. dissertation]. Istanbul, Turkey: Istanbul Technical University, 2017.
22. V, J. S. Kumar, Y. Singh, and S. Sood, "Optimal Economic Load Dispatch Using Genetic Algorithms," *World Acad. Sci. Eng. Technol. Int. J. Electr. Comput. Eng.*, vol. 9, no. 4, pp. 463–470, 2015.
23. S. Li, L. Kang, and X. M. Zhao, "A survey on evolutionary algorithm based hybrid intelligence in bioinformatics," *BioMed Res. Int.*, vol. 2014, p. 362738, 2014. [CrossRef]
24. E. Aydin, M. Purlu, and B. E. Turkay, "Economic dispatch of multi-microgrid systems by using particle swarm optimization," in 13th International Conference on Electrical and Electronics Engineering (ELECO), IEEE Publications, 2021, pp. 268–272.

cigre Turkey

TEPES
TURKISH JOURNAL OF ELECTRICAL POWER AND ENERGY SYSTEMS

TEPES, Vol. 2, Issue. 2, 158-167, 2022 **DOI:** 10.5152/tepes.2022.22021

RESEARCH ARTICLE

# Hybrid Optimization Technique for Solving Combined Economic Emission Dispatch Problem of Power Systems

**Tijani Muhammed Adekilekun[1], Adepoju Gafari Abiola[2], Okelola Muniru Olajide[2], Sanusi Mufutau Adewolu[1], Bamikefa Isaac Adekunle[1]**

[1]Department of Electrical and Electronic Engineering, Federal Polytechnic, Ede, Nigeria
[2]Department of Electronic and Electrical Engineering, Ladoke Akintola University of Technology, Ogbomoso, Nigeria

**Cite this article as:** T. Muhammed Adekilekun, A. Gafari Abiola, O. Muniru Olajide, S. Mufutau Adewolu and B. Isaac Adekunle, "Hybrid optimization technique for solving combined economic emission dispatch problem of power systems," *Turk J Electr Power Energy Syst*, 2022; 2(2), 158-167.

## ABSTRACT

Mathematical optimization provides the best possible results to a problem. The latest trend in optimization, called hybrid optimization methods, combines two or more optimization techniques, deterministic and non-deterministic, with the aim of overcoming the limitation of one technique by the advantage(s) of the other technique(s). A hybrid particle swarm bat algorithm optimization technique that uses the frequency tuning technique of bat algorithm at the velocity updating stage in particle swarm optimization (PSO) was developed for avoiding premature convergence limitation of PSO using the potential of BA to escape being trapped at local optimum. Implementation of the developed optimization method for solving the combined economic emission dispatch problem of 28 Bus 7 Generators Nigeria power network showed that H-PS-BA optimization method performed better than PSO by 0.07%.

**Index Terms—**Bat algorithm, combined economic emission dispatch, hybrid optimization, non-deterministic optimization, particle swarm optimization.

## I. INTRODUCTION

The determination of the best desirable solution to a problem, known as optimization, is a commonly encountered mathematical problem in engineering. Numerous optimization routines have been evolved for solving different optimization problems. These methods are classified as deterministic, non-deterministic, and hybrid optimization procedures [1]. Different techniques of optimization have been deployed in solving electric power system problems. These methods include linear programming (LP), interior point method (IPM), and quadratic programming (QP) which all belong to the deterministic optimization class [2-5]. Non-deterministic methods of optimization such as bat algorithm (BA), artificial bee colony (ABC), genetic algorithm (GA), and particle swarm optimization (PSO) techniques were also employed for power system problem solutions [6,7].

A solution to complex power system problems using deterministic optimization methods was found to be difficult and expensive, the possibility of getting a global solution also decreases when the size of the problem increases, and the quality of global solution obtained cannot be guaranteed in the case of non-deterministic methods [8]. The realization of the fact that there is no perfect solution brought about the development of a successful trend in optimization: combination of different algorithms to form a hybrid. Hybrid optimization uses the superiority of a method to conquer the drawbacks of other methods [1,9]. Hybrid algorithms promise high-quality solutions and stability of convergence. They have a quick operation and are flexible in modeling compared to each separate technique [10].

The optimal allocation procedure of electrical energy production amidst participating generating units, satisfying all operational limitations while reducing generation cost, and the amount of emission produced simultaneously is termed combined economic emission dispatch (CEED) [12]. Combined economic emission dispatch has emerged as a very important optimization problem in contemporary deregulated power systems [13]. Optimal CEED problem (CEEDP) is necessitated because of shortage of resources, surging power generation costs, and soaring demands for electric energy [6]. Several elements influencing CEED include loss in transmission, characteristics of fuel consumption, valve point loading, ramp rate, prohibited zones of operation, and constraint conditions of the CEEDP [3,14,15].

**Corresponding author:** Tijani Muhammed Adekilekun, muhammedtijani@gmail.com

**Received:** May 19, 2022
**Accepted:** September 15, 2022
**Publication Date:** October 10, 2022

Different hybrid techniques of optimization have been evolved and applied to solve CEEDP in power systems. These include hybrid ABC-simulated annealing algorithm [16], hybrid firefly–bat algorithm [17], quantum-inspired PSO [18], hybrid ABC with fuzzy technique [19], and hybrid whale optimization algorithm with PSO [20]. The results of these works revealed that the hybrid algorithms solved the CEEDP more efficiently than the hybrid constituent methods applied separately.

This work develops a hybrid particle swarm bat algorithm (H-PS-BA) optimization technique which uses the frequency tuning technique of BA at the velocity updating stage of PSO to avoid premature convergence limitation of PSO. Particle swarm optimization is a favored and successful non-deterministic optimization method. It is robust with easy implementation but with limitations of premature convergence and it can be trapped at a local optimum [3]. The BA, however, is more efficacious in exploiting global best for determining feasible best solutions and has the ability to escape being trapped at a local minimum [11]. The developed optimization technique was employed to solve the CEEDP of Nigerian 28 bus 7 generators practical power network. This is one of the first configurations of the Nigerian deregulated power networks and its CEEDP has not been adequately considered [3].

## II. METHODOLOGY

### A. Particle Swarm Optimization

Particle swarm optimization, an organically motivated, community-based optimization method, was advanced and developed in 1995 by Kennedy and Eberhart [5,21]. The social behavior of birds thronging for food sets up the foundation for PSO. During birds' hunt for food, all bird tells one another the best food source it has discovered. Each bird then modifies its pathway in line with its best position and the group's best position.

In PSO, a separate bird is a particle having its own position and velocity in an n-dimensional search area, representing the position and velocity of a particle, respectively, with *x* and *y*. The *x* stands for the objective variable in the optimization. The velocity, *y*, denotes the step size the particle will move in subsequent iterations [22,23].

The position and velocity of ath particle are represented in n-dimensional search area as:

$$x_a = \left(x_{a1}, x_{a2}, \cdots, x_{an}\right) \tag{1}$$

$$y_a = \left(y_{a1}, y_{a2}, \ldots, y_{an}\right) \tag{2}$$

Each particle keeps a recollection of the present prime position discovered all the while and the present prime position established by all of the particles in the group denoted as *pbest* and *gbest* respectively in the n-dimensional search space and are given as follows:

$$pbest_a = \left(pbset_{a1}, pbest_{a2}, \ldots, pbest_{an}\right) \tag{3}$$

$$gbest_a = \left(gbset_{a1}, gbest_{a2}, \ldots, gbest_{an}\right) \tag{4}$$

The velocity of the ath particle is updated using the following equations:

$$y_{an}^{j} = wy_{an}^{j} + c_1 r_1 \left(pbest_{an}^{j} - x_{an}^{j}\right) + c_2 r_2 \left(gbest_{n}^{j} - x_{an}^{j}\right) \tag{5}$$

The position is updated by the following equation:

$$x_{an}^{j+1} = x_{an}^{j} + y_{an}^{j+1} \tag{6}$$

where,

$y_{an}^{j+1}$ = updated velocity of ath particle in n-dimensional space;

$w$ = inertial weight factor;

$y_{an}^{j}$ = velocity of ath particle at jth iteration;

$c_1, c_2$ = acceleration coefficients;

$r_1, r_2$ = random numbers [0,1];

$x_{an}^{j+1}$ = particle updated position for ath particle in n-dimensional space; and

$x_{an}^{j}$ = position of ath particle at iteration j.

Inertial weight factor helps in boosting the convergence rate of PSO algorithm speed based on descending linear function. Inertial weight factor is found using (7). The standard practice allocates the range between 0.4 ($w_{min}$) and 0.9 ($w_{max}$) [5].

$$\varphi = \varphi_{max} - \left(\frac{\varphi_{max} - \varphi_{min}}{iter_{max}}\right) iter \tag{7}$$

where,

$\phi_{min}$ = minimum value of weighting factor;

$\phi_{max}$ = maximum value of weighting factor;

iter = current iteration; and

$iter_{max}$ = maximum number of iterations.

Figure 1 shows PSO algorithm flowchart. It highlighted steps in solving optimization problems using PSO.

### B. Bat Algorithm Optimization

Bat algorithm is an environment-inspired optimization technique that uses the echolocation behaviors of real bats and was introduced by Xin-She Yang in 2010 [24]. Bats were observed to be the only mammal with wings and are classified as microbats and megabats. The major difference between the classification is that microbats use echolocation [25]. Echolocation is a type of sound navigation and ranging (SONAR) technique that microbats use to locate their roosting crevices in the dark, avoid obstacles, and detect prey [7].

Echolocation of bats is a perceptual system where a series of loud ultrasound waves are sent out by bats to create echoes in their environment while the bats listen to the echoes. The position of food/prey is identified by bats based on the returned echoes with delays

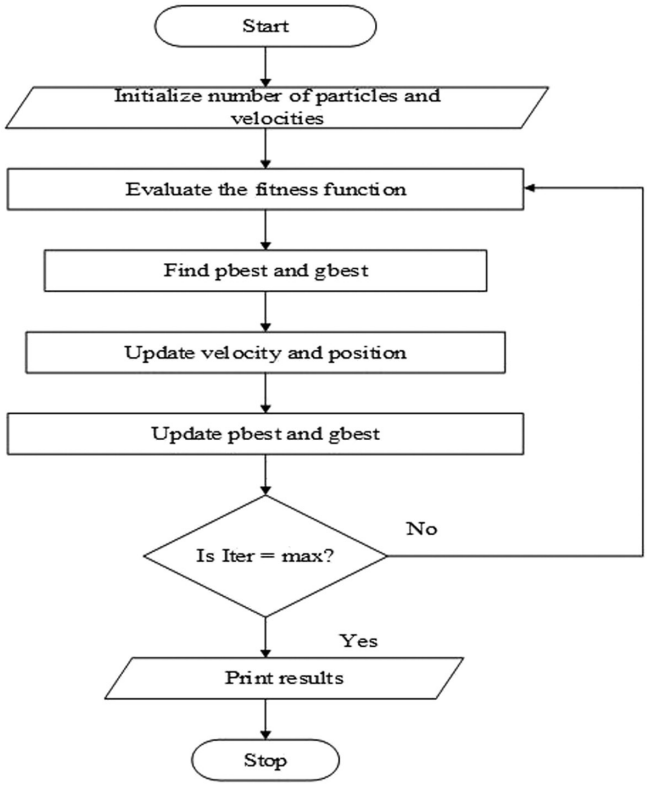


**Fig. 1.** Flowchart of particle swarm optimization algorithm.

and variations in sound levels [26,27]. The following assumptions were made to simplify the problem of BA [28]:

(i) Every microbat employs echolocation to decide distance and differentiate between food/prey and roadblock.
(ii) Individual microbat flies haphazardly with its own velocity and position having a constant frequency, different wavelength, and loudness to track prey.
(iii) Every microbat can modify, automatically, its wavelength or frequency of its discharged pulses. The pulse emission rate is modified depending on its closeness to its target.
(iv) Loudness is assumed to vary from maximum to minimum constant value.

Bat algorithm mimics the behavior of bats when they are hunting for food. Frequency-modulated signals are used by bats for distance perception. Each signal pulse can last little thousands of seconds (8–10 ms) within 25–100 kHz frequency range. The bats typically emit 10–20 of such pulses in a second. When bats are stalking, they can discharge over 200 pulses in a second [28]. For every idealized bat, the pulse frequency, velocity, and position at a particular time t are defined as follows [7]:

$$f_a = f_{\min} + \beta\left(f_{\max} - f_{\min}\right) \tag{8}$$

$$y_a^{t+1} = y_a^t + (x_a^t + x_{best}^t) f_a \tag{9}$$

$$x_a^t = x_a^t + v_a^{t+1} \tag{10}$$

where,

$f_{\min}$ = emitted pulse minimum frequency;

$f_{\max}$ = emitted pulse maximum frequency;

$\beta$ = a uniformly dispensed haphazard number between [0, 1];

$f_a$ = ath bat frequency;

$x_{best}^t$ = current foremost position at the time step t in the present population;

$t$ = current iteration number;

$y_a^t$ = velocity of ath bat;

$x_a^t$ = position of the ath bat.

Local random work is then used to execute a new search as follows:

$$x_{a(new)}^{t+1} = x_{best}^t + \xi A^t \tag{11}$$

where,

$\xi$ = uniformly distributed random number = $\xi\epsilon$niformly

$A^t$ = average loudness at time step $t$.

After the bats have succeeded in identifying prey, their loudness will be reduced and the pulse discharge rate will be shooting up. These features are described mathematically as follows:

$$A_a^{t+1} = \alpha A_a^t \tag{12}$$

$$r_a^{t+1} = r_a^0(1 - \exp(-\varphi t)) \tag{13}$$

where,

$r_a^0$ = initial emission pulse rate'

$\alpha$ = constant in the range of [0, 1]; and

$\phi$ and tant in the ran.

The step-by-step solution algorithm for optimization problems using BA is shown in Fig. 2.

**C. Development of Hybrid-Particle Swarm-Bat Algorithm Optimization technique**

Hybrid optimization method, H-PS-BA, was formulated and modeled in this work, and the developed H-PS-BA optimization technique was an embedded type hybrid algorithm that increases the diversity and avoids premature convergence by enhancing the PSO ability for local

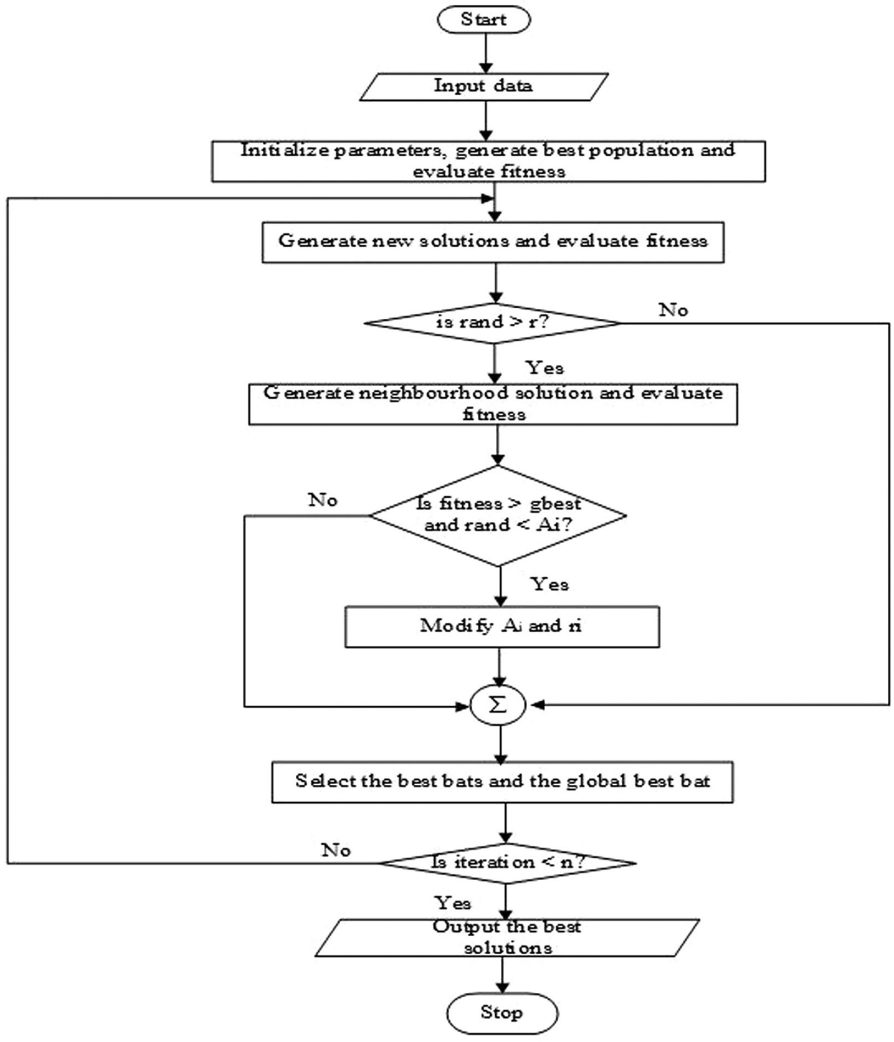


**Fig. 2.** Flowchart of bat algorithm.

search using the frequency tuning techniques of BA at the velocity updating stage of PSO algorithm. The algorithm combined the speedy convergence ability of PSO with the potential of BA to avoid local optimum.

Each microbat, for the original BA, sends out a pulse with a frequency value, $f_{min}$, and variable wavelength as represented in (8) above. In the developed H-PS-BA, two different pulses were assumed to be sent out by each bat in two separate directions, one toward the best bat (solution) and the other toward an erratically chosen bat. The frequencies of these introduced pulses were updated in equations (14) and (15) respectively in the direction of bat and in the direction of random bat.

$$f_{a1} = f_{\min} + \left(f_{\max} - f_{\min}\right) * \beta_{a1}. \quad (14)$$

$$f_{a2} = f_{\min} + \left(f_{\max} - f_{\min}\right) * \beta_{a2}. \quad (15)$$

where,

$f_{a1}$ = emission in the direction of best bat;

$f_{a2}$ = emission in the direction of random bat;

$f_{min}$ = minimum frequency;

$f_{max}$ = maximum frequency; and

$\beta_{a1}$ and $\beta_{a2}$ = random vectors between 0 and 1.

The velocity and position update equations of PSO given in (5) and (6) are given in (16) and (17), respectively:

$$y_{an}^{j+1} = w y_{an}^{j} + c_1 r_1 \left(pbest_{an}^{j} - x_{in}^{j}\right) + c_2 r_2 \left(gbest_{n}^{j} - x_{an}^{j}\right). \quad (16)$$

$$x_{an}^{j+1} = x_{an}^{j} + y_{an}^{j+1}. \quad (17)$$

where,

$y_{an}^{j+1}$ = updated velocity of ath particle in n-dimensional space;

$\Phi$ = inertial weight factor;

$y_{an}^{j}$ = velocity of ath particle at jth iteration;

$c_1, c_2$ = acceleration coefficients;

$r_1, r_2$ = random numbers [0,1];

$x_{an}^{j+1}$ = updated position of jth particle in n-dimensional space; and

$x_{an}^{j}$ = position of ath particle at iteration j.

Equation (16) is modified by introducing the Cartesian distance linking the bat position and local best position into the cognitive component of the equation and the Cartesian distance linking the best position and global position into the social component of the equation. The modification was formulated as follows:

Let $x_a$ = bat position

$Pbest_a$ = local best position

The Cartesian interval between the bat position $x_a$ and the local best position $pbest_a$ is given in (18):

$$PBEST_a = \sqrt{\sum_{k=1}^{N} \left(Pbest_a - x_a\right)^2} \tag{18}$$

where,

$PBEST$ = Cartesian interval between bat position and local best position;

$Pbest_a$ = local best position;

$X_a$ = bat position; and

$N$ = number of bats

Let $x_a$ = bat position

$Gbest_a$ = global best position

The Cartesian interval between the bat position and the global best position is given in (19):

$$GBEST = \sqrt{\sum_{k=1}^{N} \left(gbset_a - x_a\right)^2} \tag{19}$$

where,

$GBEST$ = Cartesian interval between bat position and local best position;

$Gbest_a$ = global best position;

$X_a$ = bat position; and

$N$ = number of bats.

The new velocity equation is given in (18).

$$y_a^{k+1} = w * y_a^k + \left(c_1 * \exp\left(-PBEST_a^2\right) * \left(pbest_a^k - x_a^k\right)\right) + \left(c2 * \exp\left(GBEST^2\right) * \left(gbest^k - x_a^k\right)\right). \tag{20}$$

Equation (20) ensures the removal of randomness in the velocity update and local and global bests were allowed to guide velocity and position updates. The H-PS-BA was finally developed by associating the pulse frequency of BA with the velocity update equation of PSO as given in (21) thereby ensuring the PSO ability to evade being trapped at local optimum.

$$y_a^{k+1} = w * y_a^k + \left(c_1 * \exp\left(-PBEST_a^2\right) * \left(pbest_a^k - x_a^k\right)\right) * f_{a1} + \left(c2 * \exp\left(GBEST^2\right) * \left(gbest^k - x_a^k\right)\right) * f_{a2}. \tag{21}$$

**D. Combine Economic Emission Dispatch Problem**

Thermal generator operation turns out various contaminants such as nitrogen oxide, sulfur oxide, and carbon oxide, released into the atmosphere. It is paramount to abate the production of contaminants by generators. This objective is realized by incorporating pollutant emissions reduction as an objective function [23].

The CEED problem's main goal is the simultaneous curtailment of the total fuel cost and amount of emission of generation in a power system. The objective function of CEEDP was modeled as follows [29]:

$$F_{total\,cost} = \sum_{i=1}^{N_g} \left[\left(a_i + b_i P_i + c_i P_i^2\right) + \left|e_i \sin\left(f_i\left(P_{i,\min} - P_i\right)\right)\right|\right] + h_i\left[\left(\alpha_i + \beta_i P_i + \gamma_i P_i^2\right) + \theta_i \exp\left(\delta_i P_i\right)\right] \tag{22}$$

Subject to:

$$\sum_{i=1}^{N_g} P_i = P_G = P_D + P_L \tag{23}$$

$$P_i^{\min} \le P_i \le P_i^{\max} \quad i = 1,2,...Ng \tag{24}$$

where,

$F_{total}$ = total fuel cost;

$F_i\,(P_i)$ = ith generating unit fuel cost;

$a_i, b_i, c_i$ = cost function coefficients function for generator i;

$P_i$ = output power of unit i;

$N_g$ = number of generators;

$E_{total}$ = total emission;

$E_i(P_i)$ = emission cost of ith generator;

$\alpha_i, \beta_i, \gamma_i$ = emission coefficients for generator i;

$P_D$ = total power demand of the system;

$P_G$ = total power generation of the system;

$P_L$ = total transmission loss of the system;

$P_i^{\min}$ = minimum power limit;

$P_i^{\max}$ = maximum power limit.

$$P_{\text{Loss}} = \sum_{i=1}^{N_g}\sum_{j=1}^{N_g} P_i M_{ij} P_j + \sum_{i=1}^{N_g} M_{oi} + M_{oo} \quad (25)$$

where,

$P_i$ = active power for ith generation unit;

$P_j$ = active power for jth generation unit;

$M_{00}$, $M_{ij}$, $M_{oi}$ = loss coefficient constant;

$F_{totalcost}$ = CEED's total fuel cost.

$$h_i = \frac{F_i(P_{i,\min})}{E_i(P_{i,\max})} = \frac{a_i + b_i P_{i,\min} + c_i P_{i,\min}^2 + e_i \sin\left(f_i\left(P_{i,\min} - P_i\right)\right)}{a_i + b_i P_{i,\max} + c_i P_{i,\max}^2 + \theta_i \exp\left(\delta_i P_i\right)} \quad (26)$$

The $h_i$ factor (price penalty factor) is utilized to harmonize emission costs and normal fuel costs [29]. The $h_i$ factor moves the definition of emission criterion, physically, from the weight of emission to cost of fuel for emission [29]:

The H-PS-BA optimization solution algorithm for CEED of power systems is given as follows:

Step 1: initialize parameters of PSO. Read power system data. The CEED dimension is the number of participating generators. The particles are generated between $P_{max}$ and $P_{min}$ haphazardly. The ith particle, for N number of units, is defined as:

$$P_i = \left[P_{i1}, P_{i2}, P_{i3}, \ldots, P_{iNg}\right]. \quad (27)$$

Step 2: generate initial velocities of the particles haphazardly in the following span:

$$\left[-y_i^{\max}, y_i^{\max}\right]. \quad (28)$$

Step 3: the objective function values of the particles are determined utilizing CEED objective function. Set the evaluated values as $P_{best}$.

Step 4: choose the best value among the $P_{best}$ as the $G_{best}$.

Step 5: calculate new velocities for all the dimensions in all particles using the hybridized velocity updating equations.

Step 6: check for constraints infringements on the lowest and highest values of the velocities.

$$\text{if } y_i^{new} > y_i^{\max}. \quad (29)$$

$$y_i^{new} = y_i^{\max}. \quad (30)$$

and

$$\text{if } y_i^{new} < y_i^{\min}. \quad (31)$$

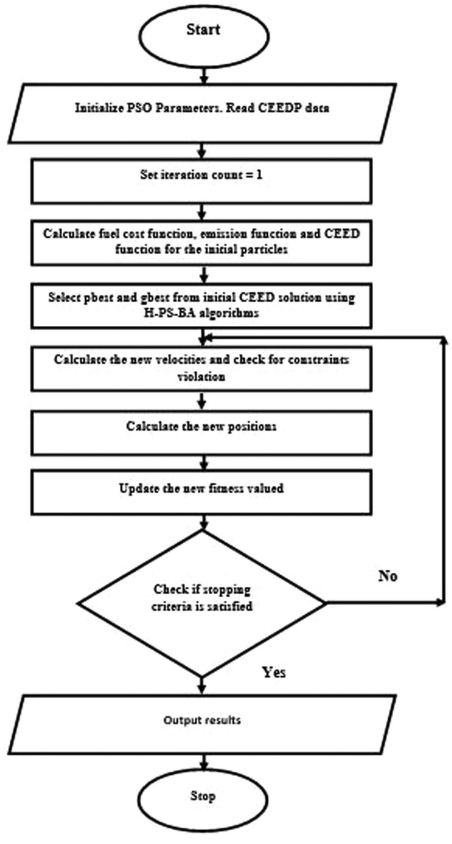


**Fig. 3.** Flowchart of H-PS-BA for CEEDP. H-PS-BA, hybrid-particle swarm-bat algorithm; CEEDP, combined economic emission dispatch problem.

$$y_i^{new} = y_i^{\min}. \quad (32)$$

Step 7: generator position in the particles is upgraded using (33):

$$P_i^{new} = P_i + y_i^{new}. \quad (33)$$

Step 8: determine, for the updated positions of particles, the objective function values. If the new value is superior to the previous $P_{best}$, the new value is set to $P_{best}$.

Step 9: $G_{best}$ for the population is updated.

Step 10: step 4 to step 10 is repeated until the maximum number of iterations

The step-by-step solution algorithm of CEEDP optimization solution using H-PS-BA is shown in Fig. 3.

## III. RESULTS AND DISCUSSION

The 28 bus 330 kV Nigerian network interconnects four thermal stations and three hydro stations to different load stations. Data for the network were acquired from National Control Center (NCC). The single-line diagram and generator data for the system are shown in Fig. 4 and Table I respectively. The shares of the hydro-generators in the total load demand of the network were taken to be fixed, while the shares of the thermal generators were evaluated [30]. The CEEDP solution was carried out using H-PS-BA optimization technique and conventional PSO to evaluate the whole generation cost of the system. The H-PS-BA and PSO techniques were subjected to same settings of parameters and data sets to allow result comparisons. The

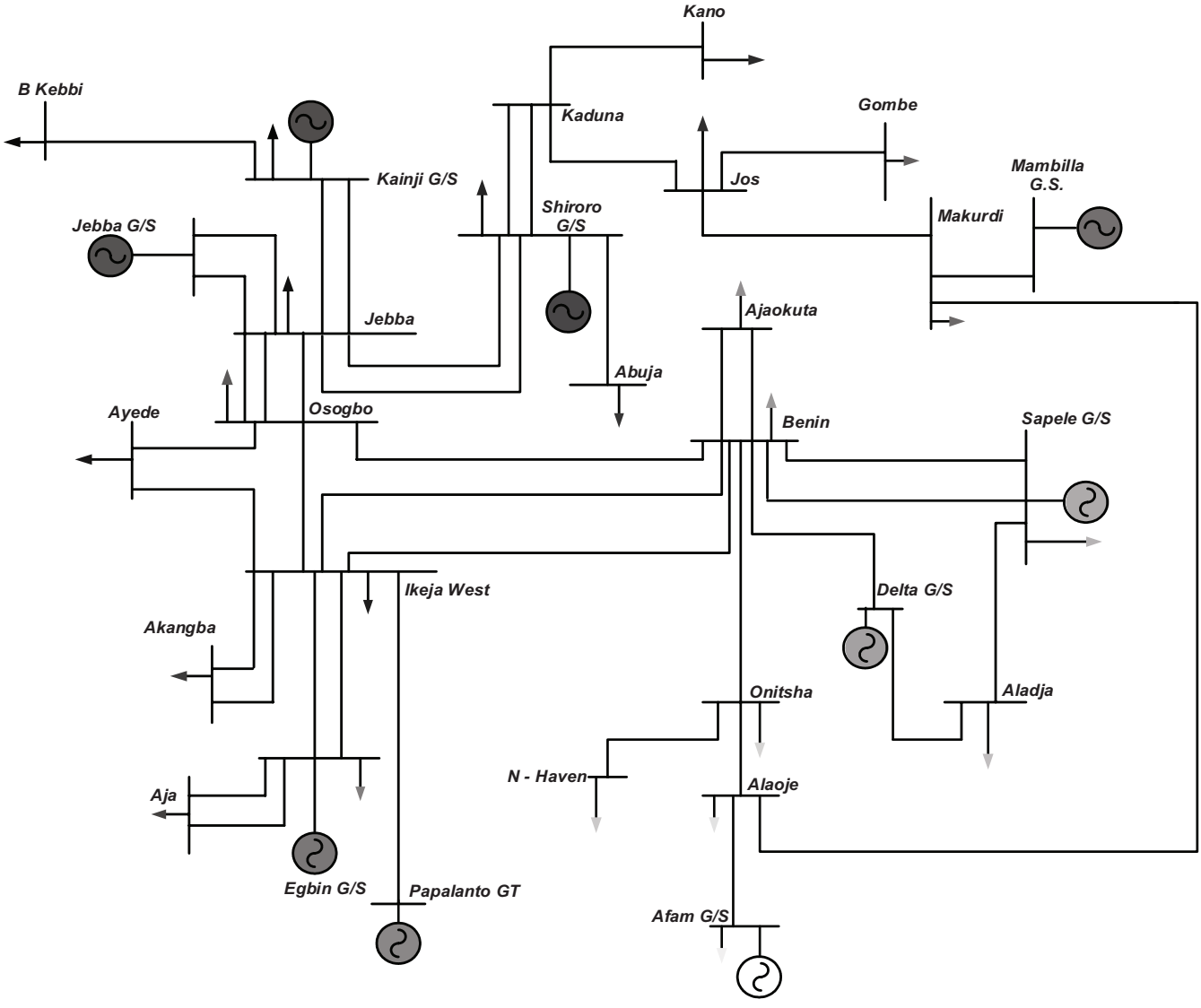


**Fig. 4.** Single line diagram of Nigerian 28 Bus 7 generator system.

**TABLE I.**
GENERATOR DATA FOR THE NIGERIAN 28 BUS 7 GENERATOR POWER SYSTEM

| Unit | $P_{min}$ (MW) | $P_{max}$ (MW) | a ($/h) | b ($/MWh) | c ($/(MW)²h) | d (($/h) | e (rad/MW) | α (lb/h) | β (lb/MWh) | γ (lb/(MW)²h) | μ (lb/h) | δ (1/MW) |
|---|---|---|---|---|---|---|---|---|---|---|---|---|
| SAPELE | 137.5 | 550 | 0.1300 | 7.84 | 6929 | 0.00419 | 0.32767 | 13.8593 | 600 | 0.052 | 0.25475 | 0.01234 |
| DELTA | 75 | 300 | 1.2000 | 6.13 | 525.74 | 0.00419 | 0.32767 | 13.8593 | 260 | 0.028 | 0.25475 | 0.01234 |
| AFAM | 135 | 540 | 0.0920 | 56 | 1998 | 0.00683 | −0.54551 | 40.2669 | 450 | 0.084 | 0.24970 | 0.01200 |
| EGBIN | 275 | 1100 | 0.0310 | 13.10 | 12787 | 0.00683 | −0.54551 | 40.2669 | 850 | 0.094 | 0.24970 | 0.01200 |
| SHIRORO | 350 | 350 | 0.0130 | 6 | 29.23 | 0.00419 | 0.32767 | 13.8593 | 260 | 0.028 | 0.25475 | 0.01234 |
| KAINJI | 450 | 450 | 0.0012 | 5 | 28.74 | 0.00419 | 0.32767 | 13.8593 | 260 | 0.028 | 0.25475 | 0.01234 |
| JEBBA | 490 | 490 | 0.0011 | 3 | 93.36 | 0.00419 | 0.32767 | 13.8593 | 260 | 0.028 | 0.25475 | 0.01234 |

**TABLE II.**
PARAMETER SETTINGS

| S/No. | Parameters | Values |
|---|---|---|
| 1 | sws | 100 |
| 2 | mni | 1000 |
| 3 | $w_{min}$ | 0.4 |
| 4 | $w_{max}$ | 0.9 |
| 5 | $c_1$, $c_2$ | 2 |
| 6 | A’ | 0.9 |
| 7 | r | 0.1 |
| 8 | $Q_{min}$ | 0 |
| 10 | $Q_{max}$ | 2 |

parameter settings for the optimization techniques are shown in Table II.

The developed H-PS-BA optimization based on the CEEDP modeling was simulated using MATrix LABoratory (MATLAB 2018a) software. An HP EliteBook Revolve 810 G1 model, Intel (R) Core i5 HP Computer Laptop with a RAM of 4 GB and a speed of 1.90 GHz, was used for simulation run. The performance metric used in this work was the overall CEEDP cost of the system in $/h. This is the overall optimized cost of electricity generation by reducing total fuel cost and total emission charges concurrently and keeping load demand and other system equality and inequality constraints satisfied.

The results of real power allocations, economic and emission dispatches, and the CEED of the Nigerian system are shown in Table III. From the table, the real power distribution on each bus by each method is shown. The total power distribution for each optimization technique is the sum of power allocated and the loss generated. The H-PS-BA gave a system total loss higher than that of PSO by 0.22%. Increase in the loss is combined with the total energy generated by the system which in turn adds up to total cost of generation.

The table also revealed that total fuel cost of generation for economic dispatch was 109 740 $/h for PSO and 109 700 $/h for H-PS-BA optimization technique. This result showed that H-PS-BA optimization technique gave a lesser cost of fuel than PSO. Hybrid-particle swarm-bat algorithm performed better than PSO by 0.036 %. For emission dispatch, PSO gave emission output of 6255.9 kg/h, while for H-PS-BA optimization technique, the amount of total system emission was 6246.6 kg/h. Hybrid-particle swarm-bat algorithm optimization technique produced a reduced amount of emission when compared to the amount of emission produced by PSO. The H-PS-BA optimization technique performed better than PSO by 0.15 %.

The solution to the CEEDP gave a total CEED cost of 176 520 $/h and 176 390 $/h for using PSO and H-PS-BA optimization technique, respectively. The H-PS-BA gave a total overall generation cost that

**TABLE III.**
ECONOMIC DISPATCH, EMISSION DISPATCH, AND CEED OF NIGERIAN 28-BUS 7-GENERATOR SYSTEM FOR A DEMAND OF 2823.1 MW

| Generating Unit | PSO | H-PS-BA |
|---|---|---|
| SAPELE (MW) | 450.4634 | 439.5794 |
| DELTA (MW) | 75.0000 | 75.0000 |
| AFAM (MW) | 392.7547 | 382.4571 |
| EGBIN (MW) | 654.7837 | 676.0545 |
| SHIRORO (MW) | 350.0000 | 350.0000 |
| KAINJI (MW) | 450.0000 | 450.0000 |
| JEBBA (MW) | 490.0000 | 490.0000 |
| Loss (MW) | 39.9018 | 39.9910 |
| Total generation (MW) | 2863.0910 | 2863.0018 |
| **Fuel cost ($/h)** | **109 740** | **109 700** |
| **Emission (kg/h)** | **6255.9** | **6246.6** |
| **CEED ($/h)** | **176 520** | **176 390** |

CEED, combined economic emission dispatch; PSO, particle swarm optimization; H-PS-BA, hybrid-particle swarm-bat algorithm.

is lesser than what was obtained for using PSO. This result showed that H-PS-BA optimization technique performed better than PSO by 0.07%.

The convergence characteristic curve for the CEED of the Nigerian power system considered is given in Fig. 5. It can be remarked from the figure that the developed H-PS-BA optimization technique performed better than PSO with reference to minimizing the objective function of CEEDP of the system by converging to a lower generation cost than that of PSO.

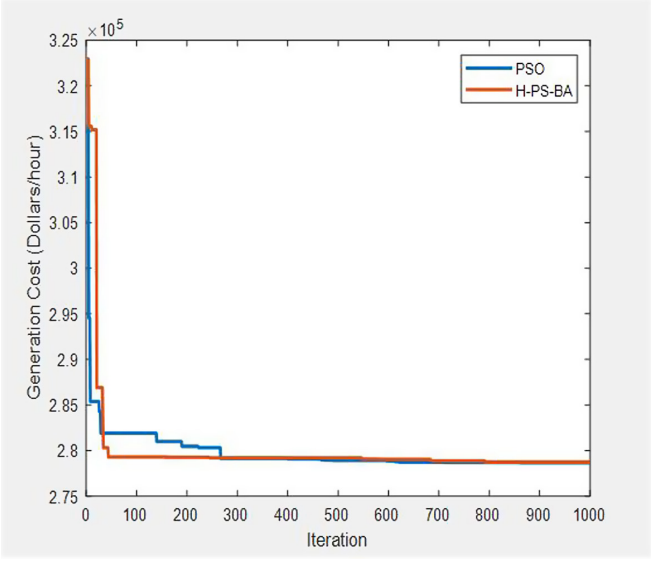


**Fig. 5.** Convergence characteristics of PSO and H-PS-BA for Nigerian 28-Bus 7-Generator Power System. PSO, particle swarm optimization; H-PS-BA, hybrid-particle swarm-bat algorithm.

## IV. CONCLUSION

This work developed an embedded type hybrid optimization technique, H-PS-BA optimization technique, that increased the diversity and avoid premature convergence of PSO. The H-PS-BA was employed to solve a paramount optimization problem in power system, the CEEDP, that needed to be solved accurately. The developed optimization technique was applied to solve CEEDP of Nigerian system. Results of the application were compared with the result obtained from using conventional PSO and it was shown that H-PS-BA gave a better performance than PSO by generating the lowest overall cost of generation. The H-PS-BA optimization technique was therefore concluded to be a better and more efficient optimization tool in solving mathematical optimization problems.

**Peer-review:** Externally peer-reviewed.

**Declaration of Interests:** The authors have no conflict of interest to declare.

**Funding:** The authors declared that this study has received no financial support.

## REFERENCES

1. M. A. Tijani, G. A. Adepoju, K. A. Hamzat, and M. A. Sanusi. *A Review of Optimization Approach to Power Flow Tracing in a Deregulated Power System*," *Arid Zone J. Eng. Technol. Environ.*, vol. 15, no. 2, pp. 435-448, 2019.
2. S. Frank, I. Steponavice, and S. Robenack, "Optimal power flow: A bibliographic survey I, formulations and deterministic methods," *Energy Syst.*, vol. 3, no. 3, pp. 221-258, 2012. [CrossRef]
3. M. A. Tijani, G. A. Adepoju, and M. O. Okelola, "Optimization approaches to generation dispatch: Review of Nigerian power system, " *Niger. J. Technol. Dev.*, vol. 19, no. 2, pp. 156–163. [CrossRef]
4. D. Rahul, G. Nikita, and S. Harsha, "Economic load dispatch problem and MATLAB programming of different methods," in International Conference of Advanced Research and Innovation (ICARI – 2014), 2014, Delhi, India, pp. 202-207.
5. M. Ellahi, G. Abbass, G. B. Satrya, M. R. Usman, and J. Gu, "A modified hybrid particle swarm optimization with bat algorithm parameter inspired acceleration coefficients for solving eco-friendly and economic dispatch problems," *IEEE Access*, vol. 9, pp. 82169-82187, 2021. [CrossRef]
6. O. O. Ade-Ikuesan, O. E. Olabode, I. K. Okakwu, and M. O. Okelola, "Sate-of-the-art approach to economic load dispatch of Nigerian hydrothermal electric power system: A review, " *J. Sci. Technol. Research*, vol. 1, no. 2, pp. 87-99, 2019.
7. W. Ruta, M. Saulo, and N. Odero, "Emission constrained economic dispatch using moth flame optimization and bat hybrid algorithm," *Int. J. Eng. Res. Technol.*, vol. 11, pp. 827-843, 2018.
8. M. Lin, J. Tsai, and C. Yu, "A review of deterministic optimization methods in engineering and management," *Math. Methods Eng.*, vol. 2012, pp. 1-15, 2012. [CrossRef]
9. M. A. Tawhid, and K. B. Dsouza, "Hybrid binary bat enhanced particle swarm optimization algorithm for solving feature selection problems," *Appl. Comput. Inf.*, vol. 16, pp.117-136, 2020.

10. D. Santra A. Modal, and A. Mukherjee, "Study of Economic Load Dispatch by Various Hybrid Optimization Techniques," *Stud. Comp. Intell.*, vol. 611, pp. 37-74, 2016.
11. T. Pan, T. Dao, T. Nguyen, and S. Chu, "Hybrid particle swarm optimization with bat algorithm," Proceedings of the 8th International Conference on Genetic and Evolutionary Computing. Nanchang, China, pp. 37-47, 2015. [CrossRef]
12. Y. Lee, and M. Tuegeh, "An optimal solution for smooth and non-smooth cost functions-based economic dispatch problem," *Energies*, vol. 13, pp. 3721-3737, 2020.
13. U. Guveric, S. Duman, Y. Sonmez, H. Kahraman, and M. Dosoglu, "Symbiotic organism search algorithm for economic load dispatch problem with valve-point effect," *Sci. Iran. D*, vol. 25, pp. 3490-3506, 2018.
14. Y. Wu, B. Zhao, and L.Liu, "Solving economic load dispatch problem with valve-point effect using mean guiding differential evolution," IECON 2017 – 43rd Annual Conference of the IEEE Industrial Electronics Society, Beijing, China, pp. 434-439.
15. M. Ellahi, and G. Abbass, "A hybrid metaheuristic approach for the solution of renewables incorporated economic dispatch problem," *IEE Access*, vol. 8, pp. 127608-127621, 2020. [CrossRef]
16. S. Arunachalam, R. Saranya, and N. Sanjeetha, "'Hybrid Artificial Bee Colony Algorithm and Simulated Annealing for Combined Economic and Emission Dispatching Including Valve-Point Effect', SEMCO2013 Part 1," *LNCS*, pp. 354-365, 2013.
17. Y. A. Gherbi, H. Bouzeboudja, and F. Lakdja, "Hybrid metaheuristic for the combined economic emission dispatch problem," 12th International Symposium on Programming and Systems. Algiers, 2015, pp. 1-7.
18. X. Ling, "Economic-environmental dispatch based on multi-objective quantum-behaved particle swarm optimization," 5th International Conference on Computer Aided Design, Manufacturing, Modeling and Simulation, 2017, Busan, South Korea, pp. 1-4.
19. M. N. Abdullah, G. Y. Sim, A. Azmi, and S. H. Shamsudin, "Combined economic and emission dispatch solution using artificial bee colony algorithm with fuzzy approach, " *Int. J. Eng. Technol.*, vol. 7, no. 3, pp. 46-51, 2018. [CrossRef]
20. S. Mehta, and H. Singh, "Solution to economic load dispatch with valve point loading effect using hybrid whale optimization algorithm, " *Int. J. Comput. Appl.*, vol. 180, no. 11, pp. 39-47, 2018. [CrossRef]
21. R. Al-Nahhal, A. F. Naiem, and Y. G. Hegazy, "Economic Load Dispatch Problem using Particle Swarm Optimization Technique considering Wind Power Penetration," International Conference on Smart Energy and Technologies. Porto, Portugal, Vol. 2019, 2019, pp. 1-6.
22. M. Neyestani, and M. M. Farsangi, "Optimization of the Economic Dispatch Problem by considering the Emission Dispatch using AMPSO," *Adv. Model. Anal.*, vol. 73, pp. 60-71, 2018.
23. M. N. Alam, "State of the art economic load dispatch of power system using particle swarm optimization," *Appl. Oper. Res. Solving Electr. Eng. Probl.*, vol. 2018, pp.1-15, 2018.
24. B. V. Kumar, and N. V. Srikanth, "Bat algorithm and firefly algorithm for improving dynamic stability of power systems using UPFC," *Int. J. Electr. Eng. Inform.*, vol. 8, no. 1, pp. 164–188, 2016. [CrossRef]
25. M. Mokhtarifard, H. Mokhtarifard, and S. Molaei, "Solution of reactive power dispatch of power system using bat search algorithm," *Int. J. Tech. Phys. Probl. Eng.*, vol. 7, no. 23, pp. 65-70, 2015.
26. V. H. Kumar, P. S. Varma, T. B. Kumar, and E. Sreelatha, "Economic and Emission Dispatch Problem Using Particle Swarm Optimization," *International Journal of Innovative Technology and Exploring Engineering*, vol. 8, pp. 939-944, 2019.
27. S. Vijayara, and R. K. Santhi, "Multi-area economic dispatch with GUPFC using improved bat algorithm," *Asian J. Appl. Sci.*, vol. 4, pp. 1217-1242, 2016.
28. B. R. Adarsh, T. Raghumatan, T. Jayabarathi, and X. Yang, "Economic dispatch using chaotic bat algorithm," *Energy*, vol. 96, pp. 666-675, 2016. [CrossRef]
29. S. Arunachalam, R. Saranya, and N. Sanjeetha, "'Hybrid Artificial Bee Colony Algorithm and Simulated Annealing for Combined Economic and Emission Dispatching Including Valve-Point Effect,' SEMCO2013 Part 1," *LNCS*, pp. 354-365, 2013.
30. A. O. Olakunle, and K. F. Folly, "'Economic Load Dispatch of Power System using Genetic Algorithms with Valve-Point Effect,' advances in Swarm and computational intelligence," *Lect. Notes Comput. Sci.*, vol. 9, pp. 276-284, 2015.

cigre Turkey

TEPES
TURKISH JOURNAL OF ELECTRICAL POWER AND ENERGY SYSTEMS

TEPES, Vol. 2, Issue. 2, 168-179, 2022 **DOI:** 10.5152/tepes.2022.22024

RESEARCH ARTICLE

# Modeling and Cost Optimization of an Islanded Virtual Power Plant: Case Study of Tunisia

**Ramia Ouederni, Bechir Bouaziz, Faouzi Bacha**

National Institute of Applied Sciences and Technology, Centre Urbain Nord, Tunis Cedex, Tunisia

**Cite this article as:** R. Ouederni, B. Bouaziz and F. Bacha, "Modeling and cost optimization of an islanded virtual power plant: Case study of tunisia," *Turk J Electr Power Energy Syst*, 2022; 2(2), 168-179.

## ABSTRACT

The renewable energy resources placed a crucial aspect in all residential, and industrial communities. In this article presents the optimal sizing for the design of virtual power plant (VPP) to plan, and operate the system proposed is a solution for Djerba Island in Tunisia also to determine the management over six different models as taking the factor cost, economics, and environment criteria, etc. An analysis is carried out by studying the potentials of wind energy, solar energy, water flow, and biomass, as well as collecting data from different sources. For the optimization of the virtual power plant, the HOMER Pro is the software utilize for help analyze an available data, also an economical utility form virtual power system project with a battery. The results showed that the best structure of virtual power plant among all feasible configurations, with a net present cost of the design proposed is 314.846 $, and a cost of energy (COE) produced are 0.4031$. We have obtained a good result to use the sources of the proposed system by providing a cleaner, and environmentally friendly environment for the communities by using renewable energies resources meeting the charge requirements as per Kyoto protocol.

**Index Terms—**Virtual power plant concept, cost of energy, optimal system design, economic and environmental optimization, HOMER Pro.

## I. INTRODUCTION

Nowadays, as renewable energy sources are developed, and the demand for them increases. At the end of their useful life, conventional power plants are expected to be replaced by renewable energy sources and cleaner technologies. While renewable energy is expected to grow incredibly in coming years, its absorption rate is very low compared to other non-renewable energy sources [1]. In addition, there is a need to integrate renewable energy technologies into hybrid power systems to improve power reliability and capacity and to effectively reduce fluctuation [2]. A many research paper on off-grid and on-grid hybrid energy system utilizing a variety of optimization and tool. In [3] has proposed an autonomous renewable hybrid system energy hydro/wind/solar/diesel/battery to supply the Persian Gulf islands utilizing Hybrid Energy Resource Optimization (HOMER) models. In [4], a hybrid solar/wind/diesel/battery energy system that is isolated from the grid was studied on HOMER for a local village called Perumal Kovilpathy, an off-grid solar/wind/hydro/battery hybrid energy system designed on HOMER to electrify the remote and hard-to-reach villages in India's Himalayan region has been suggested by [5]. In [6], a comparative study of off-grid and grid-connected solar/battery systems for a rural community in Rwanda was examined by using HOMER.

Electrical energy has become a basic requirement for people to live in both rural and urban places, and the request is urban and island areas, and the request is rising day by day [7]. The huge increase in the fossil fuel prices [8] and decreasing fossil fuel reserves have led to an energy emergency. Alternative renewable sources of energy are suggested to face this energy crisis and reduce harmful gas emissions. Yet, a single renewable energy source could not satisfy the energy demand of the meet the energy demands due to the uncertainty of production renewable energy sources. As a result, hybrid renewable energy systems, including a variety of sources such as solar, wind, biomass, hydro, and energy storage systems are being recommended [9]. Hybrid energy system can be developed to operate off-grid or grid-connected systems and can use Energy Storage System (ESS) [10].

To use the renewable energy sources efficiently, and economically, each component must be aggregated, and selected. To ensure

**Corresponding author:** Bechir Bouaziz, bechir.bouaziz@isimg.tn

**Received:** August 26, 2022
**Accepted:** September 29, 2022
**Publication Date:** October 21, 2022

minimum investment and full utilization of the virtual power plant, we have chosen sizing and optimization techniques. As a result, the system can operate in optimal conditions with the appropriate configuration. In these locations, renewable resource has been the best alternative source of electricity generation. The most recognize alternatives of electricity generation are hydroelectricity, wind plant, tidal plant, photovoltaic also the biomass [11].

This system configuration offers greater reliability, and down cost than single-feed system. However, sizing of the system components is an important factor in the technical and economic viability of the system [13].

Generally, virtual power plant uses a both operating modes: on-grid, and islanded (off-grid). In two operating modes, virtual power plants system has there are some implications for consumer, and power systems. In [14], a hybrid system supplies the energy from Wind Turbines (WT), PhotoVoltaic (PV), Tidal Turbines (TT), Hydraulic source (Hy), Biomass source (Bio), and battery. Fuel cells, and storage batteries store the excess energy generated by the generators and release it in the event of a power outage.

The HOMER program provides a robust frame for user to compare many different economic, and technological options. In addition, it is possible to account for numerous variations, and uncertainties in the input data. A HOMER simulates the energy systems performances at every time of the year and display the energy available supply patterns and life cycle costs.

During the optimization process, the program searched for different possible configuration, renewable resource sizes, and demand satisfactions, taking into account the constraints to reach the most economical state [15] [16].

In this paper proposes the optimal solution of virtual power system composed by PV,WT,TT,Hy,Bio, and battery using HOMER software.

This article is organized as follows: section II presents the HOMER software, section III presents a description of study area location, section IV presents the energy demand, resources, and metrological data of proposed community, section V includes the best model of VPP and its components, and section VI includes main component models of the VPP. The evaluation of the system includes the economic and environmental criteria presented in section VI and section VII demonstrates the results and discussion of the work. In the end, the conclusion is presented in section VIII.

**Main Points**

- The core capabilities of the HOMER software make it easier to evaluate any possible system configurations and more precise in simulation, optimization, and sensitivity analysis.
- This study presents a virtual power plant's (VPP) optimal design and comparative studies based on real data on the Djerba Island, Tunisia, of six models and how it can be beneficial to the island to adapt to the frequent disturbances.
- With proper planning and sizing, it is possible to provide electricity to the island community in Tunisia.
- The results showed that the best structure of VAA among all feasible configurations, with a net present cost of the system, is 314,846$ and the cost of energy produced is 0,4031$.

## II. HOMER SOFTWARE

A Hybrid Optimization of Multiple Electric Renewable (HOMER) software system simplified the assignment of designed on-grid and off-grid distributed generation (DG) systems for a variety of application.

In this study, the HOMER software was used for designing VPP. The HOMER is an optimization tool for VPP developed by National Renewable Energy Laboratory [5][6]. The basic functions of HOMER are imitative, optimization, and sensitivity analysis.

The HOMER Software helps in configuration of the suggested renewable electrical hybrid system, and leads to the answer to the following two questions:

- Which component makes sense including in the system design.
- You must use the quantity and size of every component.

A core capability from HOMER software helping with the evaluation them any possible system configuration, too more precisely in:

- *Simulation*: It attempts to create a feasible configuration for every possible combination you would like to take into consideration.
- *Optimization*: HOMER is an economical optimization model, allows to reduce fuel consumption. It's possible to define the criteria, so that you can see the best possible fits. Analog systems are classified also according to these criteria.
- *Sensibility testing*: It's a stage that models the effect of a variable on the control, e.g., the meteorological data, fuel cost, besides view the responses in the optimization virtual power plant.

The objective of using the HOMER function is to obtain a minimum net present value (NPC) is the present value of the system costs, e.g., of installing also operating all component over their lifetime less the current value of the components income he has been making money all his life. The cost includes capital cost, replacement cost, operation and maintenance cost, fuel cost, also network purchasing power costs. Revenue includes residual value and turnover of the network, in this case zero, because there is no connection to the network.

## III. LOCATION OF THE STUDY AREA

Figure 1 present the geographic position of the study area on a plan. The study zone is situated in the Djerba quarter of Medenine, Tunisia. Djerba is an island of the Mediterranean Sea region of 514 square kilometers (25 kilometers by 20 kilometers, with a coastline of 150 kilometers), located to the east of the east coast of Tunisia. It is the biggest island on the North African coast and is located southeast of the Gulf of Gabes, bordering the eastern coast; Djerba is the closest to the southern bay of Boughrara.

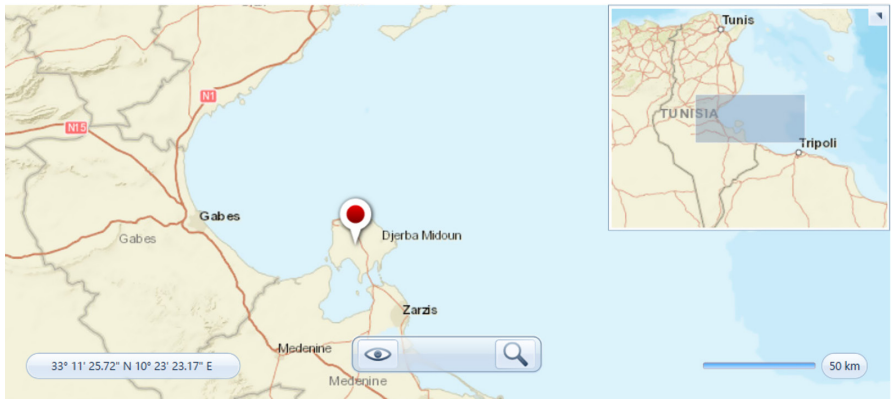


**Fig. 1.** Geographical location of the study area.

The island of Djerba, Tunisia, is chosen as the case study to assess and analyze the potential resource and the feasibility of a proposed VPP for the community while considering the cost factor, economics, environmental criteria, etc.

## IV. ENERGY DEMAND AND RESOURCES

### A. Load Profile Assessment

The monthly charge profiles for the suggested communities are calculated with the residential charge demands in mind. Fans and lights are basic devices for charge calculation. The loading is divided into two seasons: winter and summer. In the summer, the charge is high due to the weather. In contrast, winter loads are lower. The HOMER profiles for daily and seasonal profiles are shown in Figure 2, and the mean power is 6.9 kW.

### B. Resources and Meteorological Data

The power output of renewable energy sources depends primarily on meteorological data and the available resources in the project location area. The HOMER program processes those variables as inputs. The relationship of the output energy to the parameters is described in Section VI. Djerba Island parameters were taken from the NASA databases.

Figure 3(a) shows live global solar radiation; on the other hand, Djerba island as caught in Solar and obtained through HOMER

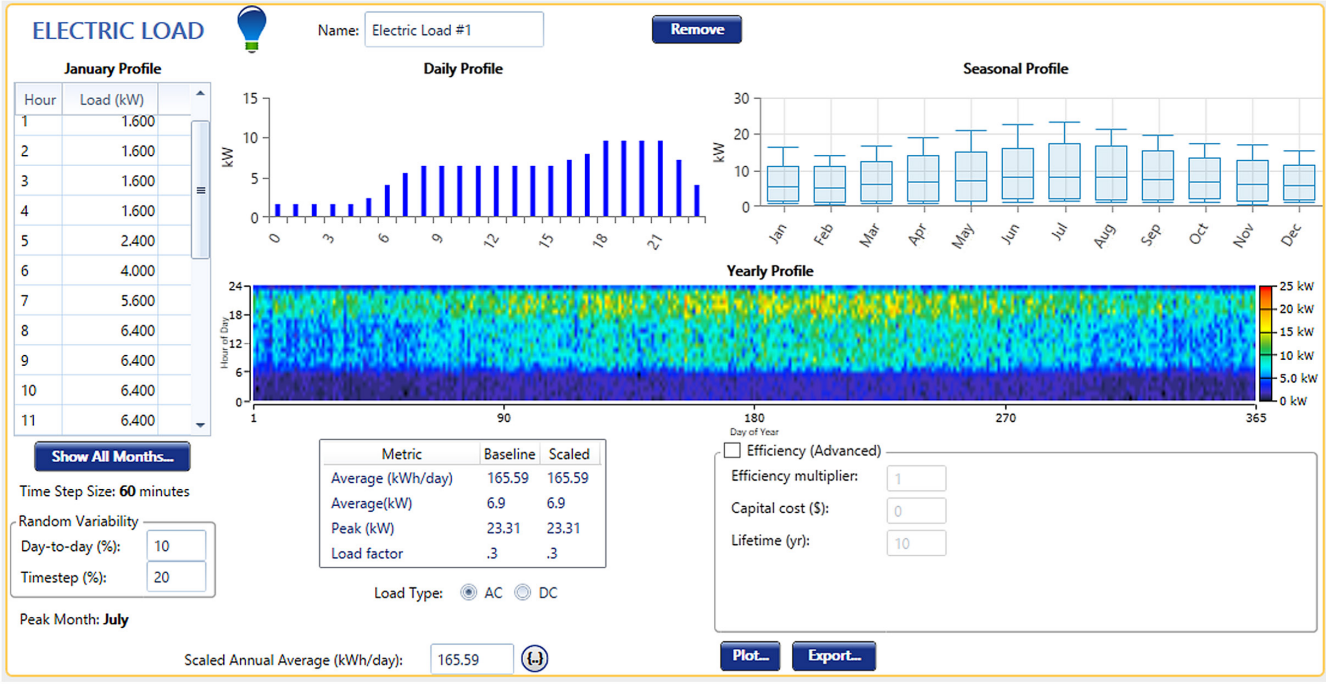


**Fig. 2.** Load profile.

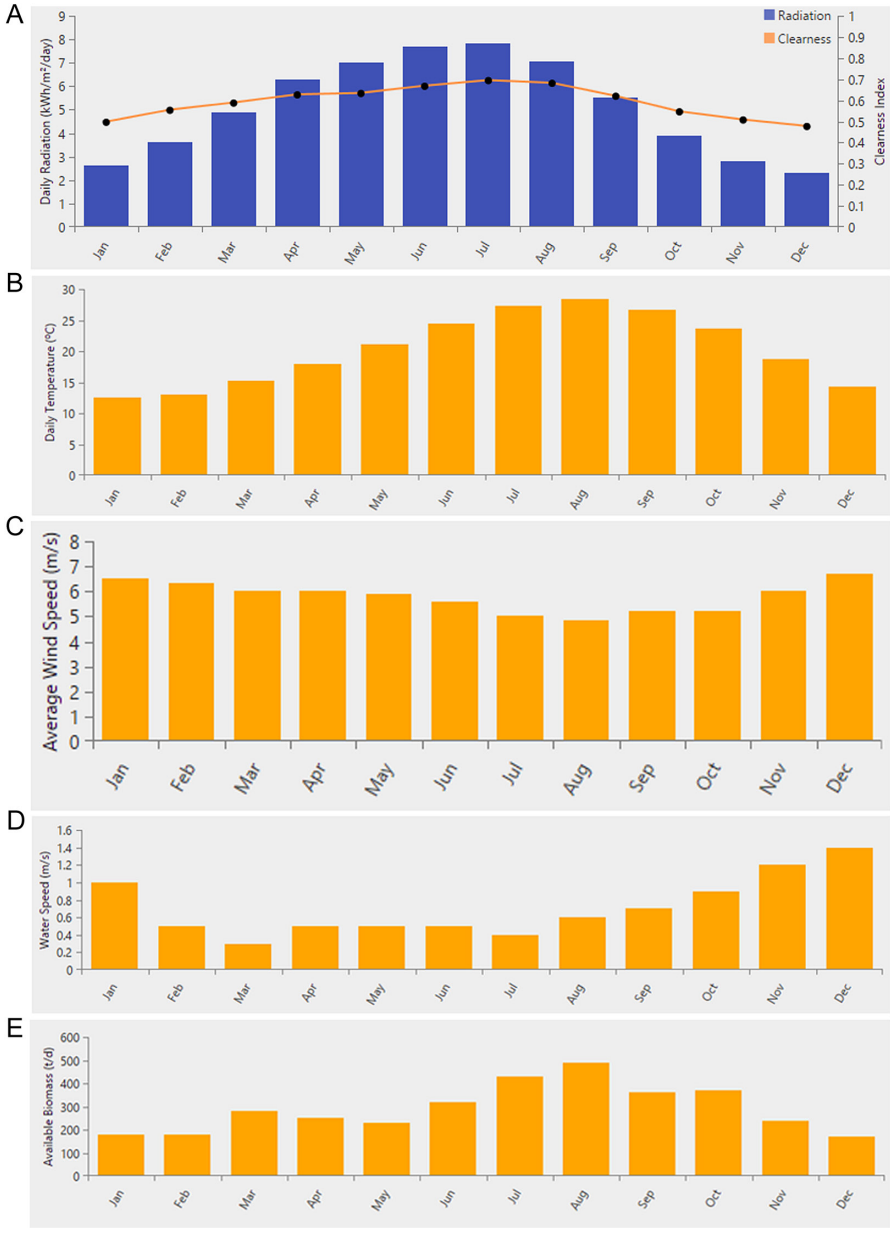


**Fig. 3.** Annual meteorological data of the Djerba Island: (a) daily irradiance; (b) daily temperature; (c) average wind speed; (d) water speed; (e) biomass resource.

software. The average solar access index was recorded at 0.6 and the average daily radiation was registered at 5.13 kWh/m$^2$/day with the mean temperature of about 21°C.

Figure 3 (b) shows the ambient daily temperature average. The mean yearly temperature was 23°C, with the top temperature in the summer from May through October and lowest temperatures in the winter. The hottest ambient temperature was recorded in August with a temperature of 28°C, while January was the coldest month with an ambient temperature of 12°C.

Figure 3(c) shows wind speed probability distribution and the average wind speed for this island was found to be 5.77 m/s. Also, the average tidal speed is 0.71 m/s as shown in Fig. 3(d). The available biomass resource for 1 year is 291.67 t/day in average value as shown in Fig. 3(e).

## V. ISLAND VIRTUAL POWER PLANT STRUCTURE

Figure 4 shows the available energy delivery options and diagrams the virtual power plant system on the island of Djerba in Tunisia. This system is composed of photovoltaic power plants, wind power plants, tidal power plants and hydro power plants are considered as a renewable energy source. The biogas producer is used for a backup power supply to be activated in case of inadequate generation, and a battery bank as a source of compensation generation, converters and controllers.

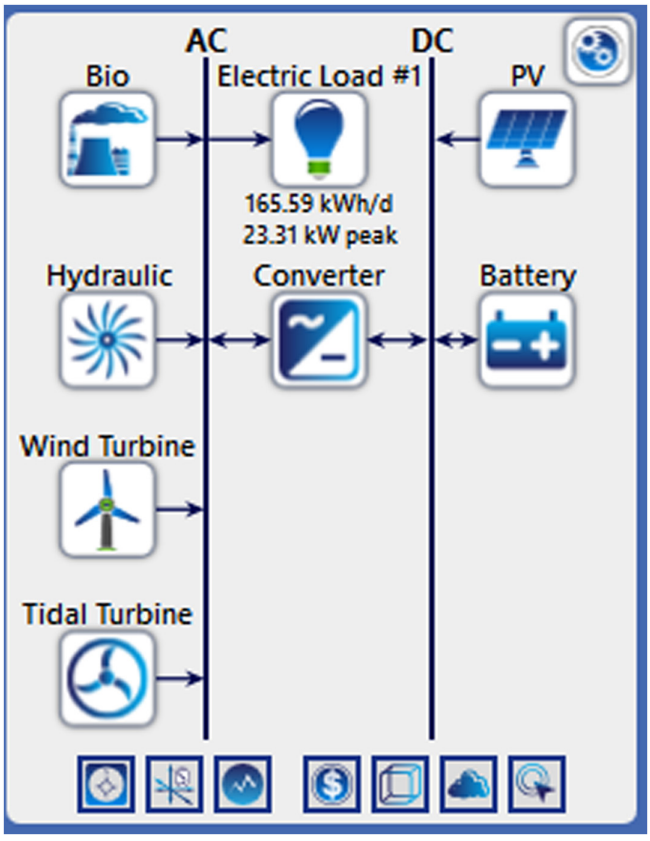


**Fig. 4.** Proposed scheme of an islanded virtual power plant in HOMER software model.

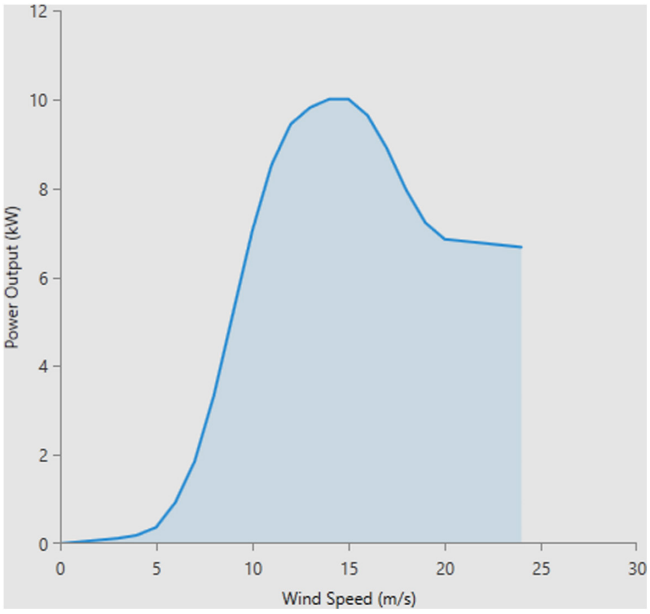


**Fig. 5.** The power curve of the generic 10 kW wind turbine.

**TABLE I.**
GENERIC 10 KW WIND TURBINE SPECIFICATIONS

| Wind Turbine | Value |
|---|---|
| Type | Generic 10 kW |
| Rated power | 100 kW |
| Startup. wind speed | 3 m/s |
| Rated wind speed | 12 m/s |
| Cut-out wind speed | 21 m/s |
| Tower height | 50 m |
| Rotor diameter | 22 m |
| Swept area | 2300 m² |

## VI. MAIN COMPONENTS OF THE ISLAND'S VIRTUAL POWER PLANT

The components of the energy optimization system involve hybrid modeling, in order to achieve its performance under various circumstances. The following mathematical model is used to demonstrate the proposed VPP system components:

### A. Windpower Plant Model

Figure 5 indicates the power graph of a generic 10 kW WT. The capital, exchange, maintenance with the life from the turbine is represented by 18 000 $, 18 000 $, 200 $/year, and 20 years, respective. The output power for the wind turbine is shown by equation (1) [3] [17]:

$$P_{wt} = \frac{1}{2}\rho_{wt} C_p R_{wt}^2 v_{wt}^3 \quad (1)$$

where $R$ is the blade radius, $\rho_{wt}$ is the density of the air, $C_p$ is the coefficient of power, and $v_{wt}$ stands for the speed of wind.

The pertinent details for the generic 10 kW wind turbine are presented in Table I.

### B. Photovoltaic Power Plant Model

The power produced by a photovoltaic module is proportional to the area of the semiconductor that is exposed to sunlight, the area of the photovoltaic module, the average temperature, and the properties of the photovoltaic cell under industry standard solar radiation test condition [18]. So, the generated power can be determined by (2):

$$P_{pv} = \eta_{pv} A_{pv} G_t \quad (2)$$

where $\eta_{pv}$ represents the rapid efficiency for the PV module table, $A_{pv}$ represents the position of the module used in this system, $G_t$ represents the total radiation. The photovoltaic panels are Trina Solar 300TSM-300PA14, with a lifespan of approximately 25 years, and the capital cost is 120 $/kW, the replacement cost is 120 $/kW, and the maintenance price is 10 $/kW/year.

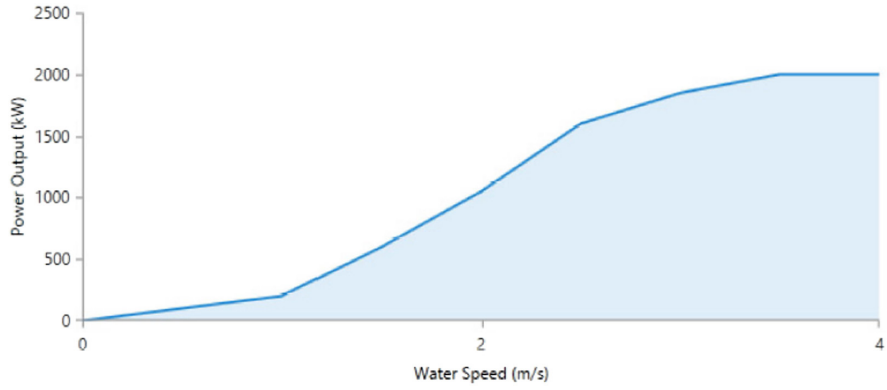


**Fig. 6.** The power curve of the AR2000 tidal turbine.

**C. Tidal power Plant Model**

The HOMER program offers various type of tidal turbine for use in Hydrokinetic, part of its component library. When selecting a Generic hydrokinetic 40kW tidal turbine, 4 cost parameters must be entered into the program, (a) capital (or installed cost and wire); (b) replacement cost; (c) maintenance cost; and (d) life span of the tidal turbine. For the purposes of this study, the following parameters were used: 14 000 $, 14 000 $ and 2700 $/year and 20 years, respectively. The power curve for the tidal turbine is shown in Figure 6. The output of the tidal turbine is represented by (3):

$$P_t = \frac{1}{2}\rho_t C_p \pi R_t^2 v_t^3 \quad (3)$$

Among them, $\rho_t$ represents the density of seawater, $R_t$ is the radius of the tidal current generator blades, $v_t$ is the tidal flow speed, and $C_p$ represents the coefficient of the power of the turbine, ranging approximately 0.35–0.5 [19].

The pertinent details for the Generic hydrokinetic 40kW tidal turbines are presented in Table II.

**TABLE II.**
TIDAL TURBINE SPECIFICATIONS

| Tidal Turbine | Value |
|---|---|
| Type | Generic hydrokinetic 40kW |
| Rated capacity | 40 kW |
| Manufacturer | SAE/GE |
| Cut-in tidal speed | 1 m/s |
| Cut-out tidal speed | 3.05 m/s |
| Operational tidal speed range | 1–4.5 m/s |
| Swept area | 314 m² |
| Rotor diameter | 20 m |

**D. Hydroelectric Power Plant Model**

The Generic 5 kW hydraulic pump component newly added in the HOMER components libraries was used to model the hybrid system for this purpose [20].

$$P_h = \rho_h g H Q \quad (4)$$

Where, is power capacity (5.494 kW),is water density (1000 kg/m$^3$), g is due acceleration at gravity (9.8 m/s$^2$), Q is the tip rate (0.0231 m$^3$/s), and H is effective gauge height through the turbine (m) is assumed by 80%. With a lifetime of approximately 25 years, it being noted that the capital cost is equal to 40 000 $/kW, and the replacement cost is 20 000 $/kW, and the maintenance and operation cost is 1200 $/kW/year.

**E. Biomass Resources**

Biomass is every organic material which can be convert to energies sources. It consists of materials of plant origins (agricultural residue, leave, and wood) and materials of animal origins (animals or humans wastes, soil organisms, animal carcass). In our case, the hotel wastes have been considered as the single biomass resources used for power generation. The input to the HOMER is the daily mean of the waste generation that could be utilized for biogas production. Based on survey conducted in the project area.

Biomass expressed as a net change in biomass, as biomass can change significantly over a specified period. The calculation is defined as [21]:

$$P_B = \frac{C_B \mathrm{h}_B m_B}{3.6} \quad (5)$$

Where, is the output power of biomass and is measured in kW. (in percentage) is the power conversion efficiency of biomass. The unit is the, and the unit is the kg/h.  is the heating value of a biomass measured by MJ/Kg.  In This study, a general-purpose biogas plant attached to an AC outlet.

HOMER considers the amount of the biogas generated when dimensioning the power plant. The capital costs, replacement costs, and maintenance cost for 1 kW biogas plant have been determined

**TABLE III.**
GENERIC 1 KWH LEAD-ACID BATTERY SPECIFICATIONS

| Properties | Ratings |
|---|---|
| Nominal voltage | 12V |
| Round trip efficiency | 80% |
| Lifetime throughput | 800 kWh |
| Maximum charging current | 16.67 A |
| Maximum discharge current | 24.33 A |

to be 3 000 $, 1 500 $, and 0.1$/hr [22], respectively. The lifetime of the generator has been fixed at 20 000 hours operating. The minimal charge ratio has been supposed by 50% capacity.

**F. Modeling Storage of Energy System**

The power storage is one of the most critical component of integration systems generated by different renewable energy sources. A 12V general-purpose lead-acid battery with 1 kWh of energy storage is provided to assure extremely reliable service and economical operation. Specifications are given in Table III. The capital costs, replacement costs, maintenance costs, and life of the battery are 300 000$, 300 000$, 10.00$/years, and 10 years, respectively.

**G. Energy Converter Model**

Universal system converters are provided to rectify the AC generator outlet to DC, which is much less expensive than a bi-directional convertor. Consider capitals, replacements, maintenances, durability, and efficiency of the converter are 250$, 250$, 10$/year, 5 years, and 95%, respectively [23].

## VII. EVALUATION CRITERIA OF THE SYSTEM

This part is reserved to evaluate the electricity production. There are different elements that affect the cost, and those cost. The cost is expressed in kWh/MWh, and typically include the capital, the discount rate, subsidy, and operating cost like fuel, maintenance, etc. The costs of a decentralized energy system need to be standardized or levelized. The mathematical representations for various costs and emissions will be discussed in the bellow.

**A. Economic Criteria**

**1) Net present cost**

The Homer program calculates the total NPC by adding up the sum of the discounted future cash flow for every year in the lifetime of the project. The NPC total, it's an economic output in HOMER software and allows for the ranking all the systems configuration in the optimum result, also calculated a total annualizes, and discounted energy costs. A mathematical representation of the NPC is described by (6).

$$C_{NPC} = \frac{C_{TAC}}{f} \tag{6}$$

where $C_{TAC}$ presents the sum of annualized costs and $f$ is the capital recovery factor.

**2) Levelized cost of energy**

Levelized cost of energy (COE) present the minimal price at which power has to be delivered to the end users in order to achieve break even over the lifetime of the project, and expressed in ($/kWh). To determine the COE from HOMER software, we simply to take the annualizes costs of power generation (total annualizes costs less for the cost of serving the thermal charge) and divided by the total electric load being served. It is the mean system operating cost to produce one kilowatt-hour of power. COE is defined as the ratio of the total annualize systems cost to the total available power generation of the system per year [24]. A mathematical equation for COE is described by (7).

$$COE = \frac{C_{a,tot} - C_{boiler} H_{serv}}{E_{serv}} \tag{7}$$

where $C_{a,tot}$ presents the total annualized costs of the system ($/year), $C_{boiler}$ presents the boiler marginal costs ($/kWh), $H_{serv}$ presents the total thermal charge served (kWh/year), and $E_{serv}$ presents the total electrical charge served (kWh/year).

**3) Cost of operation**

The operating costs are the estimated value of every cost and revenue other than initial capital cost. The HOMER software displays operating costs in an optimization result list. To calculate the operating cost, we use (8).

$$C_{op} = C_{an,tot} - C_{an,cap} \tag{8}$$

where $C_{op}$ is a sum of annualized costs of the system ($/year), and $C_{an,cap}$ is a total annualized capital costs ($/year).

**4) Initial capital costs**

The capital costs of the components are the total installed costs of component at the beginning of the project.

**5) Renewable fraction**

A renewable fraction is the portion of the energy supply to the loads that are derived from renewable energy source. The HOMER software calculates a renewable fraction using (9).

$$f_{ren} = 1 - \frac{E_{nonren} - H_{nonren}}{E_{serv} + H_{serv}} \tag{9}$$

where $E_{nonren}$ presents the nonrenewable electrical production (kWh/year), $E_{grid,sales}$ presents the energy sold to the grid (kWh/yr) (included in $E_{serv}$), $H_{nonren}$ presents the nonrenewable thermal production (kWh/year), $E_{serv}$ presents the sum of electrical charge served (kWh/year), $H_{serv}$ presents the sum of the thermal load served (kWh/year).

## VIII. RESULTS AND DISCUSSIONS

HOMER software analyzes the engineering practicability, and life cycle cost of the virtual plant for every year, and test the inputs for the given time period. Simulation capacity is long-term to Homer. Optimization, and sensitivity analysis are performed to find the simulation capacity with user specified classes. The less costs for the virtual power plant depend on the total net costs. The optimization is performed on

**TABLE IV.**
OPTIMAL SIMULATED ELECTRICAL COMPONENT

| Specification Model | Component | Unit | Best Hybrid System Per Model | | | | | |
|---|---|---|---|---|---|---|---|---|
| | | | Model 1 | Model 2 | Model 3 | Model 4 | Model 5 | Model 6 |
| System architecture | PV Array (TrinaSolar300TSM-300PA14) | kW | 62.6 | 69.2 | 79.5 | 119 | - | - |
| | Wind Turbine (Generic 10 kW) | Number | 1 | - | 1 | - | 6 | 15 |
| | Biogas (Generic Biogas Genset) | kW | 5 | 5 | - | - | 5 | - |
| | Pumped Hydro (10kW Generic) | kW | 11 | 11 | 11 | 11 | 11 | 11 |
| | Tidal turbine (AR2000) | Number | 1 | 1 | 1 | 1 | 1 | 1 |
| | Converter | kW | 18.3 | 16.7 | 20.8 | 22.8 | 18.7 | 37.8 |
| | Battery | Number | 100 | 120 | 208 | 224 | 336 | 728 |
| | Dispatch strategy | LF or CC | LF | LF | CC | CC | CC | CC |
| Cost | COE | $ | 0.403 | 0.413 | 0.458 | 0.484 | 0.740 | 1.29 |
| | NPC | $ | 314.846 | 322.628 | 357.454 | 377.675 | 577.651 | 1.01M |
| | Operating cost | $/year | 11.206 | 12.711 | 12.940 | 15.114 | 19.666 | 32.018 |
| | Initial capital | $ | 169.985 | 158.303 | 190.169 | 182.292 | 323.419 | 593.740 |
| Power production | PV Array | kWh/year | 94.087 | 104.097 | 119.518 | 178.434 | - | - |
| | Wind Turbine | kWh/year | 23.366 | - | 23.366 | - | 140.197 | 350.492 |
| | Biogas | kWh/year | 8.590 | 11.350 | - | - | 12.160 | - |
| | Tidal Turbine | kWh/year | 20.792 | 20.792 | 20.792 | 20.792 | 20.792 | 20.792 |
| Capacity factor | PV Array | % | 64.1 | 76.4 | 73 | 89.6 | - | - |
| | Wind Turbine | % | 15.9 | - | 14.3 | - | 81 | 94.4 |
| | Biogas | % | 5.85 | 8.33 | - | - | 7.02 | - |
| | Tidal Turbine | % | 14.2 | 15.3 | 12.7 | 10.4 | 12 | 5.6 |

**TABLE V.**
FINANCIAL ANALYSIS SUMMARY

| Component | Capital ($) | Replacement ($) | O&M ($) | Fuel ($) | Salvage ($) |
|---|---|---|---|---|---|
| Hydraulic | 80 000 | 0 | 31 026,04 | 0 | 0 |
| Tidal Turbine | 14 000 | 4 463,30 | 34 904,29 | 0 | −251 536 |
| Battery | 30 000 | 26 781,44 | 12 927,52 | 0 | −3 348,96 |
| Biogas | 15 000 | 5 497,79 | 12 856,42 | 5 611,94 | −769,21 |
| Power Converter | 5 476,39 | 2 323,49 | 2 359,87 | 0 | −437,30 |
| PV Array | 7 508,99 | 0 | 8 089,39 | 0 | 0 |
| Wind Turbine | 18 000 | 5 738,53 | 2 585,50 | 0 | −3 234,03 |

the basis of these inputs, and the table results. During optimization, HOMER considers the profile of every generator based on the specifications of the user.

In this sense, Table IV presents six the most efficient system architectures and their respective costs. Six the inputs to the model of design have been provided as follow:

- Model 1:PV+WT+Bio+Bat+Hy+TT
- Model 2: PV+Bio+Bat+Hy+ TT
- Model 3: PV+WT+Bat+Hy+TT
- Model 4: PV+Bat+Hy+TT
- Model 5: WT+Bio+Bat+Hy+TT
- Model 6: WT+Bat+Hy+TT

Table IV indicates the component details, and a technical, economical specification for the optimal hybrid systems in all the model.

We can see that the optimum solution composed of 62.6 kW photovoltaic plants, a 10 kW WT plant, a 5 kW biogas generator, 100

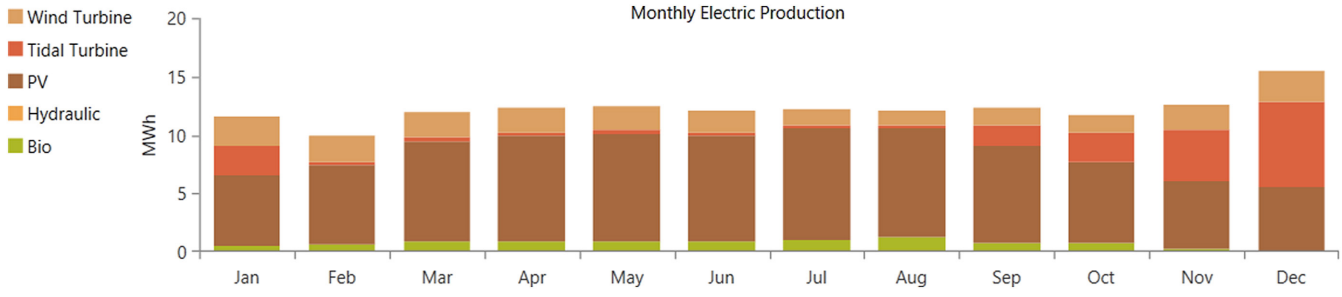


**Fig. 7.** Monthly average electrical outputs from the optimal configuration system.

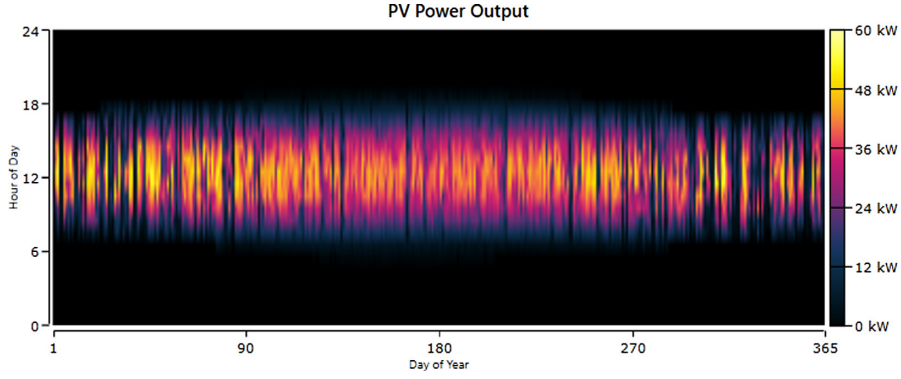


**Fig. 8.** The PV array output.

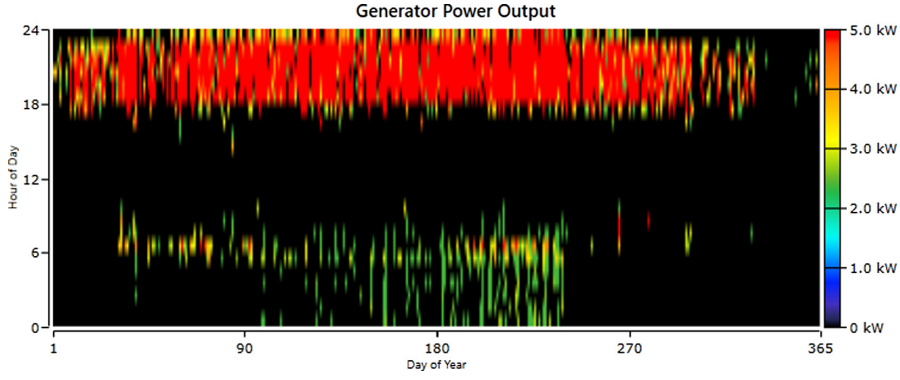


**Fig. 9.** Biogas generator output.

batteries, an 11 kW pumped hydroelectric storage, a 1 tidal turbine, and an 18.3 kW generator bidirectional converters with one load following dispatch strategies. All sources are presented. Its costs of power (COE) and its total NPC was 0.403$ and 314,846$ respectively, and the renewable fraction is 100%.

The assessment of the virtual power system in term of investment, operation, also maintenance cost is shown from Table V. The capital costs in the system are owned by the hydraulic system power is higher, and the operation and maintenance costs. A total cost of the systems over the life for the project is calculate at 314,846$ based on this assessment.

Figure 7 presents the monthly contribution of the virtual power system (all sources used in the system) throughout the year. The HOMER Pro indicated that the energy supplied by PV was 64.1%, the energy supplied by WT was 15.9%, the energy supplied by TT was 14.2%, and the biogas produced was 5.85%.

The production of the photovoltaic generator all year long, presented in Figure 8, shows that the photovoltaic power production occurred from 06:00 a.m. to 06:00 p.m. and was most likely to peak (55.7 kW) from 10:00 a.m. to 2:00 p.m. In addition, the total yearly photovoltaic electricity production is 94.087 kWh/year, which corresponds to a system capacity factor of 17.2%.

Figure 9 demonstrates the performance of the biogas plant throughout the years. It has been very likely that the generator would be turned on from 06:00 p.m. till midnight. Also, the biogas producer was able to supply its maximum electrical power (5 kW) from 06:00 p.m. to 00:00 a.m. The yearly electricity generation of the biogas production was 8.590 kWh/year, which is a system capacity factor of 19.6%.

Figure 10 presents the energy and the production profile from the converter for a period of 1 year with a capacity factor of 13.3% for the inverter and 0.862% for the rectifier. Fig. 11 shows the state of load of the battery storing station for 1 year.

A randomly selected week's energy situation of generation and consumption in 1-year period of a VPP operation is given in Fig. 12. In Fig.12, the PV power production, wind turbine power, tidal turbine

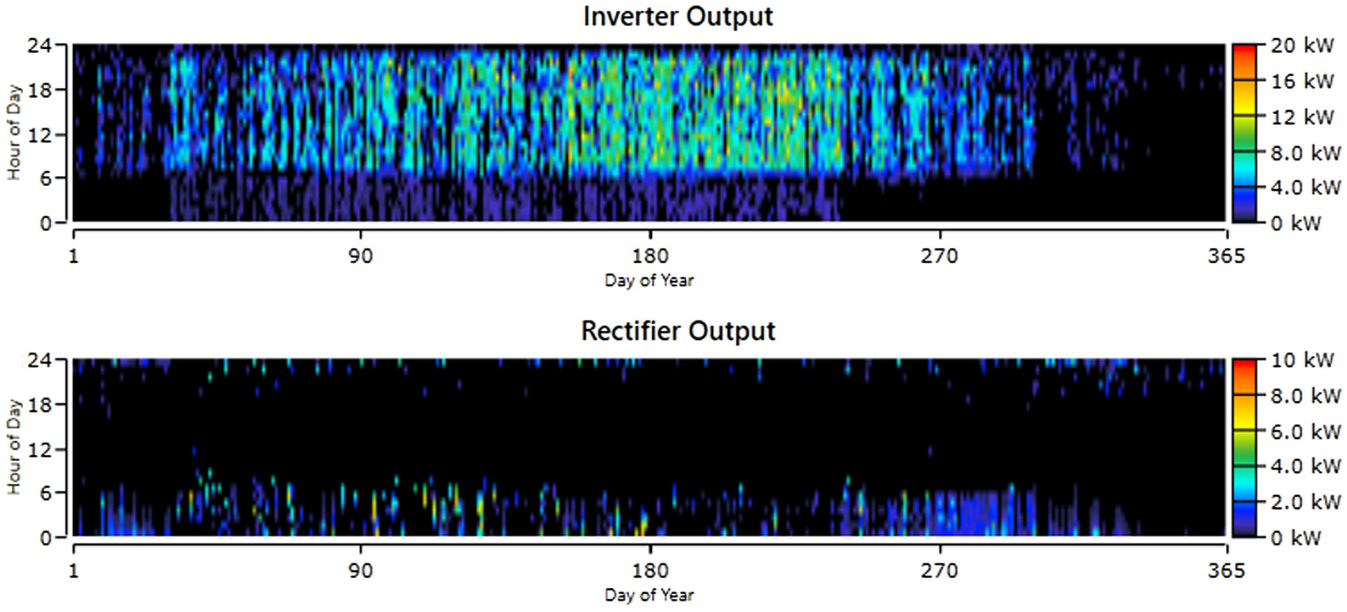


**Fig. 10.** The energy output profile of converter during period of 1 year.

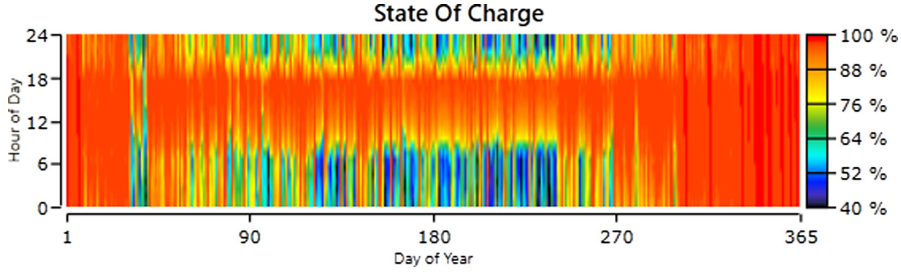


**Fig. 11.** State of charge of the pumped-hydro storage station.

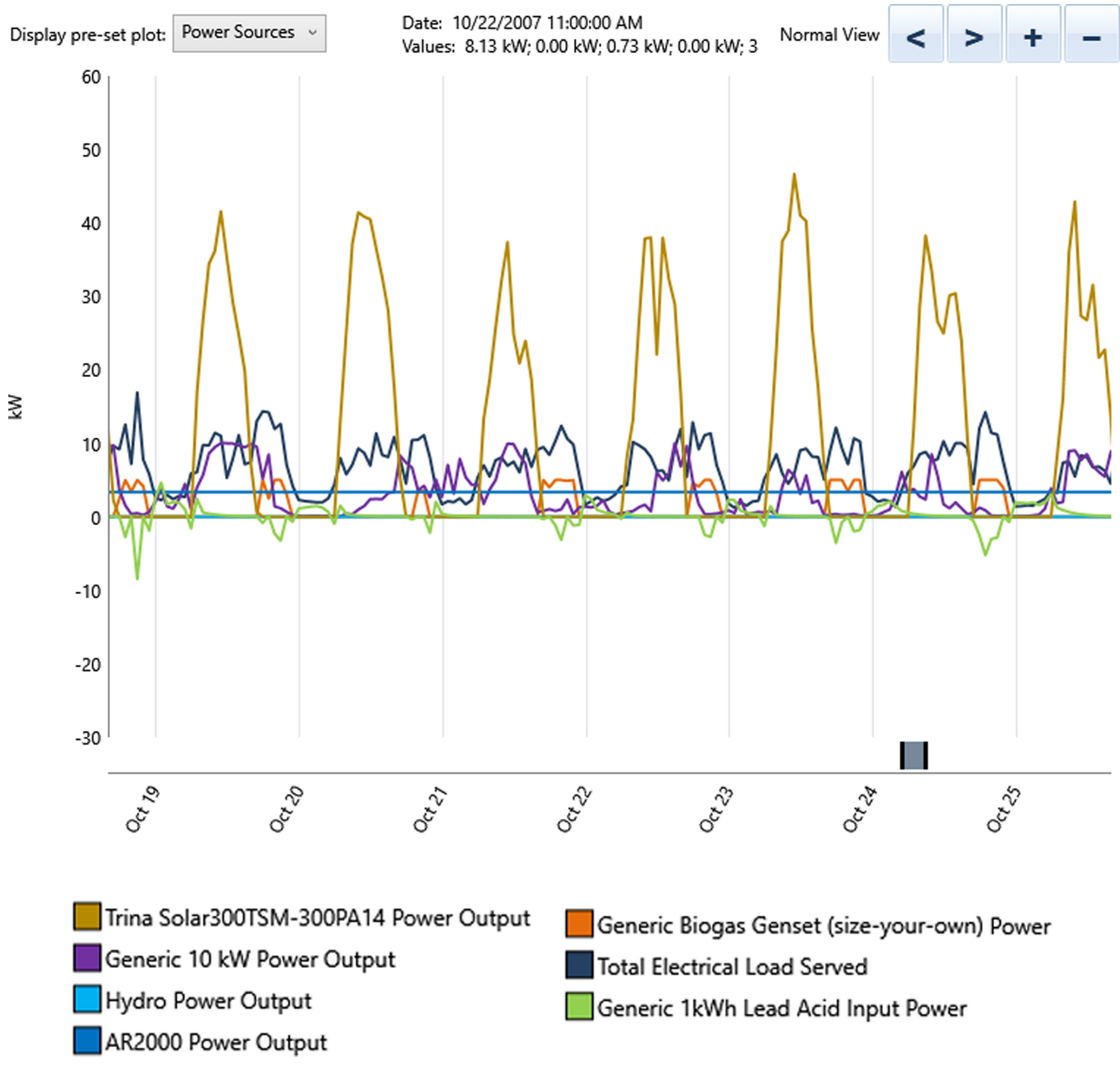


**Fig. 12.** One-week energy generation–consumption graph of the virtual power plant.

power, load, and the amount of load energy are presented. When all the sources of the VPP production are more than just the uptake, the energy is provided to the charge alone of a VPP system, and excess power is sent to the utility grid. When PV production is below the consumption, necessary energy is bought from the network. In this operating strategy, the battery is used.

## IX. CONCLUSION

This study provides a detailed overview of how the potential of renewable energies can be realized in Tunisia with optimal design and is a comparison study of real data for Djerba Island. The study compared six categories, and how it can be beneficial to Djerba Island to address the frequent power outages and disruptions and to encourage the utilization of renewable energy sources in these communities.

In this study, a proposed VPP consists of a photovoltaic energy plant, a wind energy plant, a tidal energy plant, a hydropower system, a biogas generator, and an energy storage system based on battery bank designed to supply power for the island of Djerba, Tunisia. Yet, the optimal for dimensioning and operating this additional system should be done properly so that maximum benefit

can be obtained. We find an optimal sizing of all components based on the available supplied irradiation in the study area, wind turbine, water turbine, biomass, water pressure, and charge data. The study also provides projected economical and environmental analyses of system based on the actual electrical load of Djerba Island over a period of 1 year.

HOMER software can be utilized to analyses a variety of structure of electrical energy systems, and is useful for calculating costs, and in the scheduling of virtual power plant where microgrid. With appropriate scheduling, and dimensioning, it may be possible to provide power to the island's community in Tunisia. In this sense, a 62.6 kW PV power source, 1 wind turbine, 1 tidal turbine, 5kW biomass generator, 11 kW hydro pump, 8.109 kWh/year energy storage unit are optimal for the chosen charge profile. The effect of virtual power plant sources degradation demand increase, grid outage, and diesel fuel price increase were studied in a PV-wind-tidal-hydraulic-biomass virtual power plant generator-batteries-inverter combination. When the effects of those factors are included in the system, the resulting increase in were observes over a baseline system. With NPC is 314.846$, the discounted COE is 0.4031$, and the operating cost is 11.205.61$, and the renewable fraction is 100%. It is expected that the systems VPP will be more economical with the further developing of the power will be more economical with further development of renewable energy and the decrease in component costs.

**Peer-review:** Externally peer-reviewed.

**Declaration of Interests:** The authors have no conflict of interest to declare.

**Funding:** The authors declared that this study has received no financial support.

## REFERENCES

1. K. Anoune *et al.*, "Optimization and techno-economic analysis of photo voltaic-wind-battery based hybrid system," *J. Energy Storage*, vol. 32, p. 101878, 2020. [CrossRef]
2. O. H. Mohammed, Y. Amirat, M. E. H. Benbouzid, and G. Feld, "Optimal design and energy management of a hybrid power generation system based on Wind/tidal/PV sources: Case study for the Ouessant French Island,"*Smart Energy Grid Des. Isl. Ctries Chall. Oppor.*, pp. 381–413, 2017. [CrossRef]
3. Q. Ma, X. Huang, F. Wang, C. Xu, R. Babaei., and H. Ahmadian, "Optimal sizing and feasibility analysis of grid-isolated renewable hybrid microgrid: Effects of energy management controllers," *Energy*, vol. 240, p. 122503, 2022. [CrossRef]
4. J. Kumari, P. Subathra, J. E. Moses., and D. Shruthi, "Economic analysis of hybrid energy system for rural electrification using Homer," 2017 International Conference on Innovations in Electrical, Electronics, Instrumentation and Media Technology (ICEEIMT), IEEE Publications, 2017, pp. 151–156.
5. S. Chauhan, R. Pande., and S. Sharma, "Techno-economic study of off-grid renewable energy system in Darma valley, Uttarakhand, India," *Curr. Sci.*, vol. 9, p. 121, 2021.
6. K. C. Chang et al., "Standalone and minigrid-connected solar energy systems for rural application in Rwanda: An in situ study," *Int. J. Photoenergy*, vol. 2021, pp. 1–22, 2021. [CrossRef]
7. S. Kanata, S. Baqaruzi, A. Muhtar, P. Prasetyawan., and T. Winata, "Optimal planning of hybrid renewable energy system using Homer in Sebesi Island,Indonseia," *Int. J. Renew. Energy Res. (IJRER)*, vol. 11, pp. 1507–1516, 2021.
8. S. Ghose, A. El Shahat., and R. J. Haddad, *'Wind-solar hybrid power system cost analysis using Homer for Statesboro, Georgia', Southeastcon*. Charlotte NC: IEEE Publications, 2017, pp. 1–3.
9. H. Sharma., and S. Mishra, "Hybrid optimization model for smart grid distributed generation using Homer," 3rd International Conference on Recent Developments in Control, Automation & Power Engineering (RDCAPE). IEEE Publications, 2019, pp. 94–99.
10. F. Ghayoor, A. G. Swanson, and H. Sibanda, "Optimal sizing for a grid connected hybrid renewable energy system: A case study of the residential sector in Durban, South Africa,"*J. Energy South. Afr.*, vol. 32, no. 4, pp. 11–27, 2021. [CrossRef]
11. B. Bhandari, K.T. Lee, G.-Y. Lee, Y.-M. Cho, and S. Ahn. "'Optimization of Hybrid Renewable Energy Power Systems', A review,"*Int. J. Precis. Eng. Manuf. Green Technol.*, vol.2, no.1, pp.99–112, 2015. [CrossRef]
12. S. Ahmed Abdul-Wahab, Y. Charabi, A. M. al-Mahruqi, and I. Osman, Design and evaluation of a hybrid energy system for Masirah Island in Oman, *Int. J. Sust. Eng.*, vol. 13, No. 4, pp. 288–297, 2020.
13. G. Zhao, T. Cao, Yudan Wang, Huirui Zhou, C. Zhang, and C. Wan, "Optimal sizing of isolated microgrid containing photovoltaic/photothermal/Wind/diesel/battery," *Int. J. Photoenergy*, vol. 2021, 2021. [CrossRef]
14. S. Salehin et al., "Modeling of an optimized hybrid energy system for Kutubdia Island, Bangladesh," *Appl. Mech. Mater.*, vol. 819, pp. 518–522, 2016. [CrossRef]
15. C. Gouveia, D. Rua, F. Ribeiro, L. Miranda, J. M. Rodrigues, C. L. Moreira, and J. A. Peças Lopes, "Experimental validation of smartdistribution grids: Development of a microgrid and electric mobility laboratory," *Int. J. Electr. Power Energy Syst.*, vol. 78, pp. 765–775, 2016.
16. A. Rezvani, M. Gandomkar, M. Izadbakhsh, and A. Ahmadi, "Environmental/economic scheduling of a micro-grid with renewable energy resources,"*J. Cleaner Prod.*, vol. 87, pp. 216–226, 2015. [CrossRef]
17. S. A. Memon, D. S. Upadhyay., and R. N. Patel, "Optimal configuration of solar and wind-based hybrid renewable energy system with and without energy storage including environmental and social criteria: A case study," *J. Energy Storage*, vol. 44, p. 103446, 2021. [CrossRef]
18. S. A. Memon, D. S. Upadhyay., and R. N. Patel, "Optimal configuration of solar and wind-based hybrid renewable energy system with and without energy storage including environmental and social criteria: A case study," *J. Energy Storage*, vol. 44, p. 103446, 2021. [CrossRef]
19. N. Shirzadi, F. Nasiri, and U. Eicker, "'Optimal Configuration and Sizing of an Integrated Renewable Energy System for Isolated and Grid-Connected Microgrids', the case of an urban university campus," *Energies*, vol. 13, no. 14, p. 3527, 2020. [CrossRef]
20. H. Pro. Available: https://www.homerenergy.com/. [Accessed March 2, 2020].
21. J. O. Oladigbolu, M. A. M. Ramli, and Y. A. Al-Turki, "Feasibility study and comparative analysis of hybrid renewable power system for off-grid rural electrification in a typical remote village located in Nigeria," *IEEE Access*, vol. 8, pp. 171643–171663, 2020. [CrossRef]
22. Kalogirou SA., "Photovoltaic systems." In: Kalogirou SA (ed) Solar energy engineering, 2nd edn', Academic Press, Cambridge, pp. 481–540, 2014.
23. Phurailatpam C., Rajpurohit B., and Wang L., "Optimization of DC micro grid for rural applications in India," In Proceedings of the 2016 IEEE Region 10 Conference (TENCON), Singapore, 22–25 November 2016.
24. J. O. Oladigbolu, M. A. M. Ramli, and Y. A. Al-Turki, "Feasibility study and comparative analysis of hybrid renewable power system for off-grid rural electrification in a typical remote village located in Nigeria," *IEEE Access*, vol. 8, pp. 171643–171663, 2020.

cigre Turkey

TEPES
TURKISH JOURNAL OF ELECTRICAL POWER AND ENERGY SYSTEMS

TEPES, Vol. 2, Issue. 2, 180-196, 2022 **DOI:** 10.5152/tepes.2022.22016

REVIEW

# Comprehensive Review on CdTe crystals: Growth, Properties, and Photovoltaic Application

**Bibin John[1], S. Varadharajaperumal[2]**

[1]Department of Physics and Electronics, CHRIST - Deemed to be University, Bangalore, India
[2]Center for Nanoscience and Engineering (CeNSE), Indian Institute of Science, Bangalore, India

**Cite this article as:** B. John & S. Varadharajaperumal. Comprehensive review on CdTe crystals: growth, properties, and photovoltaic application. *Turk J Electr Power Energy Syst*, 2022; 2(2), 180-196.

## ABSTRACT

Despite the deep interest of materials scientists in cadmium telluride (CdTe) crystal growth, there is no single source to which researchers can turn for comprehensive knowledge of CdTe compound semiconductor synthesis protocols, physical characteristics, and material performance. Considering this, the present review work focuses on bridging these shortcomings. The CdTe crystals with direct band gap ($E_g$) have been in limelight in the photovoltaic application (PV) as the optoelectronic properties such as $E_g$ (1.49 eV), absorption coefficient (~$10^5$ $cm^{-1}$), *p*-type conductivity, carrier concentration ($6 \times 10^{16}$ $cm^{-3}$), and appreciably high mobility (1040 $cm^2$/V s) at the room temperature are reported, which are optimum for solar cells. Additionally, Cd-based crystals have also been widely studied and implemented in the field of $\alpha$ and $\gamma$-ray radiation detectors because of their extraordinary advantages like a large atomic number, low weight, high mechanical as well as thermal stability, flexibility, and the availability of the constituent materials. Cadmium telluride has demerits like toxicity (ecological damage) and high chances for defects/dislocations due to high thermal conductivity at melting temperature and high melting temperature, which will complicate the growth of stoichiometric CdTe crystals at high temperatures. Even though CdTe has the aforementioned issues, on the other hand, the absorber material reached a milestone (solar cell efficiency in the order of 22%), which enhances the attractiveness of this binary compound more and more in the field of crystal growth technology. In this regard, the review work focused on the periodic evolution of the growth protocols until now for the production of bulk, good quality CdTe crystals. The different synthesis methods, characterization, and recent progress in the field of crystalline CdTe were discussed briefly. Important physicochemical characteristics are presented in the tables and remaining issues due to chemical in-homogeneity, defects, imperfections, etc., have been discussed, which could facilitate the researchers who are working on this class of compound semiconductors. The applications of CdTe crystals to PV fields are also discussed separately in this review paper.

**Index Terms**—Cadmium telluride (CdTe), traveling heater method, horizontal traveling heater method, sublimation method, dislocation density, photovoltaic application

## I. INTRODUCTION

Compound semiconducting materials have gained tremendous attention in the past few years as basic absorber materials for photovoltaic applications. Fundamental characterization and studies of cadmium telluride (CdTe) crystals began around 60 years ago due to their potential application in optical and electrical fields [1]. This material comes under the category of II–VI binary compound semiconductors. Cadmium telluride is one of the technologically important semiconductor materials with a range of applications that require high-quality and defect-free substrates. It is also used as a radiation detector because of its large average atomic number (Z = 50), relatively large stopping power, and high resistivity at room temperature [2]. It is an economical, earth-abundant material, which facilitates its value in sustainable development in electronic as well as photonic systems [3, 4]. Like other solar cell absorbers such as Si and GaAs, CdTe also has an optimum bandgap (1.49 eV) and high absorption coefficients near the band edge, making it an excellent material for photovoltaic technology [5]. Even though CdTe possesses ecological damage due to toxicity, this semiconductor is a robust and chemically stable material for this reason. It can be deposited with a large variety of methods, making it very much ideal for production in a large area. Along with this, CdTe has a wide range of applications; however, the synthesis of this compound with high quality and stoichiometry is still difficult. The complexity of growing chemically homogeneous large dimensional crystals has hindered the fast development of many devices based on the CdTe substrate. Therefore, the synthesis technologies for the growth of high-quality CdTe and related compounds have rapidly been enhanced in recent

**Corresponding author:** Bibin John, bibin.john@res.christuniversity.in

**Received:** February 21, 2022
**Accepted:** April 16, 2022
**Publication Date:** May 23, 2022

decades [6]. Various crystal growth methods have been developed for the production of CdTe materials, like sublimation, the vertical Bridgman method, horizontal traveling heater method, traveling solvent method, and Liquinert-processed vertical Bridgman (LPVB) or detached growth method, etc. [7-12]. Rudolph et al. [13] reported that there is a strong influence between the stoichiometry and electrical as well as optical properties of the crystals. Hence, the control of composition during the crystal growth process is extremely important both from the physical and structural points of view. However, this homogeneity problem is one of the major drawbacks of the CdTe crystals grown from the melt due to the lack of thermodynamic data, growth methods, and physicochemical properties. Generally, the growth of CdTe single crystals with the Czohralski method has not been very successful. The CdTe crystals are always characterized by a coarse-grained structure with ~1 $cm^3$ of crystallites and a high number of twin lamellae. The inhomogeneity and steep axial temperature gradient of the melt are the primary sources of high defect content. Al-Hamdi et al. [14] have discussed the safe, efficient, and cost-effective growth of crystalline CdTe samples from the elements Cd and Te, which is rather challenging in a silica-sealed growth ampoule owing to the large vapor pressure (above 1 atm) of the cadmium element. The preparation of the high melting point CdTe compound from the low melting point elements tends to exhibit unreacted molten Cd and Te as the mixture is heated. This is due to the high vapor pressure of elemental cadmium; the pressure from the overheated pools of Cd can increase well above 1 atm at high temperatures. On the other hand, this may pose explosion risks in traditional synthesis methods using sealed quartz ampoules [15]. Also, the probability of over depositing un-reacted Cd is higher in larger-volume loads; therefore, the scalability is limited by the strength of the quartz ampoules. Generally, the CdTe growth methods and the quality of the material naturally affect the cost of CdTe device technologies. Small-volume synthesis of CdTe in sealed silica ampoules tends to be expensive due to high labor and consumable costs. Therefore, it is imperative to explore the appropriate and systematic review of the CdTe synthesis processes to finalize the robust, scalable, low-cost CdTe feedstock growth that provides high purity, doping control, and the flexibility to produce from both Cd and Te rich melts when necessary. Thus, this review paper mainly deals with the history of CdTe research, crystallization of good-quality crystals, material properties, structure and bonding, the electronic structure of CdTe, optoelectronic properties, defects, applications, and conclusion.

## II. HISTORY OF CdTe RESEARCH

Cadmium telluride is an II–VI family chalcogenide compound that has a zinc-blend crystal structure that belongs to the cubic noncentrosymmetric space group $F\bar{4}3m$ ($T_d^2$). This crystal is iso-structural with diamond except for the alternation of the two different elements (Cd and Te) on the successive lattice sites. The CdTe compound has a long research history; all these findings are beneficial to unearthing the physical properties of the crystal through a systematic review of these published works. Hence, the present review article attempts to spotlight or present the various growth methods for the production of high-quality CdTe crystals and their physical as well as chemical characteristics for photovoltaic applications. The schematic depiction of the atomic model of the zinc-blende structure is depicted in Fig. 1a. Furthermore, the precisely calculated lattice parameters of the CdTe samples, $a = 6.47832$ Å, are almost identical to standard data [13, 14]. In the past few years, researchers have developed new crystal growth technologies for the production of ~1 kg size of CdTe crystals from the elemental precursors of Cd and Te with high purity for photovoltaic applications [14]. From the 1960s to the 2000s, the number of research reports on the physical properties of CdTe gradually increased. As a result, the basic understanding of the structural, optical, and electrical properties of the material expanded significantly [1-5, 7, 9-10, 12-15]. It is interesting to note that the role of the CdTe semiconductor is transformed from being a radiation detector to being an absorber medium in photovoltaic applications [16]. Fig. 1b shows the image of a grown CdTe:Ge single crystal with a 25 mm diameter that can be cleaved into wafers for diverse device applications. The current density versus voltage plot of the device (Fig. 1d) is depicted in Fig. 1c. This shows that the CdTe-based heterojunction solar cell has a high fill factor of 73.6% and power conversion efficiency of 17%, which is close to the famous silicon-based photovoltaic devices. The inset of Fig. 1c shows the other solar cell parameters obtained from the device. In the current era of solar cell fabrication, most thin films have different absorber or window layers of various materials to absorb or collect the maximum number of photons from the sunlight (Fig. 1d).

**Main Points**

- Review of different growth methods for the production of good quality bulk cadmium telluride (CdTe) crystals.
- Comprehensive review of CdTe compound semiconductor synthesis protocols, properties, and performance.
- Suitability of bulk CdTe crystals for photovoltaic applications.
- Impact of growth method on the quality of CdTe crystals.

## III. MATERIAL PROPERTIES

In general, the major factor affecting the conversion efficiency of the solar cell is the quality of the CdTe absorber material. The yield of defect-less CdTe crystals is limited due to the formation of Te clusters in the melt during the melt growth process. This is a special property of the II–VI group materials [17]. Hence, pure phase, good crystalline, and large grain size are inevitable criteria for the semiconducting materials for photovoltaic applications. The low melting point and vapor pressure help the synthesis of this crystal in the atmospheric pressure furnace with the utilization of quartz ampoule [6]. The high absorption coefficient of this sample enhances the effective absorption of a large amount of light energy and thereby generates more photogenerated carriers before their recombination. Also, the direct absorption of solar radiations without any momentum assistance makes the CdTe absorber more attractive than crystalline silicon. In addition to these optical parameters, melt-grown crystalline CdTe exhibits less resistivity and high carrier mobility at room temperature, which is suitable for PV applications. A high internal electric field at the *p*-*n* region ensures the separation of the electron–hole pairs. Hence, the selection of a suitable active absorber material for the absorption of light relies not only on the bandgap value but also on the other properties of materials, such as readily attainable *p*-type or *n*-type conductivity, charge–carrier lifetime,

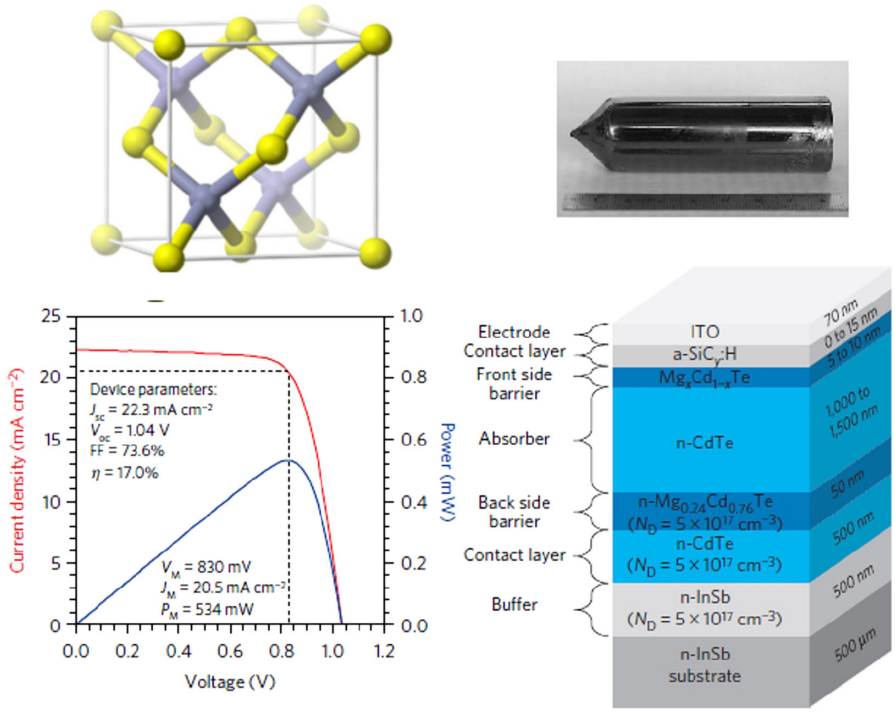


**Fig. 1.** (a) CdTe atomic structure, blue-shaded balls correspond to Te and yellow balls to Cd. (b) Image of CdTe:Ge crystal with 25 mm [16]. (c) Measured ***J–V*** curve and associated device parameters. (d) Layer structure of the CdTe/$Mg_xCd_{1-x}Te$ DH solar cell with an a-$SiH_y$:H (y = 0–6%) hole-contact layer [3].

carrier concentration, dielectric constant, and low excitation binding energy. However, there is no single comprehensive research finding focusing only on the CdTe crystals for photovoltaic applications, despite the fact that CdTe is the second most popular solar cell active layer. Therefore, in the present review work, the physicochemical properties of the CdTe crystals are tabulated in Table I. For the following reasons, the solidification of this binary compound with high quality is quite difficult:

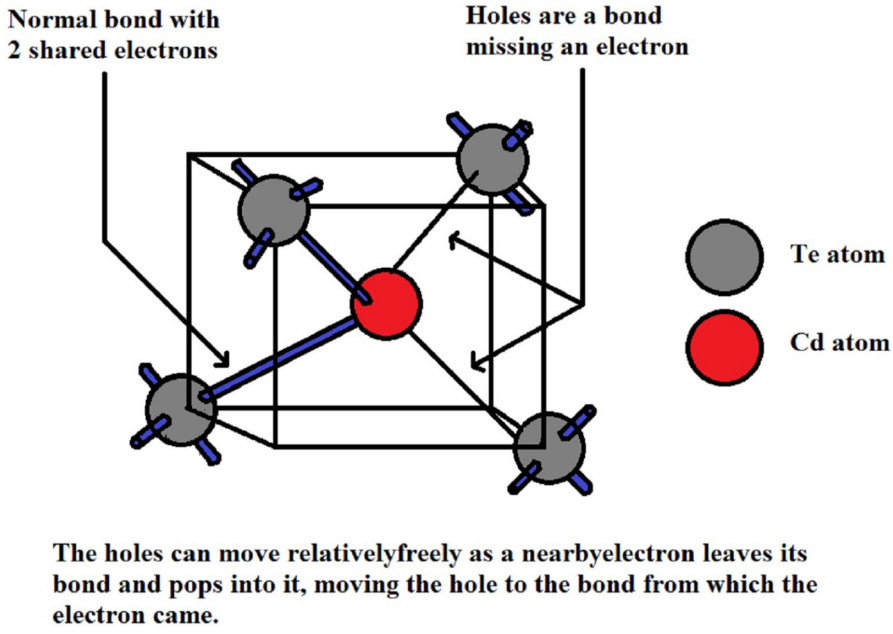


**Fig. 2.** Two valance electron impurity (Cd) in a Te crystal is normally bonded except two of the bonds are missing the electrons, that is, is a hole.

i) Thermal conductivity is very low because of which the dissipation of heat during the growth of the melt is difficult. Hence, a smooth solid–liquid interface cannot be easily achieved in the melt.
ii) Shear stress is low, so dislocations are easily generated by thermal stress.
iii) Stacking fault energy is low because of this, twins are easily formed.

## IV. STRUCTURE AND BONDING

### A. Basic Structure

Compound semiconducting materials are the central focus of crystal growth technology in the current era due to the huge revolutionary development witnessed in the field of optoelectronic devices. In particular, in the energy sector, like photovoltaic, fuel cells, hydrogen production, sensors, and detector applications. For harnessing energy from sunlight, the quality and purity of the absorber materials are essential, which can be achieved through the right absorber medium and their growth without any defects. From this point of view, CdTe has a relatively high atomic number compared to the other elemental photovoltaic material like silicon (Cd: 48, Te: 52, and Si: 14). The valance electronic configuration of cadmium (Cd) and tellurium (Te) atoms are $4d^{10}5s^2$ and $4d^{10}5s^2\ 5p^4$, respectively. As the electronegativity of Te atoms is much stronger than Cd atoms, Te captures two electrons from the Cd atom which leads to a change in the electronic configuration of Cd from $4d^{10}5s^2$ to $4d^{10}5s^0$ and that of Te to $4d^{10}5s^2\ 5p^6$. Cadmium and Te were labeled in a black square box in the periodic table (see appendix, Fig. S1.). The physical and chemical parameters of the melt-grown CdTe crystals are also presented in Table I. These functional properties help the research of those who are working on the growth of low dislocation density semiconducting CdTe material. A large-dimensional stoichiometric CdTe compound has been mainly prepared using the melt growth method (Bridgman–Stockbarger). There are a few reports on the Czochralski technique (CZ), the traveling heater method (THM), the vertical gradient freeze technique, and the LPVB method [2, 5, 8, 11-13, 18-25] (Fig. 2). A brief account of crystal growth using the aforementioned techniques is explained in section 6. Cadmium telluride is a group II–VI semiconducting compound material having a zinc-blend crystal system and belongs to the cubic noncentrosymmetric space group $F\bar{4}3m$ ($T_d^2$). The schematic of the atomic replica of CdTe crystals is depicted in Fig. 3. The reported lattice parameter of the CdTe crystal is "$a = 6.47832$ Å," which is almost identical to recently reported data [16, 17]. The CdTe semiconducting materials grown by the LPVB method have a zinc-blend crystal structure as discussed by Sekine et al. [12].

**TABLE I.**
PHYSICOCHEMICAL PROPERTIES OF CDTE CRYSTALS

| Properties of Material | Symbol | Value |
|---|---|---|
| Chemical formula | | CdTe |
| Molecular weight | W | 240.01 |
| Group | | Cadmium: 12<br>Tellurium: 16 |
| Crystal structure | | Cubic [11] |
| Lattice constant | A | 6.482 Å [11] |
| Dielectric constant | | 10.2 |
| Hole mobility | $\mu_h$ | 65 $cm^2/V\ s$ |
| Electron mobility | $\mu_e$ | 700 $cm^2/V\ s$ |
| Carrier concentration | P | $6 \times 10^{16}\ cm^{-3}$ [1] |
| Carrier mobility | μ | 1040 $cm^2/V\ s$ [1] |
| Density | D | 5.85 $g/cm^3$ |
| Melting point | M.P | 1092°C [17] |
| Boiling point | B.P | 1130°C |
| Young's modulus | Y | $3.7 \times 10^{11}$ dyne/$cm^2$ |
| Rupture modulus | | $2.2 \times 10^8$ dyne/$cm^2$ |
| Refractive index | | 2.67 |
| Band gap | $E_g$ | 1.5 eV (room temperature) [18] |
| Nature of band gap | | Direct optical band gap [18] |
| Absorption coefficient | A | $>10^5\ cm^{-1}$ [18] |
| Thermal expansion coefficient | | $5.9 \times 10^{-6}$/K |
| Specific heat capacity | H | 0.21 J/g K |
| Thermal conductivity | Σ | ~ 4 W/m K [11] |
| Thermal expansion coefficient | | $5.9 \times 10^{-6}$/K |

## V. PHASE DIAGRAM OF CDTE

The engineering of crystals, as well as the fabrication of optoelectronic device, is very much essential to understand the response of CdTe crystal at different chemical composition. Fig. 3 shows the phase diagram of CdTe crystals. As compared to the phase diagram of other ternary or quaternary materials, the diagram of this sample is very simple. The melting point of the pure CdTe samples (50:50 at.%) was reported to be 1092°C as per the phase diagram, which is applicable for the monophase as well as stoichiometric CdTe samples [26]. Suppose the atomic ratio of CdTe deviates from the 50/50 at.% during the crystal growth process, the material will phase separate into CdTe and Cd or Te, whichever has the greater composition. Because both Cd and Te have higher vapor pressure than crystalline CdTe, these elemental components will try to re-evaporate before they could be incorporated into the growing crystal [27]. Minute changes in the purity of the crystal result in large sub-liquidus regions of liquid + CdTe with a Cd-rich liquid phase for Cd-enriched compositions and a Te-rich liquid for Te-rich compositions. Fig. 4 shows that Cd-rich compositions melt at 322°C, solidus temperatures and 450°C for Te-rich compositions. This represents the melting points of pure Cd and pure Te, respectively. Hence, this graph represents that for even small deviations from stoichiometric CdTe, some amount of

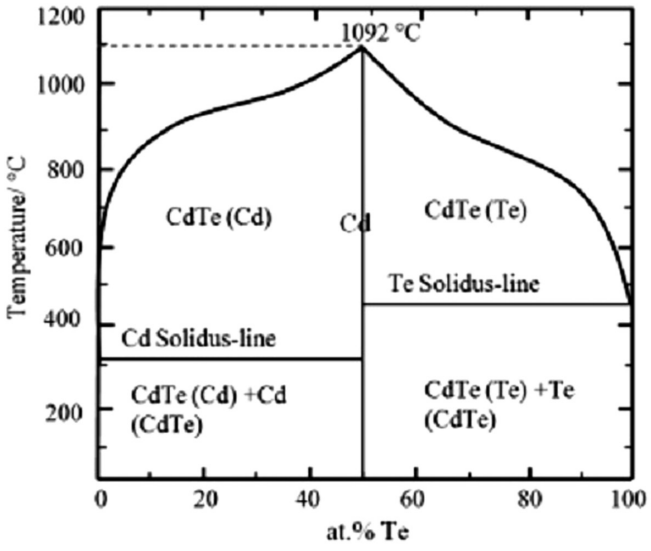


**Fig. 3.** Phase diagram of CdTe crystal for the effect of stoichiometry and temperature [27].

liquid phase will be present above 322°C for Cd-rich compositions and above 450°C for Te-rich compositions. The relative amounts of liquid will increase as a function of the amount of deviation from pure stoichiometry. This has implications for the processing of CdTe devices that are not chemically pure and which may be processed at temperatures above 322°C or 450°C, depending on the process methodology. Determination of elemental percentage also suggests that for equilibrium conditions, temperatures greater than 600°C

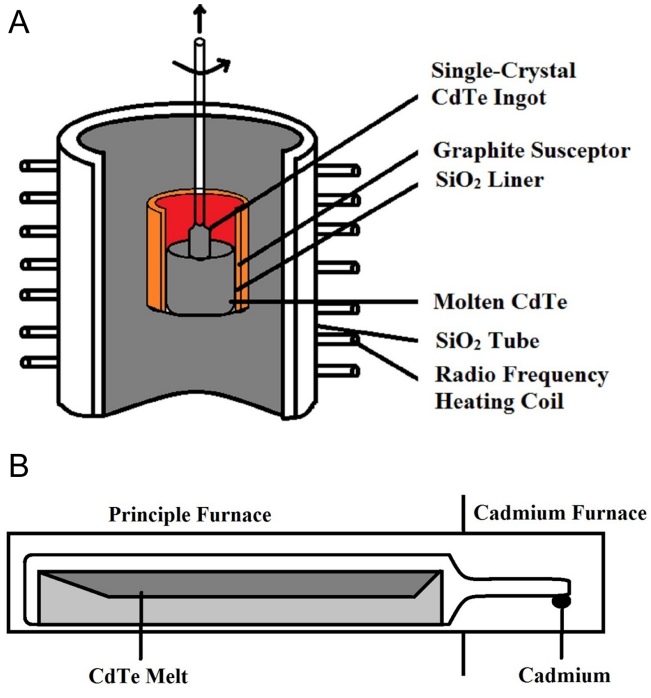


**Fig. 4.** Schematic of the (a) Czochralski growth apparatus and (b) liquid encapsulated Czochralski growth apparatus.

can exhibit a large amount of Te or Cd compared to temperatures below 500°C [26]. The stoichiometric deviation adversely affects all the physical properties, including the performance of solar cell device. Therefore, the phase diagram will help the crystal growers to adopt a suitable growth method for the production of high-quality CdTe crystals. The phase diagram of the CdTe samples also facilitates the fabrication of devices without many defects or problems.

## VI. BULK CRYSTALLIZATION OF CDTE CRYSTAL GROWTH

### A. Melt Growth Method

#### 1) Czochralski Process and Liquid Encapsulated Czochralski (LEC) Method

The growth of crystals by pulling from the melt was first introduced by Czochralski in the year of 1971. It results in a single crystal with fewer imperfections and is free of the physical constraints imposed by the crucible. Fig. 4a shows the schematic depiction of the Czochralski growth apparatus. The necessity to maintain the melt in a crucible often acts as a contamination source, which is the main disadvantage of this growth approach. Initially, a tiny single crystalline CdTe seed is placed on top of the molten material of the purified CdTe. After a small interval of the period, the seed crystal is slowly elevated up to less than 10 cm/h and rotated to attain proper homogeneity. As the CdTe semiconducting compound rises slightly from the melt, CdTe freezes on its surface, extending the single-crystal structure. The final product is most probably a cylindrical ingot, or boule, typically the container's diameter and many times that in length. Meantime, liquid encapsulated Czochralski (LEC) method has been developed for the growth of CdTe crystals in the 1970s but it was unsuccessful. The Czochralski and LEC methods are found to be unsuitable for the synthesis of CdTe compounds due to their tendency to form twins during the growth process. Hobgood et al. [28] have grown CdTe ingots of 50 mm in diameter and weighing up to 1 kg by precisely adjusting the synthesis parameters (in a modified Melbourn crystal puller). However, only a few LEC growth trials were conducted for the growth of CdTe compound semiconductors because this synthesis method is not appropriate for the growth of CdTe crystals. These authors investigated the microstructure of the CdMnTe ingots and observed a mosaic-like array of sub-grains corresponding to misorientations from the true (111) growth axis. Also, the etch pit density (EPD) is reported as being in the order of ~$10^6$ $cm^2$. The schematic diagram of the LEC growth apparatus is depicted in Fig. 4b. The value of the EPD of the CdTe is larger than the other compounds and elemental semiconducting crystals. The addition of magnetic fields (greater than 2000 G) helps to adjust the thermal fluctuations in the LEC growth of CdTe and CdMnTe melts, which control the twinning of the crystals. The axial temperature gradient of the LEC method is high, leading to the development of dislocation densities in the final product, which may adversely affect the material properties [7].

#### 2) Heat Exchanger Method (HEM)

Because of this demerit, the poor thermal conductivity of the CdTe crystal prevents the growth of the latter via the directional solidification growth method. It is very difficult to control the solid–liquid (β-α) interface shape during crystal growth. Also, it is well known that the planar solid–liquid interface is favorable for the growth of high-quality samples. Since it has difficulty in controlling the shape and the β-α interface and the movement during the synthesis process,

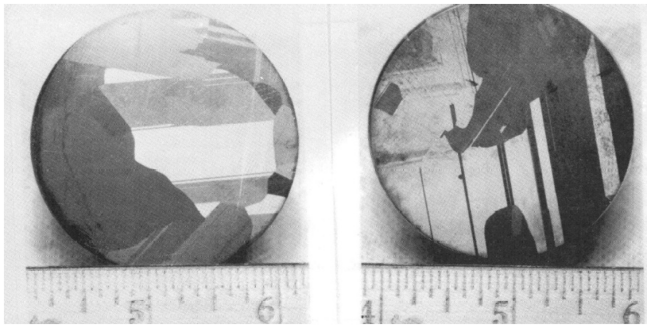

**Fig. 5.** Structure of (a) top and (b) bottom surfaces of 5.5 cm diameter CdTe ingot grown in HEM. HEM,

spontaneous nucleation will occur during the growth process in unseeded crystal growth. On the other hand, 5–7.5 cm diameter CdTe ingots were grown using the heat exchanger method (HEM). Khattak and Schmid [29] have reported that CdTe crystals with high stoichiometry and large twin-free samples could be obtained through the heat exchanger growth method. The EPD is calculated in the range of $10^3$–$10^5$ $cm^{-2}$. The dislocation density of the CdTe crystals grown using this method is lower compared to the Czochralski technique. Most of the HEM-grown CdTe samples have *p*-type conductivity, but the resistivity is found to be high (in the order of $10^5$ Ω cm). The optical properties like absorption coefficient have been reported in the range of 0.07 $cm^{-1}$. In order to nucleate larger grains, higher superheat temperature treatment of 80°C in 44 hours was utilized. Fig. 5 shows the cleaved CdTe structures, the top and bottom surfaces of the 2 cm long and 5.5 cm diameter wafer with 400 g ingot.

**3) Horizontal traveling heater method (HTHM)**

The horizontal traveling heater method (HTHM) was implemented by Genzel et al. [30] for the growth of $Hg_{1-x}Cd_xTe$ crystal. Rotation of the ampoule is necessary for the crystallization of the whole material in a cylindrical cross-section of the ingot with respect to the partially filled solution zone (Fig. 6). It is important to note that the HTHM crystal growth technique required complex experimental equipment to grow high-quality crystals, without presenting a definite advantage over vertical THM with ampoule rotation which is much easier to implement.

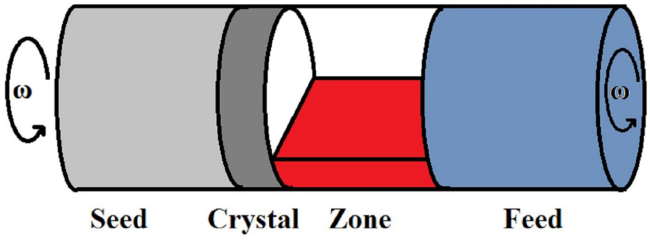


**Fig. 6.** Schematic representation of a horizontal traveling heater method crystal growth arrangement [9].

**4) Bridgman-growth method**

To the best of my knowledge, Shin et al. [31] are the first researchers who grew CdTe compound semiconducting material through the Bridgman method in the year 1983. However, they observed the presence of Te precipitate on the crystal surface and also predicted that there is a correlation between the presence of Te agglomerates and optical transmission. Route et al. [19] have investigated the melt/solid interface during vertical Bridgman growth with the aid of the autoradiography technique. Melt interfaces were controlled as convex shapes through thermal modifications, but no significant improvement was seen in the grain structure. Oda et al. [32] have grown CdTe single crystals by vertical Bridgman method with a translation rate regulated from 1 to 5 mm/h. The CdTe crystals were chemically etched using 3% of $Br_2$ methanol etchant for 3 minutes to calculate the dislocation density. Bridgman growth method is one of the economic and simple melt synthesis approaches for bulk crystallization, in which the ingot material is filled in a closed quartz/glass ampoule and melted under varying temperature gradients with an optimized translation rate. Many researchers have adopted the Bridgman growth method, because of its simplicity and relatively large growth rates as compared with the solution and vapor growth [20, 33-42]. Fiederle et al. [20] have synthesized CdTe crystals with 25, 45, and 75 mm diameters by the vertical Bridgman method, respectively. The reduced twins and growth of large single-crystalline grains in the order of 40 × 40 $mm^2$ helped to improve the crystallinity of the latter. The CdTe:Ge crystal of 75 mm diameter wafer with only seven small grains, two twins, and a large single crystal is grown by the modified Bridgman technique. To produce a good-quality wafer (Fig. 7a), high pure-source materials of 7N purity were selected, that is, high-quality quartz ampoules coated with carbon, also the temperature profile of the furnace was modified [20]. Modified Bridgman technique with the fabricate furnace, which allows the minute regulation of different degrees of superheating of the ingot melt before the growth process, is employed to synthesize CdTe single crystals by Saucedo et al. [38]. High-quality CdTe crystals with appreciable structural perfection and reduced Te precipitate concentration through modified Bridgman method with artificial seeding. Fig. 7b shows the CdTe crystal image grown via the modified Bridgman method; from the latter Fig. 7a, it is clear that the synthesized semiconductor has a 9 cm length with a 1 cm diameter. Also, region (2) represents the interface between seed and crystal, (1) corresponds to the seed material, and (3) is the grown crystal portion. The interface will determine the quality of the crystal; it may be planar, convex, or even concave. The critical optimization of the liquid–solid interface will play a vital role in all types of melt growth methods. There is a piece of wonderful information about the interface shape discussed by Cheuvart et al. [43]. On the other hand, the transverse gradient induces a strong thermal oscillation and turbulence, and the convection in a liquid increases the effective liquid thermal conductivity Kliq as well as the ratio $K_{liq}/K_{sol}$, which directly influences the shape of the liquid–solid interface during the crystal growth. Casagrande et al. [44] have grown 64 mm diameter single crystals of CdTe through a multi-zone vertical Bridgman furnace. Melt adhesion or spurious nucleation was optimized with the careful preparation and selection of the ampoule. The interface curvature

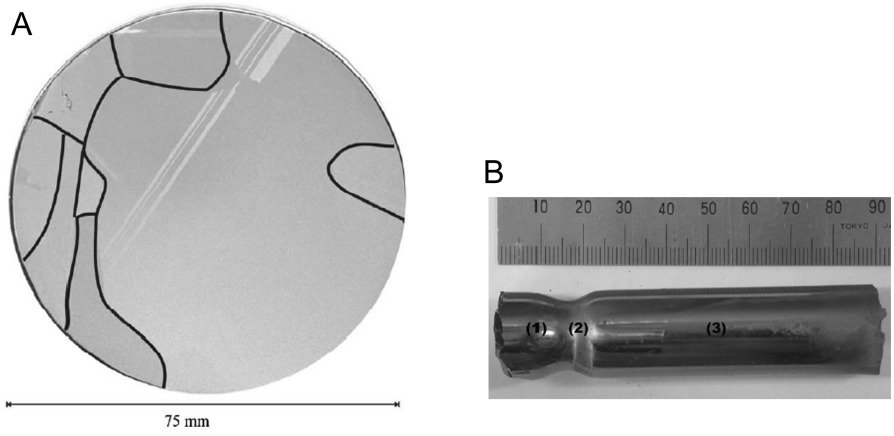


**Fig. 7.** (a) CdTe:Ge wafer with 75 mm diameter [18], (b) Typical CdTe crystal obtained by the modified Bridgman technique. The marked zones correspond to the seed to (1) the interface between the seed and the crystal, (2) the as-grown crystal (3) [36].

as well as the thermal stress during the crystallization portion of the boule is minimized by adjusting the hot and cold zone temperatures. They suggest that the post-solidification process is primarily important to reduce the slip defects in crystals. Bruder and co-workers [45] reported that when the cooling rates are greater than 10°C/h will result from an increase in the strain and low-angle grain boundaries. The high-pressure Bridgman technique offers an appreciable growth rate and good control of purity and chemical homogeneity, and the grown CdTe crystals gain size is comparable with the ingot formed inside the quartz ampoule synthesized by the vertical Bridgman method [46]. The careful optimization of melt–solid interface (to attain atomically flat interface) by controlling growth conditions like rotation speed, translation velocity, supercooling, etc., was reported by several authors [47-50].

**5) Gradient Freeze Method**

Tanaka et al. [51] reported that the vertical Bridgman and gradient freeze growth methods are appropriate for the crystallization of high-quality large CdTe crystals. In the gradient freeze method (Fig. 8a), the charge CdTe materials were sealed in an evacuated quartz ampoule (Fig. 8b) under a pressure of $10^{-6}$ torr. The pyrolytic carbon is coated inside the wall of the ampoule to avoid the reaction of residual Cd-oxide with the quartz. The pyrolytic layer will help to eliminate the contamination from oxides and the impurity particles from the inner walls of the ampoule as well as to prevent the adhesion of the ingot to the crucible inner wall [29]. The gradient freeze-grown CdTe crystals were found to be stoichiometric in the ratio of Cd:Te as 49.9:50.1.

**6) Liquinert-processed vertical Bridgman (LPVB) or Detached growth method**

The single crystals of CdTe were grown by the LPVB method. In this method, $SiCl_4$ strongly reacts with $H_2O$, following the reaction formula:

$$SiCl_4 + 2H_2O \rightarrow 2HCl + SiO_2$$

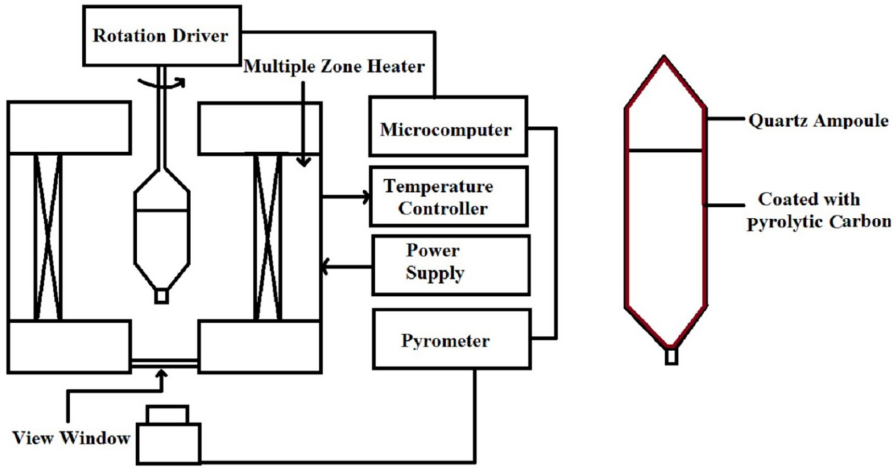


**Fig. 8.** (a) Schematic block diagram of a gradient freeze growth system [45] and (b) quartz ampoule for crystal growth.

As per the chemical reaction, the water content in the ampoule is adequately removed to obtain the liquinert state. Liquinert means that liquid is in an inert state. Thus, here $SiCl_4$ was used for the reduction of residual $H_2O$ in the growth container, raw material, and atmosphere during synthesis. The liquinert process for CdTe crystals is a two-step procedure, where the first stage involves the removal of the oxides from the base elements Cd and Te for the preparation of high-quality CdTe crystals, various processes such as vacuum distillation, reduction with hydrogen, and chemical etching, etc. Sekine et al. [12] have grown CdTe single crystals by adopting the LPVB method. The following are the emergent problems in CdTe crystal growth:

(i) Wetting and sticking on the crucible during crystal growth.
(ii) Avoiding crucibles with high thermal conductivity such as carbon.
(iii) Obtaining crystal growth with a stoichiometric composition.

The LPVB growth method is schematically illustrated in Fig. 9a. This schematic depiction of the experimental route systematically explains the various steps involved in this growth method. Photograph and XRD profile of the LPVB grown single crystal and the cleaved portion are shown in Fig. 9b-c. The single crystalline nature and the growth direction of the CdTe along (110) plane were confirmed with the assistance of X-ray diffraction (XRD) by Sekine et al. [12]. Yamada et al. [52] synthesized CdTe crystals in the bare quartz ampoule utilizing the vacuum distillation method, which helps to eliminate the presence of oxygen from the raw materials Cd and Te.

**B. Vapor Growth Method**

**1) Sublimation Method**

As reported by Teramoto [53], the bulk form of cadmium telluride binary chalcogenide semiconductor is grown from the vapor phase by the sublimation method, and recrystallization of the material is performed along a temperature gradient in the $N_2$ atmosphere. The vapor-deposited CdTe crystals have a cubic zinc-blende structure. The growth chamber used for the synthesis of single-crystalline CdTe through the sublimation method is portrayed in Fig. 10. High crystalline CdTe material is prepared mostly through melting by the Bridgman and zone-melting methods. The vapor growth method is not fair enough for the production of bulk crystals, but vapor-deposited crystals are superior for studying the growth mechanism and stoichiometric preparation of compound materials and probing various physical properties on as-grown faces. Important factors that affect the quality of the sublimation of CdTe crystal are listed below:

1. sublimation speed of CdTe precursor powder (function of the temperature of the powder),
2. particle size,
3. follow rate of the nitrogen carrier gas.

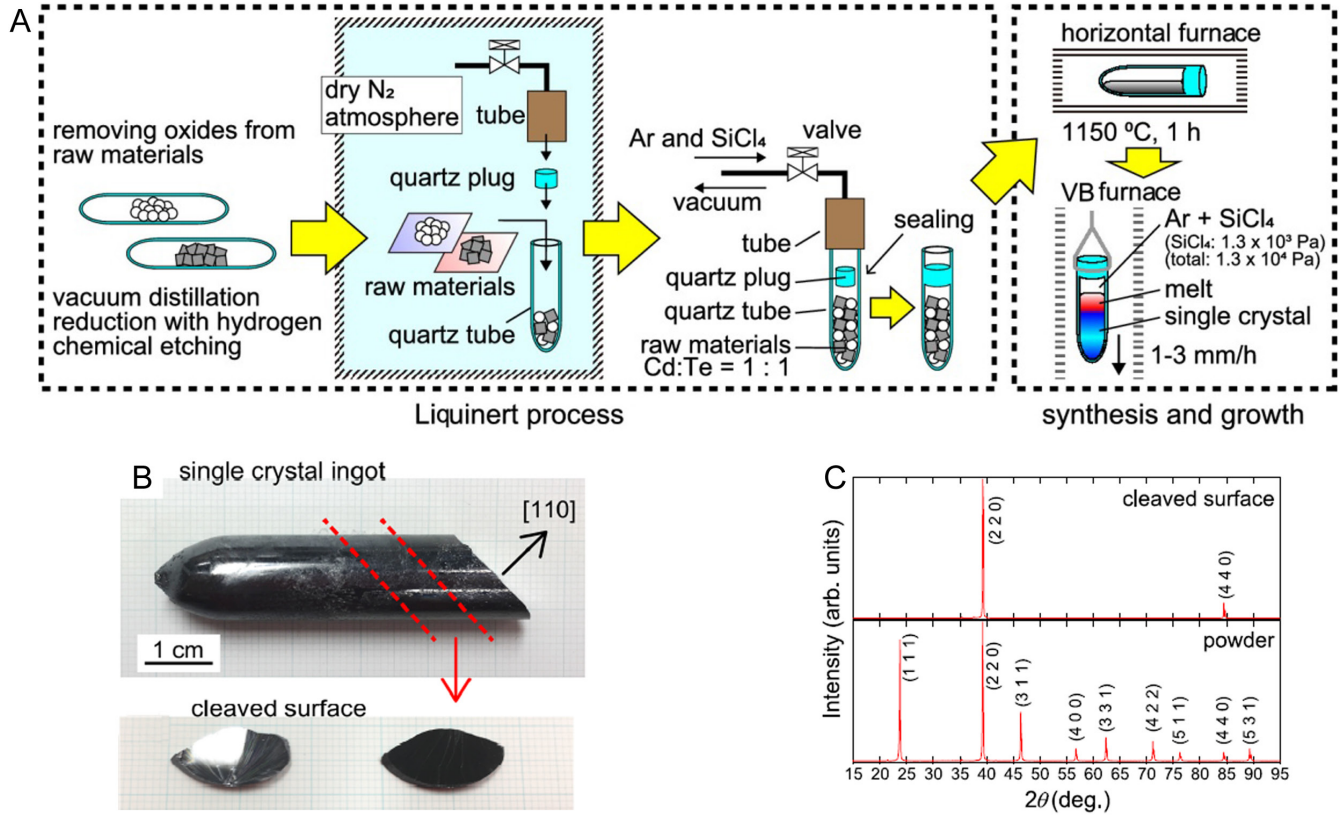


**Fig. 9.** (a) Schematic depiction of the LPVB furnace and crystal growth; (b) Photograph of CdTe single crystal and the cleaved portion and (c) XRD profile of the cleaved crystal as well as the powdered material [12]. LPVB, Liquinert-processed vertical Bridgman.

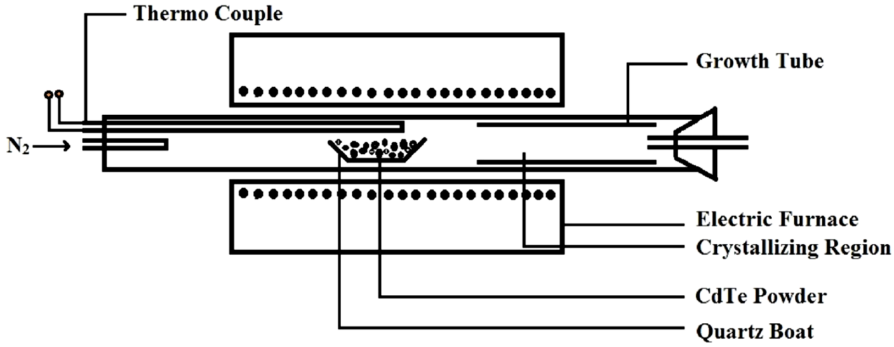


**Fig. 10.** Apparatus for crystal growth [45].

The vaporized CdTe powders are carried by the flow of nitrogen gas toward the boat region/low-temperature region of the growth zone. The problem associated with this vapor transport method is the contamination due to carrier agents during the synthesis process. This will adversely affect the physical properties of the CdTe crystal. The crystal habits depend on different factors such as (1) sublimation temperature, (2) growth temperature, and (3) flow rate of the nitrogen gas. The author [53] also reported that it is not possible to determine an accurate degree of supersaturation (*S*) and the temperature profile in the growth region. At low *S,* the dodecahedra and the hexagonal plates are formed, while at higher supersaturation, the other crystal morphologies are formed. Halliday et al. [54] reported the crystallization of CdTe by a new multi-tube vapor growth technique at a temperature of 700°C. Photoluminescence studies were implemented to probe the distribution of impurities and defects through the crystals. Synthesis occurred at a low temperature (700°C) compared to the melting point (1090°C) to produce high-quality crystal with reduced defect density, but the critical resolved shear stress increases with decreasing temperature. Reduction in thermal strain and background contamination are also benefits of the reduced growth temperature. In addition, the CdTe phase diagram favors the synthesis of the stoichiometric sample through the intentional reduction of temperature. Crystal synthesis via sublimation is in the spotlight in the field of crystal growth technology because of the versatile characteristics like stoichiometric preparation of compound materials, less contamination, and no moving parts in the growth furnace. This method could be able to produce diverse crystalline habits (surface morphology) and growth patterns, having superior properties to other melt or solution that has grown counterparts. Large dimensional (15 $cm^3$) CdTe single crystals are grown via the self-nucleation vapor method as reported by Grasza [55] but involving the translational movement of the ampoule along with the presence of hydrogen inside the tube. The grown crystals are found to be twinned in 30–80 vol% of the crystals and are oriented along the (110), (111), or (100) crystallographic direction. The pressure at which the vapor growth is performed inside the ampoule is 130 torr of hydrogen enclosed in a cold ampoule ensuring the reproducibility of the growth conditions and stable growth.

**2) Chemical Vapor Transport (CVT) Method**

Deposition of CdTe single crystals by employing the chemical vapor deposition in a closed tube arrangement is discussed in the literature [56, 57]. Paorici et al. [58] reported the growth of CdTe crystals by chemical vapor transport and using $NH_4Cl$ as a transporting agent. The use of carrier gases may contaminate the crystal lattice because of that additional cleaning or polishing is essential to remove such impurities from the crystal surface. Grasza [55] synthesized crystals 3.5 cm in length and 5.5 cm in diameter under 130 torr hydrogen atmosphere by vapor growth method of self-nucleation and the growth was carried out in a non-contact mode between the crystal and ampoule wall. Paorici and Pelosi [59] discussed the CVT growth of CdTe semiconductor. The chemical route is outlined below:

$$CdTe(s)+2HX(g)\rightarrow CdX_2(g)+H_2(g)+0.5Te_2(g)$$

Where, X = Cl, Br, and I provided that the thermodynamic environment is selected so that the Te partial pressure is balanced below its saturated value. This could help to avoid the formation of melt–solid interface during the chemical transport process. In this case, the CdTe crystal is synthesized by solid–liquid–vapor technique. On the other hand, the carrier gases may incorporate into the lattice sites during the growth, which will badly affect the optoelectronic properties of the sample. Moreover, in the presence of a solid phase constituted by chemically homogeneous CdTe, three independent heterogeneous equilibria can be written as follows:

$$CdTe(s)+I_2(g)\rightarrow CdI_2(g)+0.5Te_2(g)$$

$$CdTe(s)+2I(g)\rightarrow CdI_2(g)+0.5Te_2(g)$$

$$CdTe(s)\rightarrow Cd(g)+0.5Te_2(g)$$

**3) Horizontal Unseeded Vapor Growth Method**

The horizontal unseeded method is one of the vapor growth methods for the bulk synthesis of crystals, in which CdTe precursors are uniformly distributed in a silica glass tube. The ampoule was etched with the help of HF and $HNO_3$ solution before filling the source materials to avoid extraneous impurities from the ampoule and later baked at 1000°C [60]. However, this growth method is suitable for the growth of good quality as well as a mirror-like CdTe crystal along with stoichiometry because carrier gases or seeds were not used for this vapor deposition process. But this growth method took a long time for the production of crystals (around 2 weeks) as discussed by Auleytner et al. [61]. The CdTe crystals harvested from this method

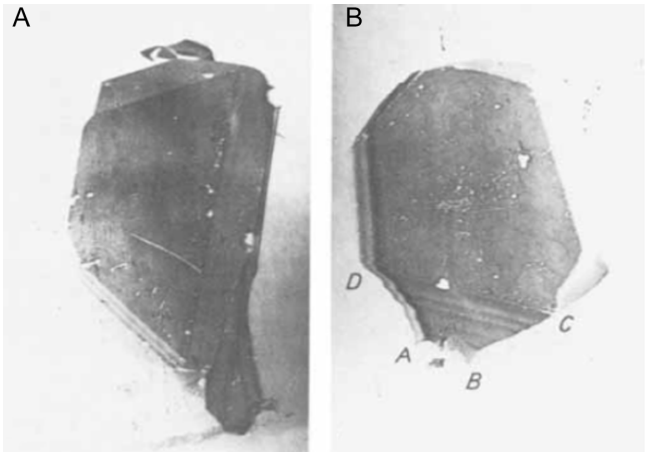


**Fig. 11.** CdTe crystals grown using horizontal vapor growth method [55].

are depicted in Fig. 11. Even though this crystal has some minute defects on the surface due to the over deposition of the atoms during the vapor growth, it has only a lower dislocation density than compared to the other melt or solution grown samples. Even though vapor growth is well known for the production of high-quality single crystals with diverse morphologies, the presence of structural defects in large single crystals of CdTe, non-stoichiometry, and the yield of small-sized crystals make this method inferior as compared to melt crystal growth [60].

### C. Solution Growth Method

#### 1) Traveling Heater Method (THM)

For decades, THM has been the most popular form of traveling solvent technique because it combines zone melting and solution growth. In THM, a molten zone is allowed to transport the source material through the slow movement of the ampoule relative to the heater, as shown in Fig. 12. Taguchi et al. [2] have grown high-quality CdTe single crystals by the THM. However, THM synthesis protocols have some demerits. It is difficult to avoid contamination from silica tubes and there is a high concentration of lattice defects during crystal growth at a temperature above the melting point. The inner pressure of the growth tube is precisely controlled by Te atoms, which are sufficiently supplied from the Te solution during crystal growth. The two emission bands from the energy range (1.42 and 1.10 eV) suggest that the grown crystals have Te vacancies, and 1.10 eV peak indicates the presence of imperfection. Taguchi et al. [2] have grown a high-purity CdTe single crystal from Te and $CdCl_2$ solutions by THM. Because of its (a) lower contamination and (b) lower defect density, THM is one of the most suitable techniques to grow high-purity single crystals. The Te and $CdCl_2$ are in the solution zone, which is melted with the help of a central resistance heater (as marked in Fig. 12). The furnace temperature is regulated to be high enough to dissolve the CdTe initial material to establish a concentration gradient. The zone-refined polycrystalline feed material dissolves into the hot solution region, diffuses down through the solution, and is deposited at the lower temperature region.

## VII. STRUCTURAL CHARACTERISTICS

The crystal structure and the quality of the unknown or known samples can be probed with the powder X-ray diffractometer. The growth method, internal and external structure, or the arrangement of atoms in the material will directly influence the physical properties. Shaaban et al. [62] discussed that the polycrystalline CdTe thin films have a zinc-blende (cubic) crystal structure. They also calculated the microstructure parameters, crystallite size, and microstrain and arrived at a conclusion that the crystalline size increases and microstrain decreases with film thicknesses. In the case of thin films, the peak intensity of the diffracted X-ray will increase with the film thickness, owing to the availability of the ordered atoms in the lattice points. In most of the optoelectronic applications, the researchers and the industries are looking for the single crystalline samples, because of the proper arrangement of atoms and bond strength which govern the performance of the device. While observing the peaks, we can be able to judge the crystallinity of the sample in a general manner. More broadness of the peak means lattice distortion or small particle size. Suppose the line width is small, it indicates good quality of the sample (proper arrangement of the atom along that direction). Careful determination of the planes and the

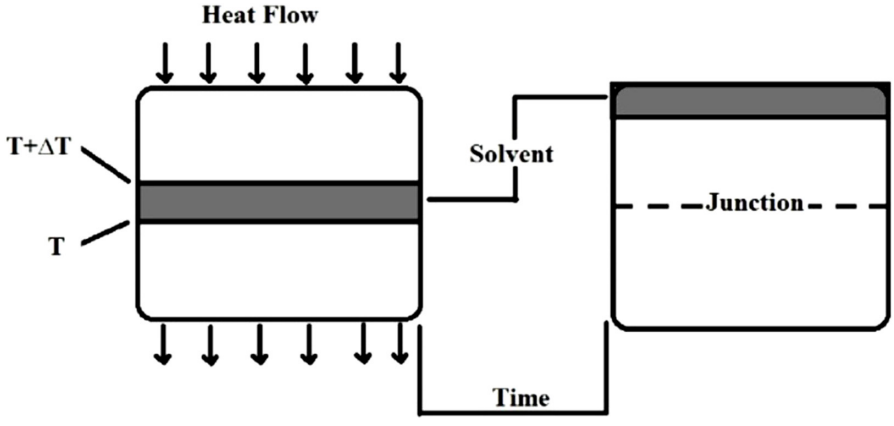


**Fig. 12.** Schematic depiction of the principle of traveling solvent method [2].

determination of the lattice parameters, density, cell volume, particle size, dislocation density, microstrain, etc. from the XRD data are enough to judge the crystal. The powder X-ray profiles of the CdTe single crystal and the powdered materials are presented in Fig. 9c. The right phase formation of the absorber material is inevitable for the fabrication of photovoltaic devices or any other electronic gadgets.

## VIII. OPTOELECTRONIC CHARACTERISTICS OF CDTE

### A. Optical Properties

Cadmium telluride single crystals have direct allowed band gap (1.43 eV). This allows the maximum absorption of photos from the sun light in a small thickness of the absorber than the indirect semiconducting materials like silicon and germanium. Even though CdTe has high toxicity and high melting temperature, the researchers are still behind this crystal due to the aforementioned reasons and its optimum electrical parameters for solar cell applications. The photoluminescence spectroscopy (PL) studies of the LPVB-grown CdTe crystals under a $SiCl_4$ atmosphere at 0 and $1.3 \times 10^3$ pa were conducted by Sekine et al. [12] and they reported the results obtained in both the atmosphere. Cadmium telluride crystals exhibit a sharp bound exciton peak at 1.59 eV, these peaks suggest the low carrier concentration. On the other hand, Halliday et al. [54] have grown CdTe single crystal through vapor growth method and measured the optical properties through PL analysis. Saha et al. [63] have reported the optical properties of the polycrystalline CdTe thin films deposited by direct method. The films were deposited at different thicknesses and the band gaps were measured. At 700 nm thickness of the film, the band gap was obtained as 1.56 eV. On the other hand, the less thickness films possess very high $E_g$ ranging from 1.62 to 1.94 eV; the micro-strain of these sample are found to be very high than the 700 nm thick film. This result suggests that as the thickness enhances, the optical band gap also increases. The CdTe crystal exhibits direct nature of absorption; hence, this material will effectively absorb the solar radiation in the visible region. Also, the band gap and absorption coefficient are optimum for the solar cell application. The dependence of optical constants on the deposition conditions of the thin film crystals, as well as the nature of doping, has also been studied. Yamada [64] reported that the melt grown CdTe have band gap of 1.43 eV, but they observed that excess of Cd and Te vacancies are the predominant canters in the crystals. The deviation of optical band gap in the CdTe thin films from 1.48 to 1.53 eV was observed, which is due to the polycrystallinity or the confinement effect of the small grins in the film surface [63].

### B. Electrical Properties

In general, the optoelectronic properties are the fundamental pillars for the selection of absorber as well as window layer for the solar cells. For an efficient photovoltaic device, the electrical parameters should be high, that is, the mobility and carrier concentration. On the other hand, the resistivity of the active or transparent layer should be low in order to enhance the carrier movement without any scattering or recombination. Inoue et al. [1] have grown CdTe crystals through the Bridgman method from the melt (melting point = 1090°C) at a pulling rate of 10 mm/h then the specimens were cut from single crystals of CdTe. However, the grown crystals have traces of Al, Si, Mg, and Ca elements. The CdTe crystals have *p*-type electrical conductivity, carrier concentrations ranging from $10^{12}$ to $10^{14}$/cm$^3$, mobility varied from 50 to 100 cm$^2$/V sec and the resistivity was in the order of 102–105 Ω cm. From the aforementioned results, it is clear that high mobility will enhance the collection efficiency of the carriers before it gets recombined. Also, the low resistivity reduces the scattering of the photogenerated carriers during the transport process in the solar cells. The uniform electrical resistivity in the order of $10^9$ Ω cm of the CdTe crystals is grown along the (100) crystallographic orientation by the vapor growth method [61]. To understand the electrical properties of the impure CdTe crystals, the Ge- and Sn-doped CdTe crystals were studied by Panchuk et al. [39]. The crystals were grown by the vertical and horizontal Bridgman method, respectively. The change in electrical properties like carrier mobility and density with respect to the extrinsic materials are presented in Table III. Numerous research efforts are going on the crystal growth to improve the quality of the final products to enhance the performance of the optoelectronic properties of the CdTe crystals. The carrier mobility of the CdTe crystal grown from $CdCl_2$ solution is much higher than the melt grown as well as the doped crystals, clear from Tables II and III. On the other hand, the carrier density of the Bridgman and solution-grown crystals was observed to be in the same order, but the doped CdTe crystals had low carrier concentration than the pure. Yamada [64] has reported that the melt-grown CdTe crystals exhibit *p*-type electrical conductivity with high resistivity at the enhanced temperature. As we discussed earlier about the importance of mobility in the solar cells, the CdTe samples show Hall mobility of 80 cm$^2$/V s, which is matching well with the standard data as presented in Tables II and III.

## IX. DEFECTS

The structural defects, impurities, dislocations, etc., on the crystals surface adversely affect the photovoltaic performance of the device.

**TABLE II.**
ELECTRICAL PROPERTIES AT ROOM TEMPERATURE IN INTRINSIC *P*-TYPE AND *N*-TYPE CDTE SINGLE CRYSTALS GROWN BY TRAVELING HEATER METHOD AND BRIDGMAN METHOD.

| Growth Method | Conduction | Carrier Life Time (μs) | Carrier Density (cm$^{-3}$) | Carrier Mobility (cm$^2$/V s) |
|---|---|---|---|---|
| Te solution [29] | *p* | 5.0 | $8 \times 10^{12}$ | 96 |
| $CdCl_2$ solution [29] | *n* | 8.2 | $1 \times 10^{16}$ | 1040 |
| Bridgman–Stockbarger [29] | *p* | <0.8 | $6 \times 10^{16}$ | 34 |
| Bridgman grown [38] | *p* | -- | $10^{12}$–$10^{14}$ | 50–100 |

**TABLE III.**
ELECTRICAL PROPERTIES OF CDTE CRYSTALS + GE(SN) AT ROOM TEMPERATURE [32].

| Growth Method | Conduction Type | Dopant | Carrier Concentration ($cm^{-3}$) | Mobility ($cm^2/V\ s$) |
|---|---|---|---|---|
| Bridgman method [34] | *P* | Ge | $10^8$–$10^{10}$ | 70 |
| Bridgman method [34] | *P* | Ge | $10^7$–$10^8$ | 70–80 |
| Bridgman method [34] | *N* | Sn | $1.5 \times 10^6$ | 850 |
| Bridgman method [34] | *n* | Sn | $2.4 \times 10^7$ | 710 |
| Bridgman method [34] | *n* | Sn | $4.7 \times 10^6$ | 610 |

In this regard, the information/study with regard to the defect formation in CdTe crystal is important. The polycrystalline structure or defects formation like twins, grains, etc. in CdTe is due to the Te-cluster as reported by Fiederle et al. [38]. They also suggest that the superheating of these products will help to overcome the formation of multiple grains during the synthesis process. Shin et al. [21] detected the presence of Te precipitates in grown CdTe crystals using diverse tools such as Auger spectroscopy, X-ray diffraction, and Raman spectroscopy. The presence of precipitate may act as a scattering center during the transport process, which will deteriorate the device's performance. Later, many researchers reduced the Te defects by annealing in Cd over pressure at 600–800°C. This leads to an improvement of the infrared transmission due to Cd annealing. The low thermal conductivity (0.06 W/cm K) of the CdTe crystal near the MP is the next main source, for twins and grains. So, the thermal distribution of the CdTe source material is not homogeneous and the solidification from liquid to solid is not constant during the crystallization process. As we all know, in melt growth, the morphology of liquid–solid interface has a significant influence on the quality of the crystals. Hence, the optimization of the interface is one of the major challenges in the field of the crystal engineering process to enhance the physical properties [47]. Several researchers employed dislocation studies to access the quality of the CdTe sample by a simple chemical etching method. On the other hand, both dislocation and inclusion density were dependent on the composition of the sample. Chemical etching is a facile chemical approach to unearth the nature and presence of dislocation on the crystal topography. During this, the solution or etchant may react with the crystal and remove the atoms or groups of atoms from the surface, if the atoms are arranged or bonded weakly. Both dislocation and inclusion density were dependent on the composition and the chemical bonding of the sample. Bissoli et al. [34] discussed the triangular-shaped etch pits on the CdTe single crystal. The micrographs of CdTe samples with different stoichiometry deviations are depicted in Fig. 13a-c. The variation of inclusion density with respect to the Te inclusion on the CdTe sample was graphically presented in Fig. 13d. On the other hand, the Bridgman grown crystals were chemically etched and the pits were found as spread in a cellular manner on the surface of the

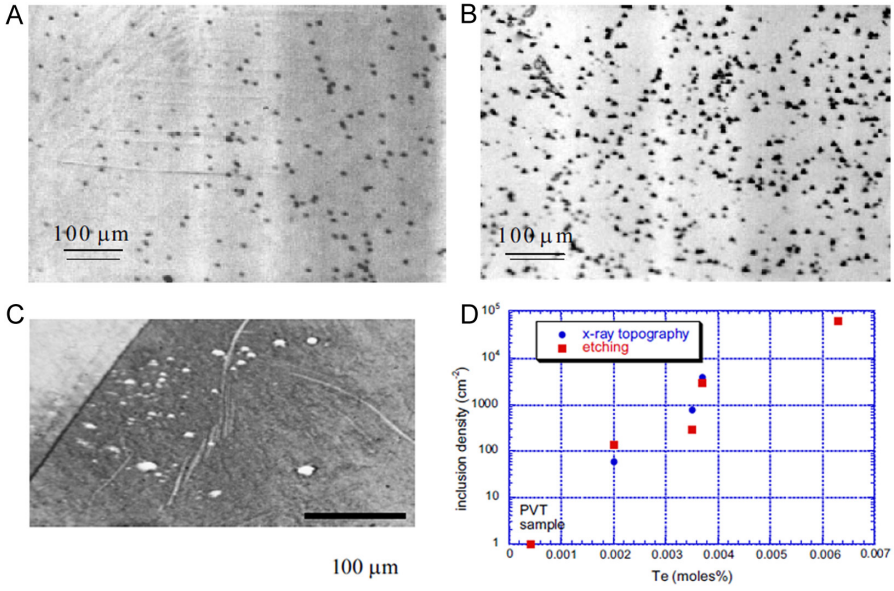


**Fig. 13.** Etching micrographs of CdTe samples with different stoichiometry deviations: (a) 0.0035 at%; (b) 0.0063 at%; (c) Te inclusions in CdTe crystals, and (d) dependence of the inclusion density on the deviation of the sample [22].

sample. This shape as well as the arrangement of the etch pits is due to the glide and climb of dislocations induced by thermal gradient at high temperature as explained by McDeitt et al. [41]. Sabinina et al. [21] studied and reported two types of grain boundaries on the melt-grown CdTe crystals, that is, high-angle and low-angle misoriented grain boundaries. The first one having more than 10° of misorientation between the adjacent grains and the low-angle grain boundary having 1° of misorientation among the adjacent sub-grain. So, the second one will not affect the functional parameters much as compared to the high-angle grain boundary. The small-angle grain boundary can be detected using the transmission electron microgram or scanning tunneling microscope. There is an argument that the dislocation in CdTe crystals is due to the condensation of point defects incorporated into the solid during its crystallization from the liquid state [39]. Hall and Vander Sande reported the relationship between deformation properties and the corresponding microstructural changes in CdTe crystals [40]. Fig. 14 shows the relationship between the shear stress ($\tau$) and the shear strain ($\gamma$) curve of CdTe crystals at different temperatures. As the temperature increased, the $\tau$ was found to decrease and $\gamma$ enhanced. This highlights the proper control of temperature during the experimental process. The dislocations, defects, and stacking faults have a deleterious effect on the performance of the crystals for any application. So, the defect-free crystals are the need of the hour to strengthen the fundamental research and device fabrication in diverse field. Oda et al. [32] reported the dislocation density of Bridgman grown CdTe which ranged from $8 \times 10^3$ to $2 \times 10^4$ $cm^{-1}$. It is interesting to point out that for any type of growth, the quality of the raw material is important, especially in the case of CdTe crystals, in which the low purity of the precursors leads to wetness in the ampoule. This is because of the sticking of the ingot material to the inner surface of the growth tube and the contamination from the ampoule, which further lead to the formation of cracks on both the ampoule as well as the crystal. The wetting is mainly due to the presence of oxygen both in CdO and $SiO_2$. At high temperature during the crystallization process, one reacts with another and produces oxide compounds such as $CdSiO_3$. This extrinsic compound formation is the fundamental reason behind the wetting of CdTe and the ampoule after the solidification process. To overcome these intricacies, the source material is properly purified and also the ampoule is cleaned thoroughly followed by drying but even the atmosphere can contribute oxygen to Cd and Te during the crystallization process. The chemical homogeneity, defects, dislocations, inclusions, etc., have a profound influence on the physical properties as well as the performance of the crystals and device. Therefore, it is imperative to reduce or optimize the chemical impurities or faults, grain boundaries, etc., in CdTe crystals by selecting the appropriate synthesis method. The following sections deal with the doping technology in CdTe crystals and the photovoltaic performance of CdTe absorber material to date.

## X. DOPING TECHNOLOGY IN CDTE CRYSTALS

The major constraints or challenges of the pure CdTe-based solar cell research is the achievement of a high hole density in the CdTe absorber layer by means of controlled acceptor doping. In this regard, Kranz et al. [61] discussed the effect of copper (Cu) doping on the resistivity of the CdTe layer on flexible glass slide, which is treated by $CdCl_2$ solution. Doping a minute amount of Cu ($0.8 \times 10^{15}$ atoms per $cm^2$) into a 5 μm thick CdTe layer drastically decreases the resistivity by the three orders of magnitude and also increases the hole density. This experimental outcome shows that the carrier hole density in the polycrystalline CdTe layers could be increased by the careful optimization concentration of the dopant. The controlled doping of Cu into the CdTe layer in the inverted heterojunction device structure by means of evaporation method and subsequent annealing treatment enables appreciable efficiencies up to 13.6%. The carrier density in the CdTe crystal can be altered by means of doping. This will help to tune the flow of current in the device (close circuit current), thereby enhancing the power conversion efficiency of the device. The first-principle calculations on the CdTe crystals suggest that Cu dopants can occupy the Cd atomic site acting as an acceptor, as well as the interstitial positions acting as a donor [66]. In situ arsenic (As) doping on the CdTe thin films by employing the metal organic chemical vapor deposition (MOCVD) method resulted in a high density of carriers, $3 \times 10^{16}$ $cm^{-3}$, as reported by Kartapou et al. [67]. Accordingly, the open-circuit voltage was increased but it became sensitive to interface recombination at the high concentration of arsenic.

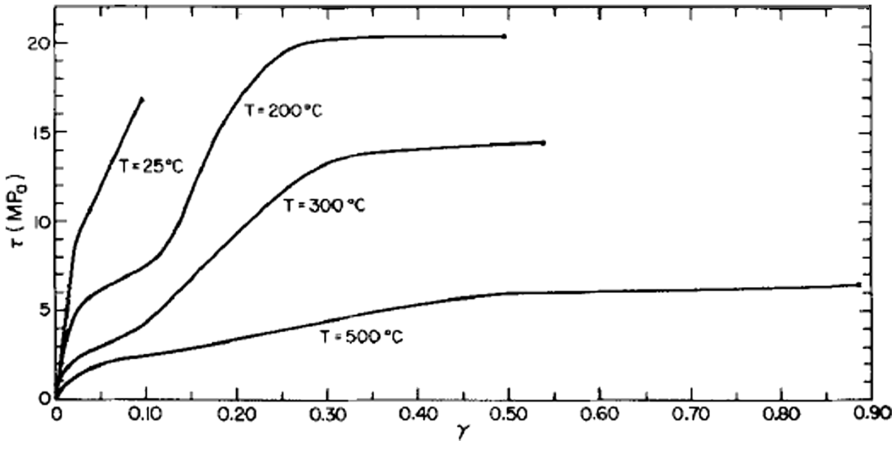


**Fig. 14.** Deformation behavior of CdTe single crystal [38].

## XI. APPLICATIONS

### A. Photovoltaic Performance

Competitions are still going on in the semiconductor industry on which absorber material will be able to overcome or rule over the elemental semiconductor silicon (Si) in the upcoming years. In this regard, drastic research is ongoing on compound semiconducting samples, especially on CdTe, GaAs, InP, etc. The GaAs materials are less attractive for the researchers because of the high toxicity problems, scarcity of the constituent elements (Ga and As), high melting temperature, and vapor pressure which facilitates complication in the growth of stoichiometric compounds. On the other hand, the CdTe solar cell reported a record cell efficiency of the order of 22.1% at the National Renewable Energy Laboratory (NREL), and the best commercial-size module efficiency is 11% [14]. The typical device structure of the CdTe solar cell includes a glass substrate, which is a transparent conducting oxide (TCO), *n*-CdS, *p*-CdTe, and finally a back conduct as reported by Halliday et al. [54]. This schematic diagram is presented in Fig. 1d. After Si-based solar cell, CdTe is the most popularly studied and well-understood material for solar cell fabrication. But still, there is a lack of a comprehensive data bank with regard to the functional parameters of CdTe crystals for energy harvesting applications. The basic knowledge of crystal, physical properties, and experimental protocols ease the fabrication of CdTe-based transistor as well as solar cell. Solar cell fabrication using CdTe crystals on the GaAs single-crystal substrates by MOCVD. Arsenic (As) and iodine (I) are used as dopants for *p*-type and *n*-type CdTe, respectively. On the other hand, the homojunction solar cell structure was fabricated by growing *n*-type CdTe directly on bulk *p*-type CdTe single-crystal substrates as reported by Su et al. [68]. Fig. 15 shows the schematic depiction of a polycrystalline wafer with randomly arranged number of grains and a single-crystal CdTe wafer. The research team also reported that the short-circuit current of the homojunction solar cell is less than 10 mA/cm$^2$. The open-circuit voltage of the device was 0.86 V. These results open up the possibility to enhance the efficacy of the CdTe solar cells as per the quality of source material like crystallinity, stoichiometry, thermal, mechanical, and optoelectronic properties.

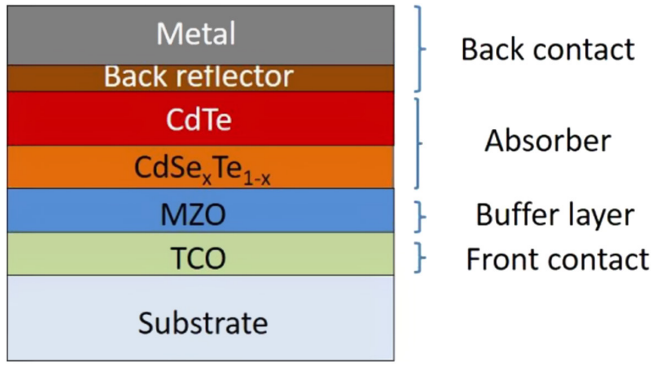


**Fig. 16.** Schematic depiction of the ITO/TCO/MZO/$CdSe_xTe_{1-x}$/CdTe/Back reflector/Metal device structure.

Romeo and Artegiani [69] reported that the CdTe solar cell has shown an improvement in the efficiency (η) during the recent years due to the development of efficient back contact or back reflector, modification of bandgap by doping $CdSe_xTe_{1-x}$ in the CdTe absorber, substitution of cadmium sulfide with MgZnO transparent buffer layer, and the novel redesign of the solar cell model (Fig. 16). For a very long time span, CdTe record efficiency had been kept constant at 16.7%, but recently, researches have reported that the CdTe single solar cell exhibited 22.1% and a module possesses 19% of efficiency [70]. Green et al. [71] demonstrated an efficiency of 15.8% on the CdTe-based solar cell. The sudden improvement in efficiency was obtained by a modified design of the CdTe solar cell device, elimination the of CdS buffer layer, considering new features such as bandgap grading using doping or the experimental protocols, copper incorporation into the lattice site of the CdTe crystals, and more transparent *n*-layer. These changes help the device to attain an efficiency of up to 21.5%, which later improved to 22.1% [72, 73]. The main reason behind these improved results has been gained from stoichiometric materials obtained from the production line. On the other hand, the open-circuit voltage value of this crystal is still below the elemental Si and GaAs absorber solar

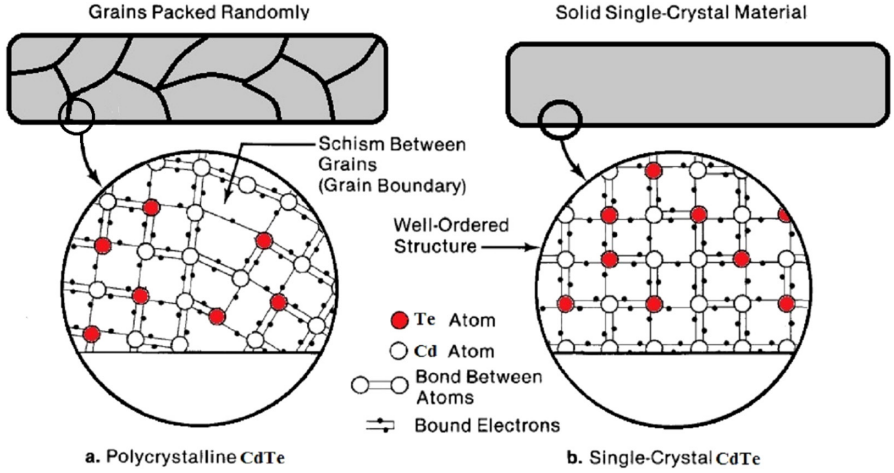


**Fig. 15.** Schematic depiction of the polycrystalline and single-crystalline CdTe crystals.

cells. This is due to the large improvement of the current density ($J_{sc}$), 30 mA/cm$^2$, [71]. Fig. 16 shows the schematic model of the thin-film solar cell, which revolutionized the CdTe device structure and enhanced the $J_{sc}$ and η. It is worthwhile to note that the comparison of quantum efficiency measurements of CdTe solar cells engineered using the CdSe buffer between CdS and CdTe by Paudel et al. [74] suggests that the enhancement in current density can be attributed to a specific fabrication of the heterojunctions. The introduction of CdSe increases the quantum efficiency response both in the blue (high energy) and in the long-wavelength region (825–930 nm). Therefore, the suitable mixing of the CdSe and CdTe layers by the activation treatment forms a photoactive $CdSe_xTe_{1-x}$ compound, which has a narrower bandgap than pure CdTe; hence, lower-energy photons are also absorbed by this semiconductor. The introduction of a Se-doped CdTe compound with $0.3 < x < 0.4$ reduces band gap of the absorber to approximately 1.4 eV. Moreover, when the CdS window layer is substituted with a more transparent MgZnO, it improves the band alignment with $CdSe_xTe_{1-x}$ decreasing in carrier loss [75]. CdSe layer of 100 nm thickness by sputtering followed by CdTe by closed sublimation process achieved a suitable $CdSe_xTe_{1-x}$ layer, recorded the current density of 29.8 mA/cm$^2$, as reported by Baines et al. [76]. The Schottky-queisser limit predicts that the CdTe absorber-based solar cell has record efficiency of around 32%; however, this η will be very difficult to attain, considering the limitations of the polycrystalline junction as well as the efficiency loss for the industrial scale. An alternative approach developed to reach very high efficiencies in a relatively short time is to combine different band gaps together in order to optimize light absorption and energy conversion. Multijunction solar cells reach very high efficiency but they need high costs for production and result in a non-particularly advantageous efficiency/cost ratio. Recently, alternative tandem-structured solar cells were fabricated with silicon crystalline in order to obtain high efficiency [77]. In the last few years, researchers are trying to grow high-quality CdTe source materials in order to enhance device efficiency. Hence, the present review pens down on the deposition and growth of less-defect CdTe crystals, which will give more insight into the enhancement of photovoltaic device characteristics.

## XII. CONCLUSION

This review work focuses on the various technologies to grow bulk CdTe crystals through melt, vapor, and solution approaches. There is no single source of information regarding the diverse types of growth methods for stoichiometric crystallization. So, this work tries to shorten the researcher's gap in comprehensive knowledge about the synthesis protocols, phase diagram, structural parameters, optical properties, electrical properties, defect formation, and applications in CdTe compound semiconductors. In terms of physical properties, we mainly focused on the structural, optical, and electrical characteristics of the CdTe crystal and the diverse factors affecting its homogeneous growth. The presence of defects in the CdTe crystals during the growth and after the growth is reviewed and discussed in detail. Moreover, the doping technology and CdTe-based applications in the field of solar cells are briefly discussed at the end of the section. Hence, this review will satisfy the CdTe crystal researchers, because all the physical properties have been tabulated and the possible CdTe growth method has been discussed.

**Peer-review:** Externally peer-reviewed.

**Acknowledgments:** The authors is grateful to Department of Physics and Electronics, CHRIST (Deemed to be University), Bangalore, Karnataka, India for the support and encouragement towards my research. The authors would also extent the thank to Prof. Peter Rudolf (former Editor of Journal of Crystal Growth) for his detailed explanations of diverse type's crystal growth techniques for CdTe single crystal during the program "Indian Summer School on Crystal Growth (ISSCG-2020)".

**Declaration of Interests:** The authors have no conflict of interest to declare.

**Funding:** The authors declared that this study has received no financial support.

## REFERENCES

1. M. Inoue, I. Teramoto, and S. Takayanagi, "Etch pits and polarity in CdTe crystals," *J. Appl. Phys.*, vol. 33, no. 8, pp. 2578–2582, 1962. [CrossRef]
2. T. Taguchi, J. Shirafuji, and Y. Inuishi, "Growth by travelling heater method and chracteristic of undoped high-resistivity CdTe," *Jpn. J. Appl. Phys.*, vol. 17, no. 8, p. 1331–1342, 1978. [CrossRef]
3. A. F. Tasch Jr., R. A. Chapman, and B. H. Breazeale, "Field-effect measurements on the HgCdTe surface," *J. Appl. Phys.*, vol. 41, no. 10, pp. 4202–4204, 1970. [CrossRef]
4. A. B. Chen, M. Van Schilfgaarde, and A. Sher, "Comparison of in 1– x Tl x Sb and $Hg_{1-x}Cd_xTe$ as long wavelength infrared materials," *J. Electron. Mater.*, vol. 22, no. 8, pp.843–846, 1993.
5. J. Shen, D. K. Aidun, L. Regel, and W. R. Wilcox, "Characterization of precipitates in CdTe and $Cd_{1-x}Zn_xTe$ grown by vertical Bridgman-Stockbarger technique," *J. Cryst. Growth*, vol. 132, no. 1–2, pp. 250–260, 1993. [CrossRef]
6. A. Sadao, "Optical constants of crystalline and amorphous semiconductors," *Numer. Data Graph. Inf.*, vol. 136, 1999.
7. O. Oda, *Compound Semiconductor Bulk Materials and Characterization*. London: World Scientific Publishing Co. Pte. Ltd, 2007.
8. T. Taguchi, J. Shirafuji, and Y. Inuishi, "Crystal growth by solvent techniques and characteristic properties of CdTe," *Rev. Phys. Appl. (Paris)*, vol. 12, no. 2, pp. 117–122, 1977. [CrossRef]
9. R. Triboulet, "Crystal growth by traveling heater method," In *Handbook of Crystal Growth*. Elsevier, 2015, pp. 459–504.
10. N. R. Kyle, "Growth of semi-insulating cadmium telluride," *J. Electrochem. Soc.*, vol. 118, no. 11, p.1790, 1971. [CrossRef]
11. T. Taguchi, J. Shirafuji, and Y. Inuishi, "Carrier transport and trapping process in high-resistivity CdTe grown by a modified THM," *Rev. Phys. Appl. (Paris)*, vol. 12, no. 2, pp. 189–193, 1977. [CrossRef]
12. R. Sekine *et al.*, "Growth and characterization of CdTe single crystals prepared by the "Liquinert processed" vertical Bridgman method for radiation detectors," *Cryst. Growth Des.*, vol. 19, no. 11, pp. 6218–6223, 2019. [CrossRef]
13. P. Rudolph, "Fundamental studies on Bridgman growth of CdTe," *Prog. Cryst. Growth Char. Mater.*, vol. 29, no. 1–4, pp. 275–381, 1994. [CrossRef]
14. T. K. Al-Hamdi *et al.*, "CdTe synthesis and crystal growth using the high-pressure Bridgman technique," *J. Cryst. Growth*, vol. 534, p. 125466, 2020. [CrossRef]
15. R. Triboulet, "Fundamentals of the CdTe synthesis," *J. Alloys Compd*, vol. 371, no. 1–2, pp. 67–71, 2004. [CrossRef]
16. J. Auleytner, J. Majewski, Z. Furmanik, and Z. Golacki, "X-ray characterization of CdTe crystals with natural faces," *Cryst. Res. Technol.*, vol. 25, no. 8, pp. 971–976, 1990. [CrossRef]

17. S. Wen-Bin, Y. Mei-Yun, and W. Wen-Hai, "Crystal growth and characterization of CdTe from the melt under controlled Cd partial pressure," *J. Cryst. Growth*, vol. 86, no. 1–4, pp. 127–131, 1988. [CrossRef]
18. Y. Zhao *et al.*, "MonocrystallineCdTe solar cells with open-circuit voltage over 1 V and efficiency of 17%," *Nat. Energy*, vol. 1, pp. 1–7, 2016.
19. R. K. Route, M. Wolf, and R. S. Feigelson, "Interface studies during vertical Bridgman CdTe crystal growth," *J. Cryst. Growth*, vol. 70, no. 1–2, pp. 379–385, 1984. [CrossRef]
20. M. Fiederle *et al.*, "Characterization of CdTe crystals grown by the Vertical Bridgman method," *Nucl. Instrum. Methods Phys. Res. A*, vol. 509, no. 1–3, pp.70–75, 2003. [CrossRef]
21. I. V. Sabinina, A. K. Gutakovski, T. I. Milenov, N. N. Lyakh, Y. O. Sidorov, and M. M. Gospodinov, "Melt growth of CdTe crystals and transmission electron microscopic investigations of their grain boundaries," *Cryst. Res. Technol.*, vol. 26, no. 8, pp.967–972, 1991. [CrossRef]
22. T. Taguchi, J. Shirafuji, and Y. Inuishi, "Crystal growth by solvent techniques and characteristic properties of CdTe," *Rev. Phys. Appl. (Paris)*, vol. 12, no. 2, pp. 117–122, 1977. [CrossRef]
23. T. Taguchi, J. Shirafuji, and Y. Inuishi, "Carrier transport and trapping process in high-resistivity CdTe grown by a modified THM," *Rev. Phys. Appl. (Paris)*, vol. 12, no. 2, pp. 189–193, 1977. [CrossRef]
24. C. H. Su, S. L. Lehoczky, B. Raghothamachar, and M. Dudley, "Crystal growth and characterization of CdTe grown by vertical gradient freeze," *Mater. Sci. Eng. B*, vol. 147, no. 1, pp. 35–42, 2008. [CrossRef]
25. R. K. Route, M. Wolf, and R. S. Feigelson, "Interface studies during vertical Bridgman CdTe crystal growth," *J. Cryst. Growth*, vol. 70, no. 1–2, pp. 379–385, 1984. [CrossRef]
26. I. M. Dharmadasa *et al.*, "Fabrication of CdS/CdTe-based thin film solar cells using an electrochemical technique," *Coatings*, vol. 4, no. 3, pp. 380–415, 2014. [CrossRef]
27. T. A. Gessert, and S. Ali, "1.19-cadmium telluride photovoltaic thin film: CdTe," In *Comprehensive Renewable Energy*. Oxford: Elsevier, 2012, pp. 423–438.
28. H. M. Hobgood, B. W. Swanson, and R. N. Thomas, "Czochralski growth of CdTe and CdMnTe from liquid encapsulated melts," *J. Cryst. Growth*, vol. 85, no. 3, pp. 510–520, 1987. [CrossRef]
29. C. P. Khattak, and F. Schmid, "Growth OfCdTe crystals by the heat exchanger method (HEMN),", In *Future Infrared Detector Materials*, Vol. 1106. International Society for Optics and Photonics, 1989.
30. C. Genzel, P. Gille, I. Hähnert, F. M. Kiessling, and P. Rudolph, "Structural perfection of $Hg_{1-x}Cd_xTe$ Grown by THM," *J. Cryst. Growth*, vol. 101, no. 1–4, pp. 232–236, 1990. [CrossRef]
31. S. H. Shin, J. Bajaj, L. A. Moudy, and D. T. Cheung, "Characterization of Te precipitates in CdTe crystals," *Appl. Phys. Lett.*, vol. 43, no. 1, pp. 68–70, 1983. [CrossRef]
32. O. Oda, K. Hirata, K. Matsumoto, and I. Tsuboya, "Growth of CdTecrustals by the vertical bridgman technique," *J. Cryst. Growth*, vol. 71, no. 1, pp. 273–276, 1985. [CrossRef]
33. S. H. Shin, J. Bajaj, L. A. Moudy, and D. T. Cheung, "Characterization of Te precipitates in CdTe crystals," *Appl. Phys. Lett.*, vol. 43, no. 1, pp. 68–70, 1983. [CrossRef]
34. F. Bissoli *et al.*, "Stoichiometry related defects in CdTe crystals," *Phys. Status Solidi (C)*, vol. 1, no. 4, pp. 735–738, 2004. [CrossRef]
35. T. Taguchi, J. Shirafuji, and Y. Inuishi, "Excitonic emission in cadmium telluride, " *Phys Stat Sol (B)*, vol. 68, no. 2, pp. 727–738, 1975. [CrossRef]
36. T. Taguchi, J. Shirafuji, T. Kobayasmt, and Y. Inuishi, "High purity CdTe and its application to radiation detectors," *Jpn. J. Appl. Phys.*, vol. 15, no. S1, p. 267, 1976. [CrossRef]
37. T. Taguchi, J. Yamamoto, J. Shirafuji, and Y. Inuishi, "Magneto-luminescence of excitons bound to neutral acceptor in cadmium telluride," *Solid State Commun.*, vol. 19, no. 11, pp. 1037–1039, 1976. [CrossRef]
38. E. Saucedo, P. Rudolph, and E. Dieguez, "Modified Bridgman growth of CdTe crystals," *J. Cryst. Growth*, vol. 310, no. 7–9, pp. 2067–2071, 2008. [CrossRef]
39. O. Panchuk *et al.*, "IV group dopant compensation effect in CdTe," *J. Cryst. Growth*, vol. 197, no. 3, pp. 607–611, 1999. [CrossRef]
40. S. Wen-Bin, Y. Mei-Yun, and W. Wen-Hai, "Crystal growth and characterization of CdTe from the melt under controlled Cd partial pressure," *J. Cryst. Growth*, vol. 86, no. 1–4, pp. 127–131, 1988. [CrossRef]
41. S. McDevitt, B. E. Dean, D. G. Ryding, F. J. Scheltens, and S. Mahajan, "Characterization of CdTe and (Cd, Zn) Te single-crystal substrates," *Mater. Lett.*, vol. 4, no. 11–12, pp. 451–454, 1986. [CrossRef]
42. E. L. Hall, and J. B. V. Sande, "Plastic deformation behavior and dislocation structure of CdTe single crystals," *J. Am. Ceram. Soc.*, vol. 61, no. 9–10, pp. 417–425, 1978. [CrossRef]
43. P. Cheuvart, U. El-Hanani, D. Schneider, and R. Triboulet, "CdTe and CdZnTe crystal growth by horizontal Bridgman technique," *J. Cryst. Growth*, vol. 101, no. 1–4, pp. 270–274, 1990. [CrossRef]
44. L. G. Casagrande, D. Di Marzio, M. B. Lee, D. J. Larson Jr., M. Dudley, and T. Fanning, "Vertical Bridgman growth and characterization of large-diameter single-crystal CdTe," *J. Cryst. Growth*, vol. 128, no. 1–4, pp. 576–581, 1993. [CrossRef]
45. M. Bruder, H. -J. Schwarz, R. Schmitt, H. Maier, and M. -O. Möller, "Vertical Bridgman growth of CD1– yZnyTe and characterization of substrates for use," in *J. Cryst. Growth*, vol. 101, no. 1–4, pp. 266–269, 1990. [CrossRef]
46. T. D. Lee, and A. U. Ebong, "A review of thin film solar cell technologies and challenges," *Renew. Sustain. Energy Rev.*, vol. 70, pp. 1286–1297, 2017. [CrossRef]
47. A. G. Kunjomana, J. Bibin, R. Karthikeyan, and S. Varadharajaperumal, "Effect of supercooling on the microstructural development and optimization of physical properties of melt grown SnSe crystals," *J. Mater. Sci. Mater. Electron.*, vol. 30, no. 15, pp. 14300–14311, 2019. [CrossRef]
48. H. N. G. Wadley, and K. P. Dharmasena, "Methods for liquid-solid interface shape and location discrimination during eddy current sensing of Bridgman growth," *J. Cryst. Growth*, vol. 172, no. 3–4, pp. 313–322, 1997. [CrossRef]
49. K. R., B. John, and A. G. Kunjomana, "Crystal growth modeling and characteristics of antimony selenide," *Int. J. Curr. Res. Rev.*, vol. 10, no. 21, p. 30–31, 2018. [CrossRef]
50. R. Schoenholz, R. Dian, and R. Nitsche, "Growth of cadmium telluride crystals by an improved travelling heater method," *J. Cryst. Growth*, vol. 72, no. 1–2, pp. 72–79, 1985. [CrossRef]
51. A. Tanaka, Y. Masa, S. Seto, and T. Kawasaki, "High quality CdTe growth by gradient freeze method," *MRS Proc.*, vol. 90, 1986. [CrossRef]
52. S. Yamada, "On the electrical and optical properties of p-type cadmium telluride crystals," *J. Phys. Soc. Jpn*, vol. 15, no. 11, pp.1940–1944, 1960. [CrossRef]
53. I. Teramoto, "Vapour growth patterns of CdTe crystals," *Philos. Mag.*, vol. 8, no. 87, pp. 357–366, 1963. [CrossRef]
54. D. P. Halliday, M. D. G. Potter, J. T. Mullins, and A. W. Brinkman, "Photoluminescence study of a bulk vapour grown CdTe crystal," *J. Cryst. Growth*, vol. 220, no. 1–2, pp. 30–38, 2000. [CrossRef]
55. K. Grasza, "Bulk vapour growth of CdTe," *J. Cryst. Growth*, vol. 146, no. 1–4, pp. 65–68, 1995. [CrossRef]
56. H. Wiedemeier, Y. R. Ge, M. A. Hutchins, and Y. G. Sha, "Growth of Hg1– xCdxTe epitaxial layers on (100) CdTe by chemical vapor transport under normal and reduced gravity conditions," *J. Cryst. Growth*, vol. 146, no. 1–4, pp.610–618, 1995. [CrossRef]
57. H. Wiedemeier, Y. -R. Ge, and M. A. Hutchins, "Effects of microgravity on Hg1– xCdxTe/(100) CdTeepitaxy by CVT under transient growth conditions," *J. Cryst. Growth*, vol. 187, no. 1, pp. 72–80, 1998. [CrossRef]

58. C. Paorici, V. Pessina, and L. Zecchina, "Interface kinetical limitations in closed-tube chemical vapour transport (I)," *Cryst. Res. Technol.*, vol. 21, no. 9, pp. 1149–1152, 1986. [CrossRef]
59. C. Paorici, and C. Pelosi, "Vapour phase chemical transport properties of the cadmium telluride-iodine system," *Rev. Phys. Appl. (Paris)*, vol. 12, no. 2, pp. 155–159, 1977. [CrossRef]
60. K. Durose, and G. J. Russell, "Structural defects in CdTe crystals grown by two different vapour phase techniques," *J. Cryst. Growth*, vol. 86, no. 1–4, pp. 471–476, 1988. [CrossRef]
61. J. Auleytner, J. Majewski, Z. Furmanik, and Z. Golacki, "X-ray characterization of CdTe crystals with natural faces," *Cryst. Res. Technol.*, vol. 25, no. 8, pp. 971–976, 1990. [CrossRef]
62. E. R. Shaaban, N. Afify, and A. El-Taher, "Effect of film thickness on microstructure parameters and optical constants of CdTe thin films," *J. Alloys Compd*, vol. 482, no. 1–2, pp. 400–404, 2009. [CrossRef]
63. S. Saha, U. Pal, A. K. Chaudhuri, V. V. Rao, and H. D. Banerjee, "Optical properties of CdTe thin films," *Phys. Stat. Sol. (a)*, vol. 114, no. 2, pp. 721–729, 1989. [CrossRef]
64. S. Yamada, "On the electrical and optical properties of p-type cadmium telluride crystals," *J. Phys. Soc. Jpn*, vol. 15, no. 11, pp. 1940–1944, 1960. [CrossRef]
65. L. Kranz *et al.*, "Doping of polycrystalline CdTe for high-efficiency solar cells on flexible metal foil," *Nat. Commun.*, vol. 4, pp. 2306, 2013. [CrossRef]
66. S. H. Wei, and S. B. Zhang, "First-principles study of doping limits of CdTe," *Phys Stat Sol (b)*, vol. 229, no. 1, pp.305–310, 2002. [CrossRef]
67. G. Kartopu *et al.*, "Study of thin film poly-crystalline CdTe solar cells presenting high acceptor concentrations achieved by in-situ arsenic doping," *Sol. Energy Mater. Sol. Cells*, vol. 194, pp. 259–267, 2019. [CrossRef]
68. P. Y. Su, R. Dahal, G. C. Wang, S. Zhang, T. M. Lu, and I. B. Bhat, "Single-crystal CdTe homojunction structures for solar cell applications," *J. Electron. Mater.*, vol. 44, no. 9, pp. 3118–3123, 2015. [CrossRef]
69. A. Romeo, and E. Artegiani, "CdTe-based thin film solar cells: Past, present and future," *Energies*, vol. 14, no. 6, p.1684, 2021. [CrossRef]
70. M. Green, E. Dunlop, J. Hohl-Ebinger, M. Yoshita, N. Kopidakis, and X. Hao, Solar cell efficiency tables. 57th version. *Progress in Photovoltaics: Research and Applications*, vol. 29, no. 1, pp.3–15, 2021.
71. J. Britt, and C. Ferekides, "Thin-film CdS/CdTe solar cell with 15.8% efficiency," *Appl. Phys. Lett.*, vol. 62, no. 22, pp. 2851–2852, 1993. [CrossRef]
72. A. Rix, J. D. T. Steyl, J. Rudman, U. Terblanche, and J. L. van Niekerk, *First Solar's CdTe Module Technology–Performance, Life Cycle, Health and Safety Impact Assessment*. Centre for Renewable and Sustainable Energy Studies, 2015.
73. M. A. Green, E. D. Dunlop, J. Hohl-Ebinger, M. Yoshita, N. Kopidakis, and X. Hao, Solar cell efficiency tables. 56th version. *Progress in Photovoltaics: Research and Applications*, vol. 28, no. 7, pp.629–638, 2020.
74. N. R. Paudel, and Y. Yan, "Enhancing the photo-currents of CdTe thin-film solar cells in both short and long wavelength regions," *Appl. Phys. Lett.*, vol. 105, no. 18, p.183510, 2014. [CrossRef]
75. X. Yang *et al.*, "Preparation and characterization of pulsed laser deposited a novel CdS/CdSe composite window layer for CdTe thin film solar cell," *Appl. Surf. Sci.*, vol. 367, pp. 480–484, 2016. [CrossRef]
76. T. Baines *et al.*, "Incorporation of CdSe layers into CdTe thin film solar cells," *Sol. Energy Mater. Sol. Cells*, vol. 180, pp. 196–204, 2018. [CrossRef]
77. S. E. Sofia, J. P. Mailoa, D. N. Weiss, B. J. Stanbery, T. Buonassisi, and I. M. Peters, "Economic viability of thin-film tandem solar modules in the United States," *Nat. Energy*, vol. 3, no. 5, pp. 387–394, 2018. [CrossRef]

**Appendix**

The position of cadmium (Cd) and tellurium (Te) in the periodic table were highlighted in a thick black square box marked in Fig. S1. Cadmium is a silvery white colored soft metal with an atomic number 48. But, tellurium is a brittle and little toxic semimetallic element with an atomic number of 52.

Romeo and Artegiani [48] have reported tha the CdTe solar cell devices with superstrate configuration (see Fig. S2) are the best option in terms of efficiency, primarily because this structure allows the necessary post deposition treatment to be effective manner without any damage of the fabricated product. Generally, the window and absorber layers in cadmium telluride cells (CdS and CdTe) are grown on the front contact, which is a degenerately-doped semiconductor, typically an oxide layer, defined as transparent conducting oxides (TCO) like indium tin oxide (ITO) or fluorine-doped tin oxide (FTO). The supporting substrate is preferably a low-cost soda-lime glass when the deposition is obtained at substrate temperatures below 450°C (melting temperature of glass ~ 500°C), otherwise a more expensive alkali-free glass needs to be applied in case of high substrate temperature.

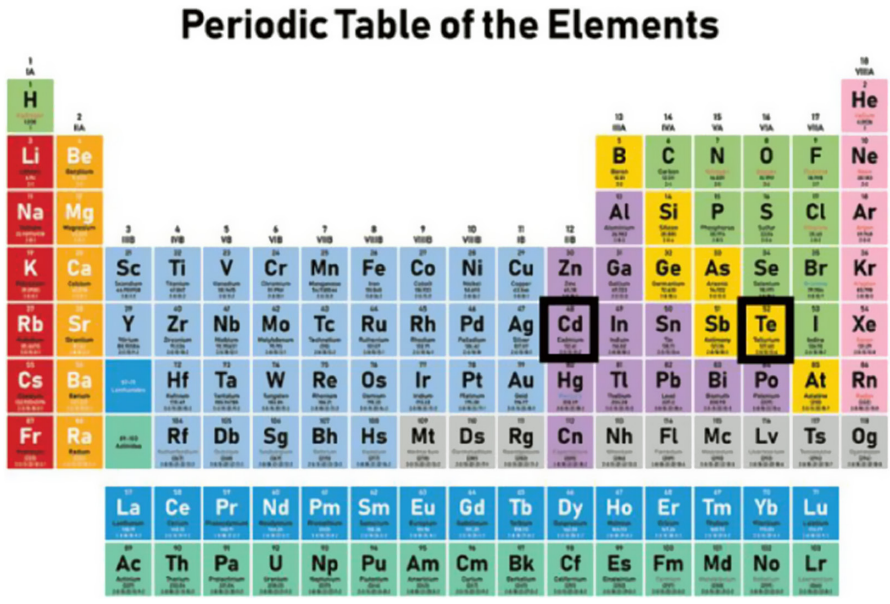


**Fig. S1.** Cd and Te were marked in the periodic table.

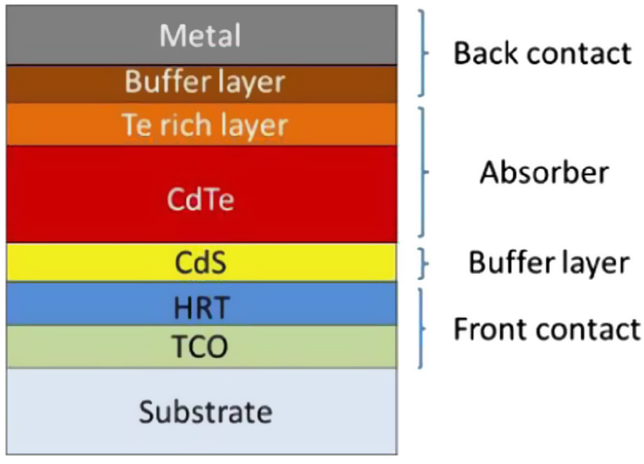


**Fig. S2.** Schematic of a standard superstrate CdTe based solar cell [54].

cigre Turkey

TEPES
TURKISH JOURNAL OF ELECTRICAL POWER AND ENERGY SYSTEMS

TEPES, Vol. 2, Issue. 2, 197-218, 2022 **DOI:** 10.5152/tepes.2022.22023

REVIEW

# A Study on Challenges in Adoption of Electric Vehicle and Vehicle-to-Grid Technologies in India

**Kola Sampangi Sambaiah**

Department of Electronics and Communication Engineering, PES University, Bengaluru, Karnataka, India

**Cite this article as:** K. S. Sambaiah, "A study on challenges in adoption of electric vehicle and vehicle-to grid-technologies in india," *Turk J Electr Power Energy Syst*, 2022; 2(2), 197-218.

## ABSTRACT

A viable remedy for lowering hazardous greenhouse gas emissions and carbon footprint is through the adoption of electric vehicles (EVs). Electric vehicles minimize fossil fuel reliance and ozone-damaging compounds by supporting large-scale renewable deployment. However, EV modeling and manufacturing are continuing to change despite extensive study on the qualities and characteristics that are evaluated from time to time. This is due to restrictions on EV adoption and their charging infrastructure. The present study addresses the numerous modeling approaches and optimization strategies used in studies of EV, hybrid, plug-in hybrid, battery, and fuel cell EV penetration and adoption rates in the market. The study is unique for a developing country like India in that it addresses crucial challenges in adoption and the lack of charging facilities for EV consumers. In addition, when renewable energy sources are unavailable, the development and deployment of the vehicle-to-grid concept is an innovative strategy to provide auxiliary supply to the grid. It is concluded that considering the unique features of EVs is vital to their adoption and mobility.

**Index Terms**—Carbon footprint, electric vehicles, optimization strategies, renewable deployment, vehicle to the grid

## I. INTRODUCTION

The automobile sector in India is modeling and manufacturing electric vehicles (EVs) at a rapid pace. People are substantially opting for EVs. The significant adoption of EVs tends to contribute to energy security, enhance air quality, and improve economic opportunity in the country. The government of India recognized the necessity to investigate viable mobility options to minimize dependency on energy sources imported, lower greenhouse gas emissions, and reduce the effect of global warming through effective compensation. Carbon dioxide ($CO_2$) emissions can be lowered by implementing preventative actions to avoid catastrophic climate change, which poses a threat to the planet's biodiversity. The major attempts are to use fossil fuels as low as possible for the production of power and transportation and to conserve energy. Electric vehicles are an alternative source to internal combustion engines (ICE) for transportation. Electric vehicles can reduce $CO_2$ emissions significantly [1].

Despite EVs' introduction, people are yet dependent on fossil fuel-powered ICEs. Electric vehicles, on the other hand, face significant challenges compared to conventional vehicles in terms of driving range, charging, and life cycle assessment (LCA). Electric vehicle production produces 59% more $CO_2$ than production. Based on tank-to-wheel, LCA increases up to 170–180 g/km $CO_2$ emissions from the ICE. Estimation of the average $CO_2$ emissions of a vehicle is measured over its entire life cycle, rather than over a single vehicle. Depending on the power source used to manufacture and drive, the overall $CO_2$ emissions over its lifetime can vary significantly [2].

A growing number of automakers are concerned about transportation-related pollution and are making significant investments in EV technology. India's adoption of EVs could be boosted by several factors including technological advancement, lower vehicle costs, government policy support, incentives for vehicle purchases, parking benefits, and good public charging infrastructure. There is a negligible amount of EVs in the Indian market because of low production. Electric vehicles can be classified into the following:

1) four-wheelers (electric cars);
2) three-wheelers (E-rickshaws); and
3) two-wheelers (E-bikes).

**Corresponding author:** Kola Sampangi Sambaiah, sambaiahks@gmail.com

**Received:** May 26, 2022
**Accepted:** July 18, 2022
**Publication Date:** August 18, 2022

During the early 2000s, an Indian company launched "The Reva," an EV that aims to produce affordable cars using innovative technology. Later, several automobile companies showed their interest in EV modeling and manufacturing. Figure 1 illustrates the evolution of EVs in India in various automobile industries [3].

Amounting to 3.2 billion metric tons of $CO_2$ equivalent, India's greenhouse gas emissions in 2014 accounted for 6.55% of global emissions. Following the manufacturing, energy sector, land utilization, forestry, and agriculture waste account for 19.6% of India's greenhouse gas emissions, while waste contributes only 1.9%. India's $CO_2$ emissions in 2020 were 2411.7 million metric tons. Over the last 50 years, India's $CO_2$ emissions have increased significantly, from 214.7 to 2411.7 million metric tons per year, reaching a peak of 11.40% in 2009 and then falling to −5.93%t in 2020 [4,5].

An EV can be employed as an adjustable load to assist grid normalization if it generates a considerable amount of stochastic renewable energy [6]. Due to single and low-power operations, the owners of EVs do not have a transaction in the power market [7]. Several authors have proposed existing practices for estimating current smart policies that are exogenous and have designed in advance for changing scenarios. Flexible load and clever charging procedures must be implemented to fully realize an EV's potential [8-13]. In another study, it is found that EV user's planning and operation information has been offered to the aggregator in terms of energy usage, and the timeliness requirement specifies how quickly a charging procedure must be finished, whereas the energy need is supported by the battery level [14]. According to a similar study, a decentralized structure and a central organization will deliver the pricing indication to EV owners, with the centralized and decentralized structures expected to overlap [15].

**Main Points**

- This study provides an overview of the hurdles and constraints of an electric vehicle (EV) in the Indian scenario (as the EV industry grows, the emphasis should shift from intervention to real adoption. It is also vital to analyze the gap between purpose and actual conduct).
- The present study's key research need is consumer awareness and abilities for assessing and estimating the economic benefit and cost of EVs.
- This study aims to determine the necessary procedures, obstacles, and problems of operating a battery-powered car in a developing nation like India.
- This study figures out why EVs have not gotten much traction in India.
- One of the goals of this study is to raise awareness in India about the benefits of battery-powered automobiles over traditional fossil fuel vehicles.
- This study also intends to investigate the various government efforts aimed at encouraging electric and hybrid vehicles.
- Future directions of research on how to best educate customers might have complications for policymakers and marketers seeking to understand the financial benefits and costs of EVs.

In 2016, an investigation was conducted on EV's stochastic simulation approach for producing a dynamic trip itinerary and charging profile for EV propulsion in a realistic scenario. Later, they determined that if the circumstances of distribution in parking time were modified, the distribution accuracy of parking time, and the model's complete accuracy, would improve [16].

A survey has been conducted on the charging behavior of EV owners, and it is found that the owners are preferring to charge their vehicles during peak demand times at home [17]. In Ireland, an investigation has been conducted to check the effectiveness and harmful effects of charging EVs during peak and off-peak hours, and it is noticed that charging during peak hours is more harmful than during off-peak hours [18]. For introducing new and innovative technologies, investigation of critical impediments to an EV in two nations is a necessary tool and strategy [19,20]. In [21], authors developed recognition of driving pattern strategy to calculate the trip portion of EVs' driving range using segmentation method. A vehicle model has been built to evaluate various driving circumstances and topographies in [22].

In [23], authors investigated the influence of EVs on Swiss distribution substations and observed that dynamic tariffs and greater integration levels increase the danger of overloading in specific zones. The range type of these parameters is then used to compare them to one another. Model-based non-linear observers were used to estimate the torque of a permanent magnet synchronous motor for hybrid EVs and to investigate the impact of various charging methods for EVs' storage utilization on the national grid as presented in [24-26]. In [27,28], authors have developed the maximum transmissible torque approach to enhance the implementation of the torque control context and the permanence of EVs.

An overview of important difficulties in the management of Li-ion batteries in an EV was presented and issues such as cell voltage, state estimate, uniformity, stabilization, and battery fault analysis may give impetus for the battery management system research and design [29].

In the literature, several authors have investigated optimal modeling of energy management systems with suitable techniques for EVs. The major communication between the grid and EVs is through charging and discharging. The three diverse ways of EV interaction with the grid are grid-to-vehicle (G2V), vehicle-to-building (V2B), and vehicle-to-grid (V2G). In G2V, the grid provides a charging facility for EV, and in V2G, it is discharged to the grid. It is important to control V2G at regular intervals due to the electrical energy bidirectional flow between the vehicle and the grid. The V2G system refers to the integration of EVs into the electrical grid. The electrical energy will be stored in a portable battery, and it can be transferred from the stored source to the building in V2B [30,31].

The major contribution of this study is as follows:

1. It provides an overview of the hurdles and constraints of an EV in the Indian scenario (as the EV industry grows, the emphasis

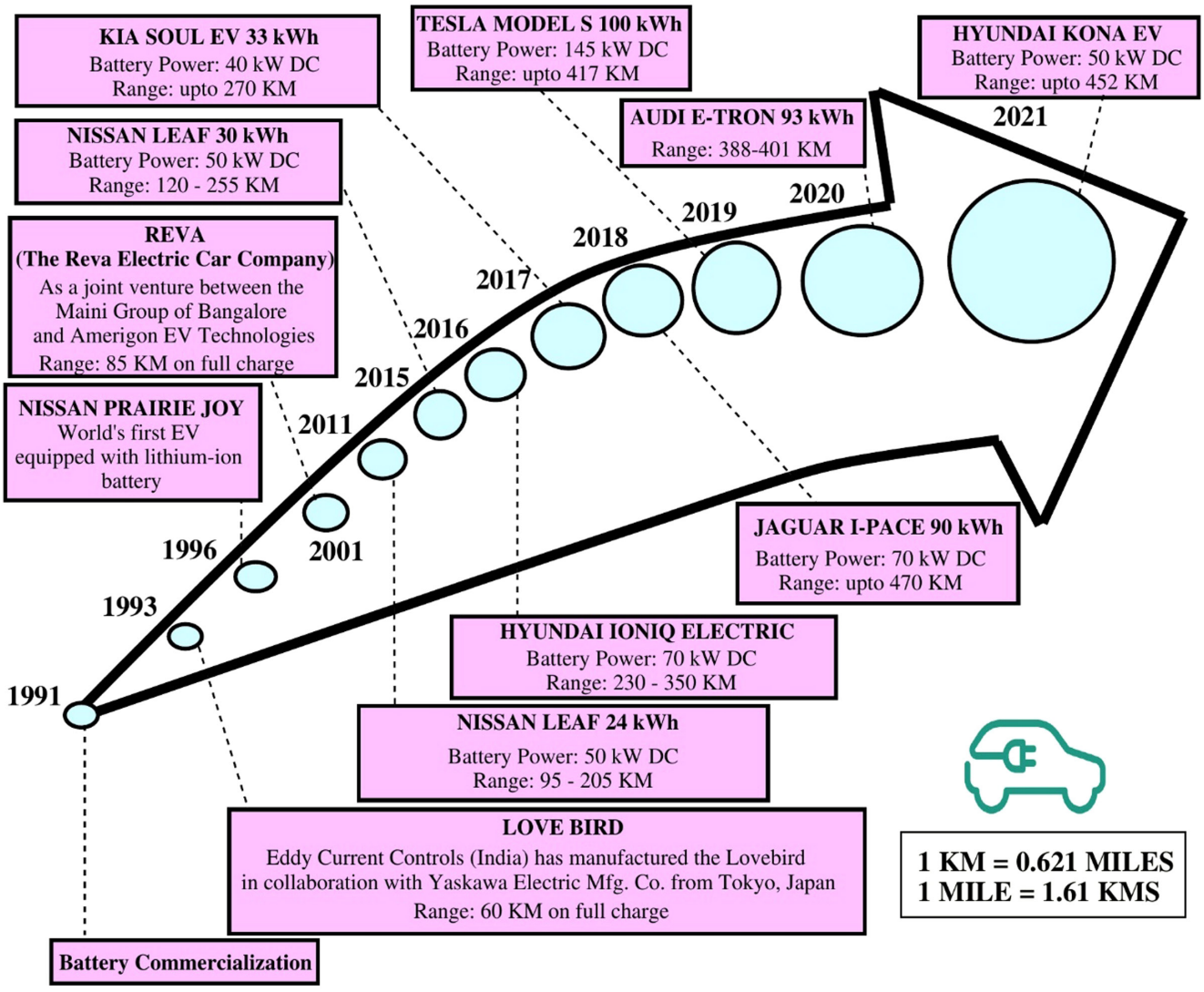


**Fig. 1.** Evolution of the electric vehicle in India.

should shift from intervention to real adoption. It is also vital to analyze the gap between purpose and actual conduct).

2. The present study's key research need is consumer awareness and abilities for assessing and estimating the economic benefit and cost of EVs.
3. This study aims to determine the necessary procedures, obstacles, and problems of operating a battery-powered car in a developing nation like India.
4. This study figures out why EVs have not gotten much traction in India.
5. One of the goals of this study is to raise awareness in India about the benefits of battery-powered automobiles over traditional fossil fuel vehicles.
6. This study also intends to investigate the various government efforts aimed at encouraging electric and hybrid vehicles.
7. Future directions of research on how to best educate customers might have complications for policymakers and marketers seeking to understand the financial benefits and costs of EVs.

Currently, there are various classes of EVs that are now on the market throughout the world. Apart from this, the major contribution of the present paper is the identification of the EV market's challenges and adoption in India. Table I summarizes the various optimization approaches that are covered. Figure 2 illustrates the complete overview of EVs.

The present study is divided into several sections, including Section II provides an overview of all forms of EV configurations, followed by Section III the scenario of EVs in India, and Section IV's The Indian market's barriers to EVs. The EV and V2G optimization approach is provided in Section V, followed by the conclusion and future directions in Section VI.

## II. OVERVIEW OF ELECTRIC VEHICLE

The main goal of the EV is to replace ICE with a motor that is powered through stored electrical energy (i.e., driven by a battery) via a power electronic traction inverter. The vehicle is powered by an

**TABLE I.**
SUMMARY OF DEVELOPMENTS AND PROCESSES IN VARIOUS ELECTRIC VEHICLE TECHNOLOGIES

| Author(s) [Reference] | Location and Country | Optimization Approach | Specific Contributions | Year |
|---|---|---|---|---|
| Qiang et al. [32] | China | Adaptive algorithm | 1. In a hybrid electric vehicle (HEV), to estimate the battery's residual energy and its state of charge, an adaptive algorithm has been employed.<br>2. This algorithm's accuracy, noise resistance, and stability make it ideal forHEV applications. | 2008 |
| Bradley and Frank [33] | United States | Structured optimization | 1. Consideration of fundamental design principles for the plug-in electric vehicle (PHEV).<br>2. The trade-off between energy storage and efficiency, battery management system, the role of drive train components, and grid connections are all described. | 2009 |
| Hajimiragh et al. [34] | Ontario, Canada | Heuristic optimization | 1. An optimization model is built based on the zonal layout of Ontario's electricity transmission network's baseload generating capacity from 2009 to 2025.<br>2. Maximum PHEV penetration levels in the transportation division are determined to determine the practicality of off-peak hours PHEVs charging. | 2010 |
| Peterson et al. [35] | USA cities | Transaction optimization | 1. The economics of employing PHEVs with vehicular batteries to store energy generated during off-peak hours for usage during peak hours are examined.<br>2. The greatest annual benefit is between $142 and $249 in three US locations with no expense for battery deterioration. | 2010 |
| Darabi and Ferdowsi [36] | United States | Heuristic method | The load profile of PHEV charging is discussed, as well as rules for three charging situations in the United States is proposed. | 2011 |
| Zoenf et al. [37] | NA | Mixed logic model | The charging procedure after PHEV travels was modeled using a random coefficient mixed logic model. | 2013 |
| Weis et al. [38] | United States | Mixed-integer linear programming (MILP) | Based on the New York independent system operator, the MILP model is developed to calculate capacity development, plant dispatch, and PHEV charging. | 2014 |
| Villalobos et al. [39] | Borup, Denmark | The weighted sum method and fuzzy control | 1. A multi-objective smart charging algorithm has been described for PHEV.<br>2. This novel technique benefits stakeholders by facilitating the integration of PHEVs into a low voltage distribution network. | 2016 |
| Reddy and Sudhakar [40] | India | A radial basis function network (RBFN) method | 1. The suggested neural network maximum power point tracking (MPPT) controller tracks the proton exchange membrane fuel cell's (PEMFC) maximum power point using the RBFN method. direct current (DC) to DC converters with a high switching frequency and a high voltage gain is required for the propulsion of fuel cell electric vehicle (FCEV).<br>2. A three-phase high voltage-gain interleaved boost converter is also created for the FCEV system to achieve high voltage gain. Interleaving minimizes the ripple in the input current and voltage stress on the power semiconductor devices. The FCEV system's performance is compared to that of the fuzzy logic controller using an RBFN-based MPPT controller. | 2017 |
| Jyotheeswara Reddy and Sudhakar [41] | India | RBFN method | 1. A high-step-up three-phase interleaved boost converter is intended to decrease the current ripples exiting the PEMFC. The interleaving approach maximizes the power capabilities of the power semiconductor devices while minimizing the voltage stress on them.<br>2. The suggested RBFN MPPT controller's performance is investigated in MATLAB/Simulink for both standalone and grid-connected PEMFC systems. | 2018 |
| Reddy and Sudhakar [42] | India | RBFN method | 1. For fuel cells, the RBFN-based MPPT controller technique is developed, while for solar photovoltaic (PV), a fuzzy logic controller is employed to extract the maximum power at various PEMFC temperatures and solar irradiation levels.<br>2. A high step-up DC–DC boost converter is used to give a high step-up voltage for the fuel cell. | 2018 |

(*Continued*)

**TABLE I.**
SUMMARY OF DEVELOPMENTS AND PROCESSES IN VARIOUS ELECTRIC VEHICLE TECHNOLOGIES (*CONTINUED*)

| Author(s) [Reference] | Location and Country | Optimization Approach | Specific Contributions | Year |
|---|---|---|---|---|
| Reddy and Sudhakar [43] | India | Adaptive neuro-fuzzy inference system (ANFIS) | 1. A maximum power point tracking controller based on an adaptive neuro-fuzzy inference system is given for a 1.26-kW PEMFC system utilized in electric car applications.<br>2. The suggested controller's performance is evaluated under normal operating settings as well as under conditions of abrupt changes in the fuel cell's cell temperature. | 2019 |
| K Kumar et al. [44] | India | ANFIS | 1. The performance of a 1.26-kW fuel cell-powered electric car system is evaluated using a modified quadratic boost converter and a neural network-based MPPT algorithm.<br>2. Acceptance of EVs in contemporary society is critical for the construction of a pollution-free environment. | 2020 |

electric motor that utilizes 90–95% of the input energy, making it extremely efficient. The charger, charging port, battery, power electronics controller, DC/DC converter, drive system, and regenerative braking are the main components of an EV. The role of an electric motor is to power the EV by utilizing the stored electrical energy in batteries. The nature of EVs is eco-friendly since low-emission power sources are utilized to recharge them. The power grid is used to charge the cells. The main purpose of the battery is to give electricity to the EV to move. Lithium-ion batteries (LIBs) are used in most EVs because they are more efficient than other cells and have less maintenance. When compared to nickel-metal hydride (NiMH) and lead-acid (Pb acid) batteries, LIBs are a bit expensive to manufacture. The lifetime of the LIBs depends on the climate and maintenance schedule.

An external power source is used to charge the battery through a charging port. The charger must absorb AC power from an electrical source and convert it to DC, which is then used to charge the battery through a charge connection. It maintains track of the battery's voltage, current, temperature, and state of charge (SoC) during charging. The DC/DC chopper is used for powering the vehicles' accessories through the conversion of the high DC voltage from the battery into low DC voltage. The controller of power electronics components is used to regulate the torque–speed characteristics.

When the car travels ahead, the electric motor provides forward momentum. The braking energy gained due to the sudden application of brakes is utilized for battery charging. This process is called regenerative braking (RB). Regenerative braking is critical for preserving vehicle power and attaining increased efficiency. This method of braking leverages the motor's mechanical energy to convert kinetic energy into electrical energy. This electrical energy is utilized to charge the battery. Because RB extends the EV range, which is used frequently in hybrid and battery electric vehicles, it can reclaim 15%

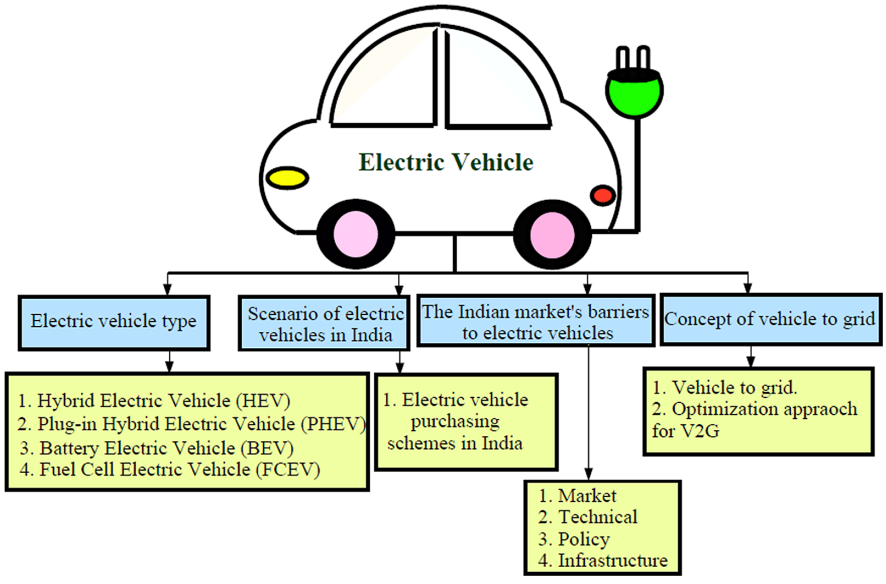


**Fig. 2.** Electric vehicle overview.

of the energy it has consumed for acceleration. However, it is unable to fully recharge the EV.

The drive system's job is to get things moving by delivering mechanical energy to the traction wheel. The electric car has many internal layouts based on the components used and does not need a traditional gearbox. Some designs, for example, employ many tiny motors to power each wheel separately. A huge electric motor, on the other hand, might be linked to the back wheels through differential housing. Compared to components of ICE, an EV's components are modest. Electric vehicles, on the other hand, would not be able to go as fast as ICE vehicles.

**A. Electric Vehicle Types**

Even though EVs are manufactured in various countries, China, the United Kingdom, the United States, and Germany account for most EV sales. Globally, the electric vehicle industry is exploding. There are four types of EVs available in the current market as illustrated in Fig. 3.

**1) Hybrid Electric Vehicle**

The hybrid electric vehicle (HEV) is a combination of an electric motor and ICE. The batteries can be charged by the energy generated by the engine when a vehicle is decelerating and brakes are applied. Due to combining an ICE with a motor as a power converter, they are now referred to as HEV. This technology is being used all over the world because of its several benefits, including the ability to provide modern performance without relying on infrastructure for charging. They reduce fuel usage by engine electrification. The HEV can be associated with numerous topologies depending on the diversity of hybrid systems. The three varieties are parallel, series, and power-split hybrid. In a series hybrid, the only power source for the wheel is the electric motor. The motor is powered by either the generator or the battery.

An ICE is used to charge the batteries. The computer has the capability of deciding and identifying power from the engine/generator or the battery. Both regenerative braking and engine/generator are used to power the battery pack. Series HEVs often have a wider battery pack and bigger motors, as well as a small ICE. They are helped by ultracapacitors to enhance the battery's efficiency, and, as a result, the loss will be reduced. They gain from a series hybrid drive train because the electric motor's perfect torque–speed characteristics reduce the need for a multi-gear gearbox, and mechanical separation among the drive wheels and the ICE enables the ICE to function in its limited optimum area.

There are some significant disadvantages to series HEVs as follows: 1) because of dual-energy conversion, the complete efficacy will be minimized, from mechanical to electrical, and vice versa; and 2) two electric machines with a large traction motor are needed to drive the wheel due to sole torque source. Since they have enough capacity for their big engine/generator combination, HEVs are commonly utilized in buses and commercial and military vehicles.

When compared to a series HEV drivetrain, the engine in a parallel HEV is linked to the wheels. Due to reduced losses and low flexibility in the mutual aligning of the mechanisms of the powertrain, the wheel is powered by the engine. Individual parallel HEVs or groups of

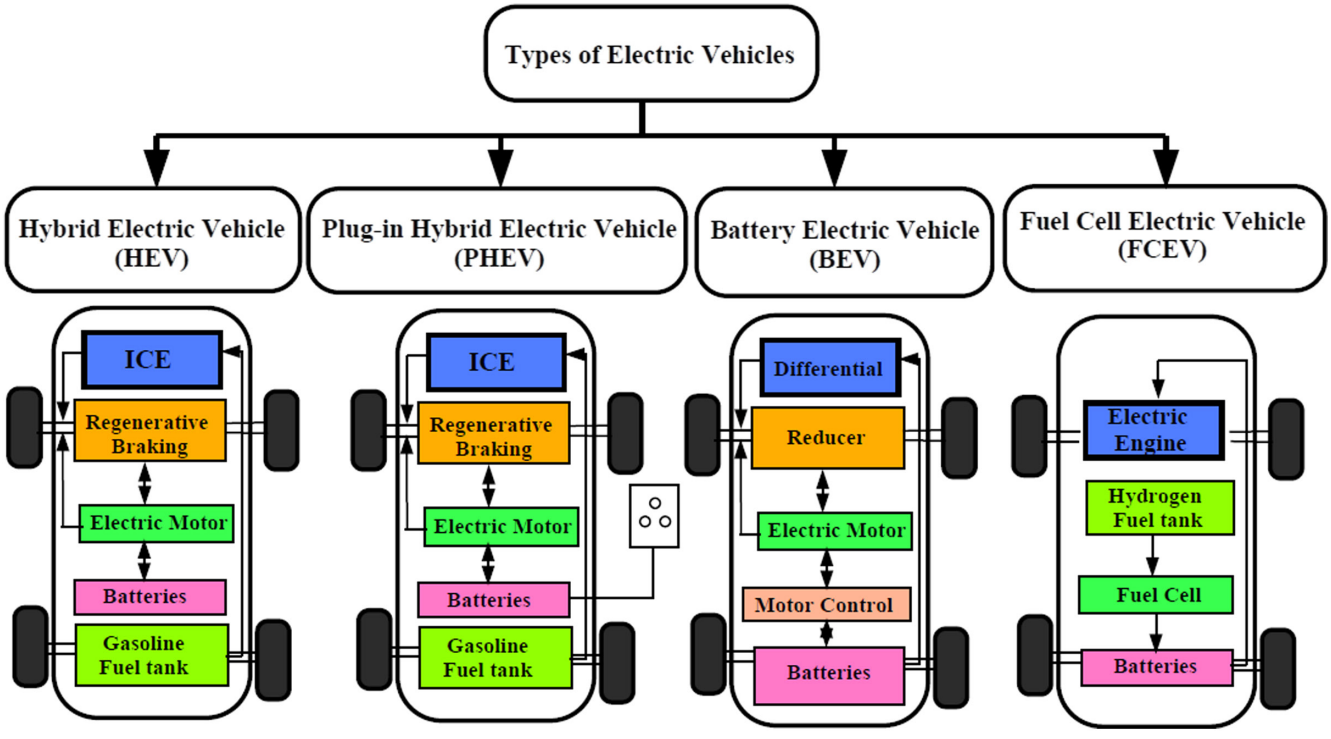


**Fig. 3.** Types of electric vehicles.

parallel HEVs can run the vehicle. It usually features a modest battery that is replenished using RB.

A planetary gearbox is used to link the engine, generator, and motor to a transmission in a power-split hybrid system. In a single frame, they can be placed in both series and parallel arrangements. The vehicle may be powered by the battery and the engine separately or jointly, and the battery can be charged at the same time by the engine. The power provided to the wheel is determined by the torque and speed of each element. To get the most out of your engine, adjust the speed and load. Figure 4 depicts the parallel HEV power flow.

**2) Plug-In Hybrid Electric Vehicle**

An ICE and an electric motor are combined in plug-in hybrid EV (PHEV). These vehicles run on gasoline and utilize electricity to charge many equipped rechargeable battery packs (RBPs). The following are some of the advantages of PHEVs:

1) The use of petroleum is reduced.
2) A PHEV consumes 30–60% less oil than a regular car.
3). Plug-in hybrids lessen oil reliance by generating power from domestic sources.
4) Emission of greenhouse gases PHEVs, on average, release fewer greenhouse gases than conventional vehicles.
5) The amount of gas emitted, on the other hand, is determined by how power is generated.

Nuclear and hydroelectric plants are more environmentally friendly compared to coal-based plants. Each will have a stipulated time duration to recharge. It is noticed that an EV can take several hours to recharge utilizing a 120-V household plug. However, it will only take 1–4 h for recharging with a 240-V charger. Also, it was observed that 30 min is enough to have a quick charge capacity of up to 80%. It is not necessary to plug in a PHEV. Gasoline can be used as fuel in PHEVs. However, they would not achieve fuel economy or maximum range if they are not charged. Calculating the fuel efficiency for combined city/highway travel, the environmental protection agency gives fuel economy estimates for gasoline only. However, a PHEV can run on gasoline, electricity, or a mix.

In 2015, China created the world's largest solar-powered EV charging station, capable of charging 80 EVs per day. It also conducted a preliminary study in Shanghai to see how well EVs can integrate renewable energy sources into the electric grid.

In 2015, solar-powered EV charging stations were started in Japan. As of December 2020, the top five countries selling EVs are China, the United States, Germany, Norway, and France [45]. Several new models have been announced by manufacturers, all of which are expected to be offered at a reasonable cost in the next years. Plug-in EVs have emerged as one of the most promising avenues for reducing $CO_2$ emissions and reducing reliance on fossil fuels. Hybrid EVs have been the subject of several investigations across the world. For instance, an agent-based method has been employed in [46].

Whereas in 2013, authors have used micro-simulation for PHEVs based on technological restrictions and individual goals [47]. China built a feed-forward model in 2013 to examine the best energy management technique for a heavy-duty parallel HEV and determined

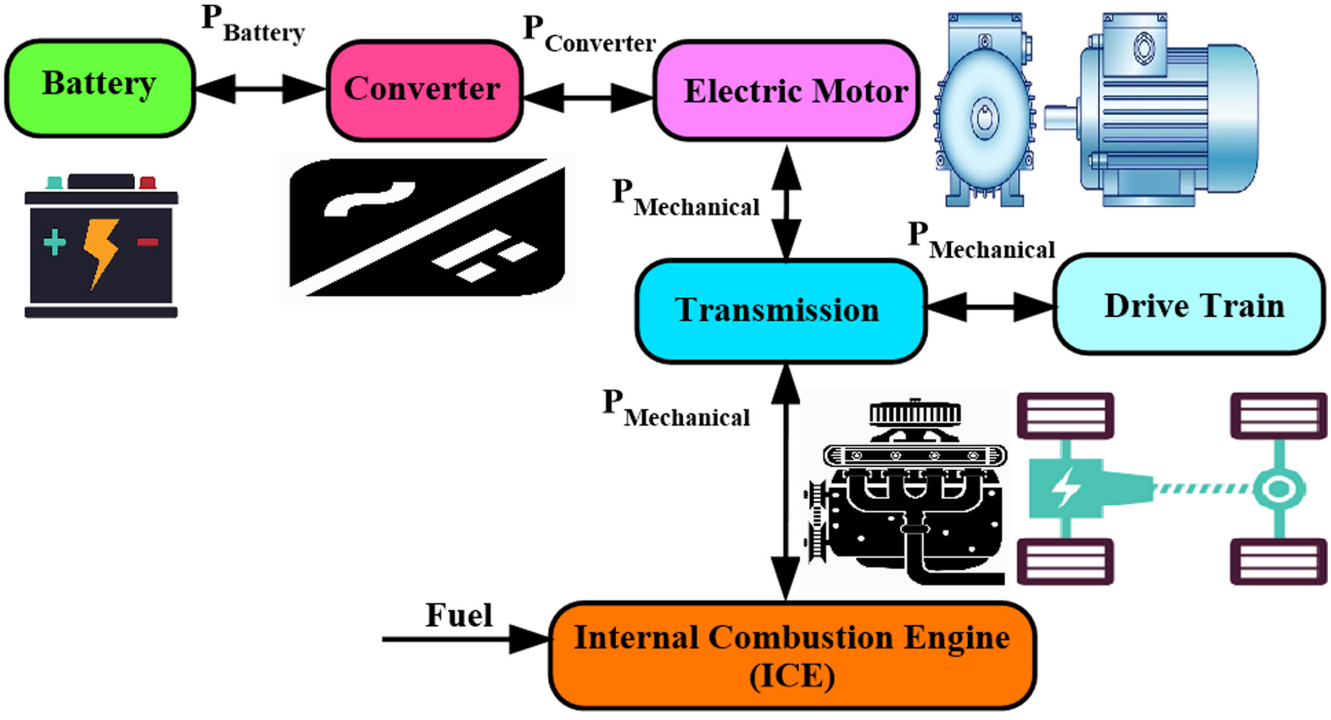


**Fig. 4.** The parallel hybrid electric vehicle power flow.

that the dynamic programming (DP) method enhances the hybrid electric truck's mileage [48]. Another study conducted in China in 2017 has found that convex programming (CP) derived from an optimum control method has an incredible closeness to DP, which is having 200 times quicker possible runs.

In [49], authors have implemented a novel CP to minimize the daily operational expense of a PHEV, in which optimal cost-control strategy has been built that flawlessly mixes the costs of the various tasks and a sensitivity evaluation optimization outcome is performed concerning price changes of battery and energy carriers. From this, it is noticed that the 0.85$ daily cost is significantly lower than the heuristics PHEV scenarios.

In 2016, authors from Chengdu, China, attempted similar work using a stochastic DP problem to optimize the distribution between the grid, household power consumption, and PHEV batteries [50]. A similar study in China was carried out in 2016, and it has been discovered that when fuel cell service life improves, the capacity option may be more convenient and the cost of the life cycle can be reduced. Their solution outperformed the current one by 1.4% recognition of the use of a 10-Ah LIB. The life cycle cost of small and big capacity LIB was greater [51]. Many researchers have reported the evolution of the trends, barriers, and economic viability of PHEVs globally and their influence on a distribution system.

**3) Battery Electric Vehicle**

A battery EV (BEV) is named a complete EV. Battery EVs have RBPs of high capacity (i.e., Ah) which are powered by an external power source. A BEV does not contain ICE.

Battery EV is the sole source of power supply to its motor and the internal electronics. This power is from the stored energy of RBPs. The BEV has the potential to reduce the emission of $CO_2$ from the ICE vehicles and the dependence on fossil fuels. Battery EVs are believed to have the greatest market share in India, accounting for more than 70% of commerce in 2017 and likely to increase in the following years. Though BEVs outsold PHEVs in several countries until 2014, PHEV sales have increased dramatically in the last 2 years, and they are now equal to BEV sales. Lead-acid batteries, NiMH batteries, and LIBs are the three types of batteries commonly used in the Indian market [52].

In India, Uttar Pradesh had the greatest amount of EV sales in 2021. In Uttar Pradesh, a total of 255 700 EVs have been registered as of December 2021. For the last few years, EV use has been expanding across India. National wise 870 141 EVs have been registered as of December 2021. It is noticed that due to the pandemic, the enhanced use of personal vehicles has led to increased demand for India's EV boom. In India, top EV selling states are Uttar Pradesh, Delhi, and Karnataka with the most EV registrations followed by Delhi with 125,347 units and Karnataka with 72,544 units. Bihar, with 58,014 EVs, and Maharashtra, with 52,506 EVs, came in fourth and fifth place, respectively, among the top five states. To accelerate the adoption and manufacturing of EVs in India, the federal government launched the Faster Adoption and Manufacturing of Electric Vehicles in India (FAME India) initiative in 2015. In April 2019, the government reintroduced FAME II for 5 years with a budgeted allocation of Rs. 10 000 crores. Additionally, the national government decreased the Goods and Service Tax (GST) on electric vehicles from 12% to 5%. Additionally, the GST on charging infrastructure was cut to encourage the construction of EV charging stations. Several state governments have also launched their EV policies to encourage the purchase of EVs. Not only have state governments increased demand but they have also provided subsidies and incentives to EV manufacturers and charging infrastructure providers to establish a comprehensive ecosystem for EVs. These reasons have contributed significantly to the increase in EV sales in India. Additionally, the skyrocketing prices of gasoline and diesel, as well as the availability of a diverse selection of electric vehicles, are boosting demand for BEVs in India [53]. Figure 5 illustrates the regional-wise EV registered between 2020 and 2021 in Indian states [54,55]. In [56], a two-step approach that first separates lane transport and their corresponding needs into an order of groups naturally and autonomously then optimizes the station assignment to the demand cluster using linear programming is suggested. This research might be valuable for city planning and constructing a BEV refueling infrastructure in a densely populated location.

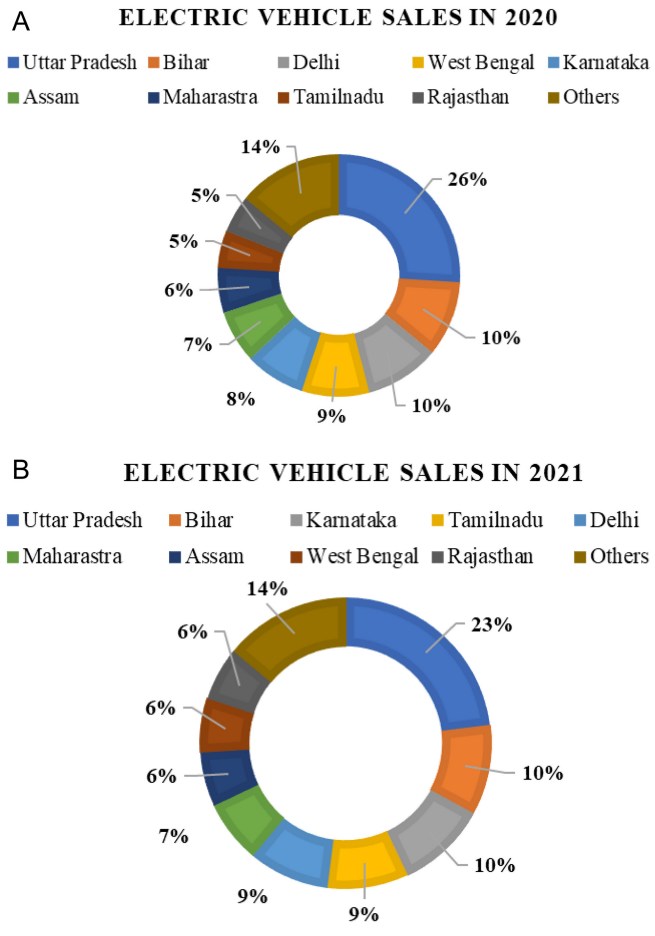


**Fig. 5.** Regional wise electric vehicles registered between (a) 2020 and (b) 2021 in Indian states [53].

In [57], authors have conducted a comparative study of hybrid and battery EV estimating strategies and techniques. Battery EVs meet two criteria: 1) an electric motor is powered by a battery that substitutes the ICE vehicle and the tank, and 2) the vehicle is hooked into a charging outlet when not in use. An overview of the various approach for determining the SoC of batteries is presented in [58]. In [59], authors have investigated standard methods such as ampere–hour (Ah) estimation and open-circuit voltage.

A review of various patents and publications associated with the SoC evaluation techniques for an EV battery has been conducted. These studies include experimental and theoretical characteristics of the evaluation techniques. These evaluation techniques are categorized into three categories: the traditional, the modern control theory, and other assorted techniques extracted from control theory algorithms on innovative ideas [60].

An EV can be classified based on its characteristics such as battery time to charge, range of driving, and the maximum weight the vehicle can hoist according to technical categorization. The charge time and driving range are two key features that customers are concerned about. The time duration of a battery to charge is defined by its capacity and the type of battery used. For each charge, the driving range might range from 20 to 400 km [61]. Similarly, some EVs' highest speeds might reach 160 km/h with a charging period of fewer than 8 h, while some vehicles' top speeds are greater. Due to considerable improvements in EVs, HEVs have sparked increased interest in developing nations such as India. Many improvements are predicted to transform the EV picture in the future as EV manufacturers strive to reduce production costs. Table II summarizes the differences between EVs, HEVsd, and BEVs.

**B. Battery Thermal Management System**

Because the usage of EVs is expected to grow shortly, producing efficient batteries is a top priority. Thermal deterioration of the batteries is a significant barrier to improving battery thermal management systems (BTMS), which has an impact on the EV's range. The BTMS's main goal is to extend battery life by controlling the temperature of the battery cell. Lithium-ion batteries are commonly utilized in EVs to store energy.

There are several obstacles to the usage of LIBs including prohibitive cost, low efficacy, decreased electrode life at extreme temperatures, low and elevated temperatures, and the strict impact on vehicle capability, dependability, and protection, as well as safety concerns about a thermal runaway. As a result, an excellent BTMS is one of the most important technologies for an EV's long-term success. Temperatures between 25°C and 40°C are the ideal working range for LIBs. The life of the battery will deteriorate when the temperature rises over 50°C.

**C. Hybridization Factor**

The hybridization factor (HF) may also be used to classify the vehicles. Hybridization of vehicles improves mileage, which is expressed in miles per gallon. Miles per gallon may be used for PHEVs, where 1 gallon of gasoline is equal to 33.7 kWh of electrical energy [62]. The HF of an EV or PHEV is expressed as follows:

$$\mathbf{HF} = P_{EM}/(P_{EM} + P_{ICM})$$

where $P_{EM}$ denotes total electric motor power and $P_{ICM}$ denotes total internal combustion engine power. For a normal automobile, HF is 0, while for all EVs, it is 1.

**TABLE II.**
COMPARISON OF HYBRID ELECTRIC, ELECTRIC, AND BATTERY ELECTRIC VEHICLES

| Parameters | HEV | EV | BEV |
|---|---|---|---|
| ***1. Technical*** | | | |
| Charging facility | Available | Available (but limited) | Available (but limited) |
| Powered by | Both internal combustion engine (ICE) and electric | Electric engine | Electric engine |
| External charging | Not required | Required | Required |
| Engine size | Medium | Small | Small |
| ***2. Economic*** | | | |
| Price range | Like ICE vehicles | High | High |
| Fuel consumption | 40–60% of ICE | None | None |
| Resale value | High | Moderate | Moderate |
| Maintenance | High | Low | Low |
| ***3. Environmental*** | | | |
| $CO_2$ emission | High | Low | Low |
| Dependence on fossil fuel | Partially dependent | Not directly dependent | Not directly dependent |

## III. THE SCENARIO OF ELECTRIC VEHICLES IN INDIA

Indian EV market is still quite modest. For the past few years, EV sales per year have been stagnant at 2000 units. However, it has been noticed since 2020, they have set a goal of selling 100% EVs by 2030, with a composite yearly growth rate of 28.12%.

Reva (Mahindra), India's first EV introduced in 2001, has only sold a few units since 2001. Later, automobile companies manufactured EVs, PHEVs, and electric buses.

Bengaluru Metropolitan Transport Corporation is the first local transportation authority to begin electric bus operation on a busy street in the city. A poll conducted in the city of Ludhiana revealed that 36% of present automobile and two-wheeler owners were excited about switching to EVs. The state government of Telangana is likewise pushing the usage of EVs by waiving road taxes for EV owners. The Telangana State Electricity Regulatory Commission established an INR 6 charging fee for EVs in 2018. The TSERC set the service rate for the whole region with the same price/kWh. In addition, to provide the charging facility for EVs power grid, Corporation of India Ltd and the Hyderabad Metro have partnered. India's first EV charging station will be incorporated in Hyderabad metro station through power grid operation and control. The city of Hyderabad is also considering replacing diesel-powered public vehicles with EVs. The New Delhi government received authority last year to build 131 public charging stations around the city. The Delhi government announced a draught strategy in November 2018 intending to transform 25% of their automobiles to EVs by giving different enticements and installing infrastructure for charging in both non-residential and residential locations.

By 2023, the same strategy aims to build an infrastructure for charging at every 3 km by providing a 100% aid (up to 30 000 USD) and waiving registration, parking fee, and road tax of EVs. A private company called Magenta Power is planning to establish infrastructure for charging EVs on the Mumbai–Pune route [61].

### A. Electric Vehicle Purchasing Schemes in India

In India, state and central governments are introducing various programs and incentives to encourage electric mobility (E-mobility). Among these schemes, few are popularized in public. The Government of India (announced the National Electric Mobility Mission Plan (NEMMP) 2020 to enhance the energy security of the nation, to reduce the detrimental effects of fossil fuel power cars on the environment, and to build local manufacturing skills. The NEMMP 2020 has saved 2.2–2.5 million tons of fossil fuel through EV sales of 6–7 million. As a result of this new strategy, vehicle emissions and $CO_2$ emissions could be reduced by 1.3–1.5%. By the end of 2021, 5.2 million EVs were on the road. The highlights are the need for industry-academia collaboration and incentives by the government. Government of India is planning to build a solar power plant of capacity 100 GW by 2022 to encourage renewable energy-powered EV charging stations and to boost the stability and utilization of renewable sources. The Indian government has established the FAME II (Faster Use and Manufacturing of Electric Vehicles) strategy, which aims to accelerate the adoption of EVs and PHEVs. This program supports EV adoption through different incentives and by creating charging infrastructure. In February 2019, for the 3-year term, the cabinet approved a budget of 10 000 crores for FAME II. This is the most awaited policy by the EV producers to develop an ecosystem for EVs, as well as production incentives and charging infrastructure made a roadmap [63]. Likewise, with the advancement of EV technology and the need to minimize automobile manufacturing sector energy demand, the E-mobility report of 2017 by the National Institution for Transforming India Aayog is transformational and established a pathway for adopting 100% EVs.

According to reports, India can become completely electric by 2030 if it adopts a transformational shared solution networked e-mobility, with 100% public transportation cars and 40% private automobiles. This concept must be shared widely for all EVs to be available shortly. By 2030, the Society of Indian Automobiles and other automakers hope to market 100% pure EVs (BEVs and fuel cell vehicles) for intracity public transportation fleets. By 2030, it is predicted that 40% of new EV sales will be on the market, and 60% of new EV sales will use cleaner technologies such as hybrid and alternative fuels. To guarantee the scheme's efficient operation, the government, industry, and different stakeholders should unite and invest in a long-term strategy to achieve a 100% electric car regime [64]. Figure 6 illustrates the various policies opted by the Indian government for EV development and faster adoption.

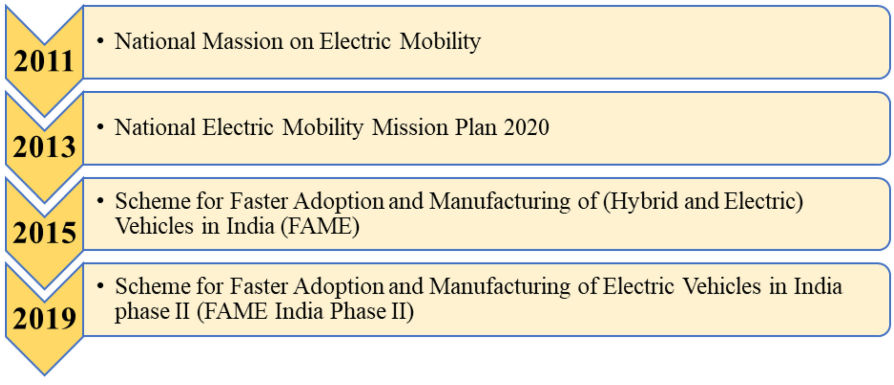


**Fig. 6.** Various policies opted by the Indian government for electric vehicle development and faster adoption.

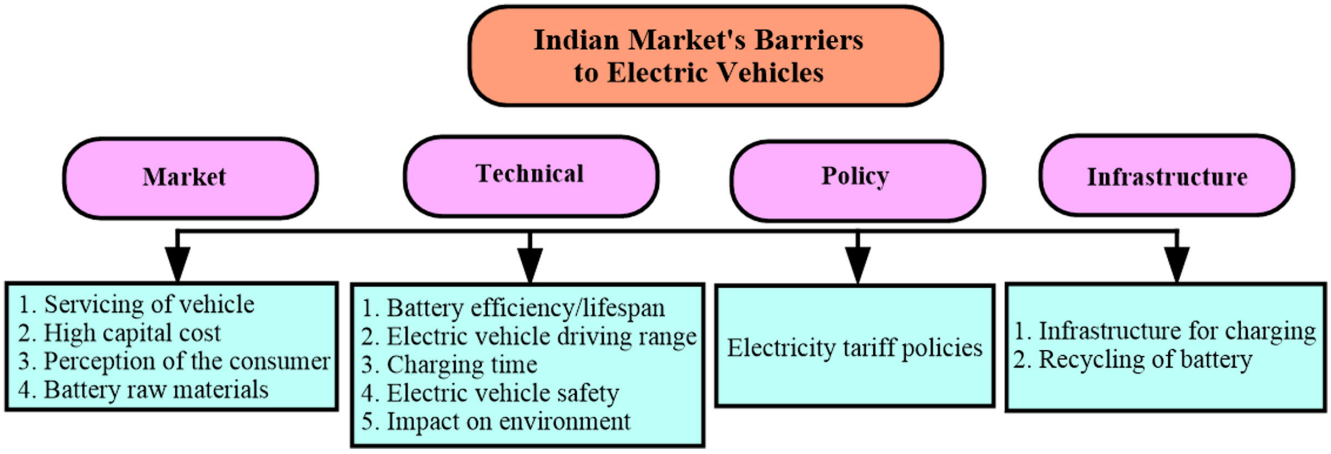


**Fig. 7.** Indian market's barriers to electric vehicle.

## IV. THE INDIAN MARKET'S BARRIERS TO ELECTRIC VEHICLES

The challenges to EV adoption in India may be approached from a variety of angles, including technical constraints, legislative impediments, and a lack of infrastructure. These are illustrated in Fig. 7.

### A. Market

#### 1) Servicing of Vehicle

It is also necessary to have proper care for an EV. The technician should be professional, and he must have hands-on experience in terms of vehicle maintenance, troubleshooting, and repair. They have to utilize their utmost skill to deal with the situation.

#### 2) High Capital Cost

Electric vehicle battery packs are expensive, and they also need to be replaced many times over the vehicle's lifetime. Gasoline-powered automobiles are less expensive than electric ones.

#### 3) Perception of the Consumer

Consumer impression is critical for acquiring new customers and retaining existing ones. Despite the expanding range of EVs on the market, the choice of purchasing an EV remains restricted and is projected to remain so soon. Thus, the client should be aware of the company's products via advertising, social media, or another channel. According to studies, a lack of understanding about the government program, economic benefits, and awareness of vehicular technology can all have a direct effect on the adoption of EVs.

#### 4) Battery Raw Materials

Lithium, nickel, phosphate, manganese, graphite, and cobalt, which are all rare earth elements, are used as basic materials in EV batteries. Aluminum, copper, and steel are necessary for an internal combustion engine. Platinum, rhodium, and palladium are required to filter hazardous gases in combustion car catalyzers. These are all rare materials, and their supply may be insufficient for battery manufacture. Lithium-ion batteries alone consume five million tons of nickel per year, which might result in a 10–20 times increase in lithium and cobalt consumption in the future.

### B. Technical

#### 1) Battery Efficiency/Lifespan

Electric vehicles are typically made by substituting chargers, controllers for batteries, and electric motors for the traditional vehicle's fuel tank and gasoline engine. Because the batteries in EVs are meant to last an extended period, they will eventually fail. Currently, most battery manufacturers give a warranty of 8 year/100 000 mile.

#### 2) Electric Vehicle Driving Range

The driving range is often seen as the primary impediment to the adoption of EVs since EVs have a shorter range than identical ICE vehicles. The range of an electric car on a single charge or full tank is viewed as a key disadvantage in terms of EV adoption in the worldwide market. The majority of BEVs have a range of fewer than 250 km per charge. However, some of the most recent versions have a range of up to 400 km. Due to the availability of liquid fuel ICEs, PHEVs currently have a range of 500 km or more. Thus, the motorist must carefully organize their travel and may be unable to make a long-distance excursion. This creates a barrier in the form of the driving range's magnitude.

#### 3) Charging Time

Charging time is inextricably linked to the issue of range. The EV can take up to 8 h to fully charge from an empty state when utilizing a 7-kW charging station with a sluggish charger. The charging time is mostly determined by the battery's capacity. The vehicle battery is directly proportional to the size of the vehicle, that is, larger automobile will consume more time to recharge from zero to full. Additionally, the battery's charging time is directly proportional to the charge point's charging rate. The higher the charging price of the charge point, the faster the battery will charge entirely. Rapid chargers are utilized in the current scenario to charge the car more quickly, hence minimizing the time necessary. Commercially available EVs are compatible with charge stations that provide a greater charge rate than the vehicles themselves can provide. This means that the battery charging at the highest rate it is capable of without experiencing any problems. It is noticed that the charging rate of the battery using a quick charger decreases during the drop in temperature or the battery is cold.

**TABLE III.**
SUMMARY OF VARIOUS OPTIMIZATION APPROACHES TO ELECTRIC VEHICLES AND THEIR SPECIFIC CONTRIBUTIONS

| Author(s) [Reference] | Optimization Approach | Specific Contributions | Year |
|---|---|---|---|
| Lam and Yin's [65] | Activity- and time-based utility theory model | 1. The activity-based model is built as a time-dependent variation inequality issue, which is solved heuristically using space–time extended networks. | 2001 |
| Perez et al. [66] | Dynamic programming (DP) | 1. The power split between the two sources is optimized to reduce fuel usage when the vehicle is operating at a certain velocity cycle.<br>2. They evaluate the constraints on the power flows from both sources.<br>3. Additionally, there is an intrinsic limitation arising from the fact that the energy in the electrical storage system must remain within safe limits to avoid physical damage. | 2006 |
| Fang and Qin [67] | Concurrent optimization using a multi-objective genetic algorithm (GA) | 1. An optimization technique based on multi-objective evolutionary algorithms is developed, which can optimize powertrain and control system parameters concurrently and effectively identify the Pareto-optimal solution set subject to user-selectable performance limitations.<br>2. This ideal parameter set enables a variety of design options that can enhance fuel efficiency and emissions without compromising vehicle performance. | 2006 |
| Wang et al. [68] | Particle swarm optimization (PSO) | 1. The fuel economy and emissions characteristics of the strategy are compared to one of the primary methods. Dividing RECTangles, the particle swarm optimization algorithm's calculation processes are explained, and a simulation study based on a series hybrid electric vehicle model is presented. | 2006 |
| Gong and Li [69] | Two scales of dynamic programing depend on trip-based power management | 1. With a micro-scale DP architecture, the actual power management may be changed during real-time vehicle operation.<br>2. The whole journey is separated into segments, and each segment's DP is solved using online traffic data provided to the car via the segment's traffic flow sensors.<br>3. The state of charge achieved in the macro-scale DP solution at the terminal site is validated as the final value. | 2007 |
| Xiaolan Wu et al. [70] | PSO | 1. The PSO method was used to optimize the control settings in a plug-in HEV.<br>2. The study is based on a charge-depleting operating strategy, and the fitness function is defined in such a way that it maximizes the fuel efficiency of the vehicle engine.<br>3. Constraints are then applied to the driving performance criteria. | 2008 |
| Kukhyun Ahn et al. [71] | A quasi-static powertrain model using DP | 1. The approach includes two types of simulations: the first is focused on minimizing equivalent fuel consumption, while the second is based on dynamic optimization.<br>2. After analyzing and comparing the data, it was shown that selecting a single optimal operating point by reducing equivalent fuel consumption resulted in high energy efficiency and maximum performance was attained from optimal control simulation. | 2008 |
| Kerem Koprubasi et al. [72] | Model-based design techniques for the control development and optimization | 1. Model-based design is a collection of approaches that place the system model at the center of the development process, from requirements generation to implementation and testing.<br>2. This technique has a variety of advantages, including decreased development time and cost, increased product quality, and a more dependable final product due to the use of computer models for system verification and testing.<br>3. Model-based design is especially advantageous in automobile control applications where calibration ease and reliability are essential features. | 2009 |

(*Continued*)

**TABLE III.**
SUMMARY OF VARIOUS OPTIMIZATION APPROACHES TO ELECTRIC VEHICLES AND THEIR SPECIFIC CONTRIBUTIONS (*CONTINUED*)

| Author(s) [Reference] | Optimization Approach | Specific Contributions | Year |
|---|---|---|---|
| Olle Sundstrom and Carl Binding [73] | Linear and non-linear approximation method | 1. It is a technique used for optimizing the charging behavior of EVs to lower charging costs, to obtain acceptable state-of-energy levels, and to achieve optimal power balance.<br>2. Two strategies for optimizing charging schedules are compared. The first formulation approximates the battery behavior linearly, whereas the second formulation approximates it quadratically.<br>3. The solutions to the two techniques are evaluated using a non-linear and state-dependent battery model. | 2010 |
| Sara Deilami et al. [74] | Maximum sensitivity selection optimization | 1. This strategy enables PHEVs to begin charging as quickly as feasible while adhering to network operating standards (such as power losses, generation restrictions, and voltage profile). | 2011 |
| Elias Wiedemann et al. [75] | Concepts based on customer-relevant characteristics | 1. During the idea stage of development, the optimization loops' objective is to obtain the best potential fulfillment of this cost function. | 2012 |
| Chenrui Jin et al. [76] | Linear programming based on the customer's perspective | 1. While the dynamic scenario is more realistic, solutions to static problems can be utilized to demonstrate the income and cost savings that can be realized through regulated pricing and thus serve as a baseline for performance evaluation.<br>2. Extensive simulation results based on real-world electricity price and load data demonstrate that optimizing charging scheduling can result in significant revenue and cost savings when compared to an unregulated baseline approach and that the proposed dynamic charging scheduling schemes also provide close-to-optimal solutions. | 2013 |
| Niangjun Chen et al. [77] | Optimality and valley filling algorithm | 1. The ideal EV charging schedule is a valley filling profile, which enables the development of a highly efficient offline method with less computing cost than centralized interior-point solvers. | 2014 |
| Mushfiqur R. Sarker et al. [78] | Optimal operation and services scheduling using inventory robust algorithm | 1. They provided an optimization approach for the battery switching station's operational model.<br>2. The suggested model considers the process of day-ahead scheduling.<br>3. Battery demand uncertainty is represented using inventory robust optimization, whereas electricity pricing uncertainty is handled using multi-band robust optimization. | 2015 |
| Shengyin Li et al. [79] | Mixed-integer linear program solved using GA | 1. The model captures network dynamics and finds the most cost-effective station rollout method in both geographical and temporal dimensions.<br>2. The multi-period location issue is expressed as a mixed-integer linear program and addressed using a genetic algorithm-based heuristic. | 2016 |
| Mostafa Rezaei Mozafar et al. [80] | Improved GA-PSO | 1. A unique strategy is given for jointly optimizing the location and size of RES and EV charging stations.<br>2. They presented an optimum technique for controlling the electric car charging process.<br>3. A multi-objective optimization problem is created using the characteristics of electric cars and a model of renewable energy sources.<br>4. The optimization problem is solved using a GA-PSO hybrid enhanced optimization technique. | 2017 |
| Abhishek Awasthi et al. [81] | Hybrid GA-PSO | 1. An innovative approach to the optimal location of electric car charging stations.<br>2. A hybrid algorithm that utilizes both GA and PSO techniques.<br>3. The voltage profile indicated an improvement in the value of the lowest voltage bus.<br>4. Higher performance in terms of solution quality with fewer iterations. | 2017 |

(*Continued*)

**TABLE III.**
SUMMARY OF VARIOUS OPTIMIZATION APPROACHES TO ELECTRIC VEHICLES AND THEIR SPECIFIC CONTRIBUTIONS (*CONTINUED*)

| Author(s) [Reference] | Optimization Approach | Specific Contributions | Year |
|---|---|---|---|
| Syuan-Yi Chen et al. [82] | Dynamic particle swarm optimization | 1. Dynamic particle swarm optimization was utilized to establish optimal solutions for hybrid electric cars' two-variable energy management and gear changing.<br>2. Six successive phases comprised the optimization process.<br>3. They have compared four distinct situations. | 2018 |
| Limmer and Rodemann [83] | Intelligent control strategy | 1. They suggested a framework for dynamically pricing and scheduling charging operations to increase the charging station operator's daily profit and lower the peak of the electrical load. | 2019 |
| Pandian Vasant et al. [84] | PSO and gravitational search algorithm | 1. They utilized PHEVs that require an adequate charge allocation strategy, which they accomplished via the use of smart charging infrastructures and smart grid systems.<br>2. To enable the everyday use of PHEVs, daytime charging stations are essential, and at this stage, only effective charging regulation and infrastructure management may result in increased PHEV adoption. | 2020 |
| Manh-Kien Tran et al. [85] | Hybrid power train technique | 1. They explored several engine designs and components to develop a hybrid powertrain that meets the EcoCAR mobility challenge performance standards.<br>2. Acceleration, driving range, braking, fuel economy, and pollutants are all included in these criteria.<br>3. They have designed in MATLAB/Simulink, a total of five distinct models. | 2021 |

The EV chargers are classified according to the recharge rate of the batteries. The EV charging has three basic types: level 1, level 2, and direct current (DC) rapid. Charging of level 1 is accomplished by converting alternating current (AC) to DC via an onboard converter utilizing a conventional 120-V outlet. Charging the EV using 120-V outlets takes 8 h and provides a range of around 120–130 km. Level 1 charging takes place mostly at home or the workplace. Level 2 chargers are frequently installed in public areas or workplaces that have a 240-V outlet. After continuous 4-h charging of the battery, the vehicle can have a driving range of 120–130km. With DC rapid charging, the transition from AC to DC is seamless and occurs at the charging station with the most advanced charging configurations. This enables stations to provide additional electricity and to charge automobiles more quickly. It charges the battery in 30 min and has a range of 145 km.

**4) Electric Vehicle Safety**

The electric car must comply with all applicable state and municipal regulations on vehicle safety. Additionally, the batteries must pass testing under adverse situations such as the impact of fire, short

**TABLE IV.**
SUMMARY OF VARIOUS OPTIMIZATION APPROACHES FOR THE V2G MECHANISM AND THEIR SPECIFIC CONTRIBUTIONS

| Author(s) [Reference] | Optimization Approach/Concept | Specific Contributions | Year |
|---|---|---|---|
| Christophe Guille and George Gross [92] | Conceptual framework | 1. They evaluated the implementation of a battery vehicle aggregation to provide frequency control, which requires extremely rapid reaction times and energy supply for peak shaving.<br>2. Additionally, the aggregated battery car charging load was evaluated for its influence on low load generation schedules and regulatory requirements.<br>3. The assessment of these implications includes an explicit portrayal of uncertainty and the critical nature of the state of charge (SoC) as a fundamental variable in the supply and demand functions of the batteries.<br>4. The role of vehicle-to-grid (V2G) in integrating renewable energy sources has been considered. | 2008 |
| Christophe Guille and George Gross [93] | Conceptual framework | 1. A conceptual framework has been successfully implemented to integrate aggregated battery vehicles into the grid as distributed energy resources that act as controllable loads during off-peak periods to help balance the system's demand and as a generation/storage device during the day to provide capacity and energy services to the grid. | 2009 |

(*Continued*)

**TABLE IV.**
SUMMARY OF VARIOUS OPTIMIZATION APPROACHES FOR THE V2G MECHANISM AND THEIR SPECIFIC CONTRIBUTIONS (*CONTINUED*)

| Author(s) [Reference] | Optimization Approach/Concept | Specific Contributions | Year |
|---|---|---|---|
| M. Musio et al. [94] | Virtual power plant structure concept | 1. The system's instability following the addition of renewable energy sources to the grid can be mitigated by energy storage devices, demand control monitoring, and grid reinforcement.<br>2. These technologies can increase the electric grid's dependability and efficiency, while also increasing the system's flexibility.<br>3. They used an optimization problem to investigate the feasibility of using electric vehicles (EVs) linked to the grid as energy storage systems inside a virtual power plant layout. | 2010 |
| João Soares et al. [95] | Particle swarm optimization | 1. They discussed network management will be critical to incorporate automobiles into the optimum scheduling issue.<br>2. They developed the PSO algorithm and evaluated the methodology's performance using a 32-bus distribution network equipped with 66 dispersed generators, 32 loads, and 50 EVs. | 2011 |
| Sayed Saeed Hosseini et al. [96] | Virtual power plant structure concept | 1. They highlighted the V2G idea and how it simplifies the integration of renewable energy into the power grid, providing a new impetus for the inevitable transition to clean energy generation.<br>2. The economic and environmental benefits of utilizing energy storage in EVs are apparent. Research has been done to elucidate the many facets of V2G in power systems.<br>3. They examined V2G from the standpoint of power system services and energy market applications in that study.<br>4. They concentrated on the relevance of smart parking lots in the V2G concept, its advantages, and disadvantages, as well as the application of V2G to provide auxiliary services. | 2012 |
| Shi Rui et al. [97] | Bidirectional power flow control | 1. They examined the interplay of wind turbines, electric car charging stations, and the active distribution grid.<br>2. They concentrated on the idea of EV charging stations offering bidirectional power flow management to distribution network operations to increase fault-ride-through of neighboring wind turbines. | 2014 |
| Sonja Studli et al. [98] | Additive Increase multiplicative decrease | 1. They presented a novel framework for implementing both the V2G idea and non-disruptive reactive power adjustment capabilities.<br>2. The algorithms can share available/desired power optimally and fairly, with little communication needs, in a highly unpredictable, constantly changing environment. | 2015 |
| Youjie Ma et al. [99] | General approach | 1. Two technological considerations are discussed in detail: bidirectional charging and charging/discharging technique.<br>2. These two technological obstacles come from two major challenges associated with the integration of EVs into the power system: pollution caused by harmonics and load fluctuation. | 2018 |
| K. Ramakrishna Reddy and S. Meikandasivam [100] | Stochastic approach | 1. Smart grid technologies are rapidly gaining prominence in the electric power sector, both in terms of updating the legacy infrastructure with a high degree of renewable energy penetration and ensuring the dependability and quality of electric power.<br>2. The utilization of modern technology to improve energy consumption and decrease greenhouse gas emissions is unavoidably the electric utility's primary focus. Renewable energy source integration introduced a slew of complications in addition to its benefits.<br>3. Plug-in electric vehicles (PHEVs) have seen dramatic market expansion over the previous decade due to lower costs and improved energy density storage.<br>4. The integration of many PHEVs with an uncoordinated charging schedule is a significant impediment to power system functioning. | 2018 |

(*Continued*)

**TABLE IV.**
SUMMARY OF VARIOUS OPTIMIZATION APPROACHES FOR THE V2G MECHANISM AND THEIR SPECIFIC CONTRIBUTIONS (*CONTINUED*)

| Author(s) [Reference] | Optimization Approach/Concept | Specific Contributions | Year |
|---|---|---|---|
| K. Ramakrishna Reddy and S. Meikandasivam [101] | Water filling algorithm (WFA) | 1. The WFA is utilized to disperse available PHEV energy, which aids in the proper scheduling of PHEVs for the day ahead.<br>2. The adaptive neuro-fuzzy inference system (ANFIS) was used to minimize charging costs and maximize PHEV power consumption.<br>3. ANFIS is trained to prioritize cars concurrently from utility and consumer viewpoints. The effect of ANFIS priority on the aggregate power availability and load flattening of PHEVs is investigated at a particular time. | 2018 |
| K. Ramakrishna Reddy and S. Meikandasivam [102] | Multi-objective genetic algorithm (GA) | 1. Prioritization of PHEVs is performed using ANFIS and five decision factors.<br>2. It has been assumed that PHEVs are available at the planned times, and while vehicle prioritization may result in minor deviations from pre-arranged periods, the target SoC is always maintained.<br>3. When PHEVs are used for load flattening, voltage regulation is done at each bus to which PHEVs are attached by managing active power transactions between the bus and the PHEVs.<br>4. The Multi-Objective Genetic Algorithm is used to determine the ideal power transfer between the grid and PHEVs while optimizing the storage use of the PHEVs without exceeding voltage constraints. | 2019 |
| K. Ramakrishna Reddy and S. Meikandasivam [103] | Fuzzy logic controller | 1. For PHEVs, an intelligent control method is designed to alleviate power oscillations caused by load demand and solar energy combined.<br>2. Additionally, the effect of scheduling PHEVs in conjunction with energy storage units (ESU) is studied.<br>3. Slack bus power fluctuations from the prescribed value are minimized while maximizing the usage of available PHEV storage capacity.<br>4. When scheduling storage units, day-ahead energy demand and solar energy generation for the next few hours are considered (ESU and PHEV) | 2019 |
| K. Ramakrishna Reddy and S. Meikandasivam [104] | Water filling energy dispatch algorithm | 1. The effective use of a PHEV's storage capacity to mitigate solar PV and load power variations.<br>2. The client and utility benefit from a win-win approach that maximizes income for the consumer and minimizes demand swings. | 2019 |
| K. Ramakrishna Reddy et al. [105] | Multi-objective GA | 1. The present study focuses only on the distribution agent level, with the primary purpose of load flattening using PHEV storage.<br>2. The energy zones necessary for load flattening are specified, along with the charging and discharging of PHEVs required to achieve load flattening.<br>3. The entire available energy from PHEVs is allocated optimally among all intervals in each zone using WFA.<br>4. Optimal Energy Distribution with WFA took into consideration the unpredictability of PHEV availability for grid assistance while assessing the available PHEV energy capacity in each zone (charging and discharging). | 2019 |
| Mina Jafari et al. [106] | Mixed-integer linear programming | 1. The concept of regenerative breaking energy (RBE) is being used to improve the functioning of the subway system in the smart city's linked subway system.<br>2. To ensure the smart city operates well, an optimization formulation is developed to reduce the city's overall cost in the presence of subway RBE.<br>3. The traffic and route length are modeled in this article using V2G and Vehicle to Subway vehicles situated in parking lots.<br>4. Additionally, the degradation model is being developed to extend the battery life of PHEVs.<br>5. A stochastic framework based on the uncertainty technique is constructed using an unscented transformation approach to manage the unpredictable behaviors of PHEVs, distributed energy resources, and loads in the smart city. | 2020 |

(*Continued*)

**TABLE IV.**
SUMMARY OF VARIOUS OPTIMIZATION APPROACHES FOR THE V2G MECHANISM AND THEIR SPECIFIC CONTRIBUTIONS (*CONTINUED*)

| Author(s) [Reference] | Optimization Approach/Concept | Specific Contributions | Year |
|---|---|---|---|
| Benedikt Tepe et al. [107] | GA | 1. The optimization techniques given here are used to optimize pool combinations based on the power and energy capacity profiles of commercial electric vehicles.<br>2. The income of the possible pools per participating EV is determined using a genetic algorithm.<br>3. This study examines two use cases: balancing power provision on Central Europe's frequency containment reserve market and energy arbitrage trading on the European power exchange's intraday continuous and day-ahead auction spot markets. | 2021 |

circuit, temperature, overcharge, pulsation, moisture, and water immersion. The design of the vehicles should include safety features like short circuit and collision detection and HV isolation.

**5) Impact on Environment**
Though EVs are eco-friendly, they may affect the environment. However, the battery components are mined and proper disposal is carried out, thereby having a negligible influence on the environment.

**C. Policy**
To accelerate India's electric car revolution, the government plans to finance the country's EV charging infrastructure. Additionally, the ministry of electricity recently confirmed that EV charging stations in India do not require a license to operate, which will help expand the nation's EV charging station infrastructure.

It is necessary to increase and encourage incentives and concessions to EV consumers by reducing the LIBs GST, and enticements must be provided for transition from public transportation to EVs.

**D. Infrastructure**

**1) Infrastructure for Charging**
Additional charging infrastructure is necessary to accommodate an increase in the number of EVs and, consequently, the demand for electrical energy. Due to a lack of charging infrastructure in India, electric car sales are limited. Chargeable batteries should be embraced by EV manufacturers from a design standpoint, allowing discharged batteries to be replaced with fully charged ones. The charging station can arrange to charge their batteries at off-peak hours when electricity rates are lower. Additionally, there should be an option for setting up a charging station for this car at home, as residents would be required to begin their day by charging their EVs. In the lack of residential charging infrastructure, individuals would rather charge their vehicles at work or at a proper charging station where they must stop for 2–3 h or more. Slow charging is excellent for locations such as the home and business, whereas rapid charging is best for highways and commercial complexes, where vehicles must stop for a shorter period. Additionally, quick charging of 30 min or less requires the EV to be capable of handling high current and voltage, or both. This will not only raise the expense of the EV but will also have a detrimental effect on the battery's life. As a result, a hybrid of slow and rapid chargers may be the best solution for EVs.

**2) Recycling of Battery**
The batteries used in EVs are typically designed to endure for the duration of the vehicle's life but will fail. Manufacturers do not notify consumers about battery replacement prices, but if a battery needs to be replaced outside of its warranty term, the manufacturer adds to the expense by replacing the old battery with a new one. Chemical components such as lithium, nickel, cobalt, manganese, and titanium not only improve the supply chain''s economic effectiveness but also have an environmental impact during the scrapping of the battery materials.

## V. OPTIMIZATION APPROACHES

**A. An Optimization Approach for Electric Vehicles**
In the present article, the charging demand for EVs is described using various frameworks in a variety of geographical areas. The framework is comprised of the following components: random utility model, activity-based equilibrium scheduling, pattern recognition in driving, stochastic model, trip prediction model, probabilistic model, fuzzy-based model, distributed optimization, forecasting model, data mining model, ant colony optimization, household activity pattern optimization, particle swarm optimization, linear programming, multi-objective optimization, and adaptive multi-objective optimization model.

The purpose of this study was to determine the possible benefits of all EVs' charging characteristics. Several investigations have been undertaken globally by various researchers to determine the optimal strategy for EV optimization. These optimization approaches are summarized in Table III.

**B. Concept of the Vehicle-to-Grid**
Kempton et al. pioneered the V2G idea in 2001. This technique is carried out by providing power to the grid with the help of a bidirectional charger. This charger is capable of G2V charging and V2G discharging [86].

The influence of bidirectional charging on LIBs has been postulated in V2G and G2V to determine their cell performance [87]. An overview of how to include various available technologies of energy storage into a distribution network for planning and operation and developments in battery technologies and policy surrounding V2G technology. Implementation of various approaches for managing battery deterioration and to improve the battery utilization for

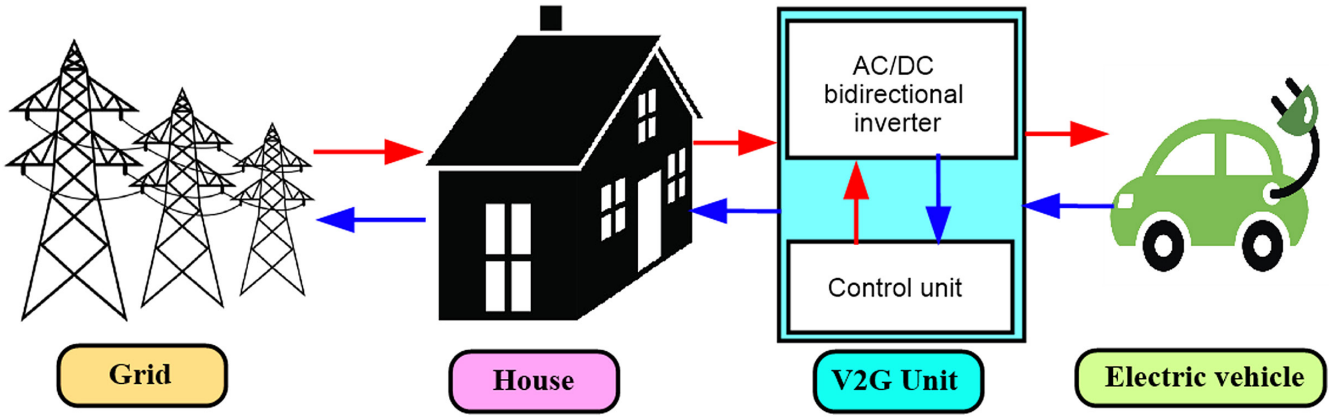


**Fig. 8.** Vehicle to-grid charging mechanism.

extending the battery life of the EV's is presented in [88-90]. Kester et al. [91] conducted a comparative analysis in the Nordic nations to determine how several EV specialists repeat strategy recommendations for V2G and EVs.

### C. An Optimization Approach for Vehicle-to-Grid

The concept of V2G eceived attention from all communities. In the present study, various investigations undertaken globally by several researchers to determine the optimal scheduling of V2G and G2V with the application of various optimization techniques are summarized in Table IV. Figure 8 illustrates the vehicle grid charging mechanism. Figure 9 illustrates the V2G with an aggregator.

Additionally, they suggested that the charging technique and aggressiveness of the vehicles might make V2G technology commercially viable. While the V2G system has various advantages, increasing the number of PHEVs may have a direct effect on the dynamics and performance of a distribution network by overloading transformers, cables, and feeders.

However, several experimental investigations have been conducted on the V2G particularly on the battery degradation concept [107-112]. Hence, the scope of the V2G technology is still under transition mode. Researchers are encouraged to conduct investigations on this technology and find an optimal solution.

## VI. CONCLUSION AND FUTURE DIRECTIONS

Hybrid EVs, PHEVs, and EVs all have the potential to improve vehicle fuel efficiency but at a higher cost than conventional vehicles. In general, their lower gasoline uses and greater productivity benefit

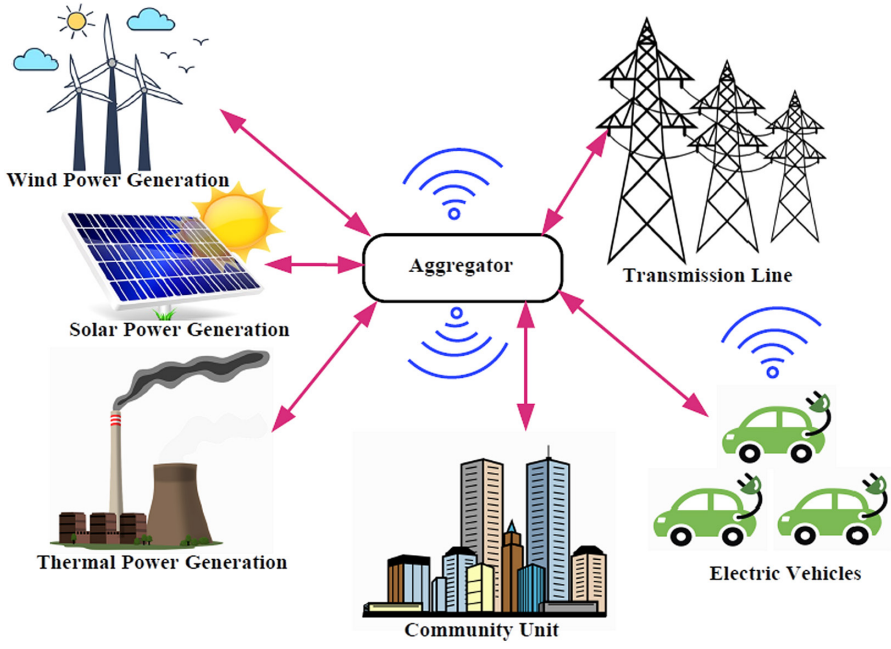


**Fig. 9.** Vehicle-to-grid system aggregator.

purchasers, society, automakers, and policymakers throughout their lives. This article includes a comprehensive review of the research, an overview, and instructions for conducting penetration rate studies of HEV, PHEV, and BEV in the Indian market. The Indian government's latest measures and different incentives will assist accelerate the country's e-mobility drive. The creation of a novel concept of V2G may be utilized to either supply electricity to the grid or to charge the battery in the absence of non-conventional energy sources. This technology is critical for energy security, renewable energy, and addressing global warming challenges. This study summarizes the challenges and issues associated with EVs in the Indian setting, which is the paper's primary innovation. However, an "intention" to adopt may not translate into a purchase. Additional research may reveal if intention will transfer to adoption. The link between intent to adopt and purchasing behavior requires extensive modeling, which is even more important when purchasing sophisticated environmentally friendly items, as the authors note. Four factors were examined in the study: Electric Converters (EC), perceived economic gain, Induction Machines (IM), and SoC. Other research might be conducted to evaluate the effects of additional confounders. These include customer perceptions of efficacy, information, skepticism, safety, risk, interest, and experience.

It would be beneficial to test this with actual EV owners in the future. With growing worldwide concern about the environment daily, this study provides enormous potential for future study.

**Peer-review:** Externally peer-reviewed.

**Acknowledgment:** The author would thank the management of the People Education Society (PES University), Bengaluru for supporting this research.

**Declaration of Interests:** The authors declare that they have no competing interest.

**Funding:** This study received no funding.

## REFERENCES

1. R. T. Doucette, and M. D. McCulloch, "Modeling the prospects of plug-in hybrid electric vehicles to reduce CO2 emissions," *Appl. Energy*, vol. 88, no. 7, pp. 2315–2323, 2011. [CrossRef]
2. Available: https://www.goldmansachs.com/insights.
3. Available: https://en.wikipedia.org/wiki/Electric_vehicle_industry_in_India.
4. Available: https://www.climatelinks.org/resources/greenhouse-gas-emissions-factsheet-india.
5. W. Kempton, and J. Tomić, "Vehicle-to-grid power implementation: From stabilizing the grid to supporting large-scale renewable energy," *J. Power Sources*, vol. 144, no. 1, pp. 280–294, 2005. [CrossRef]
6. Available: https://knoema.com/atlas/India/CO2-emissions.
7. R. J. Bessa, and M. A. Matos, "Economic and technical management of an aggregation agent for electric vehicles: A literature survey," *Euro. Trans. Electr. Power*, vol. 22, no. 3, pp. 334–350, 2012. [CrossRef]
8. N. Daina, A. Sivakumar, and J. W. Polak, "Modelling electric vehicles use: A survey on the methods," *Renew. Sustain. Energy Rev.*, vol. 68, pp. 447–460, 2017. [CrossRef]
9. F. Koyanagi, and Y. Uriu, "Modeling power consumption by electric vehicles and its impact on power demand," *Elect. Eng. Jpn*, vol. 120, no. 4, pp. 40–47, 1997. [CrossRef]
10. J. E. Kang, and W. W. Recker, "An activity-based assessment of the potential impacts of plug-in hybrid electric vehicles on energy and emissions using 1-day travel data," *Transp. Res. D*, vol. 14, no. 8, pp. 541–556, 2009. [CrossRef]
11. J. Dong, C. Liu, and Z. Lin, "Charging infrastructure planning for promoting battery electric vehicles: An activity-based approach using multiday travel data," *Transp. Res. C*, vol. 38, pp. 44–55, 2014. [CrossRef]
12. C. Weiller, "Plug-in hybrid electric vehicle impacts on hourly electricity demand in the United States," *Energy Policy*, vol. 39, no. 6, pp. 3766–3778, 2011. [CrossRef]
13. J. Axsen, and K. S. Kurani, "Anticipating plug-in hybrid vehicle energy impacts in California: Constructing consumer-informed recharge profiles," *Transp. Res. D*, vol. 15, no. 4, pp. 212–219, 2010. [CrossRef]
14. O. Sundström, and C. Binding, "Charging service elements for an electric vehicle charging service provider," *IEEE Power Energy Soc. Gen. Meet.*, 2011.
15. M. D. Galus, M. G. Vayá, T. Krause, and G. Andersson, "The role of electric vehicles in smart grids," *Wiley Interdiscip. Rev. Energy Environ.*, vol. 2, no. 4, pp. 384–400, 2013. [CrossRef]
16. J. Brady, and M. O'Mahony, "Modelling charging profiles of electric vehicles based on real-world electric vehicle charging data," *Sustain. Cities Soc.*, vol. 26, pp. 203–216, 2016. [CrossRef]
17. P. Morrissey, P. Weldon, and M. O'Mahony, "Future standard and fast charging infrastructure planning: An analysis of electric vehicle charging behaviour," *Energy Policy*, vol. 89, no. 2016, pp. 257–270, 2016. [CrossRef]
18. A. Foley, B. Tyther, P. Calnan, and B. Ó. Gallachóir, "Impacts of Electric Vehicle charging under electricity market operations," *Appl. Energy*, vol. 101, no. 2013, pp. 93–102, 2013. [CrossRef]
19. S. Steinhilber, P. Wells, and S. Thankappan, "Socio-technical inertia: Understanding the barriers to electric vehicles," *Energy Policy*, vol. 60, pp. 531–539, 2013. [CrossRef]
20. H. Yu, F. Tseng, and R. McGee, "Driving pattern identification for EV range estimation," 2012 IEEE International Electric Vehicle Conference, Greenville, SC, USA: 2012, pp. 1-7. [CrossRef]
21. J. G. Hayes, R. P. R. De Oliveira, S. Vaughan, and M. G. Egan, "Simplified electric vehicle power train models and range estimation," 2011 IEEE Vehicle Power and Propulsion Conference, Chicago, IL, USA: 2011, pp. 1-5. [CrossRef]
22. F. Salah, J. P. Ilg, C. M. Flath, H. Basse, and Cv van Dinther, "Impact of electric vehicles on distribution substations: A Swiss case study," *Appl. Energy*, vol. 137, pp. 88–96, 2015. [CrossRef]
23. N. Hartmann, and E. D. Özdemir, "Impact of different utilization scenarios of electric vehicles on the German grid in 2030," *J. Power Sources*, vol. 196, no. 4, pp. 2311–2318, 2011. [CrossRef]
24. F. Yang, Y. Sun, and T. Shen, "Nonlinear torque estimation for vehicular electrical machines and its application in engine speed control," *Proc. IEEE Int. Conf. Control Appl., no. October*, 2007, pp. 1382–1387.
25. X. Yu, T. Shen, G. Li, and K. Hikiri, "Regenerative braking torque estimation and control approaches for a hybrid electric truck," in Proceedings of the 2010 American Control Conference, ACC 2010, Baltimore, MD, USA: 2010, pp. 5832–5837. [CrossRef]
26. X. Yu, T. Shen, G. Li, and K. Hikiri, "Model-based drive shaft torque estimation and control of a hybrid electric vehicle in energy regeneration mode," *ICCAS-SICE*, vol. 2009, pp. 3543–3548, 2009.
27. L. Lu, X. Han, J. Li, J. Hua, and M. Ouyang, "A review on the key issues for lithium-ion battery management in electric vehicles," *J. Power Sources*, vol. 226, pp. 272–288, 2013. [CrossRef]
28. A. Panday, and H. O. Bansal, "A review of optimal energy management strategies for hybrid electric vehicle," *Int. J. Veh. Technol.*, vol. 2014, 1–19, 2014. [CrossRef]

29. S. F. Tie, and C. W. Tan, "A review of energy sources and energy management system in electric vehicles," *Renew. Sustain. Energy Rev.*, vol. 20, pp. 82–102, 2013. [CrossRef]
30. J. Y. Yong, V. K. Ramachandaramurthy, K. M. Tan, and N. Mithulananthan, "A review on the state-of-the-art technologies of electric vehicle, its impacts and prospects," *Renew. Sustain. Energy Rev.*, vol. 49, pp. 365–385, 2015. [CrossRef]
31. I. Miri, A. Fotouhi, and N. Ewin, "Electric vehicle energy consumption modelling and estimation—A case study," *Int. J. Energy Res.*, vol. 45, no. 1, pp. 501–520, 2021. [CrossRef]
32. J. Qiang, G. Ao, J. He, Z. Chen, and L. Yang, "An adaptive algorithm of NiMH battery state of charge estimation for hybrid electric vehicle," in IEEE International Symposium on Industrial Electronics, Cambridge: 2008, pp. 1556–1561. [CrossRef]
33. T. H. Bradley, and A. A. Frank, "Design, demonstrations and sustainability impact assessments for plug-in hybrid electric vehicles," *Renew. Sustain. Energy Rev.*, vol. 13, no. 1, pp. 115–128, 2009. [CrossRef]
34. A. Hajimiragha, C. A. Canizares, M. W. Fowler, and A. Elkamel, "Optimal transition to plug-in hybrid electric vehicles in Ontario, Canada, considering the electricity-grid limitations," *IEEE Trans. Ind. Electron.*, vol. 57, no. 2, pp. 690–701, 2010. [CrossRef]
35. S. B. Peterson, J. F. Whitacre, and J. Apt, "The economics of using plug-in hybrid electric vehicle battery packs for grid storage," *J. Power Sources*, vol. 195, no. 8, pp. 2377–2384, 2010. [CrossRef]
36. Z. Darabi, and M. Ferdowsi, "Aggregated impact of plug-in hybrid electric vehicles on electricity demand profile," *IEEE Trans. Sustain. Energy*, vol. 2, no. 4, pp. 501–508, 2011. [CrossRef]
37. S. Zoepf, D. Mackenzie, D. Keith, and W. Chernicoff, "Charging choices and fuel displacement in a large-scale demonstration of plug-in hybrid electric vehicles," *Transp. Res. Rec.*, vol. 2385, no. 1, pp. 1–10, 2013. [CrossRef]
38. A. Weis, P. Jaramillo, and J. Michalek, "Estimating the potential of controlled plug-in hybrid electric vehicle charging to reduce operational and capacity expansion costs for electric power systems with high wind penetration," *Appl. Energy*, vol. 115, no. x, pp. 190–204, 2014. [CrossRef]
39. J. García-Villalobos, I. Zamora, K. Knezović, and M. Marinelli, "Multi-objective optimization control of plug-in electric vehicles in low voltage distribution networks," *Appl. Energy*, vol. 180, pp. 155–168, 2016. [CrossRef]
40. K. J. Reddy, and N. Sudhakar, "High voltage gain interleaved boost converter with neural network based mppt controller for fuel cell based electric vehicle applications," *IEEE Access*, vol. 6, pp. 3899–3908, 2017.
41. K. Jyotheeswara Reddy, and N. Sudhakar, "A new RBFN based MPPT controller for grid-connected PEMFC system with high step-up three-phase IBC," *Int. J. Hydr. Energy*, vol. 43, no. 37, pp. 17835–17848, 2018. [CrossRef]
42. J. R. K., and S. N., "Design and analysis of a hybrid PV-PEMFC system with MPPT controller for a three-phase grid-connected system," *J. Green Eng.*, vol. 8, no. 2, pp. 151–176, 2018. [CrossRef]
43. K. J. Reddy, and N. Sudhakar, "ANFIS-MPPT control algorithm for a PEMFC system used in electric vehicle applications," *Int. J. Hydr. Energy*, vol. 44, no. 29, pp. 15355–15369, 2019. [CrossRef]
44. K. Kumar, R. Tiwari, P. V. Varaprasad, C. Babu, and K. J. Reddy, "Performance evaluation of fuel cell fed electric vehicle system with reconfigured quadratic boost converter," *Int. J. Hydr. Energy*, vol. 46, no. 11, pp. 8167–8178, 2021. [CrossRef]
45. Available: en.wikipedia.org/wiki/Electric_car_use_by_country.
46. M. D. Galus, and G. Andersson, "'Demand management of grid connected plug-in hybrid electric vehicles (PHEV)," in 2008 IEEE Energy 2030 Conference, 2008, pp. 1-8. [CrossRef]
47. R. A. Waraich, M. D. Galus, C. Dobler, M. Balmer, G. Andersson, and K. W. Axhausen, "Plug-in hybrid electric vehicles and smart grids: Investigations based on a microsimulation," *Transp. Res. C*, vol. 28, pp. 74–86, 2013. [CrossRef]
48. Y. Zou, H. Shi-Jie, L. Dong-Ge, G. Wei, and X. S. Hu, "Optimal energy control strategy design for a hybrid electric vehicle," *Discret Dyn. Natl Soc.*, vol. 2013, 1–8, 2013. [CrossRef]
49. X. Hu, C. M. Martinez, and Y. Yang, "Charging, power management, and battery degradation mitigation in plug-in hybrid electric vehicles: A unified cost-optimal approach," *Mech. Syst. Signal Process.*, vol. 87, pp. 4–16, 2017. [CrossRef]
50. X. Wu, X. Hu, X. Yin, and S. J. Moura, "Stochastic optimal energy management of smart home with PEV energy storage," *IEEE Trans. Smart Grid*, vol. 9, no. 3, pp. 2065–2075, 2018. [CrossRef]
51. Z. Hu *et al.*, "Multi-objective energy management optimization and parameter sizing for proton exchange membrane hybrid fuel cell vehicles," *Energy Convers. Manag.*, vol. 129, pp. 108–121, 2016. [CrossRef]
52. S. M. Rezvanizaniani, Z. Liu, Y. Chen, and J. Lee, "Review and recent advances in battery health monitoring and prognostics technologies for electric vehicle (EV) safety and mobility," *J. Power Sources*, vol. 256, pp. 110–124, 2014. [CrossRef]
53. Available: https://auto.hindustantimes.com/.
54. Available: https://jmkresearch.com/registered-ev-sales-in-india-in-2020-dropped-by-26-on-yoy-basis/.
55. Available: https://jmkresearch.com/registered-ev-sales-drop-20-y-o-y-in-fy2021/.
56. B. Yağcitekin, M. Uzunoğlu, and A. Karakaş, "A new deployment method for electric vehicle charging infrastructure," *Turk. J. Electr. Eng. Comput. Sci.*, vol. 24, no. 3, pp. 1292–1305, 2016.
57. M. U. Cuma, and T. Koroglu, "A comprehensive review on estimation strategies used in hybrid and battery electric vehicles," *Renew. Sustain. Energy Rev.*, vol. 42, pp. 517–531, 2015. [CrossRef]
58. M. Danko, J. Adamec, M. Taraba, and P. Drgona, "Overview of batteries State of Charge estimation methods," in *Transp. Res. Procedia*, vol. 40, pp. 186–192, 2019. [CrossRef]
59. H. E. A. Chacón, E. Banguero, A. Correcher, Á. Pérez-Navarro, and F. Morant, "Modelling, parameter identification, and experimental validation of a lead acid battery bank using evolutionary algorithms," *Energies*, vol. 12, no. 9, 2018.
60. M. Zhang, and X. Fan, "Review on the state of charge estimation methods for electric vehicle battery," *World Electr. Veh. J.*, vol. 11, no. 1, pp. 1–17, 2020. [CrossRef]
61. K. Sreeram, P. K. Preetha and P. Poornachandran, "Electric Vehicle Scenario in India: Roadmap,Challenges and Opportunities," 2019 IEEE International Conference on Electrical, Computer and Communication Technologies (ICECCT), Coimbatore, India: 2019, pp. 1-7. [CrossRef]
62. Available: https://ideas.4brad.com/comparing-electricity-gallon-gasoline.
63. Available: economictimes.indiatimes.com.
64. Available: www.siam.in.
65. W. H. K. Lam, and Y. Yin, "An activity-based time-dependent traffic assignment model," *Transp. Res. B Methodol.*, vol. 35, no. 6, pp. 549–574, 2001. [CrossRef]
66. L. V. Pérez, G. R. Bossio, D. Moitre, and G. O. García, "Optimization of power management in a hybrid electric vehicle using dynamic programming," *Math. Comput. Simul.*, vol. 73, no. 1–4, pp. 244–254, 2006. [CrossRef]
67. L. C. Fang, and S. Y. Qin, "Concurrent optimization for parameters of powertrain and control system of hybrid electric vehicle based on multi-objective genetic algorithms," in 2006 SICE-ICASE International Joint Conference, Busan, Korea (South): 2006, pp. 2424–2429. [CrossRef]
68. Z. Wang, B. Huang, W. Li, and Y. Xu, "Particle swarm optimization for operational parameters of series hybrid electric vehicle," in IEEE

International Conference on Robotics and Biomimetics, ROBIO; Kunming, China: 2006, 2006, pp. 682–688. [CrossRef]
69. Q. Gong, Y. Li, and Z. R. Peng, "Trip based power management of plug-in hybrid electric vehicle with two-scale dynamic programming," in VPPC 2007, Proceedings of the 2007 IEEE Vehicle Power and Propulsion Conference, Arlington, TX, USA: 2007, pp. 12–19. [CrossRef]
70. X. Wu, B. Cao, J. Wen, and Y. Bian, "Particle swarm optimization for plug-in hybrid electric vehicle control strategy parameter," in 2008 IEEE Vehicle Power and Propulsion Conference, Harbin, China: 2008, pp. 1-5. [CrossRef]
71. K. Ahn, S. Cho, and S. W. Cha, "Optimal operation of the power-split hybrid electric vehicle powertrain," in *Proc. Inst. Mech. Eng. D*, vol. 222, no. 5, pp. 789–800, 2008. [CrossRef]
72. K. Koprubasi *et al.*, "Application of model-based design techniques for the control development and optimization of a hybrid-electric vehicle," *SAE Technical Papers* 2009-01-0143, 2009. [CrossRef]
73. O. Sundström, and C. Binding, "Optimization methods to plan the charging of electric vehicle fleets," in *Proceedings of the International Conference on Control Communication and Power Engineering*, Vol. 1, no. 2, 2010, pp. 28–29.
74. S. Deilami, A. S. Masoum, P. S. Moses, and M. A. S. Masoum, "Real-time coordination of plug-in electric vehicle charging in smart grids to minimize power losses and improve voltage profile," *IEEE Trans. Smart Grid*, vol. 2, no. 3, pp. 456–467, 2011. [CrossRef]
75. E. Wiedemann, J. Meurle, and M. Lienkamp, "Optimization of electric vehicle concepts based on customer-relevant characteristics," *SAE Technical Papers 2012-01-0815*. 2012. [CrossRef]
76. C. Jin, J. Tang, and P. Ghosh, "Optimizing electric vehicle charging: A customer's perspective," *IEEE Trans. Veh. Technol.*, vol. 62, no. 7, pp. 2919–2927, 2013. [CrossRef]
77. S. Y. Chen, C. H. Wu, Y. H. Hung, and C. T. Chung, "Optimal strategies of energy management integrated with transmission control for a hybrid electric vehicle using dynamic particle swarm optimization," *Energy*, vol. 160, pp. 154–170, 2018. [CrossRef]
78. M. R. Sarker, H. Pandžić, and M. A. Ortega-Vazquez, "Optimal operation and services scheduling for an electric vehicle battery swapping station," *IEEE Trans. Power Syst.*, vol. 30, no. 2, pp. 901–910, 2015. [CrossRef]
79. S. Li, Y. Huang, and S. J. Mason, "A multi-period optimization model for the deployment of public electric vehicle charging stations on network," *Transp. Res. C*, vol. 65, pp. 128–143, 2016. [CrossRef]
80. M. R. Mozafar, M. H. Moradi, and M. H. Amini, "A simultaneous approach for optimal allocation of renewable energy sources and electric vehicle charging stations in smart grids based on improved GA-PSO algorithm," *Sustain. Cities Soc.*, vol. 32, pp. 627–637, 2017. [CrossRef]
81. A. Awasthi, K. Venkitusamy, S. Padmanaban, R. Selvamuthukumaran, F. Blaabjerg, and A. K. Singh, "Optimal planning of electric vehicle charging station at the distribution system using hybrid optimization algorithm," *Energy*, vol. 133, pp. 70–78, 2017. [CrossRef]
82. N. Chen, C. W. Tan, and T. Q. S. Quek, "Electric vehicle charging in smart grid: Optimality and valley-filling algorithms," *IEEE J. Sel. Top. Signal Process.*, vol. 8, no. 6, pp. 1073–1083, 2014. [CrossRef]
83. S. Limmer, and T. Rodemann, "Peak load reduction through dynamic pricing for electric vehicle charging," *Int. J. Electr. Power Energy Syst.*, vol. 113, no. September 2018, pp. 117–128, 2019. [CrossRef]
84. P. Vasant, J. A. Marmolejo, I. Litvinchev, and R. R. Aguilar, "Nature-inspired meta-heuristics approaches for charging plug-in hybrid electric vehicle," *Wirel. Netw.*, vol. 26, no. 7, pp. 4753–4766, 2020. [CrossRef]
85. M.-K. Tran, M. Akinsanya, S. Panchal, R. Fraser, and M. Fowler, "Design of a hybrid electric vehicle powertrain for performance optimization considering various powertrain components and configurations," *Vehicles*, vol. 3, no. 1, pp. 20–32, 2020. [CrossRef]
86. W. Kempton, J. Tomic, and S. Letendre, "UC Davis recent work title vehicle-to-grid power: Battery, hybrid, and fuel cell vehicles as resources for distributed electric power in California publication date," *IEEE Trans. Smart Grid*, 2001.
87. M. Dubarry, A. Devie, and K. McKenzie, "Durability and reliability of electric vehicle batteries under electric utility grid operations: Bidirectional charging impact analysis," *J. Power Sources*, vol. 358, pp. 39–49, 2017. [CrossRef]
88. H. Saboori, R. Hemmati, S. M. S. Ghiasi, and S. Dehghan, "Energy storage planning in electric power distribution networks – A state-of-the-art review," *Renew. Sustain. Energy Rev.*, vol. 79, pp. 1108–1121, 2017. [CrossRef]
89. C. K. Das, O. Bass, G. Kothapalli, T. S. Mahmoud, and D. Habibi, "Overview of energy storage systems in distribution networks: Placement, sizing, operation, and power quality," *Renew. Sustain. Energy Rev.*, vol. 91, pp. 1205–1230, 2018. [CrossRef]
90. M. A. Awadallah, and B. Venkatesh, "Energy storage in distribution system planning and operation: Current status and outstanding challenges," *Can. J. Electr. Comput. Eng.*, vol. 42, no. 1, pp. 10–19, 2019. [CrossRef]
91. J. Kester, L. Noel, G. Zarazua de Rubens, and B. K. Sovacool, "Promoting Vehicle to Grid (V2G) in the Nordic region: Expert advice on policy mechanisms for accelerated diffusion," *Energy Policy*, vol. 116, pp. 422–432, 2018. [CrossRef]
92. C. Guille, and G. Gross, "'Design of a conceptual framework for the V2G implementation," in 2008 IEEE Energy 2030 Conference, Atlanta, GA, USA: 2008, pp. 1-3. [CrossRef]
93. C. Guille, and G. Gross, "A conceptual framework for the vehicle-to-grid (V2G) implementation," *Energy Policy*, vol. 37, no. 11, pp. 4379–4390, 2009. [CrossRef]
94. M. Musio, P. Lombardi, and A. Damiano, "Vehicles to grid (V2G) concept applied to a virtual power plant structure," in 19th International Conference on Electrical Machines, ICEM; Rome, Italy: 2010, 2010, pp. 1-6. [CrossRef]
95. J. Soares, T. Sousa, H. Morais, Z. Vale, and P. Faria, "An optimal scheduling problem in distribution networks considering V2G," in IEEE SSCI 2011 - Symposium Series on Computational Intelligence - CIASG 2011: 2011 IEEE Symposium on Computational Intelligence Applications in Smart Grid, Paris, French Guiana: 2011, pp. 1-8. [CrossRef]
96. S. S. Hosseini, A. Badri, and M. Parvania, "The plug-in electric vehicles for power system applications: The vehicle to grid (V2G) concept," in 2012 IEEE International Energy Conference and Exhibition (ENERGYCON), Florence, Italy: 2012, pp. 1101-1106. [CrossRef]
97. S. Rui, C. Zhong, C. Yanxia and L. Zhou, "Bidirectional power transfer control based on V2G concept," 2014 IEEE PES Asia-Pacific Power and Energy Engineering Conference (APPEEC), Hong Kong, China: 2014, pp. 1-5. [CrossRef]
98. S. Stüdli, E. Crisostomi, R. Middleton, and R. Shorten, "Optimal real-time distributed V2G and G2V management of electric vehicles," *Int. J. Control*, vol. 87, no. 6, pp. 1153–1162, 2014. [CrossRef]
99. Y. Ma *et al.*, "An overview on V2G strategies to impacts from EV integration into power system," in 2016 Chinese Control and Decision Conference (CCDC), Yinchuan, China: 2016, pp. 2895-2900. [CrossRef]
100. K. Ramakrishna Reddy, and S. Meikandasivam, "Smart distribution network with integration of stochastic renewable energy sources and plug-in electric vehicles: Challenges and issues," *J. Green Eng.*, vol. 8, no. 4, pp. 431–474, 2018.
101. K. Ramakrishna Reddy, and S. Meikandasivam, "Optimal Distribution of Plug-In-Electric Vehicle's Storage Capacity Using Water Filling Algorithm for Load Flattening and Vehicle Prioritization Using ANFIS," *Electr. Power Syst. Res.*, vol. 165, pp. 120–133, 2018.

102. K. R. Reddy, and S. Meikandasivam, "Load flattening and voltage regulation using plug-in electric vehicle's storage capacity with vehicle prioritization using ANFIS," *IEEE Trans. Sustain. Energy*, vol. 11, no. 1, pp. 260–270, 2020. [CrossRef]
103. K. Ramakrishna Reddy, and S. Meikandasivam, "A Novel Strategic Scheduling of Plug-in-Electric Vehicles to Reduce Power Fluctuations in an Active Distribution Network," *Applications of Computing, Automation and Wireless Systems in Electrical Engineering*, vol. 553, pp. 859–863, 2019.
104. K. Ramakrishna Reddy, and S. Meikandasivam, "Maximization of Plug-In Electric Vehicle's Exploitation for Load Flattening with Consideration of Customer Satisfaction," *Applications of Computing, Automation and Wireless Systems in Electrical Engineering*, vol. 553, pp. 859–863, 2019.
105. K. Ramakrishna Reddy, S. Meikandasivam, and D. Vijayakumar, "A novel strategy for maximization of plug-in electric vehicle's storage utilization for grid support with consideration of customer flexibility," *Electr. Power Syst. Res.*, vol. 170, pp. 158–175, 2019. [CrossRef]
106. M. Jafari, A. Kavousi-Fard, T. Niknam, and O. Avatefipour, "Stochastic synergies of urban transportation system and smart grid in smart cities considering V2G and V2S concepts," *Energy*, vol. 215, 2021. [CrossRef]
107. B. Tepe, J. Figgener, S. Englberger, D. U. Sauer, A. Jossen, and H. Hesse, "Optimal pool composition of commercial electric vehicles in V2G fleet operation of various electricity markets," *Appl. Energy*, vol. 308, p. 118351, 2022. [CrossRef]
108. J. Guo, J. Yang, Z. Lin, C. Serrano, and A. M. Cortes, "Impact analysis of v2g services on ev battery degradation -a review," in 2019 IEEE Milan PowerTech, Milan, Italy: 2019, pp. 1-6. [CrossRef]
109. M. Dubarry, G. Baure, and A. Devie, "Durability and reliability of EV batteries under electric utility grid operations: Path dependence of battery degradation," *J. Electrochem. Soc.*, vol. 165, no. 5, pp. A773–A783, 2018. [CrossRef]
110. A. Ahmadian, M. Sedghi, A. Elkamel, M. Fowler, and M. A. Golkar, "Plug-in electric vehicle batteries degradation modeling for smart grid studies: Review, assessment and conceptual framework," *Renew. Sustain. Energy Rev.*, vol. 81, no. June, pp. 2609–2624, 2018. [CrossRef]
111. A. W. Thompson, "Economic implications of lithium ion battery degradation for Vehicle-to-Grid (V2X) services," *J. Power Sources*, vol. 396, no. April, pp. 691–709, 2018. [CrossRef]
112. G. Baure, and M. Dubarry, "Durability and reliability of EV batteries under electric utility grid operations: Impact of frequency regulation usage on cell degradation," *Energies*, vol. 13, no. 10, 2020. [CrossRef]